Durham E-Theses

Crustal structure of the Cape Verde Swell: Insights into the flexural response of the lithosphere to loading

WILSON, DEAN,JAMES

How to cite:

WILSON, DEAN,JAMES (2011) *Crustal structure of the Cape Verde Swell: Insights into the flexural response of the lithosphere to loading*, Durham theses, Durham University. Available at Durham E-Theses Online: http://etheses.dur.ac.uk/3230/

Use policy

The full-text may be used and/or reproduced, and given to third parties in any format or medium, without prior permission or charge, for personal research or study, educational, or not-for-profit purposes provided that:

- a full bibliographic reference is made to the original source
- a link is made to the metadata record in Durham E-Theses
- the full-text is not changed in any way

The full-text must not be sold in any format or medium without the formal permission of the copyright holders.

Please consult the full Durham E-Theses policy for further details.

Academic Support Office, Durham University, University Office, Old Elvet, Durham DH1 3HP
e-mail: e-theses.admin@dur.ac.uk Tel: +44 0191 334 6107
http://etheses.dur.ac.uk

CRUSTAL STRUCTURE OF THE CAPE VERDE SWELL:

INSIGHTS INTO THE FLEXURAL RESPONSE OF THE LITHOSPHERE TO LOADING

D J WILSON

PhD

2011

Crustal structure of the Cape Verde Swell: Insights into the flexural response of the lithosphere to loading

Dean James Wilson

A thesis submitted for the degree of
Doctor of Philosophy
at Durham University

Department of Earth Sciences
July 2011

Copyright © D.J. Wilson, 2011

The copyright of this thesis rests with the author. No quotation from it should be published without the prior written consent and information derived from it should be acknowledged.

Software used:

This thesis was written in Microsoft Word. Most figures were plotted with the *Generic Mapping Tools* (GMT) written by Wessel & Smith (1998). *Seismic Unix* (Cohen & Stockwell, 2000) was used for seismic data plotting.

Crustal structure of the Cape Verde Swell: Insights into the flexural response of the lithosphere to loading

Dean J. Wilson

Throughout the ocean basins many broad regions of anomalously shallow topography exist that do not fit the widely accepted model of conductive plate cooling and subsidence as a function of lithospheric age. These 'swells' often coincide with positive geoid, Free-air gravity and heat flow anomalies as well as groups of ocean islands and seamounts. Various mechanisms have been proposed to explain how this anomalous topography is isostatically supported at depth, including increased crustal buoyancy and dynamic asthenospheric support.

The Cape Verde Swell is the largest oceanic mid-plate swell on Earth at ~1800 km in diameter, with a crest ~2.2 km high, and positive geoid, gravity and heat flow anomalies of 8 m, 30 mGal and 10-15 mW m^{-2}, respectively. These characteristics and its location on the slow-to-stationary African Plate, which concentrates the volcanism and associated geophysical anomalies within a relatively small areal extent, makes the Cape Verde Swell an ideal location to test the various proposed mechanisms for swell support.

Wide-angle seismic refraction data along an ~474 km profile, extending from the Cape Verde Swell crest, is analysed and modelled to produce a 2-D velocity-depth model of the crustal structure. The resulting model reveals no widespread thickening of the lower oceanic basement, despite evidence for localised thickening beneath the islands from other studies. Subsequent 3-D 'whole plate' lithospheric flexure modelling reveals that, on a regional scale, the plate is stronger than expected based on its age, with some evidence for localised weakening around the islands.

Overall, the results of this study suggest that the anomalously shallow topography of the Cape Verde Swell is primarily maintained by a dynamic upwelling of hot, low density material impinging on the base of the lithosphere. Over time, conduction from this hot column has thermally rejuvenated the lithosphere on a local scale, leading to additional uplift, melting and volcanism associated with the islands.

Declaration

This thesis describes my original work except where acknowledgement is made in the text. It does not exceed the word limit and is not substantially the same as any work that has been, or is being submitted to any other university for any degree, diploma or any other qualification.

Dean J. Wilson

July 2011

Acknowledgements

As a humble reader of these acknowledgements, and quite possibly of the entirety of this hefty tome, you are much deserving of my gratitude. I am indebted to you for your personal contribution whether it was through the development of my skills and enhancement of my studies or indirectly by helping me to maintain a good sense of humour about everything.

It is with great *certainty* that I can say:

"without you this would *probably* not have been possible".

Christine, you have been an excellent supervisor with a great deal of patience. I hope that I have managed to fulfil (at least in part) your expectations. Your dedication to your work has been, and will continue to be, an inspiration to me. Tony and Ingo, you have both offered excellent opportunities to work outside of Durham, allowing me to develop a greater understanding of the project and the acquisition, processing and modelling of geophysical data. Ultimately, you have all helped me to become a better researcher. I have received some great advice, improved my critical thinking and time management (special thanks to Christine's amazing powers of organisation and concentration) and built up a vast array of technical skills that will benefit me long into the future.

Thanks to the scientists, officers and crew aboard R/V *Meteor* cruise M62/3, without whom I would have had no data to work with. Also, thanks to Wiebke Brunn and others at IFM-GEOMAR who very kindly provided their 2-D velocity-depth models so that I could constrain the 3-D flexure modelling results described in the latter half of this work. Funding was provided by the Durham University Doctoral Fellowship Scheme.

Alan, I have been an excellent minion for you! Of course this was all thanks to your impressive mentoring. Thank you for all the great memories (so far) of life at sea. Yo ho, yo ho, and a nice cup of tea. A pirate's life for me! Thank you to all the other scientists (and crew) that I've been to sea with and those that I've met at conferences, as well as the stalwart bunch of grog-swilling geology postgrads in the department (also those at Oxford and IFM-GEOMAR) who have provided the entertainment and chances to escape from the daily struggle with science.

Special thanks to my reviewer and proof-reader extraordinaire. You did a great job of noticing all of the broken... There would certainly have been a lot more speeling mistakes without your eagle eyes.

Last, but not least, to my family for their outstanding support and unwavering belief in me, as always. You have offered fantastic encouragement throughout and given me the determination to persevere at the times when I needed it most.

Thank you one-and-all.

Glossary of terms, abbreviations and acronyms

The following terms, abbreviations and acronyms are used throughout this thesis:

2-D	two-dimensional
3-D	three-dimensional
b.s.l.	below sea level
CHARISMA	Cape Verde Hotspot: A Seismic Refraction study of ISostasy and MAgmatic underplating
CDP	common depth point
DSDP	Deep Sea Drilling Program
FAA	Free-air gravity anomaly
F-STR	Fogo-Santiago Ridge
GEBCO	General Bathymetric Chart of the Oceans
MAR	Mid-Atlantic Ridge
MCS	multichannel seismic
OBH	ocean bottom hydrophone
OBS	ocean bottom seismograph
P_w	water wave
P_{wm}	water wave multiple
P_s	*P*-wave shallow subseabed refraction
P_{g1}	*P*-wave upper crustal refraction
P_{g2}	*P*-wave lower crustal refraction
P_n	*P*-wave mantle refraction
P_mP	*P*-wave Moho reflection
rms	root-mean-square
RRS	Royal Research Ship
R/V	Research Vessel
SEG-Y	Society of Exploration Geophysicists seismic recording standard Y (Barry *et al.*, 1975)
SNR	signal-to-noise ratio
T_e	effective elastic thickness of the lithosphere
TWTT	two-way traveltime
WA	wide-angle

Contents

List of figures

List of tables

1. Introduction and geological setting

1.1 Intra-oceanic plate volcanism

Plate tectonic theory (e.g. Dewey & Bird, 1970) attempts to explain the cause, origin and location of the majority of the most striking dynamic geological features that are observed on the surface of the Earth, from mountain belts to oceanic trenches. These dynamic features largely result from complex interactions between adjacent lithospheric plates, especially collision and subduction. However, despite the general acceptance of plate tectonics as an all-encompassing theory, describing the evolution of the oceanic and continental lithosphere, numerous anomalous features are observed, including aseismic ridges, oceanic core complexes and seamounts, and these are often located at a great distance from any plate boundaries. The most striking of these features is, arguably, large-scale intra-oceanic plate volcanism (Koppers & Watts, 2010).

Intra-plate sites of persistent, long-term volcanic activity were initially termed 'hotspots' (Wilson, 1963) due to the vast volumes of melt produced form the mantle, apparently without the aid of external tectonic forces, even though they are often associated with a similar scale of volcanism to that observed at plate boundaries. Formation of hotspot-related volcanic edifices occurs either contemporaneously with crustal accretion at a mid-ocean ridge axis, at a plate age of 0 Ma (e.g. Iceland; Bijwaard & Spakman, 1999; Jones, 2003), or any time subsequently in a mid-plate setting as the underlying plate cools and mechanically ages.

Intra-oceanic plate seamounts and volcanoes are often observed in clusters or linear chains. Radiometric $^{40}Ar/^{39}Ar$ dating of samples from ocean island basalts (e.g. Duncan & Keller, 2004; Koppers *et al.*, 2004; Holm *et al.*, 2008) reveals that hotspot volcanism may be intermittently active for >75 Ma, often with more than 5 Ma between major eruptive phases. Some linear chains of ocean islands and seamounts, such as the Hawaiian Islands (Watts & ten Brink, 1989) or the Louisville Ridge (Contreras-Reyes *et al.*, 2010), demonstrate a distinct age-progression and these

hotspot tracks can often be traced back to large igneous provinces using records of palaeoplate motions relative to a fixed mantle hotspot reference frame (Duncan & Richards 1991).

Large volcanic island groups stand out as clear topographic anomalies in the surrounding ocean basins and exert a considerable load on the lithosphere. Such loads must be supported at depth to maintain isostatic equilibrium. Several mechanisms have been proposed which may act to support surface loads or cause an upward acting load to counteract them. Using a model for the standard evolution of oceanic lithosphere it is possible to quantify the surface loads and investigate how the lithosphere beneath differs compared to 'normal' lithosphere leading, in turn, to an improved understanding of the underlying support mechanisms.

1.1.1 Evolution of the oceanic lithosphere

Oceanic lithosphere is created at mid-ocean ridges to accommodate divergent plate motion following the conclusion of a continental rifting event. Acting as the outer thermal mechanical boundary layer of the Earth, the oceanic lithosphere buffers the transfer of excess thermal energy, above background radiogenic production, from the underlying asthenosphere to the hydrosphere. As thermal energy from the asthenosphere is gradually dissipated through the lithosphere, the geothermal gradient decreases, the lithosphere becomes denser and it undergoes subsidence to maintain isostatic equilibrium. A characteristic pattern of cooling and subsidence, increasing from the ridge axis to the continental margin, can be observed, which can be explained by an exponential decrease in surface heat flow and an increase in bathymetry with age (Figure 1.1; Davis & Lister, 1974: Sclater *et al.*, 1980; Stein & Stein, 1992).

Seafloor morphology and crustal structure vary depending on the nature of the mid-ocean ridge system at which the crust was created, and are controlled by factors including the along-axis magma supply and the rate of plate separation. Through a compilation of rare earth element abundances and seismic data, White *et al.* (1992) determined average crustal thickness and velocity-depth profile estimates for the Pacific and Atlantic oceans (Figure 1.2) using a simplistic three-layer model of vertical crustal structure: layer 1 – sediments; layer 2 – extrusive pillow basalts and intrusive dykes; layer 3 – massive gabbros.

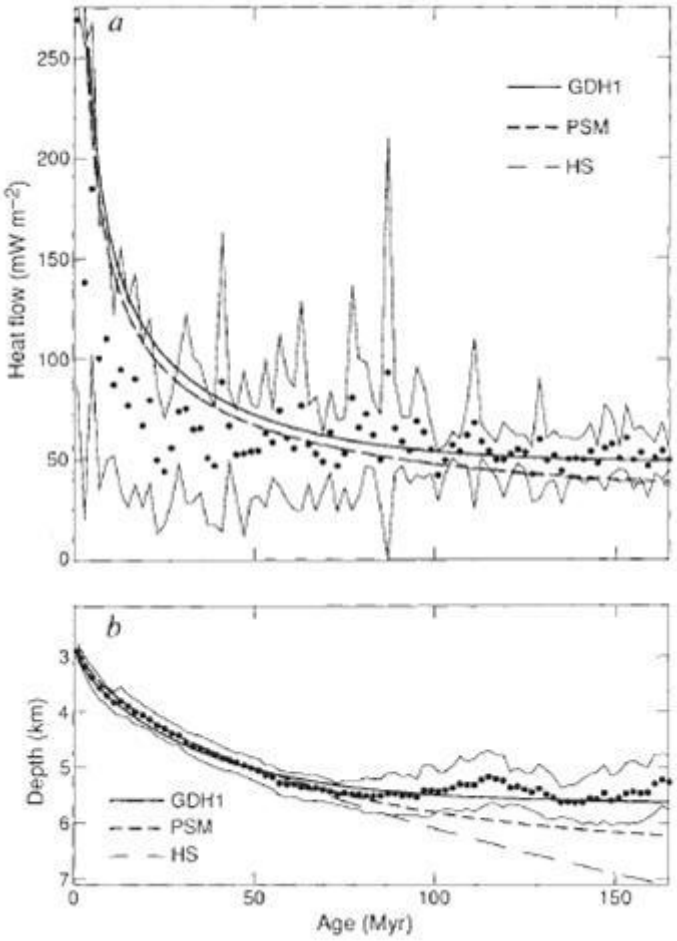

Figure 1.1 Models to explain the exponential decrease in surface heat flow, a), and increase in bathymetry, b), with age of the oceanic lithosphere (after Stein & Stein, 1992). The GDH1 model represents a better fit to the data for ages >80 Ma compared to the plate model of Parsons & Sclater (1977) and a simple cooling half space model, referred to in the figure as PSM and HS, respectively.

In their definition, standard Atlantic oceanic crust is ~1 km thicker than standard Pacific crust, manifest as a clear distinction in the thickness of oceanic crustal layer 2 (Figure 1.2a & b). At the slow-spreading Mid-Atlantic Ridge (MAR), a thick extrusive section of the crust is observed at the axis. A range of velocity-depth profiles for mature Atlantic crust (Figure 1.2c) demonstrates a more pronounced upper crustal velocity gradient compared to standard Atlantic crust (Figure 1.2b), that may be related to secondary processes such as hydrothermal circulation, and a discrete step in *P*-wave velocity is more apparent at the boundary between oceanic crustal layer 2 and layer 3.

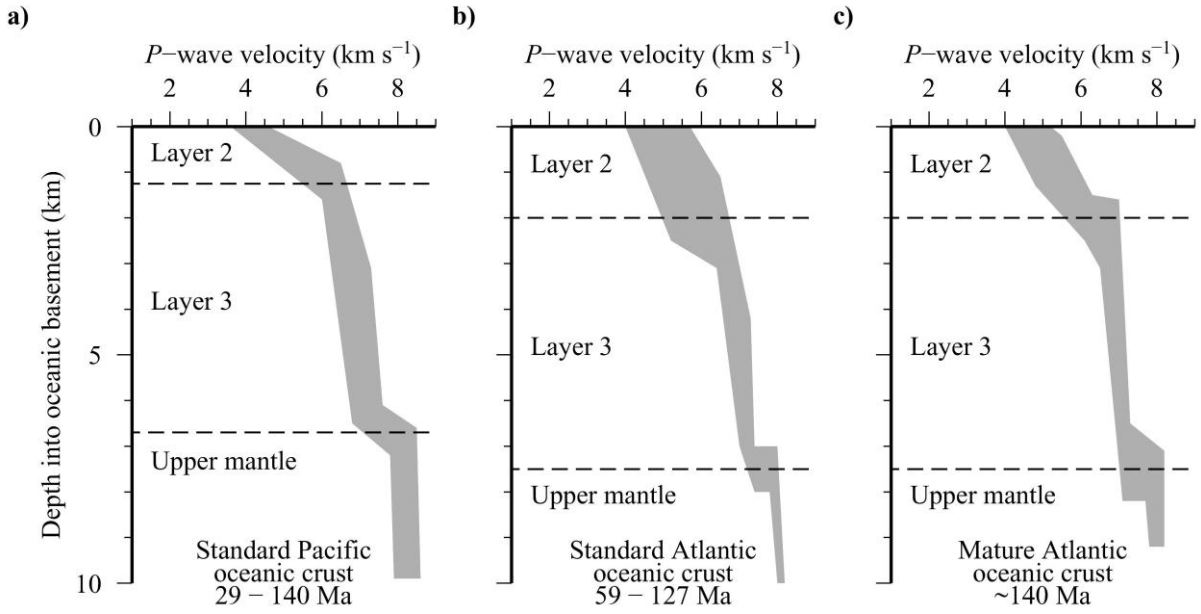

Figure 1.2 Range in the expected velocity-depth structure for standard Pacific oceanic crust aged between 29 and 140 Ma, a), standard Atlantic oceanic crust aged between 59 and 127 Ma, b), and mature Atlantic oceanic crust aged ~140 Ma, c) (after White *et al.*, 1992). Horizontal dashed black lines indicate the approximate depths of the boundaries between oceanic layer 2 (extrusive pillow basalts and intrusive dykes), layer 3 (gabbros) and the uppermost mantle.

As the rheology of the oceanic lithosphere is strongly temperature dependent its mechanical strength increases as it cools. The expected long-term strength (>0.1 Ma) of the lithosphere can be predicted from its age and the elastic thickness of the lithosphere (T_e) is used to express this strength numerically. The expected T_e is roughly equivalent to the depth of the 450 °C isotherm (Watts, 2001; Figure 1.3). The apparent strength of the lithosphere can be measured by its flexural response to loading, through analysis of the amplitude and wavelength of subsidence recorded by the thickening of moat infill sediments following volcanic island construction (e.g. Collier & Watts, 2001). Unusual variation in the thermo-mechanical structure of the lithosphere can be detected by comparing the apparent strength of the lithosphere with the expected T_e. Measurement of lithospheric structure by seismic experiments and subsequent flexure modelling will, therefore, provide insights into the local and regional compensation of intra-oceanic plate loads.

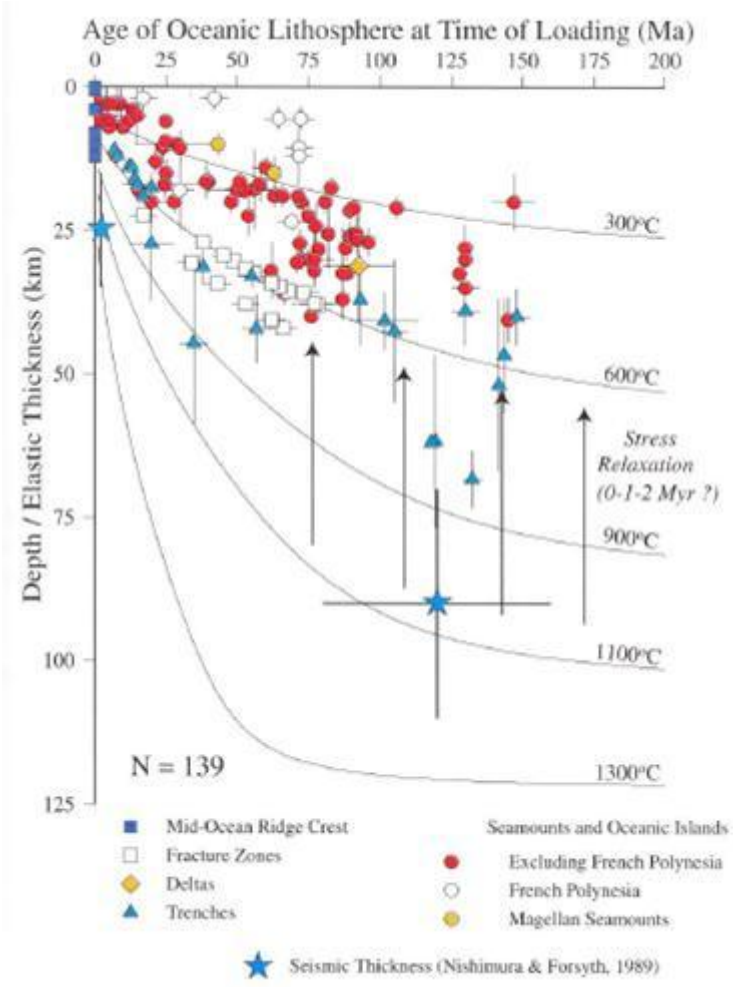

Figure 1.3 Relationship between the elastic thickness of the oceanic lithosphere (T_e) and the age of the lithosphere at the time of loading for oceanic features including seamounts and oceanic islands (after Watts & Zhong, 2000). T_e is defined as being approximately equivalent to the depth to the 450 °C isotherm.

1.1.2 Islands supported by undercrustal material

The addition of large volumes of igneous material onto the upper surface of oceanic crust results in local and regional lithospheric isostatic disequilibrium. Flexural adjustment, to re-establish equilibrium, may occur over a period of 0.1 to 1-2 Ma (Watts, 2001). However, many ocean islands and seamounts maintain considerable topography above the surrounding regional seabed depth and are much older than this re-adjustment timescale, suggesting that the downward-acting surface load is counteracted at depth in some manner. One possible explanation is that they are partially supported at depth by a 'root' of buoyant material added to the base of the crust, similar to models of crustal thickening at orogenic continental mountain ranges

(e.g. Avouac & Burov, 1996). If the root is thick enough, it is possible to image it seismically and there is evidence for additional undercrustal material beneath several oceanic islands.

In this thesis, the term undercrustal material is used to describe the thickened root that is often present beneath ocean islands rather than the term underplate, which is widely used in the literature. This substitution is made to avoid confusion between the various swell support hypotheses that are being tested, which include material added to the base of the crust or the base of the plate and, hence, the use of the term underplate would be ambiguous in the context of this study.

The Hawaiian Islands are the most renowned and well-studied example of intra-oceanic plate volcanism. Located in the centre of the Pacific Ocean on lithosphere aged between 80 and 100 Ma, the islands are the focal point of recent volcanic activity (5-0 Ma) along an ~3500 km hotspot trace of islands and seamounts extending to the northeast. An increase in crustal thickness, from a background value of ~7 km, has been interpreted from expanding spread seismic profiles extending either side of Oahu (Watts *et al.*, 1985) and located near the island of Kauai (Lindwall, 1988). In both cases, an additional layer of material ~300 km in width and between 2 and 4 km thick was imaged beneath the base of the pre-existing crust with *P*-wave velocities >7.3 km s^{-1}, exceeding the range expected for standard oceanic basement rocks (4.0 to 7.3 km s^{-1} – White *et al.*, 1992; Mutter & Mutter 1993).

In the East Pacific, the Marquesas Islands (aged 6-1 Ma) are located on lithosphere that is ~55 Ma old (Filmer *et al.*, 1993). Caress *et al.* (1995) found evidence from wide-angle (WA) seismic refraction data for an increase in thickness of the igneous component of the crust from a background of ~7 km to between 15 and 17 km (including the volcanic platform) beneath the island chain. At the base of the crust, in a region 275 km wide and between 2 and 8 km thick, unusually high *P*-wave velocities of 7.3 to 7.75 km s^{-1} are required to fit the observed traveltime data (Figure 1.4). Two WA reflections were observed and were subsequently interpreted to be reflecting from interfaces at the base of the pre-existing oceanic crust and the base of the addional undercrustal material. The total volume of undercrustal material was estimated to be twice that of the surface volcanics (Caress *et al.*, 1995).

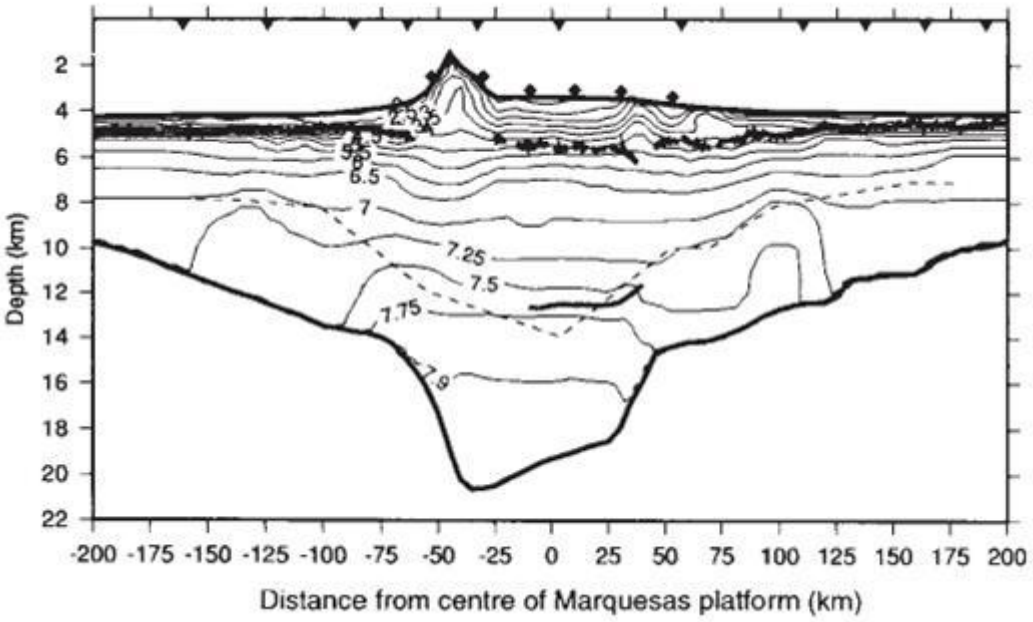

Figure 1.4 *P*-wave velocity model of the oceanic crust beneath the Marquesas Islands (after Caress *et al.*, 1995) demonstrating a clear body of undercrustal material. High *P*-wave velocities (7.30-7.75 km s^{-1}), typical of undercrustal material, were found to be present in a 2-8 km thick layer at the base of the standard thickness oceanic crust.

A combination of multichannel seismic (MCS) reflection and WA seismic refraction data was used to model variations in crustal thickness along the western Galápagos Spreading Centre (Canales *et al.*, 2002). The depth to the Moho, approaching the Galápagos Islands from the west, was found to increase by ~2 km over a lateral distance of ~300 km, similar to the dimensions of the root imaged beneath Hawaii.

A seismic experiment to determine the crustal structure beneath the Ninetyeast Ridge in the Indian Ocean (Grevemeyer *et al.*, 2001a) revealed a layer of undercrustal material up to 5 km thick extending ~250 km along profile, with a high *P*-wave velocity (~7.5 km s^{-1}) intermediate between those expected for lower crust and upper mantle. A strong WA reflection was observed in the data, similar to that observed at the Marquesas Islands (Caress *et al.*, 1995), and was interpreted to represent the interface between the newly added undercrustal material and the pre-hotspot influenced crust. Grevemeyer *et al.* (2001a) suggest that the undercrustal material had been added to the base of the crust over a period of 15-20 Ma, implying that the process leading to emplacement of a significant volume of material is gradual.

At the island of La Réunion (aged 5-2.1 Ma), an undercrustal body with high *P*-wave velocities of 7.5 to 7.8 km s^{-1} is observed over a distance of ~200 km along profiles extending from the northwest to the southeast, and is consistently 3 km thick (Charvis *et al.*, 1999). The ratio of the volume of undercrustal to erupted material at La Réunion (0.50) is less than that seen at both the Marquesas Islands (1.90) and Hawaii (0.75) despite a similar age for all of the islands.

Modelling of traveltime picks from WA seismic refraction data acquired along profiles over both the Josephine Seamount (Peirce & Barton, 1991) and the Great Meteor Seamount (Weigel & Grevemeyer, 1999) in the North Atlantic, revealed high *P*-wave velocities, >7.2 km s^{-1}, at the base of the crust that had been thickened by up to 5 km over regions ~100 km wide.

A summary of the thickness, extent and the range of *P*-wave velocities observed at the various islands and seamounts, as well as the age of the islands and the lithosphere on which they sit can be found in Table 1.1. There is no immediately apparent relationship between the age of the lithosphere and the thickness of the undercrustal material, as can be seen by comparing data for the Hawaiian, Galápagos and Marquesas islands. The Marquesas Islands show evidence for the greatest thickness of material but the age of the lithosphere is intermediate between that beneath Hawaii and the Galápagos Islands. It is possible that the observed variation in the volume of undercrustal material beneath islands is instead due to non age-related structural differences in the pre-hotspot lithosphere or differences in the temperature elevation of the underlying asthenospheric mantle.

Table 1.1 Summary of the thickness, lateral extent and *P*-wave velocities of undercrustal material observed beneath young and old islands and seamounts located on oceanic lithosphere of varying age. * Negative thickness denotes intracrustal intrusion. † Indirect estimate from amplitude modelling.

Island(s) or seamount	Thickness (km)	Lateral extent (km)	*P*-wave velocities (km s^{-1})	Age of lithosphere (Ma)	Age of islands or seamounts (Ma)
Hawaiian	2-4	~300	>7.30	80-100	0-5
Marquesas	2-8	275	7.30-7.75	55	1-6
Galápagos	<2	~300	~7.45	~7	≤7
Ninetyeast	<5	~250	~7.50	40-80	N/A
La Réunion	3	~200	7.50-7.80	~60	2-5
Josephine	1-2	100	7.20-7.40	110	108-109
Great Meteor	<2	100	7.20-7.70	80	15
Louisville	-2*	<100	7.20-7.60	90	≤80
Tenerife	0	N/A	N/A	>140	6-16
Gran Canaria	6-8	<60	7.60-7.80	>140	<15
Society	0	N/A	>7.10†	80-90	0-4

1.1.3 Islands without undercrustal material

Although there is a large catalogue of islands and seamounts where direct evidence has been found for the existence of an undercrustal body with high *P*-wave velocities, such bodies are not observed beneath all ocean islands.

In the South Pacific Ocean, the Louisville Ridge extends from the current location of the hotspot at 50° S 140° W, to its intersection with the Tonga-Kermadec Trench at 25° S 175° W. Contreras-Reyes *et al.* (2010) produced a two-dimensional (2-D) velocity-depth model for the Louisville Guyot from WA seismic refraction data, that indicated a core of high *P*-wave velocities, between 7.2 and 7.6 km s^{-1}, in the lowermost crust but, contrary to the other examples presented in the previous section, demonstrated no significant crustal thickening (Figure 1.5). Models of lithospheric flexure with a T_e of 10 km fit the observed Moho depth beneath the seamount, which was matches the age of the northwest end of the Louisville Ridge estimated from dredge samples (60-80 Ma, Koppers *et al.*, 2004), and the age of the lithosphere determined from magnetic anomalies (~90 Ma, Müller *et al.*, 2008). Contreras-Reyes *et al.* (2010) propose from these observations, that intracrustal or undercrustal emplacement depends on the thermal state of the lithosphere. Whereas in previous examples undercrustal emplacement occurred, in this case intracrustal intrusion dominated as the oceanic lithosphere at time of volcanism was young (~10 Ma) and hot, causing intrusion and reworking of the existing crust rather than addition of distinct material.

In the Canaries, at Tenerife (aged 16-6 Ma), located in the North Atlantic, the age of the lithosphere is >140 Ma. Watts *et al.* (1997) found no evidence, within the resolution limits of their seismic data, for a (>1 km thick) region of high *P*-wave velocities (>7.3 km s^{-1}) at the base of the crust, elsewhere suggested to be indicative of undercrustal material that is added during concurrent extrusive volcanism (e.g. Caress *et al.*, 1995). However, at Gran Canaria there was some evidence, from a limited number of WA reflections identified on record sections from a single land station, for a region of undercrustal material with *P*-wave velocities of 7.6-7.8 km s^{-1} extending 6-8 km beneath the base of the crust, limited to within 20 km of the island (Ye *et al.*, 1999). Although the results of these two studies are contradictory, the absence of irrefutable seismic evidence like that for Hawaii (e.g. Watts *et al.*, 1985)

and the Galápagos Islands (Canales *et al.*, 2002) suggests that undercrustal material is not prevalent beneath the Canary Islands.

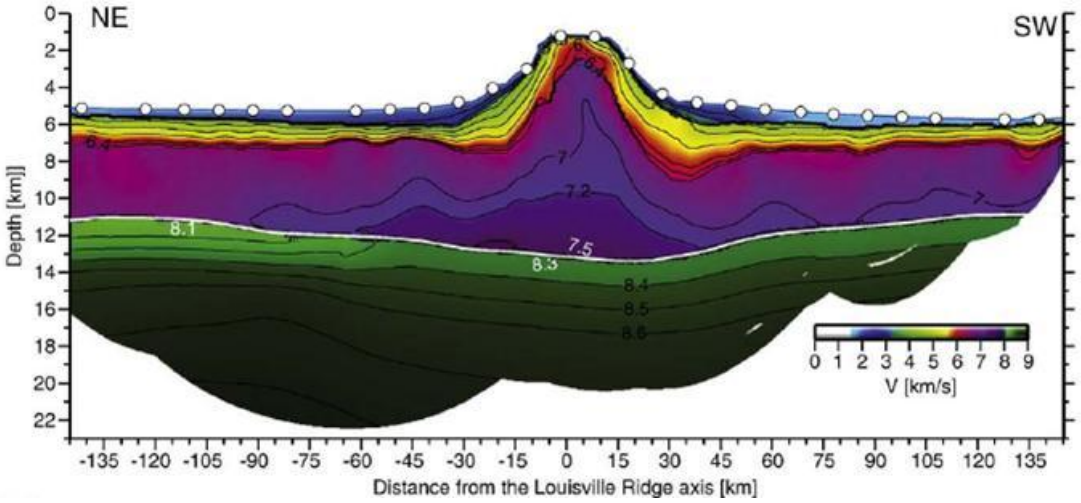

Figure 1.5 *P*-wave velocity model of the oceanic crust beneath the Louisville Guyot (after Contreras-Reyes *et al.*, 2010) demonstrating an absence of undercrustal material. High *P*-wave velocities (7.20-7.60 km s^{-1}) were found to be present, however, in the lowermost 2 km of the crust directly beneath the seamount that could indicate intracrustal magmatic intrusion.

The Society Islands (aged 4.3-0.0 Ma) are located in the middle of the Pacific Ocean on lithosphere aged between 80 and 90 Ma. Traveltimes picked from WA seismic refraction data (Grevemeyer *et al.*, 2001b) were modelled to show a *P*-wave velocity-depth structure that lies within the range expected for standard Pacific oceanic crust, generally ~7 km in thickness (White *et al.*, 1992; Grevemeyer *et al.*, 1998). Thickening of the upper crustal layer 2 was observed close to the islands and the surface load was found to be compensated by regional flexure of strong lithosphere. Although there was no direct evidence for *P*-wave velocities >7.1 km s^{-1}, synthetic seismograms were modelled to match the observed amplitude variation with offset of *P*-wave arrivals reflected from the Moho, that suggested elevated velocities (>7.1 km s^{-1}) at the base of the crust. A process of late stage intrusion or accumulation of sill-shaped bodies in the region of the crust-mantle boundary was suggested to explain these high amplitude arrivals. A similar explanation to this was subsequently used to explain observations at the Louisville Guyot (Contreras-Reyes *et al.*, 2010).

The attributes of the above examples can be compared to the islands that show evidence for undercrustal material, as summarised in Table 1.1. There is a common observation of high *P*-wave velocities, >7.3 km s^{-1}, for almost all of the islands and seamounts that have been considered suggesting that the under/intracrustal material

is of a similar composition, but it remains unclear as to why undercrustal material develops beneath some islands (e.g. Hawaii) but not at others that are otherwise similar (e.g. Society Islands).

1.1.4 Hotspot swells

Following the development of the model for the thermal evolution of the oceanic lithosphere, global maps of the age of the oceanic lithosphere (e.g. Heirtzler *et al.*, 1968; Müller *et al.*, 2008), derived from the correlation of magnetic lineations to a timescale of reversals in the polarity of the Earth's magnetic field (LaBrecque *et al.*, 1977; Cande & Kent, 1992; 1995), have been compared to global maps of bathymetry derived from shipboard and satellite data (GEBCO – IOC, IHO & BODC, 2003). Many anomalous bathymetric highs were identified throughout the ocean basins (e.g. Hayes, 1988; Marty & Cazenave, 1989) with no apparent pattern to their spatial distribution, although they commonly coincide with spatially concentrated intra-oceanic plate volcanism. These highs, or swells as they are commonly called, range in size from 900 to 2000 km in diameter, with topography up to 2.2 km shallower (Monnereau & Cazenave, 1990) than expected based on plate age alone (Figure 1.6 – Crough, 1983; Stein & Stein, 1992).

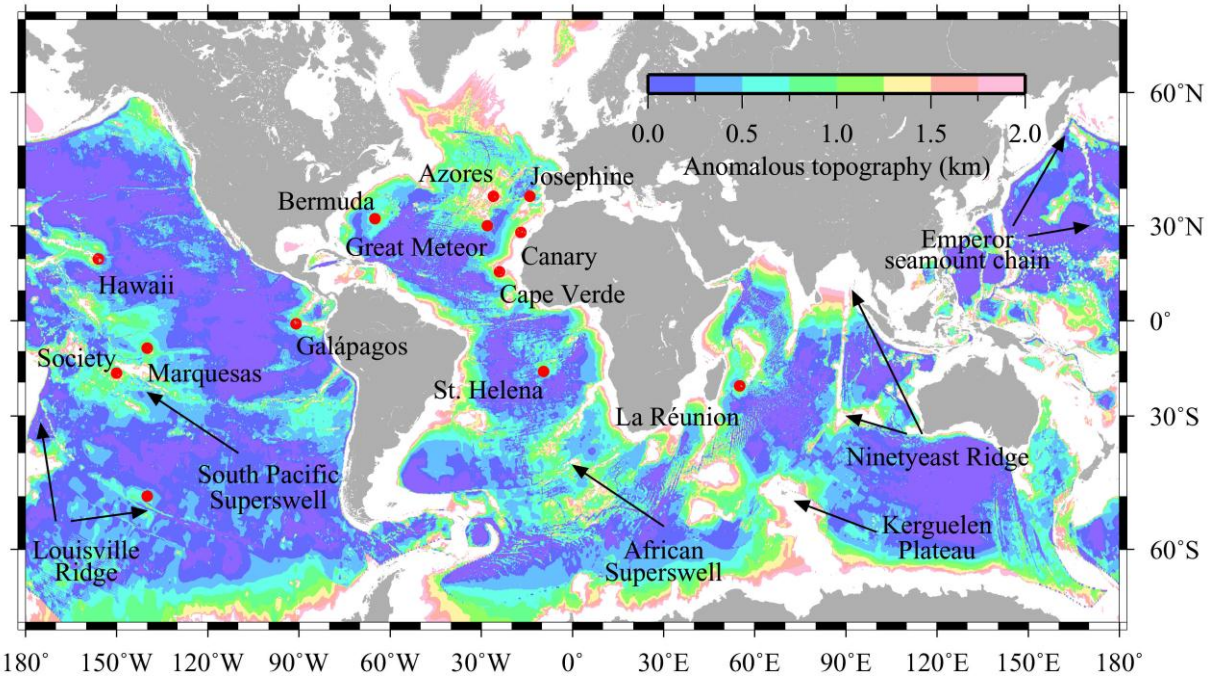

Figure 1.6 Anomalous topography in the ocean basins, created by subtracting the expected depth of the seafloor, calculated using the GDH1 model of Stein & Stein (1992) and the plate ages of Müller *et al.* (2008), from the observed GEBCO 1' bathymetry (IOC, IHO & BODC, 2003). The locations of hotspots and groups of ocean islands discussed in the text are indicated (black arrows and red dots).

Oceanic mid-plate swells are also associated with long-wavelength gravity and geoid anomaly highs and excess heat flow (e.g. Crough & Jurdy, 1980; Pollack *et al.*, 1993), implying that the lithosphere is thermally reheated and/or mechanically weakened in some way. The magnitude and longevity of hotspot swells and their associated volcanism also indicates that they are the surface expressions of a significant melting process that may also act to dissipate excess heat energy from the deep interior of the Earth.

The amplitude of anomalous swell topography (Figure 1.6) and the corresponding geoid anomaly varies considerably (Table 1.2). Although Monnereau & Cazenave (1990) observed a potential correlation between swell height and age of the affected oceanic lithosphere, the lateral extent of the anomalous topography is much greater than that of the associated islands and undercrustal material (where observed), and shows no such correlation with the thickness of undercrustal material. This lack of correlation between swell size and thickness of undercrustal material is evident when comparing observations for Hawaii, Marquesas and Galápagos (Table 1.2; Table 1.1).

Table 1.2 Summary of the topography, long-wavelength geoid anomaly and lateral extent of hotspot swells (after Monnereau & Cazenave, 1990).

Hotspot swell	Swell height (km)	Geoid anomaly (m)	Swell extent (km)
Hawaii	1.15	5.0	1450
Marquesas	0.95	2.2	1300
Galápagos	0.60	0.5	1200
Society	0.85	1.8	900
Azores	1.10	4.0	1100
Great Meteor	1.20	2.5	1100
Bermuda	1.10	5.3	1800
Canary	1.35	7.5	1500
Cape Verde	2.20	8.0	1750
St. Helena	0.80	1.5	1100
La Réunion	1.20	3.0	1000

At Hawaii, there is a clear decay in the height of the swell to the northwest, due to the motion of the Pacific plate over a supposedly stationary hotspot (Duncan & Richards, 1991; Steinberger, 2000). The intermediate size of the observed swell may, therefore, be explained if the buoyancy provided by the support mechanism increases with residence time, either by the coupling of a dynamic asthenospheric upwelling

with the base of the lithosphere or the gradual transfer of thermal energy from a hot asthenospheric source (e.g. Courtney & White, 1986).

The swells associated with the Marquesas and Society Islands are located on a broad region of anomalously shallow bathymetry termed the South Pacific Superswell (McNutt & Fischer, 1987). Despite the collective extent of this 'superswell', the individual swells are some of the smallest in terms of both anomalous topography and geoid height.

At the Canary Islands, Filmer & McNutt (1989) found no evidence of a high amplitude topographic swell or long wavelength geoid or gravity anomaly high, which would be expected if the islands were formed due to significant thermal reheating of the lithosphere or dynamic support from material upwelling in the asthenosphere (e.g. Morgan *et al.*, 1995; Sleep, 1992). Conversely, Monnereau & Cazenave (1990), and more recently Crosby & McKenzie (2009), did find evidence for an anomalous swell ~1.35 km high and 1500 km in diameter, with a geoid anomaly of +7.5 m, similar to the swell anomaly observed at the Cape Verde islands to the south.

There are many factors that contribute to the size of the observed hotspot swells, including the addition of undercrustal material (Section 1.1.2), the residence time of a region of hot asthenospheric material beneath the lithosphere and the amplitude of its elevated temperature. In combination, or acting independently, such factors have been incorporated into several models of swell support that can then be tested, using a range of geophysical data and modelling techniques, to determine the mechanism that produces the anomalous swell topography.

1.2 Proposed support mechanisms for hotspot swells

Comparison of bathymetric and geoid anomalies to those expected for standard oceanic lithosphere (Monnereau & Cazenave, 1990) suggests that there must be some form of regional load support acting at mid-plate swells. Several mechanisms have been proposed to explain how the topography of large-scale swells can be sustained over geological timescales (Figure 1.7, based on Crough, 1983):

1. Shallow support within the crust (Figure 1.7a, e.g. Morgan *et al.*, 1995). The construction of volcanic islands on top of the oceanic crust is often accompanied by the accumulation of neutrally buoyant magma by intrusion

and emplacement at the base of the pre-existing crust (e.g. Charvis *et al.*, 1999; Grevemeyer *et al.*, 2001a). A thickened oceanic basement provides additional buoyancy, due to its lower density relative to the underlying mantle, analogous to the deep crustal roots that support continental mountain belts (e.g. Avouac & Burov, 1996).

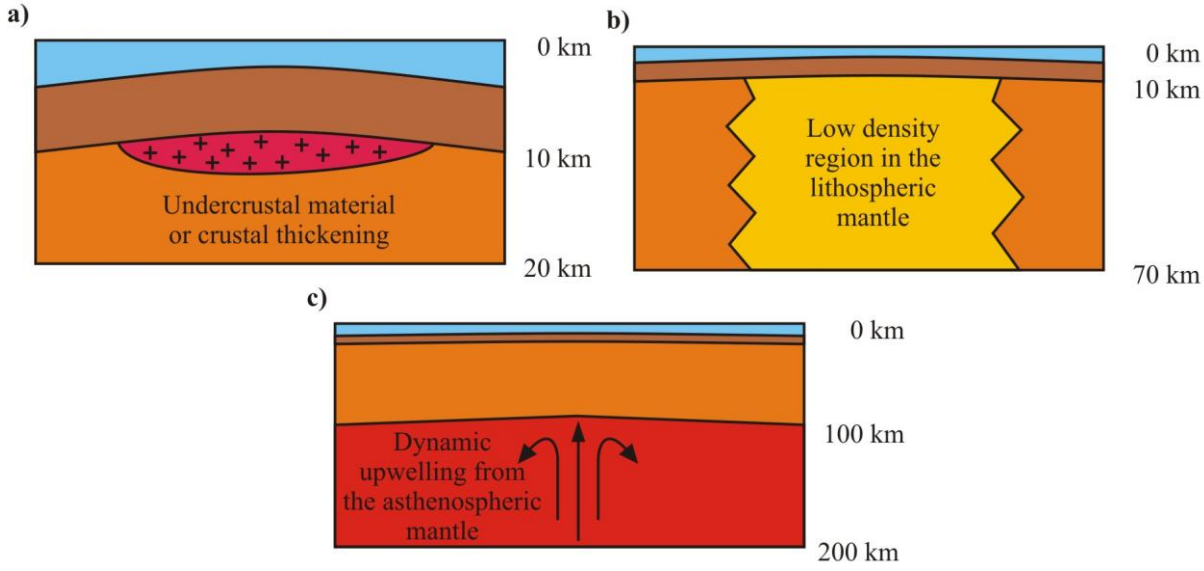

Figure 1.7 Mechanisms proposed to explain how large-scale topographic swells are sustained over geological timescales (after Crough, 1983). a) Shallow support in the crust. b) Support in the lithospheric mantle. c) Upwelling in the asthenospheric mantle.

2. Support within the upper mantle (Figure 1.7b, e.g. Detrick & Crough, 1978; Robinson, 1988). A region of low density in the lithospheric mantle, either due to elevated temperature or compositional variation, may provide significant upwards force to elevate the lithosphere. Morgan *et al.* (1995) observed a strong correlation between the volume of oceanic volcanism and the size of the associated bathymetric swell along the Hawaiian chain, and showed that the density reduction in the lithospheric mantle and the upper asthenosphere due to thermal reheating and basaltic melt extraction contributes significantly to the swell topography.
3. Dynamic mantle upwelling (Figure 1.7c, e.g. Sleep, 1995). Material actively rising through the asthenosphere acts as a negative load on the base of the lithosphere that causes flexural uplift of the entire plate. Monnereau *et al.* (1993) used numerical models to simulate dynamic uplift resulting from the ascent of low density material through a convective mantle to the base of a

rigid lithosphere. Uplift was observed to occur in two stages: pure dynamical support during initial ascent, and a larger stage of uplift following ductile thinning of the lithosphere as the upwelled material impinges on the convective boundary layer.

It is possible that these mechanisms occur either separately or in combination to support a variety of different global topographic swells given the range of observations considered in Sections 1.1.2, 1.1.3 & 1.1.4.

1.3 Regional setting of the Cape Verde Swell

The Cape Verde Swell is the largest observed mid-plate swell on Earth; the approximately circular bathymetry anomaly alone encompasses a region >1500 km in diameter with a crest >2.0 km shallower than the surrounding abyssal plain (Figure 1.8). The slow-to-stationary absolute motion of the African Plate in the Cape Verde region, <10 mm yr^{-1} (Morgan, 1983; Pollitz, 1991), also results in a concentration of the associated uplift and volcanism into an approximately circular area and, consequently, makes this the ideal site to test the various proposed models for mid-plate swell support.

Although the crest of the swell is located only 600 km from the passive continental margin of West Africa, it is 1500 km to the nearest plate boundary, which is the MAR located to the southwest. The affected lithosphere is entirely oceanic, as demonstrated by the observation of linear, ridge-parallel magnetic anomalies throughout the region. Magnetic anomalies M0-M21 (Hayes & Rabinowitz, 1975) have been identified, offset by several large fracture zones (Williams *et al.*, 1990; Figure 1.8), suggesting that the oceanic crust was accreted during the separation of the African continent from the Americas in the early Cretaceous (Berriasian to Albian, ~150-110 Ma). The corresponding geoid anomaly of the swell reaches a maximum of +8 m (Monnereau & Cazenave, 1990). Heat flow measurements show an increase from 43.5 mW m^{-2} away from the swell to 60.5 mW m^{-2} near the swell crest (Courtney & White, 1986; Figure 1.8), with the maximum heat flow anomaly 16 mW m^{-2} higher, using the cooling model of Parsons & Sclater (1977), than predicted for the (regional average) 130 Ma oceanic lithosphere on which the swell is imposed.

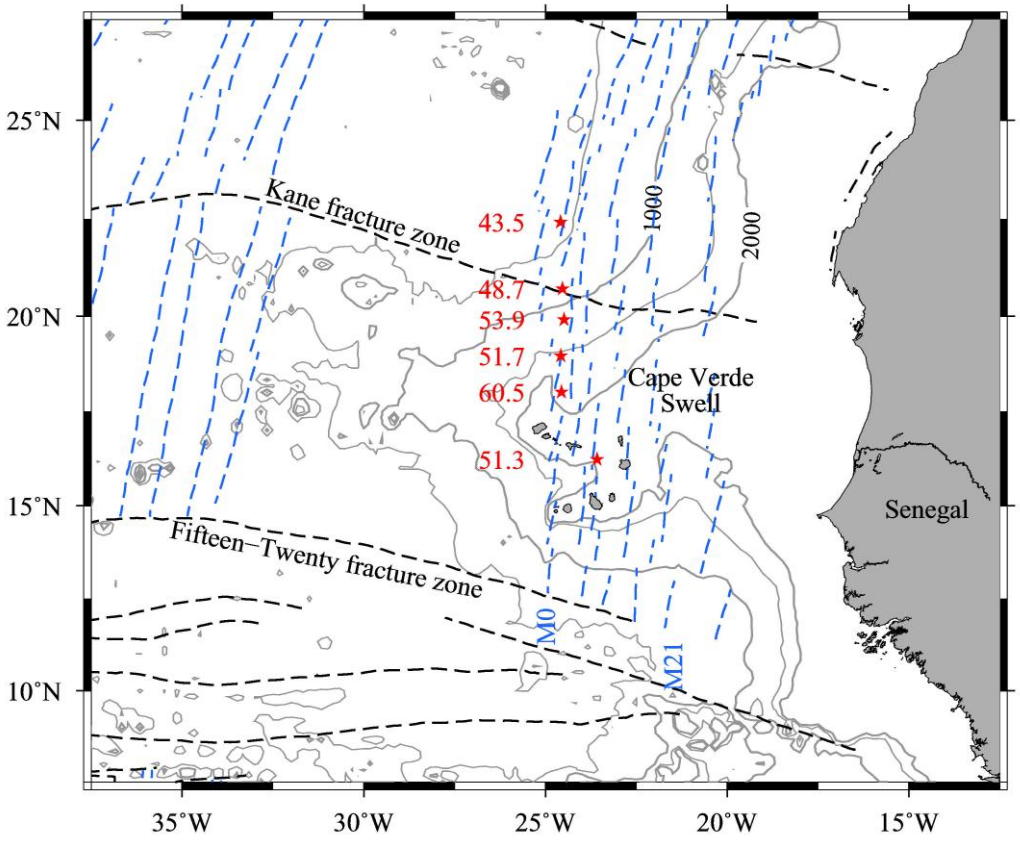

Figure 1.8 Tectonic setting of the Cape Verde Swell. Contours of anomalous topography (grey lines; see Figure 1.6), with a 500 m contour interval, highlight the extent of the swell. Magnetic anomaly isochrons (blue dashed lines) show agreement with plate ages of Müller *et al.* (2008) and offsets correlate with fracture zone locations (black dashed lines). Courtney & White (1986)'s heat flow measurements, in mW m^{-2} (red stars and text), show a positive heat flow anomaly over the swell.

During studies of the continental slope of West Africa, it was observed that the continental shelf is exceptionally wide to the east of the Cape Verde Islands. Rona (1970) hypothesised that this extended shelf region was sedimentary in composition and resulted from the enhanced aeolian transport of terrigenous sediments derived from the continent by the strong trade winds. This hypothesis was largely discounted after the consideration of maximum aeolian sedimentation rates, which would require 85-170 Ma to accumulate enough material, and following the observation along an airgun profile to the northeast of the islands, of a discontinuity in the sediments that mirrored the topography of the Cape Verde Rise (Seibold & Hinz, 1974). Seibold & Hinz (1974) suggested that at least part of the anomalous bathymetry of the Cape Verde Rise is structural, rather than depositional, and that it is a relatively young feature that formed following significant sedimentation of the margin.

Limited information is available regarding the age of swell formation but a study of the concentration of carbonate nannofossils in the cores of Deep Sea Drilling Program (DSDP) site 368 (Lancelot *et al.*, 1978b) on the crest of the swell, in comparison to those at DSDP Site 367 (Lancelot *et al.*, 1978a) in the basin to the south, reveals a sudden increase in abundance from lower to upper Miocene. Assuming that there has not been a dramatic change in nutrient availability or palaeo-climate in this region, this would suggest that the seabed was raised above the carbonate compensation depth ~20 Myrs ago, although it is not entirely possible to discount the likelihood that the carbonate compensation depth has also changed.

1.3.1 Existing studies at the Cape Verde archipelago

The Cape Verde archipelago is centred to the southwest of the crest of the associated swell and consists of nine main islands, clustered in a circular area ~350 km in diameter, that can be subdivided into a crescent of six islands to the southeast and a chain of three aligned towards the northwest (Figure 1.9). Despite its optimal attributes including large topography, gravity, geoid and heat flow anomalies and the semi-stationary plate environment, there have been relatively few geological or geophysical investigations of the Cape Verde Swell and the islands situated upon it. A summary of the existing data is provided in the following subsections.

1.3.1.1 Geology and radiometric dating

The Cape Verde Islands are composed of plutonic intrusions, a series of extrusive sequences, and volcaniclastic and mass wasting volcanic deposits. In some cases there is evidence of uplifted marine sediments, predominantly carbonates, that predate the island building volcanism. The islands were all constructed in the last ~20 Myrs, and the volcanism appears to have occurred in three to four periods with overlapping timeframes (Figure 1.9): the oldest islands of Sal, Boa Vista and Maio in the east; the intermediate islands of Santo Antão, São Vicente and São Nicolau to the northwest; the young island of Santiago to the south, with the possible distinction of the most recent volcanism at the islands of Fogo and Brava in the southwest.

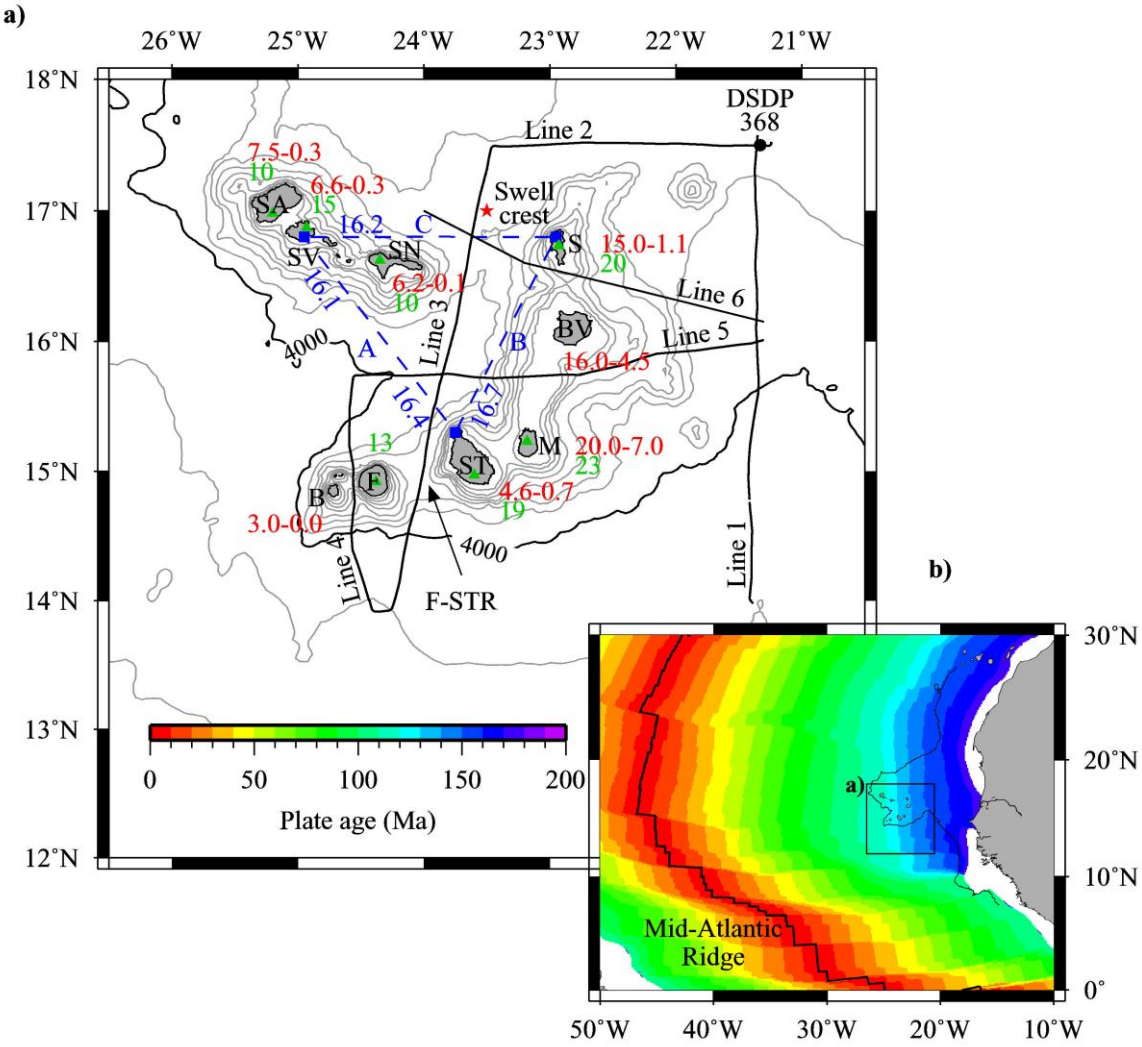

Figure 1.9 Geophysical surveys conducted at the Cape Verde archipelago. The 4000 m bathymetric contour is used to outline the extent of the swell and the red star indicates the location of the swell crest. Bathymetric contours (grey) are plotted with a 500 m contour interval. a) Location of MCS profiles from RRS *Charles Darwin* 1985 (black lines), see Ali *et al.* (2003). DSDP site 368 is indicated with a black dot. Lodge & Helffrich (2006)'s Moho depths beneath islands, in km, are shown (green triangles and text) together with Dash *et al.* (1976)'s 1-D seismic profiles and Moho depth determinations, in km (blue dashed lines, squares and text). Radiometric dates outlining volcanic evolution timescales (Mitchell *et al.*, 1983; Plesner *et al.*, 2003; Duprat *et al.*, 2007; Holm *et al.*, 2006, 2008; Dyhr & Holm, 2010; Madeira *et al.*, 2010), in Ma, are also shown (red text). Islands: SA, Santo Antão; SV, São Vicente; SN, São Nicolau; S, Sal; BV, Boa Vista; M, Maio; ST, Santiago; F, Fogo; B, Brava. F-STR, Fogo-Santiago Ridge. b) Plate ages of Müller *et al.* (2008). Black box shows the extent of the area in a).

Stillman *et al.* (1982) found evidence in the geological record on Maio for the deposition of pelagic limestone between ~140 Ma and 100 Ma, that had a relatively scarce component of organic material compared to the same succession at nearby DSDP site 367 (Lancelot *et al.*, 1978a). Locally, the seafloor remained elevated above the carbonate compensation depth and from 100 Ma an increase in turbidite

flow deposits and terrestrial input signified considerable uplift, culminating in emergence around 90 Ma marked by tuff deposits as a result of substantial pyroclastic volcanism. However, from the clear exposure of crustal pillow basalts and seafloor pelagic sediments on Maio, Holm *et al.* (2008) suggest that this island was primarily the product of localised uplift and built up by additional volcanic construction initiating ~24 Myrs ago, with a lack of sediment deposition in the Palaeogene alluding to a period of erosion and/or non-deposition before the initiation of Neogene volcanism ~10 Myrs ago.

K-Ar and $^{40}Ar/^{39}Ar$ ages determined for plutonic and volcanic rock samples from Maio (Mitchell *et al.*, 1983) confirm the island building process described by Stillman *et al.* (1982), of a likely gradual plutonic growth leading up to the major Neogene plutonic growth, emergence and subsequent volcanic activity initiating 15-20 Myrs ago and continuing until ~7 Ma. Radiometric dating of samples from the most northerly island of the eastern chain, Sal (Holm *et al.*, 2008), contributed dates of 15 to 1.1 Ma, further substantiating the idea of a shared period of volcanic activity. This is also in agreement with the results from recent $^{40}Ar/^{39}Ar$ analyses of volcanic and plutonic rocks samples from the island of Boa Vista. Dyhr & Holm (2010) obtained dates ranging from >16 to 4.5 Ma, providing strong evidence that the three eastern islands began to form distinctly earlier than those to the northwest or southwest.

Geochronology of samples from lava flows and minor dyke intrusions on the northwestern island of Santo Antão (Plesner *et al.*, 2003) provided dates ranging from 7.6 to 0.1 Ma, implying that the oldest volcanism, representing the initiation of island building, occurs contemporaneously with a decrease in activity recorded for the eastern islands. Holm *et al.* (2008) report similar dates (6.6-0.3 Ma) for São Vicente. At São Nicolau, the third island in the northwest chain, Duprat *et al.* (2007) dated volcanic activity to between >6.2 to <0.1 Ma, with the main period of activity between 4.7 and 2.6 Ma.

Holm *et al.* (2008) present new ages of between 4.6 and 0.7 Ma for volcanic rock formations on Santiago that were initially thought to have been erupted much earlier in the mid-Miocene, ~12 Ma. Madeira *et al.* (2010) report $^{40}Ar/^{39}Ar$ and U–Th ages that reveal three stages of volcanic growth on Brava. Submarine pillow lavas erupted 3-2 Ma followed by intrusion of a plutonic complex 1.8-1.3 Ma and, finally, following a period of widespread erosion, multiple volcanic domes, cones, lava flows

and pyroclastic sequences are observed, dated to between 0.25 Ma and the present. Fogo is the only island to experience historically recent volcanic activity, with an eruption on the west side of the main cone in 1995 that lasted for ~1 month (Heleno da Silva *et al.*, 1999). Recent evidence for seismic activity at the Cadamosto seamount (Grevemeyer *et al.*, 2010), located ~25 km to the southwest of Brava, provides further indication that volcanic and tectonic activity is now located to the southwest of the archipelago.

1.3.1.2 Seismic reflection data

Using a large number of single channel reflection profiles and six MCS reflection profiles acquired during the Royal Research Ship (RRS) *Charles Darwin* geophysical survey in 1985 (Figure 1.9), Ali *et al.* (2003) mapped the shallow crustal structure down to the top of the igneous basement. Four main stratigraphic units were identified and lithologically correlated using core and log data from DSDP site 368 (Lancelot *et al.*, 1978b), located at the northeastern corner of the survey area. The two lowermost units demonstrated a gradual decrease in overall thickness from east to west, and were interpreted as terrestrial sediments derived from the African continent. In stark contrast to this, the two uppermost units showed evidence for a concentric thickening around the islands, marking the flexure that occurred following the volcanic construction of the islands.

By modelling the geometry of this flexural marker, the degree of flexure could be quantified and compared to that obtained from numerical models of viscoelastic plates subjected to loads of comparable dimensions to the islands to determine the T_e of the underlying lithosphere (Ali, 2003; Ali *et al.*, 2003). Their calculated T_e of 29 km agrees well with that predicted from the magnetic anomaly-derived plate age predicted value, signifying that the lithosphere has not been significantly, if at all, thermally rejuvenated as part of load emplacement. However, the interpretation (and subsequent modelling) of flexural markers picked in the reflection data depends upon the accuracy of the time-to-depth conversion which, in turn, depends on accurate velocity information. Only a few sparse and poor quality velocity data were available to Ali *et al.* (2003), including: stacking velocities; a sonobuoy at the edge of their study area; and one-dimensional (1-D) estimates from Dash *et al.* (1976). All of these velocity sources have limitations in accuracy, depth sampled below the surface and areal extent, and are far from ideal, even taken collectively.

1.3.1.3 Wide-angle seismic refraction data

The earliest WA seismic refraction experiment in the Cape Verde region was by Dash *et al.* (1976) who undertook a refraction survey using land-based recording instruments deployed on the islands of Sal, Santiago and São Vicente. Shots were fired during linear transits between pairs of the land stations (profiles A, B & C; Figure 1.9) and first-arrival traveltime data were recovered from the seismograms. The station on Sal did not detect any arrivals at shot-receiver offsets >30 km, despite recording strong arrivals up to this point, and the attenuation of seismic energy was hypothesised to be caused by a heavily faulted or fractured zone within the crust. The remaining four time-distance graphs, a split-spread profile between São Vicente and Santiago and two single profiles from São Vicente and Santiago in the direction of Sal, were analysed using a 1-D slope-intercept method.

Five distinct layers were identified from the traveltime data (Dash *et al.*, 1976), according to common *P*-wave velocities as summarised in Table 1.3. The velocities and thicknesses of these five layers were found to correlate between all four profiles and were interpreted as follows: water column, semi-consolidated sediment, upper and lower oceanic basement and the uppermost mantle. The resulting 1-D velocity-depth profiles indicate a velocity structure similar to that expected for standard oceanic crust (White *et al.*, 1992), except for a consistently deeper Moho (16.1-16.7 km b.s.l.). As these results are based on the assumptions of planar intracrustal layering and homogeneity within layers in the subsurface, they may reflect a bias towards local crustal thickening concentrated beneath the islands given the recording instrument locations.

Table 1.3 Summary of the layering structure of the 1-D velocity depth models determined from slope intercept analysis of WA refraction data collected in the Cape Verde archipelago (after Dash *et al.*, 1976).

Layer	*P*-wave velocity (km s^{-1})	Interpretation
1	1.50	Water column
2	3.10-3.20	Sediments
3	4.40-4.80	Pillow basalts
4	6.30-6.60	Gabbros
5	7.90-8.10	Upper mantle

1.3.1.4 Passive seismic data

Lodge & Helffrich (2006) analysed receiver functions from a series of teleseismic recordings at a Global Seismographic Network station on Santiago and seven temporary broadband seismic recording stations located on six more of the islands (Figure 1.9). This analysis provided seven additional 1-D estimates of crustal thickness and velocity-depth structure of the lithosphere beneath the Cape Verde Islands (Table 1.4). Allowing for a standard oceanic crustal thickness of 7 km, the results were interpreted as providing evidence for crustal thickening, particularly beneath the older islands to the east (Figure 1.9), suggesting a gradual addition of material to the base of the crust occurring contemporaneously with island construction. The data are unable to establish whether the apparent crustal thickening is localised and related to island building, or a regional undercrustal body related to the support of the entire swell. Beneath the crust, the lithospheric mantle was modelled as a high *P*-wave velocity, low density layer overlying a low velocity layer, and was interpreted as a depleted residue following basaltic melt extraction.

Table 1.4 Summary of the depth to Moho and low velocity zone at the base of the lithosphere beneath the Cape Verde Islands, determined from receiver function analyses (after Lodge & Helffrich, 2006).

Island	Station latitude (N)	Station longitude (W)	Moho depth (km)	Depth to low velocity zone (km)
Santo Antão	16° 59'	25° 12'	~10	~76 ±15
São Vicente	16° 52'	24° 56'	~15	~68 ±12
São Nicolau	16° 37'	24° 21'	~10	~91 ±16
Sal	16° 44'	22° 56'	~20	~108 ±15
Maio	15° 14'	23° 11'	~23	~76 ±12
Santiago	14° 58'	23° 36'	~19	~90 ±14
Fogo	14° 55'	24° 23'	~13	~60 ±10

1.3.2 The Cape Verde Swell experiment

This study aims to evaluate the three proposed swell support mechanisms, using a series of both forward and inverse modelling methods, applied to a range of geophysical data acquired during the 'Cape Verde Hotspot: A Seismic Refraction study of ISostasy and MAgmatic underplating' (CHARISMA) experiment (Grevemeyer *et al.*, 2004).

The primary objective is to determine the crustal structure in the region of the Cape Verde Swell and Islands as a test of the undercrustal material hypothesis. Anomalously thick crust with standard velocity structure would suggest that the swell is an old feature that originated during enhanced magmatic crustal accretion at a mid-ocean ridge, perhaps under the influence of enhanced mantle upwelling. If the crust is thickened and also demonstrates an anomalous velocity structure, it is likely that the addition of material occurred some time after initial crustal accretion.

Secondly, using the *final* model of crustal velocity-depth structure to constrain surfaces that record subsidence due to surface loading and crustal densities, three-dimensional (3-D) flexure modelling will be performed to obtain an estimate of the apparent T_e in the region. The apparent T_e, together with a consideration of the long-wavelength gravity and geoid anomalies, can then be used to infer mechanical properties of the lithosphere, testing the hypotheses of lithospheric rejuvenation and dynamic upwelling, with implications for overall swell support.

Ultimately, the conclusions that can be drawn from this study will be compared to studies of other oceanic hotspots, leading to an evaluation of common themes and a discussion of the possible cause of the variation in swell amplitude and extent that is sometimes observed at otherwise comparable hotspots.

1.4 Structure of this thesis

This thesis is divided into seven chapters.

In this chapter the geological and geophysical characteristics of hotspot islands and their associated swells have been summarised and illuminated using descriptions of various geophysical studies of mid-oceanic plate volcanism. The hypotheses that are tested in this thesis have been outlined and a catalogue of existing work on the Cape Verde Swell has been provided.

Chapter 2 contains details of the acquisition, analysis and forward modelling of the CHARISMA WA seismic refraction data along an ~474 km north-south trending profile through the Cape Verde archipelago. Traveltime data are iteratively modelled using a ray-tracing approach to produce a 2-D velocity-depth model of the crust and uppermost mantle that can be considered as a representative radial transect through the Cape Verde Swell.

The 2-D velocity-depth model obtained using the forward modelling method is presented in Chapter 3 and an appraisal of the shallow subseabed is carried out through a comparison with the coincident MCS reflection data. At this point, the resolution of the deeper model structure is determined by assessing the potential for variation of velocity and depth nodes whilst maintaining a fit within the uncertainties of the traveltime data. Calculation of the 2-D crustal gravity anomaly provides an additional check on areas of the model that are less well constrained by the seismic data.

In Chapter 4, the uniqueness of the 2-D velocity-depth model obtained by forward modelling is tested using a series of inversions of both first-arrival traveltime data and reflections from the Moho. Resolution tests of the models produced by the inversion programs are compared to the forward modelling results and the *final* 2-D velocity-depth model is determined.

In Chapter 5, the flexural response of the lithosphere to loading is calculated to determine the rheology of the lithosphere and test various models for the support of the regional swell. The *final* 2-D velocity-depth model is used to constrain both the crustal structure along the 'swell transect' profile and the regional sediment thickness, using the two-way traveltime (TWTT) data of Ali *et al.* (2003).

A synthesis of the results obtained in this study is presented in Chapter 6, together with comparisons to results from studies at other ocean island groups and hotspot swells, incorporating a discussion of the wider significance and implications. Suggestions are made for further research using available data and also for new experiments both at the Cape Verde Swell and at the Bermuda Swell.

Finally, Chapter 7 contains a summary of the main conclusions of this study.

2. Seismic data acquisition, analysis and forward modelling

2.1 Introduction

As discussed in Chapter 1, investigation of the origin of anomalous regional-scale bathymetric swells requires the analysis, comparison and joint interpretation of a broad range of geophysical and geological data. Analysis of the WA seismic refraction data acquired during the CHARISMA experiment provides an opportunity to determine the velocity-depth structure of the oceanic crust and upper mantle along an ~474 km profile across the largest observed oceanic mid-plate swell on Earth, with the resulting 2-D velocity-depth structure model providing constraint on the key parameters required for 3-D, whole lithosphere, visco-elastic flexural modelling, in order to determine the rheological state.

In this chapter, the analysis and forward ray-trace modelling of the CHARISMA WA seismic refraction data is presented, including an interpretation of previously acquired MCS reflection data (RRS *Charles Darwin* cruise CD8/85; Hill, 1985), which is used to inform the shallow subseabed structure of the initial velocity-depth model. An overview of the acquisition configuration and data processing steps (Section 2.2) is followed by interpretations of both the shipboard swath bathymetry and the MCS reflection data (Sections 2.3 & 2.4). Section 2.5 contains a detailed description, classification and traveltime analysis of the primary refracted and reflected *P*-wave arrivals. The approach adopted to forward modelling is discussed in Sections 2.6 & 2.7.

2.2 Wide-angle seismic refraction data

The CHARISMA marine geophysical survey of the Cape Verde mid-plate swell was conducted in September 2004 aboard the Research Vessel (R/V) *Meteor* (cruise M62/3; Grevemeyer *et al.*, 2004). The main objective of this cruise was to acquire

WA seismic data to investigate the velocity-depth structure of the crust and upper mantle of the swell.

The location of the main seismic profile, P01, across the swell (Figure 2.1a) was chosen to coincide with an existing MCS reflection profile (Line 3), acquired during a previous cruise from October 1985 aboard the RRS *Charles Darwin* (cruise CD8/85 – Hill, 1985; Ali *et al.*, 2003). This pre-existing MCS reflection profile (Section 2.4) is used to inform the initial 2-D velocity-depth model, in terms of the layering and internal structure of the shallow subseabed and the depth to the oceanic basement (defined here as the igneous section of the oceanic crust – Section 2.6.4).

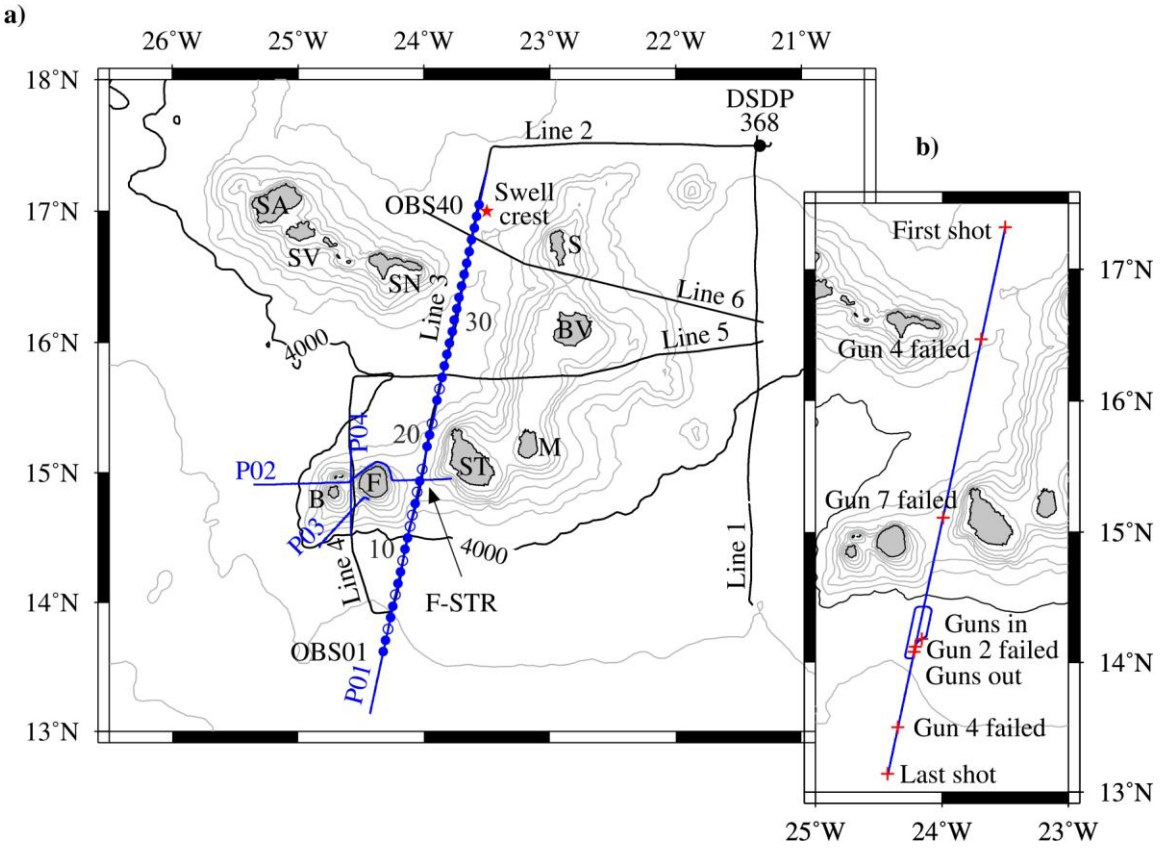

Figure 2.1 Data acquisition geometry of MCS reflection and WA seismic refraction surveys conducted at the Cape Verde archipelago. The 4000 m bathymetric contour is used to outline the southwest extent of the Cape Verde Swell and the red star indicates the location of the swell crest. Bathymetric contours (grey) are plotted with a 500 m contour interval. a) Location of MCS profiles from RRS *Charles Darwin* 1985 (black), see Ali *et al.* (2003), and the WA seismic refraction profiles from R/V *Meteor* 2004 (blue). Filled/open blue circles mark OBS/OBH locations; OBSs 01, 10, 20, 30 and 40 are labelled to indicate deployment orientation (south to north). DSDP site 368 is indicated with a black dot. Islands: SA, Santo Antão; SV, São Vicente; SN, São Nicolau; S, Sal; BV, Boa Vista; M, Maio; ST, Santiago; F, Fogo; B, Brava. F-STR, Fogo-Santiago Ridge. b) The ship track during the shooting phase of profile P01 (blue). Red crosses with annotations mark the first and last shots, airgun failures and the clockwise loop where the guns were recovered for repairs then redeployed north of the recovery point.

Three additional WA seismic profiles (P02, P03 & P04), located around the island of Fogo to the west of profile P01 (Figure 2.1a), were also acquired for 3-D tomographic imaging beneath the island. This tomographic study does not form part of the primary research presented in this thesis. However, Wiebke Brunn and others at IFM-GEOMAR (pers. comm.) have independently modelled these data to create a series of 2-D velocity-depth models that can be correlated to each other and to the velocity-depth model of this study at a series of intersections. The depth to key flexural horizons (Moho and top-basement) and the velocity-density-depth structure from all of the CHARISMA models are investigated as a means of constraining the 3-D whole lithosphere visco-elastic flexure modelling presented in Chapter 5.

2.2.1 Acquisition

A total of forty ocean bottom seismographs (OBS) and ocean bottom hydrophones (OBH) were deployed at 10 km intervals from south to north along profile P01, in water depths ranging from 2533 to 4496 m (Figure 2.1a). Each OBS comprised a three-component geophone package (KUM GmbH) and a hydrophone (OAS, Inc. E-2PD or High Tech, Inc. HTI-01-PCA). The geophones had a resonant frequency of either 4.5 or 15 Hz. Each OBH had a hydrophone as the only sensor. The output from each sensor was sampled at a rate of 200 or 250 Hz, depending on instrument type (OBH or OBS, respectively), and recorded onto a flash drive. Henceforth, the OBS and OBH will be referred to collectively as OBS for simplicity.

The seismic source consisted of eight 'G-gun' airguns, configured as two subarrays towed at 8 m depth, providing a total air volume of ~4000 in^3 (64 l). The airguns were operated at ~210 bar (~3000 psi). The source was triggered at 90 s intervals at a surveying speed of four knots, resulting in an average shot spacing of 180 m. For profile P01, WA seismic data were acquired along an ~474 km profile running north-south through the Cape Verde archipelago, subparallel to the West African continental margin and radial to the crest of the Cape Verde mid-plate swell (Figure 2.1a).

After shot number 509, ~95 km from the start of the profile, one of the airguns failed. Another airgun failed after shot number 1336, just past the mid-point of the profile (Figure 2.1b). The failure of these two airguns changed the characteristics of the source significantly, reducing the amplitude and altering the frequency content of the seismic wavelet. During shooting of the final third of the profile (Figure 2.1b),

the failure of a third airgun reduced the source to 62.5% by volume, further reducing the amplitude and modifying the frequency content of the seismic wavelet beyond acceptable limits. The airgun array was, consequently, recovered for repairs before being redeployed north of their recovery point on the original shooting line (Figure 2.1b) to ensure that the amplitude and frequency content of the seismic wavelet were as consistent as possible for the entire profile. A total of 2614 shots were fired from north to south. Discounting the region of overlap where the guns were recovered, repaired and re-deployed, each record section in the final SEG-Y dataset consists of 2535 traces.

Although all 40 instruments were successfully recovered without incident, subsequently, during data download, it became apparent that two instruments had failed to record any usable data (OBH18 & OBH22). Hydrophone and vertical geophone record sections presented in this thesis are primarily plotted against shot-receiver offset, or 'offset from instrument', and an example record section showing features characteristic of all record sections is shown in Figure 2.2. In addition, the position of each OBS, traveltime pick and the subsequent velocity-depth models are referenced to a horizontal range, where the profile offset, or 'offset along profile', increases from north to south, starting at 0 km at the location of the first shot fired (17° 19.11' N 23° 29.94' W) and passing through the location of the final shot (13° 08.12' N 24° 25.72' W) at ~474 km (e.g. Figure 2.4b; Figure 2.14).

2.2.2 Processing

The OBS data were processed onboard the R/V *Meteor*, and subsequently at IFM-GEOMAR, by the sea-going scientific party. Instruments were corrected for clock drift, and then the continuous data recording was split into 90 s traces, relative to the time of each shot fired. For the purposes of setting the experiment geometry in preparation for forward modelling of the traveltime data (Section 2.6.3), the seabed position of each OBS was adjusted from its sea surface deployment location to its seabed profile offset, using the traveltime of the direct arriving water wave.

Figure 2.2 Complete record section of hydrophone data recorded by OBS23. A bandpass filter of corner frequencies 0-5-70-80 Hz has been applied. Seismic energy that has travelled through the subsurface has been recorded to shot-receiver offsets of at least ±70 km. The main arrival types have been annotated.

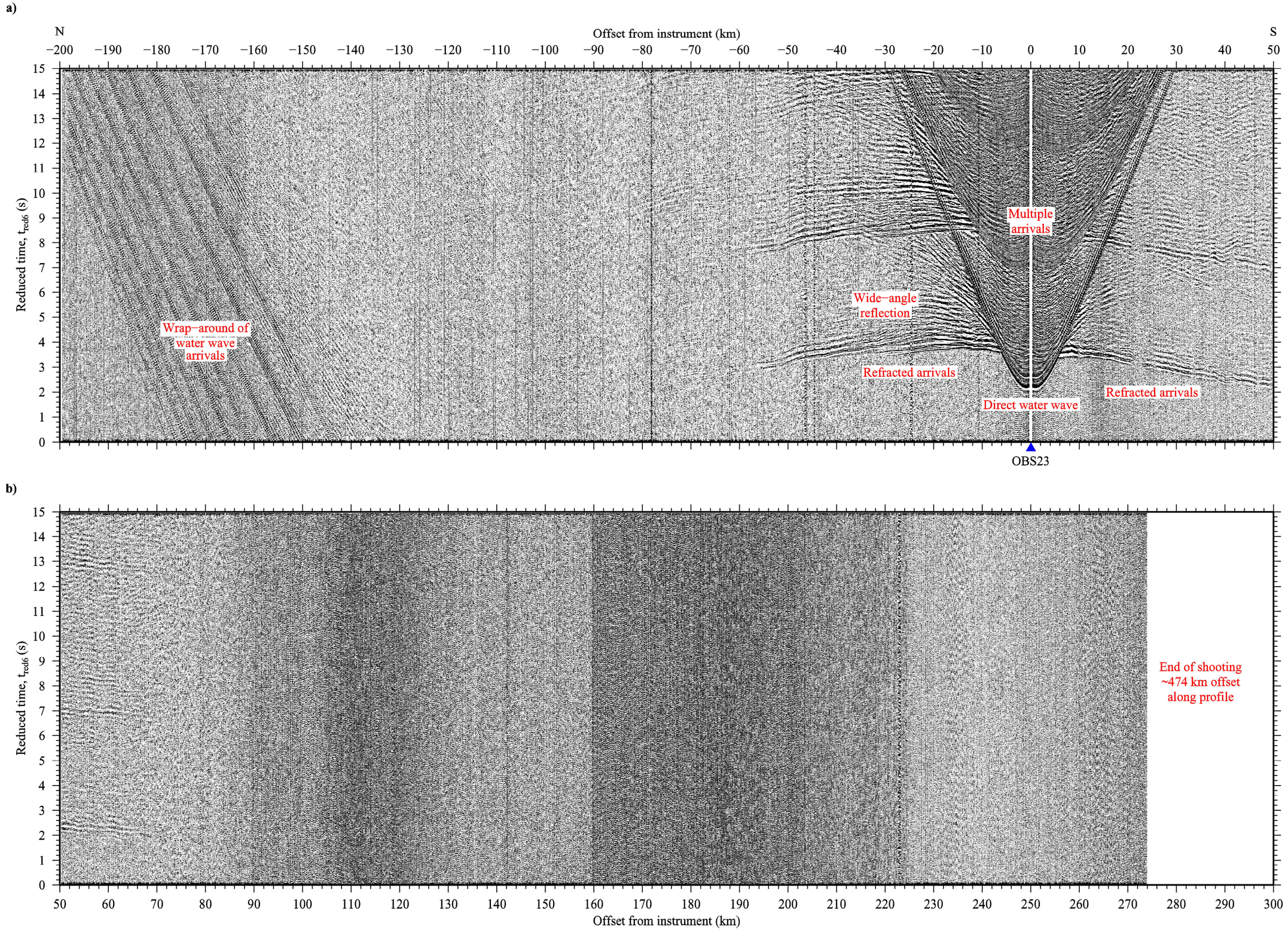
a)
N
Offset from instrument (km)
S
−200 −190 −180 −170 −160 −150 −140 −130 −120 −110 −100 −90 −80 −70 −60 −50 −40 −30 −20 −10 0 10 20 30 40 50
Reduced time, t_{red6} (s)
0 1 2 3 4 5 6 7 8 9 10 11 12 13 14 15
Wrap−around of water wave arrivals
Wide−angle reflection
Multiple arrivals
Refracted arrivals
Direct water wave
Refracted arrivals
OBS23
b)
Reduced time, t_{red6} (s)
0 1 2 3 4 5 6 7 8 9 10 11 12 13 14 15
End of shooting ~474 km offset along profile
50 60 70 80 90 100 110 120 130 140 150 160 170 180 190 200 210 220 230 240 250 260 270 280 290 300
Offset from instrument (km)

In order to minimise individual data file size, each data set was stored in reduced time ($t_{red'v'}$, s) by applying a shift to the start time (t, s) of each trace according to the shot-receiver offset (x, km) and a specified reduction velocity (v, km s^{-1}) of 6 km s^{-1}:

$$t_{red'v'} = t - \left(\frac{x}{v}\right) \quad \textbf{(2.1)}$$

The traces were truncated at 15 s length in reduced time and stored in SEG-Y format. Shot-receiver offsets were defined as negative to the north and positive to the south, relative to each OBS.

An example unfiltered hydrophone record section from OBS04 is shown in Figure 2.3a. Spectral analysis of these data shows that the seismic wavelet produced by the source had a dominant frequency bandwidth of 5-70 Hz (Figure 2.3b). The application of a zero-phase sine-squared tapered bandpass filter (0-5-70-80 Hz) was chosen to remove the low and high frequency noise, thus enhancing the seismic signal (Figure 2.3d), and revealing arrivals at greater shot-receiver offsets than originally observable in the raw data (Figure 2.3c).

2.3 Shipboard swath bathymetry data

During R/V *Meteor* cruise M62/3, shipboard swath bathymetry data, with a spatial resolution of 0.24' (~440 m) both in latitude and longitude post-processing and gridding, were continuously recorded using a *HYDROSWEEP DS2* multibeam system. The full length of profile P01 was surveyed as a series of parallel transects acquired during instrument deployment and recovery and during shooting. The seabed in the survey area around the island of Fogo (Figure 2.4a) was mapped in a similar manner. The higher spatial resolution of the shipboard swath bathymetry data (compared to the GEBCO 1' global dataset; IOC, IHO & BODC, 2003) also allows the small-scale morphology of the seabed to be analysed and considered in the context of its effect on the down-going seismic wavefield, the interpretation of phases and on the interpretation of the resulting 2-D velocity-depth model.

Figure 2.3 A comparison of filtered and unfiltered hydrophone data from OBS04. a) The unfiltered record section is dominated by low frequency noise that masks all but the highest amplitude arrivals. Some arrivals can be identified up to ±40 km shot-receiver offset. b) The frequency spectrum of the unfiltered data shows that the source predominantly contained frequencies ranging from 5 to 70 Hz. c) The record section following the application of a bandpass filter with corner frequencies 0-5-70-80 Hz. Arrivals are now clear to ±70 km shot-receiver offset. d) The frequency spectrum of the filtered data shows that the low-frequency noise has been removed.

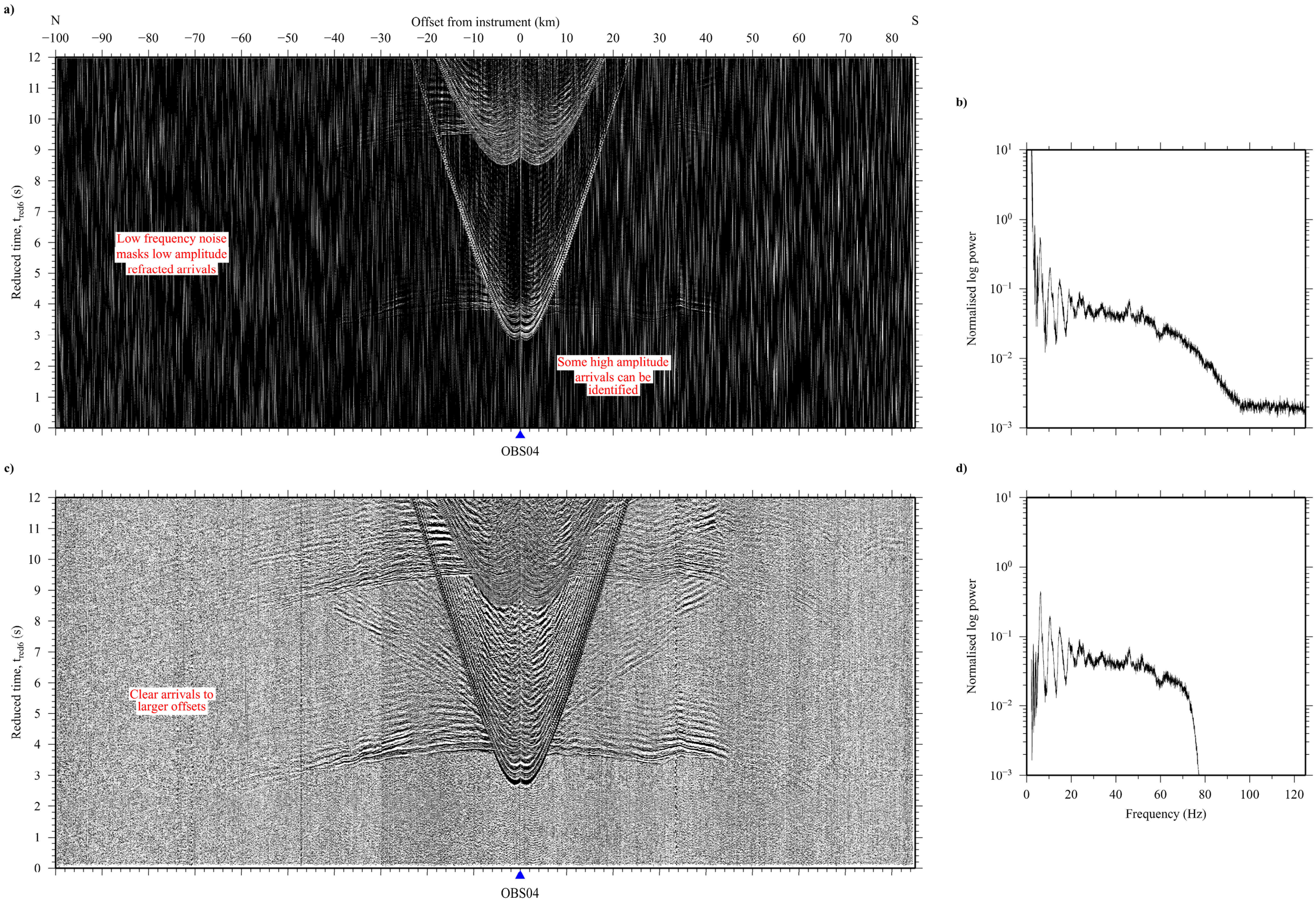
a)
N
Offset from instrument (km)
S
−100 −90 −80 −70 −60 −50 −40 −30 −20 −10 0 10 20 30 40 50 60 70 80
Reduced time, t_{red6} (s)
0 1 2 3 4 5 6 7 8 9 10 11 12
Low frequency noise masks low amplitude refracted arrivals
Some high amplitude arrivals can be identified
OBS04
b)
Normalised log power
10^{1} 10^{0} 10^{-1} 10^{-2} 10^{-3}
c)
Reduced time, t_{red6} (s)
0 1 2 3 4 5 6 7 8 9 10 11 12
Clear arrivals to larger offsets
OBS04
d)
Normalised log power
10^{1} 10^{0} 10^{-1} 10^{-2} 10^{-3}
0 20 40 60 80 100 120
Frequency (Hz)

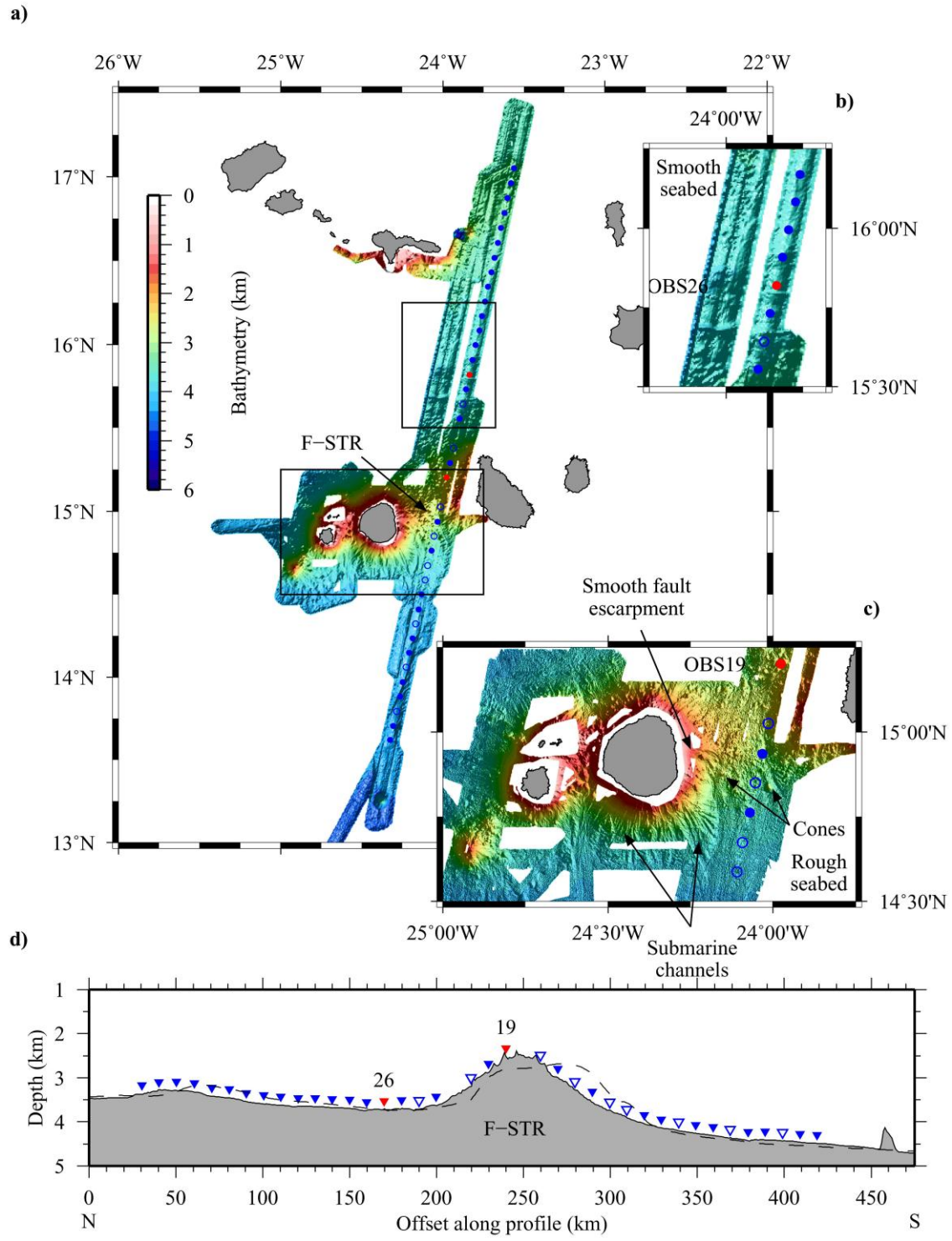

Figure 2.4 Shipboard swath bathymetry data from R/V *Meteor* cruise M62/3. a) The full swath bathymetry data gridded at 0.24' (~440 m) intervals in latitude and longitude. Filled/open blue circles mark OBS/OBH locations; OBS19 and OBS26 are indicated with filled red circles. F-STR, Fogo-Santiago Ridge. For island names see Figure 2.1. b) and c) Morphology of the seabed at OBS26 and OBS19, respectively. Key features, as discussed in the text, are labelled. The subset of the bathymetry data in c) is gridded at 0.055' (100 m) intervals in latitude and longitude. d) A comparison of the seabed along profile p01 obtained from swath bathymetry (black line, with grey subseabed fill) to the GEBCO 1' (IOC, IHO & BODC, 2003) global bathymetry (black dashed line), highlighting the importance of obtaining high resolution water depths during seismic data acquisition. Filled/open blue inverted triangles mark OBS/OBH locations; OBS19 and OBS26 are indicated with filled red inverted triangles.

To the east of Fogo, on the Fogo-Santiago Ridge (F-STR; Figure 2.4c), the seabed has an irregular, hummocky texture. A number of larger circular features can also be observed amongst the rough surface of the F-STR that may represent partly buried volcanic cones. There are also notable lineations that radiate outwards to the south from Fogo, perhaps indicating submarine channels. These lineations are apparently absent on the eastern flank of Fogo, where a smooth surface is evident. These observations suggest that at least part of the F-STR may comprise volcaniclastic debris from past landslide and flank collapse events originating on the adjacent islands of Fogo and Santiago (Day *et al.*, 1999; Masson *et al.*, 2008). Elsewhere along profile P01, the seabed appears to be smooth (Figure 2.4b) and the bathymetry varies less dramatically (Figure 2.4d).

2.4 Multichannel seismic reflection data

An MCS reflection survey of the Cape Verde mid-plate swell was conducted in 1985 aboard the RRS *Charles Darwin* (cruise CD8/85; Hill, 1985). Data were acquired along six profiles, ranging from ~220 to ~400 km in length, in a network amongst the islands of the archipelago (Figure 2.1a). The objective of this cruise was to image flexural markers in the shallow subseabed to enable calculation of the mechanical properties of the lithosphere and ascertain the potential volume of buoyant undercrustal material beneath the Cape Verde Islands (Ali *et al.*, 2003). For the current study the MCS reflection data along Line 3 provides a means by which to inform and constrain the structure of the shallow subseabed for construction of the initial WA forward model.

For CD8/85, the seismic source consisted of an array of five Bolt airguns which, combined, provided a total air volume of ~1600 in^3 (~25.7 l). The source was triggered at 25 s intervals at a surveying speed of four knots and reflected energy, in the form of *P*-wave arrivals, was recorded using a 2.4 km long, 48-channel hydrophone streamer, resulting in an average common depth point (CDP) spacing of 25 m. The processing flow included pre-stack deconvolution, CDP gathers, normal move-out correction, 24-fold stacking, post-stack deconvolution, the application of a time-varying bandpass filter (0-6.4 s TWTT, 8-12-70-77 Hz; 6.5-10 s TWTT, 8-12-40-60 Hz) and residual migration. For further details of the acquisition and processing procedures refer to Ali *et al.* (2003) and Ali (2003). When projected into

the same spatial reference framework used for profile P01, the MCS data along Line 3 lie between -14 and 388 km profile offset, primarily to the north of the F-STR.

MCS Line 3 (Figure 2.5a) features a succession of reflector packages and seismically opaque layers either side of the F-STR, between the seabed and ~6.25 s TWTT, where the lowest coherent reflector marks the top of the oceanic basement. The reflectors above the top-basement surface are concordant with it until about halfway between the top-basement and the seabed, where an angular unconformity is observed. Above the unconformity, the reflectors are concordant with the unconformity, including the seabed.

Ali *et al.* (2003) divided the shallow subseabed into five layers after developing a seismic stratigraphic classification for the Cape Verde region (Figure 2.5b) using all MCS reflection profiles acquired during CD8/85. These layers each have distinct internal reflector characteristics, consisting of either packages of strong, laterally continuous reflectors or seismically opaque regions. The two lowermost, oldest layers (Unit I & Unit II) were interpreted by Ali *et al.* (2003) to be terrigenous sediments derived from the West African margin, which formed following the rifting apart of North America and Africa during the formation of the North Atlantic ocean basin. In contrast, the three uppermost, youngest layers were interpreted to be volcaniclastic sediments or debris flow material derived from the Cape Verde Islands (Unit IIIa & Unit IIIb) and pelagic sediments (Unit IV) infilling the flexural moats that were formed by island-related plate loading. The angular unconformity reflects the subsidence that occurred due to plate loading and flexure, and defines a change in the primary sediment provenance from the African margin to the Cape Verde Islands.

Figure 2.5 Interpretation of the MCS reflection data from RRS *Charles Darwin* cruise CD8/85 to define the shallow subseabed layering. a) MCS reflection line 3, which is coincident with WA seismic refraction profile P01 (see Figure 2.1 for location). A bandpass filter of corner frequencies 8-12-70-77 Hz has been applied the data (for further processing details refer to Ali *et al.*, 2003). b) Seismic stratigraphic classification and interpretation following the analysis of all MCS reflection profiles (Lines 1 to 6) located around the Cape Verde archipelago (after Ali *et al.*, 2003). c) Annotated interpretation of MCS reflection Line 3 showing the five subseabed horizons identified following the seismic stratigraphy defined by Ali *et al.* (2003) shown in b). The angular unconformity, shown in blue, represents subsidence due to plate loading and flexure, and defines a change in the primary sediment provenance from the African margin to the Cape Verde Islands. Subseabed units are named according to the terminology of Ali *et al.* (2003). Tie points with the other MCS reflection lines are indicated with annotated arrows. Filled/open blue circles mark OBS/OBH locations. d) A summary of the available 1-D velocity-depth profiles for the shallow subseabed: black line – stacking velocity from MCS Line 5, black dashed line – stacking velocity at DSDP site 368, blue line – 1-D seismic refraction model of Dash *et al.* (1976) (after Ali *et al.*, 2003).

a)

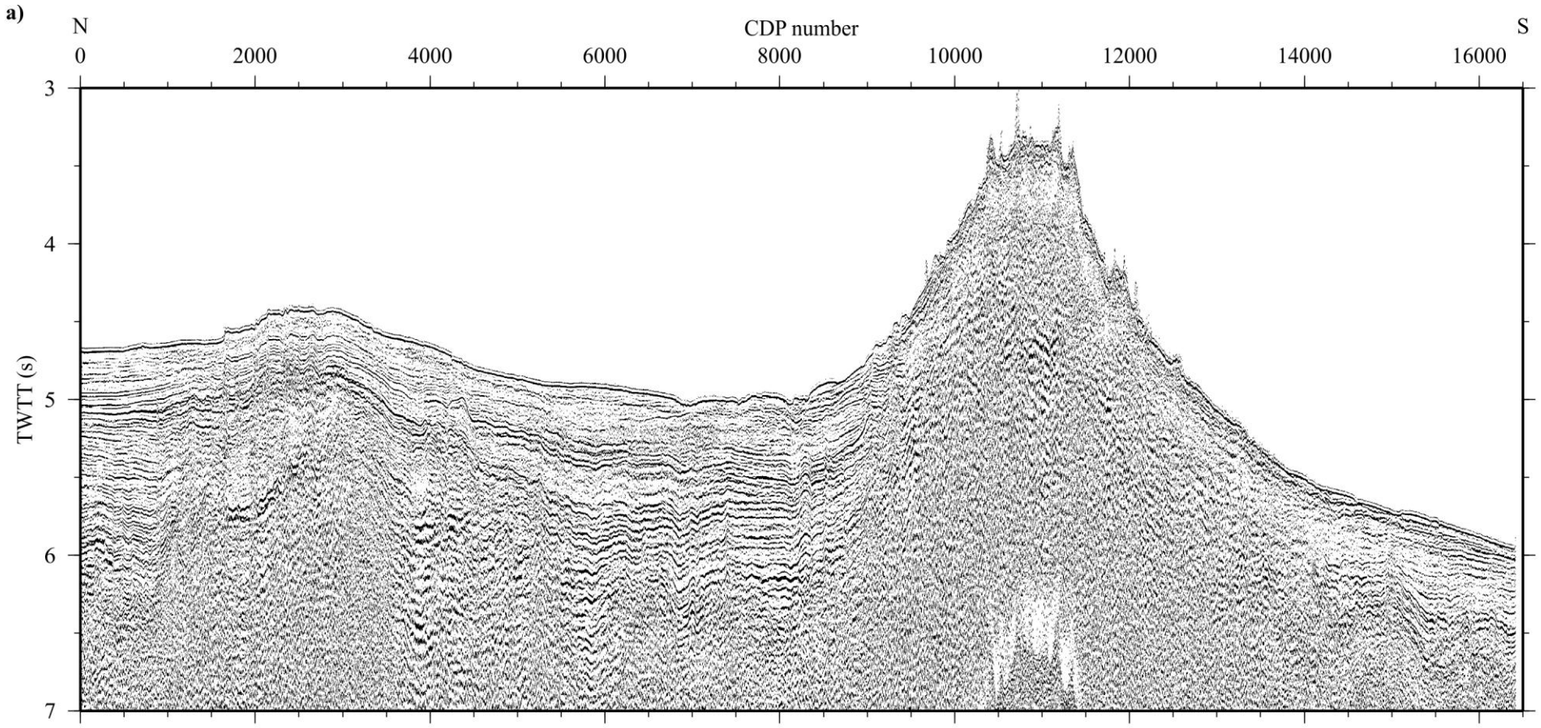

b)

Units	Reflector characteristics and geometry	Typical seismic data	Interpretation
IV	Uppermost reflector, high reflectivity, parallel seafloor, not as many reflectors as other units and laterally continuous.		Pliocene to recent
III	Bright laterally continous reflectors, wedge shape, onlap at base. Basal unconformity marked by a high amplitude reflection.		Early Miocene to late Miocene? Moat infill
II	High reflectivity and generally laterally continuous reflections with some low amplitude intervals.		Late Cretaceous to late Oligocene Margin sediments
I	High reflectivity, reflector geometry controlled by underlying basement.		Jurassic to Early Cretaceous Margin sediments
Basement	High reflectivity and irregular high amplitude reflection at top.		Jurassic/Early Cretaceous oceanic crust

c)

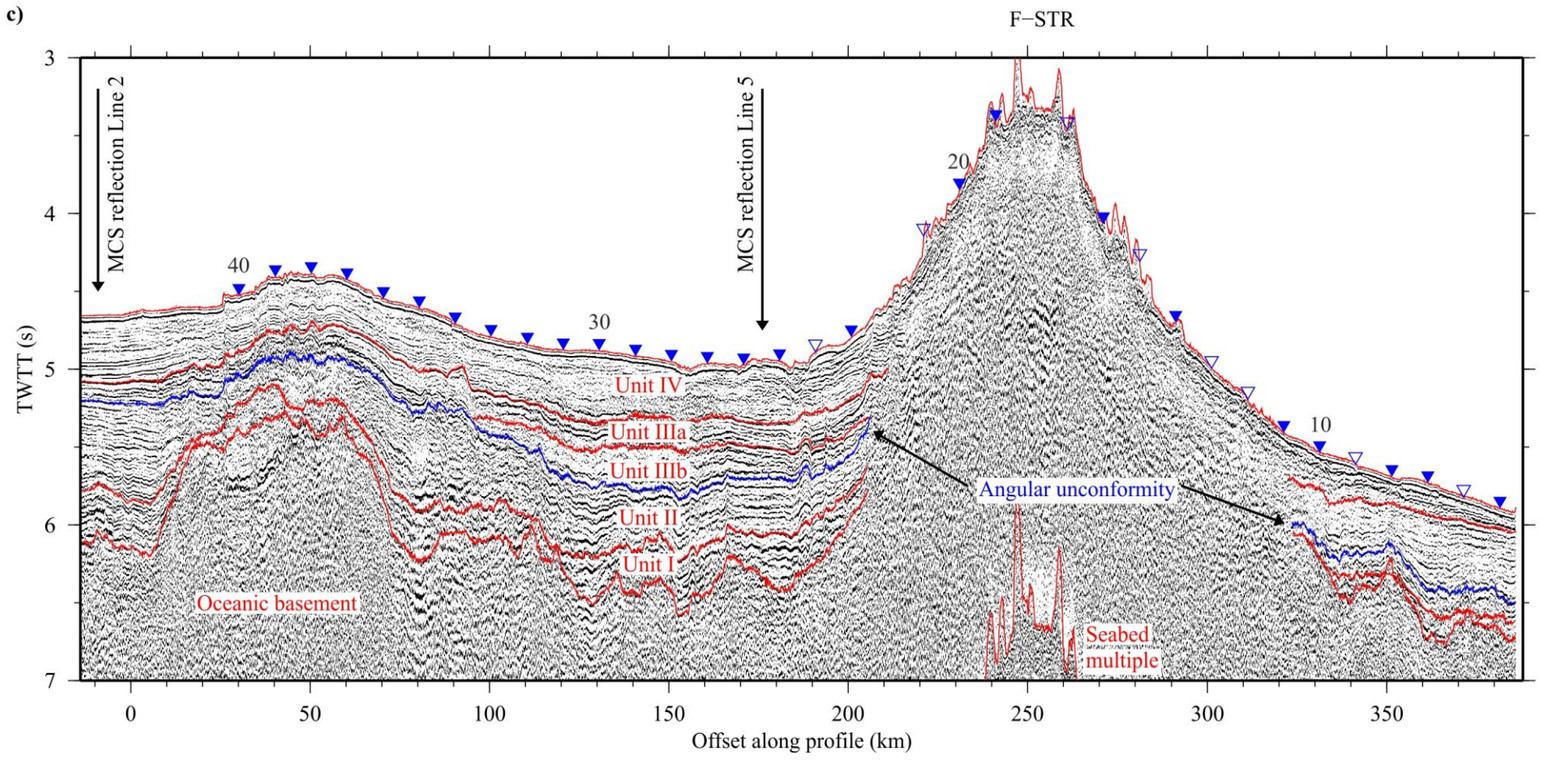

d)

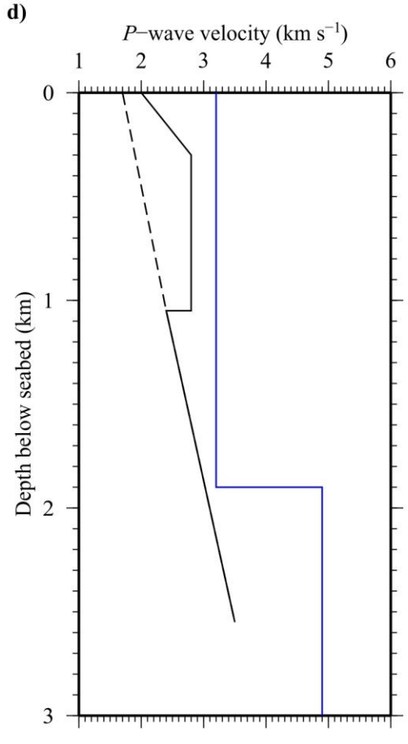

The horizons between these layers, usually high amplitude reflectors, can be mapped laterally and correlated between the MCS reflection lines at their point of intersection (see Figure 2.1a). Using the TWTT picks of the intra-layer horizons at the intersection of Lines 2 and 5 with Line 3 (Ali, 2003), together with the description of the seismic facies (Ali *et al.*, 2003), the horizons have been traced along the northern section of Line 3 (Figure 2.5c). To the south of the F-STR where there are no ties with other profiles, the seismic facies characteristics alone were used to determine which prominent reflector represented each of the inter-layer horizons.

There is an absence of coherent reflectors in the MCS reflection data along Line 3 beneath the F-STR (Figure 2.5a). Instead, there is an intermittent high amplitude event at about 4.5 s TWTT, beneath which there are chaotic high amplitude reflectors, similar to the characteristics of those typically observed beneath the top-basement reflector. The F-STR, therefore, shows reflection characteristics consistent with either igneous material erupted onto the seafloor or mass transport material derived from the adjacent islands, which is corroborated by observations of small-scale seafloor morphology in the shipboard swath bathymetry (Section 2.3). Both of these evaluations suggest that, when compared to elsewhere along the profile, the F-STR is an intra-sediment ridge comprising igneous material covered by a thin veneer of sediment.

This shallow subseabed layering structural definition, consistent along most of profile P01, will be used together with the available 1-D velocity information (Figure 2.5d) to construct the topmost section of the initial 2-D velocity-depth model (Section 2.6.4) prior to forward modelling of traveltime picks from the WA seismic refraction data (Section 2.7).

2.5 Wide-angle seismic refraction data analysis

Seismic energy that has travelled through the subseabed and is recorded as a first arrival at shot-receiver offsets >5 km, generally arrives at an OBS along a near-vertical ray path. The fidelity of recording of this energy by the vertical geophone depends on the quality of the coupling between the OBS and the seabed, and the degree of consolidation of the shallow subseabed sediment. A comparison of two vertical geophone record sections (Figure 2.6), one from OBS19, located on the F-STR, and one from OBS26, located on an area of smooth bathymetry within the

archipelago (Figure 2.4b & c), demonstrates the attenuation effect that poor seabed-instrument coupling can have on vertical geophone data.

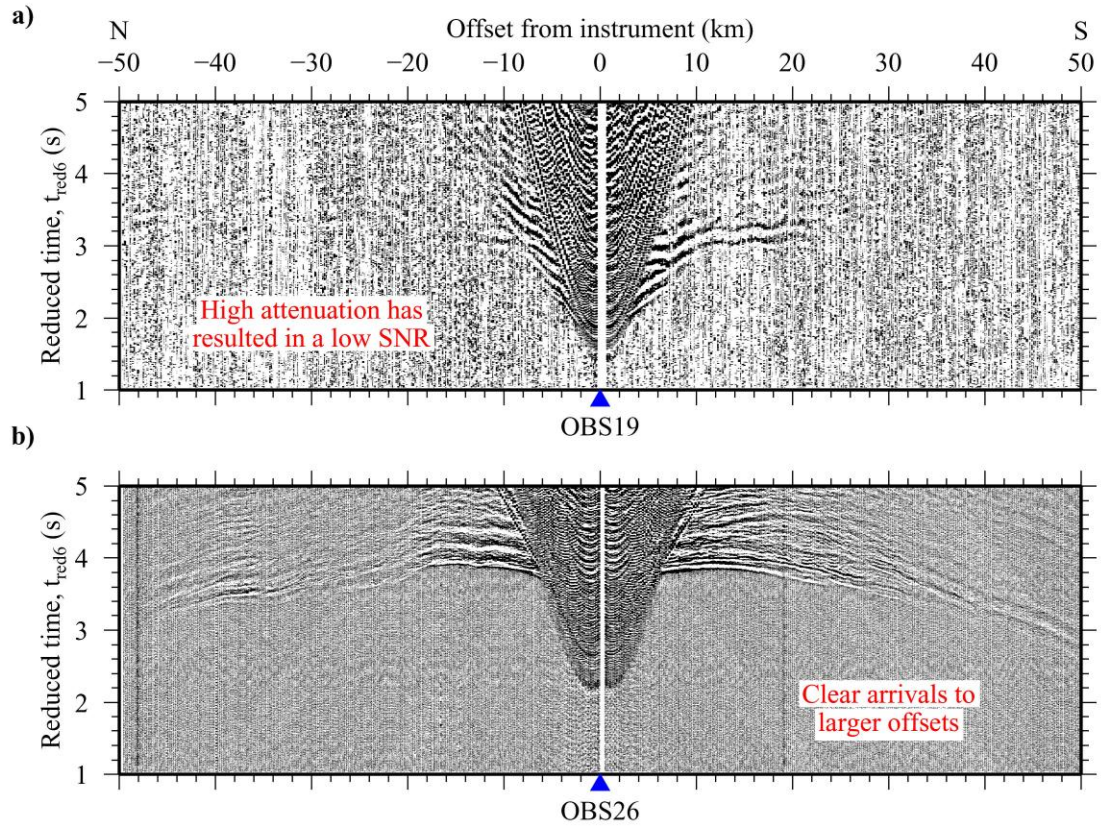

Figure 2.6 The attenuation effect of poor seabed-instrument coupling. Vertical geophone record sections for a) OBS19 and b) OBS26 (see Figure 2.1 and Figure 2.4 for locations). Primary refracted arrivals can be identified at larger shot-receiver offsets where the seabed beneath the OBS is smooth and/or the subsurface is more consolidated, see text for discussion. A bandpass filter of corner frequencies 0-5-70-80 Hz has been applied to the data and both record sections are plotted with a reduction velocity of 6 km s^{-1}.

For most instruments, the hydrophone, measuring changes in pressure in the water column, offers the clearest recording of the refracted wavefield (Figure 2.7) because it has a better signal-to-noise ratio (SNR) and a higher frequency response. Where possible, the hydrophone record section is, therefore, preferentially used for both phase identification and traveltime picking.

On record sections with a high (>2) SNR, arrivals can be identified to >60 km shot-receiver offset (Figure 2.8a). However, for instruments deployed on the crest of the F-STR (Figure 2.1), record sections have a low (<2) SNR (e.g. Figure 2.8c) resulting in arrivals only being clearly observed at much shorter offsets, <10 km in this example.

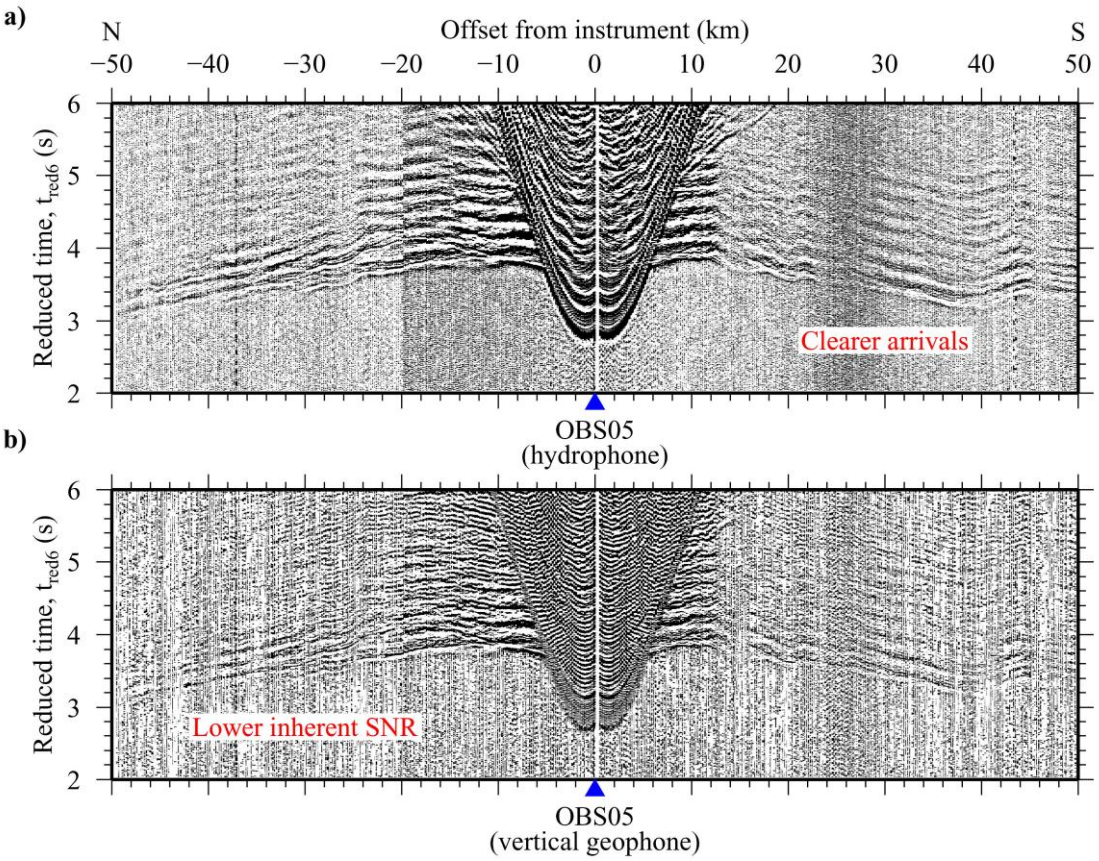

Figure 2.7 A comparison of hydrophone data and vertical geophone data from OBS05. The refracted arrivals on the hydrophone record section, a), are clearer than those on the corresponding vertical geophone record section, b), due to a higher inherent SNR, see text for discussion. A bandpass filter of corner frequencies 0-5-70-80 Hz has been applied to the data and both record sections are plotted with a reduction velocity of 6 km s^{-1}.

2.5.1 Phase identification

High resolution record sections, with a bandpass filter of frequencies 0-5-70-80 Hz applied, were used for initial arrival identification and classification (Figure 2.8). Prior to traveltime picking, the direct and primary refracted arrivals and the secondary reflected arrivals were grouped into seven major phase types that could be correlated between adjacent instruments along the entire profile. The first two phase groups are the direct water wave arrival, the P_w phase, and the reflected water wave multiple arrival, the P_{wm} phase, which are both easily recognisable on all record sections, including those with extremely low SNR (Appendix A).

Figure 2.8 Examples of phase identification on hydrophone record sections from OBSs 14, 19, 23, 27, 29 and 33, and on the vertical geophone record section from OBS07, a) to g) respectively. A bandpass filter of corner frequencies 0-5-70-80 Hz has been applied to the data. P_s, shallow subseabed arrival; P_{g1} and P_{g2}, crustal arrivals; P_mP, wide-angle reflections from the Moho; P_n, arrival from the upper mantle. Record sections are plotted with a reduction velocity of 6 km s^{-1}. h) Filled/open triangles indicate the profile offset locations of the OBSs that successfully recorded data. OBSs from which the record sections in a) to g) are included are highlighted in red. See Figure 2.1 for profile location, definitions and abbreviations.

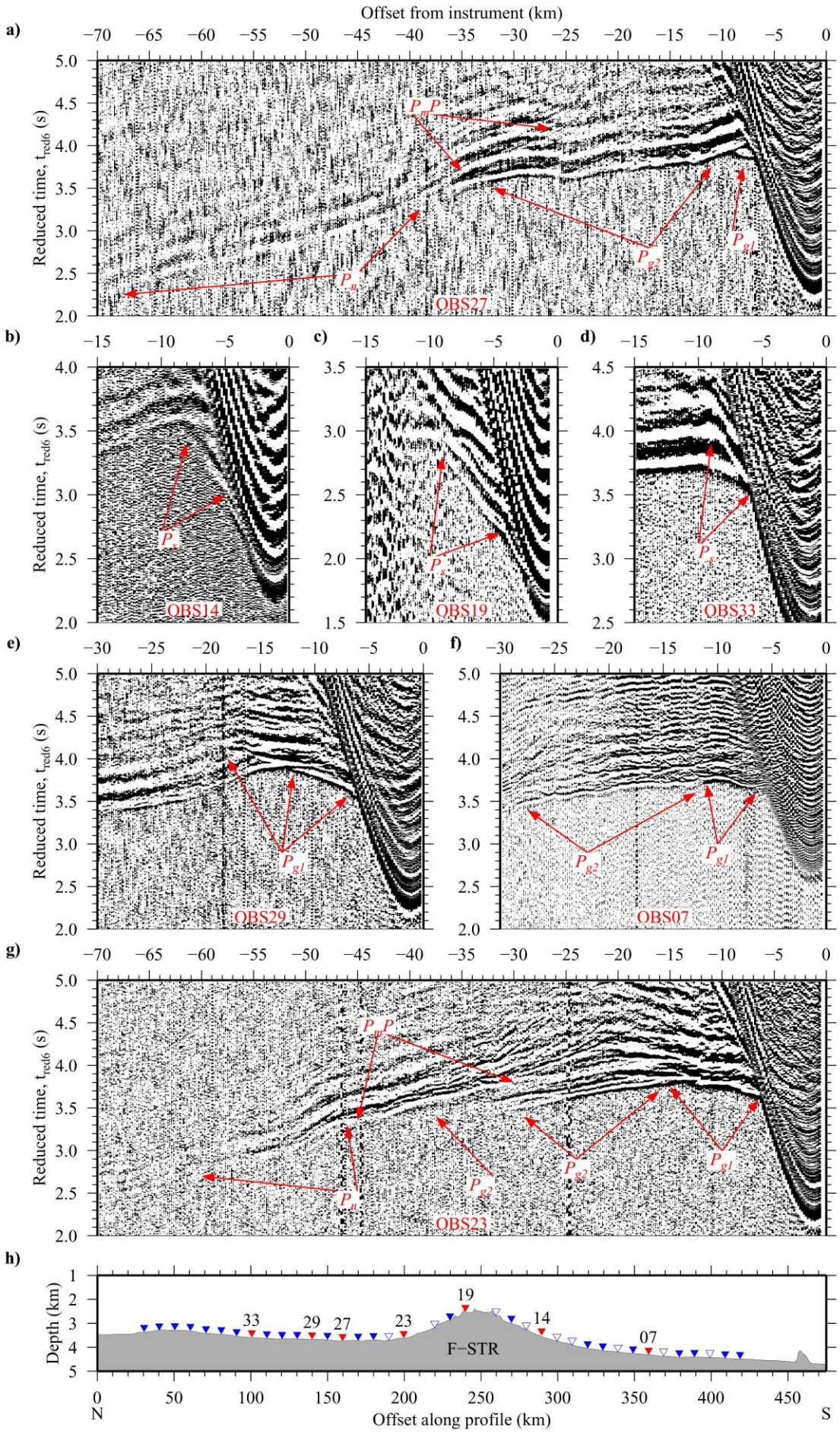
a)
Offset from instrument (km)
Reduced time, t_red6 (s)
P_mP
P_n
P_g2
P_g1
OBS27
b)
OBS14
c)
OBS19
d)
OBS33
e)
OBS29
f)
OBS07
g)
OBS23
h)
Depth (km)
33
29
27
23
19
14
07
F−STR
N
S
Offset along profile (km)

The four phase groups representing the primary refracted arrivals were named according to the expected subseabed structure and phase type (Figure 2.8) as follows: shallow subseabed arrivals, the P_s phase, which are often masked by other phases; two predominant sets of crustal arrivals, phases P_{g1} and P_{g2}; and upper mantle arrivals, the P_n phase. The final phase group, the P_mP phase, comprises secondary arrivals reflected from the Moho.

2.5.1.1 Direct and multiple water wave arrivals, P_w and P_{wm} phases

The most readily identifiable arrivals on any WA refraction record section are the direct water wave and reflected water wave multiple arrivals, phases P_w and P_{wm}. The P_w phase can always be recognised as the first arrivals recorded on the zero-offset and near-offset traces and from its apparent *P*-wave velocity of ~1.50 km s^{-1}. The intercept time of the P_{wm} phase is roughly three times the intercept time of the P_w phase because the seismic energy has travelled three times through the water column, reflecting twice (firstly at the seabed and secondly at the sea surface) before being recorded by the OBS. These two water wave phases were used to calibrate the *P*-wave velocity of the water column and to check the location of the OBSs on the seabed, as well as confirming that the record sections are correctly orientated (Section 2.6.3).

2.5.1.2 Shallow subseabed arrivals, P_s phase

Following the analysis of all record sections, it is evident that the P_s phase has an apparent velocity in the range of 3.50 to 4.00 km s^{-1}. This phase is identified as a primary arrival at small shot-receiver offsets (<10 km) exclusively on records from instruments deployed on the F-STR, located between 220 and 310 km profile offset. The shot-receiver offset range over which this phase is observed increases towards the summit of the F-STR (250 km profile offset), suggesting that the layer through which the seismic energy (recorded as P_s phase arrivals) travels increases in thickness in this vicinity (Figure 2.8b & c).

Although the coincident MCS reflection data reveal a succession of sedimentary layers along the entire profile, except at the F-STR (Figure 2.5c), the seismic energy travelling through these layers is not distinguishable as primary refracted arrivals in the WA seismic refraction data. A previous interpretation of all of the MCS reflection data in this region (Ali *et al.*, 2003; Ali, 2003) and direct evidence gained from the analysis of core samples collected at DSDP site 368 (Lancelot *et al.*,

1978b), indicate sediment thicknesses of <2 km and bulk sediment *P*-wave velocities of <2.50 km s^{-1}, respectively. Ringing of the airgun source during data acquisition resulted in a long seismic wavelet which prevents independent identification of a distinct sediment phase because it has arrivals with very similar traveltimes to those of the P_w, P_{g1} and P_{g2} phases which, as a result, are hidden in the high amplitude wavelet of the primary.

2.5.1.3 Crustal arrivals, P_{g1} and P_{g2} phases

Upper-mid crustal arrivals, the P_{g1} phase, are identified as clear, high-amplitude events at shot-receiver offsets of <10 to 15 km on record sections from OBSs along the entire profile (Figure 2.8e). These phases typically exhibit apparent velocities between 4.50 and 5.50 km s^{-1}, within the range expected for typical basaltic oceanic crustal layer 2 (White *et al.*, 1992). The transition to the mid-lower crustal arrivals, the P_{g2} phase, can be observed by a reduction in amplitude and an increase in apparent velocity, which is either a discrete velocity increase of magnitude 0.5 km s^{-1} or continuous (Figure 2.8a & f). The P_{g2} phase characteristically displays a gradual increase in apparent velocity from ~5.75 km s^{-1} at the top of the layer to ~7.25 km s^{-1} at the base, a range that is comparable to that of gabbroic oceanic crustal layer 3 in the North Atlantic (White *et al.*, 1992). The low vertical velocity gradient (~0.2 s^{-1}) in the lower oceanic crust means that variation in P_{g2} phase arrival time with shot-receiver offset is mainly controlled by the topography of the seabed and the top-basement surface. Two examples of this proxy for top-basement surface topography can be seen on the record sections for several OBSs deployed between 100 and 170 km profile offset, where relatively late P_{g2} arrivals are consistently observed around 128 and 155 km profile offset (Figure 2.9). There is no significant change in the seabed topography at these locations, implying that this delay in arrival times must reflect a change in the basement topography. There is evidence for basement topography changes at the equivalent profile offsets on the MCS reflection data (Figure 2.5). Mid-lower crustal arrivals are consistently observed as primary arrivals to shot-receiver offsets of 30 to 40 km, suggesting that there is no significant change in crustal thickness (i.e. <1.5 km) along the entire profile.

Figure 2.9 Record sections from several OBSs located between and 100 and 170 km profile offset showing evidence for changes in basement topography. Red ovals indicate relatively late P_{g2} arrivals that can be correlated at the same profile offset on the record sections from a) OBS32, b) OBS31, c) OBS28 and d) OBS27. e) There is no evidence for changes in bathymetry at the profile offsets corresponding to the locations of the relatively late P_{g2} arrivals.

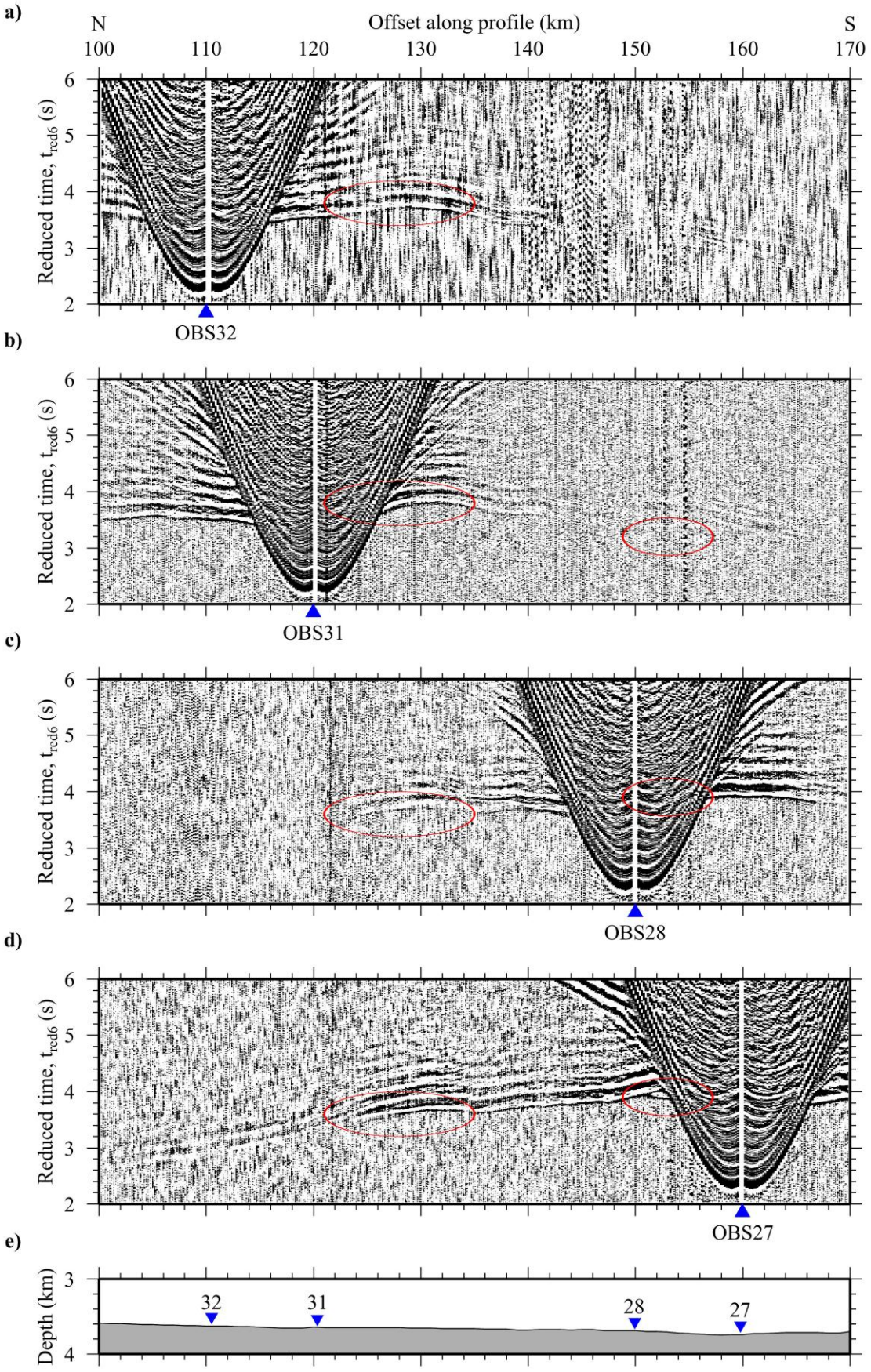
a)
N
Offset along profile (km)
S
100
110
120
130
140
150
160
170
Reduced time, t_{red6} (s)
6
5
4
3
2
OBS32
b)
OBS31
c)
OBS28
d)
OBS27
e)
Depth (km)
3
4
32
31
28
27

2.5.1.4 Arrivals from the Moho and upper mantle, P_mP and P_n phases

Arrivals that are reflected at the Moho, the P_mP phase, are observed intermittently along the profile (Figure 2.8a & g). The presence of a Moho as a distinct interface is interpretable from the change in the apparent velocity of the first arrivals from 7.25 to 8.00 km s^{-1}, which is consistently observed at ~35 km shot-receiver offset. A decrease in the amplitude of phase P_{g2} arrivals is sometimes observed leading up to this transition (Figure 2.8g). Unfortunately, arrivals from the upper mantle, the P_n phase, generally have a low SNR and are rarely observed at shot-receiver offsets >50 km. The lack of discernable events at shot-receiver offsets >50 km limits the vertical depth range of the velocity-depth model that is constrained by the traveltime modelling, due to the proportional relationship between shot-receiver offset and turning ray penetration (Section 2.7).

There is no evidence for the secondary, deep-crustal WA reflections that have been observed at some intraplate settings (e.g. Watts *et al.*, 1985; Caress *et al.*, 1995; Grevemeyer *et al.*, 2001a). Such deep-crustal reflections, together with unusually high lower crustal velocities (>7.3 km s^{-1}), have been interpreted as an indication of the presence of an additional relic Moho, which separates pre-hotspot crust from undercrustal material. The absence of these reflections in the Cape Verdes data set suggests, at this early stage of the interpretation process, that there has been no significant (i.e. thicker than the vertical resolution of the seismic data at that depth) volume of undercrustal material added to the base of the crust anywhere along the profile.

2.5.2 Traveltime picking

To facilitate efficient traveltime picking of the arrivals in every phase group, each record section was converted from SEG-Y into '*z format*' for input into the interactive plotting and picking tool, *zplot* (Zelt & Smith, 1992). Traveltime picks were made primarily from unfiltered data, except on traces where the SNR was low and the noise had a predominant frequency within the frequency band of the seismic source (see Section 2.2.2; Figure 2.3).

For traces with clear primary arrivals, the onset of the seismic wavelet was picked (Figure 2.10b). For secondary arrivals, and primary arrivals with a low SNR, the

zero-crossing immediately preceding the maximum amplitude peak of the seismic wavelet was picked (Figure 2.10c & d).

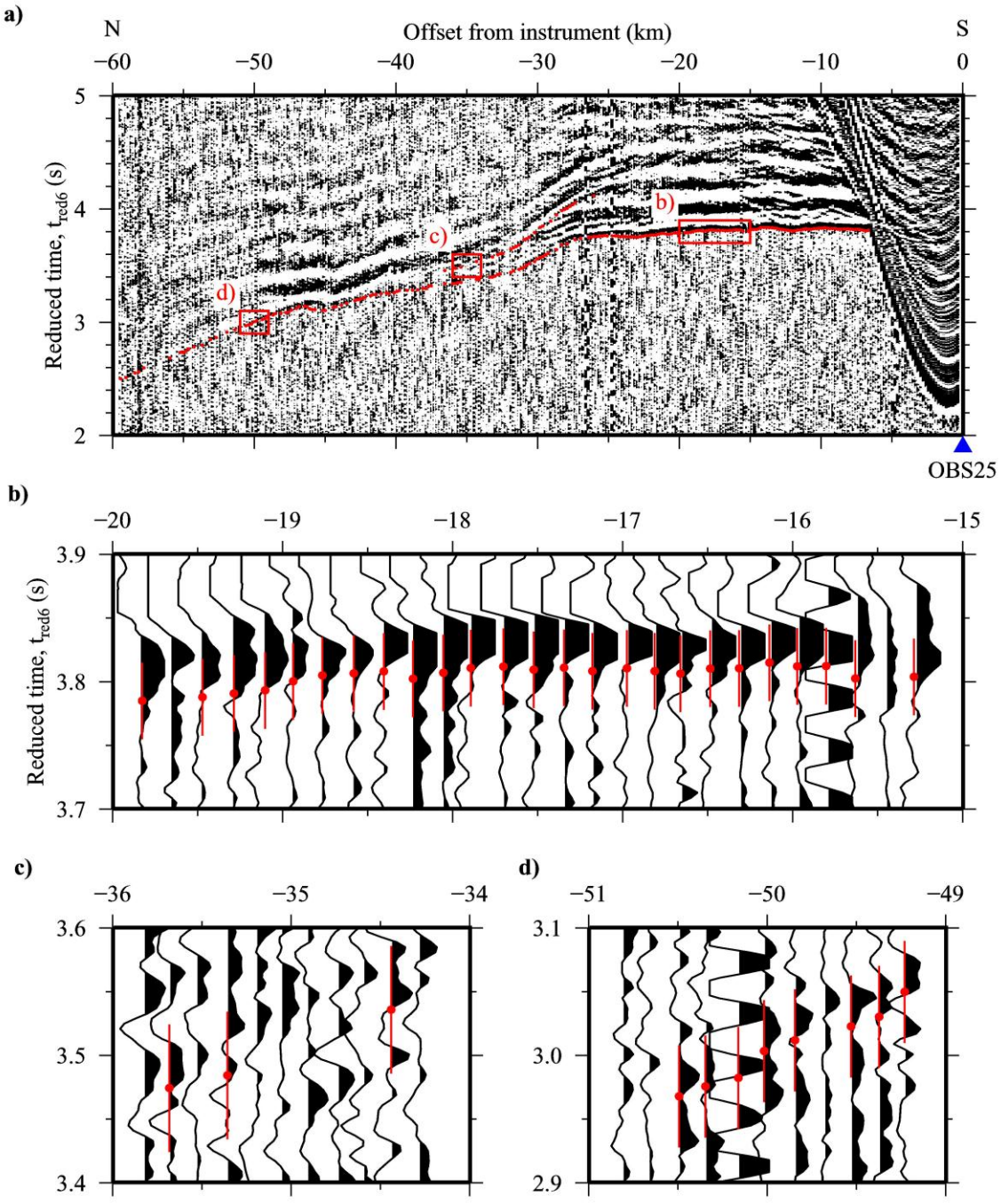

Figure 2.10 Traveltime picking of primary refracted arrivals and secondary reflected arrivals from the hydrophone record section of OBS25. a) All traveltime picks made on traces from the north of the OBS deployment location. Red boxes indicate the regions shown in greater detail in b) to d). b) Picks made at the onset of the seismic wavelet. c) and d) Picks made at the zero-crossing immediately preceding the maximum amplitude peak of the seismic wavelet. Red dots indicate the traveltime pick and vertical bars represent the total uncertainty assigned to each pick. A bandpass filter of corner frequencies 0-5-70-80 Hz has been applied to the data and all record sections are plotted with a reduction velocity of 6 km s^{-1}.

In some cases, where the onset or the zero-crossing could not be identified due to high levels of background noise, the maximum amplitude peak of the seismic wavelet was still visible. Where only the maximum amplitude peak could be picked, the pick inaccuracy error factor was increased to account for the delay between onset and the maximum amplitude arrival times of the seismic wavelet (Section 2.5.3).

A summary of the labelling system that was defined to assist modelling and indicate the phase type of each traveltime pick is summarised in Table 2.1. This labelling system enabled consistency in phase identification to be maintained across all OBS record sections. Consistency in phase identification is an important consideration in preparation for use of the forward modelling program, *rayinvr* (Zelt & Smith, 1992) to enable labelled phases to be easily correlated with distinct ray packages used to calculate similarly labelled traveltime arrivals for seismic energy that has refracted through a particular layer of the velocity-depth model. This labelling nomenclature becomes especially important when undertaking quantitative analysis of the fit of the traveltimes calculated using the velocity-depth model to the observed traveltimes (Section 2.7.1).

Table 2.1 Summary of phase grouping applied to observed traveltime picks. Apparent *P*-wave velocities and pick uncertainties for each phase group identified in the WA data set are included.

Phase	*P*-wave velocity (km s^{-1})	Traveltime uncertainty (ms)
P_w	1.49-1.51	10-20
P_{wm}	1.49-1.51	10-20
P_s	3.50-4.00	20-30
P_{g1}	4.50-5.50	20-30
P_{g2}	5.75-7.25	30-40
P_n	~8.00	40-50
P_mP	N/A	50

2.5.3 Traveltime uncertainties

The total uncertainty of each traveltime pick (T_u) depends upon several error factors: the sampling interval (t_{u1}); OBS clock drift (t_{u2}); bathymetry uncertainty (t_{u3}); instrument location on the seabed (t_{u4}); shot location (t_{u5}); and the delay between seismic wavelet onset and the maximum amplitude (t_{u6}). These error factors are constant for each OBS and are calculated using the following equation:

$$T_u = \left(\sqrt{\left((t_{u1})^2 + (t_{u2})^2 + (t_{u3})^2 + (t_{u4})^2 + (t_{u5})^2 + (t_{u6})^2 \right)} \right) + t_p \qquad \textbf{(2.2)}$$

An additional error factor, the pick inaccuracy (t_p), is independently added to the OBS error factor for each individual pick and accounts for the variable SNR. The pick inaccuracy generally increases with increasing shot-receiver offset. The ranges of the total traveltime uncertainty for each phase type are summarised in Table 2.1.

2.6 Initial model construction

In this section the construction of the initial 2-D velocity-depth model for profile P01 (Figure 2.11) is outlined. The experiment geometry is converted into a 2-D model space and complementary geological and geophysical data pertaining to the expected depth and velocity gradient of layers in the shallow subseabed, oceanic basement and upper mantle are incorporated to provide a suitable starting point for traveltime modelling.

2.6.1 Model definition

The initial 2-D velocity-depth model comprised six layers: the water column; the sedimentary cover and one for each of the four labelled primary refracted phase arrival groups (Table 2.1). Each layer is defined by an upper boundary surface and *P*-wave velocity values at the top and base of the layer that control the vertical and horizontal velocity gradients. An array of depth nodes define changes in the topography of the boundary surface and two arrays of velocity nodes control the vertical and horizontal velocity gradients throughout the layer. The profile offset interval between depth nodes is 5 km, except for the seabed which has a node spacing of 1 km. To begin with, each layer had a pseudo-1-D velocity-depth profile, whereby the lateral velocity gradients were only affected by changes in the geometry of the boundary surfaces and the layer thickness. The thickness and velocity structure of each layer in the initial 2-D velocity-depth model is summarised in Table 2.2.

2.6.2 Seafloor bathymetry

The topmost layer in the initial model defines the water column. A comparison of the shipboard swath bathymetry data and the corresponding GEBCO data along profile P01 (Figure 2.4d) reveals a marked difference in the accuracy of the two datasets, highlighting the importance of obtaining near-field measurements of the water depth wherever possible.

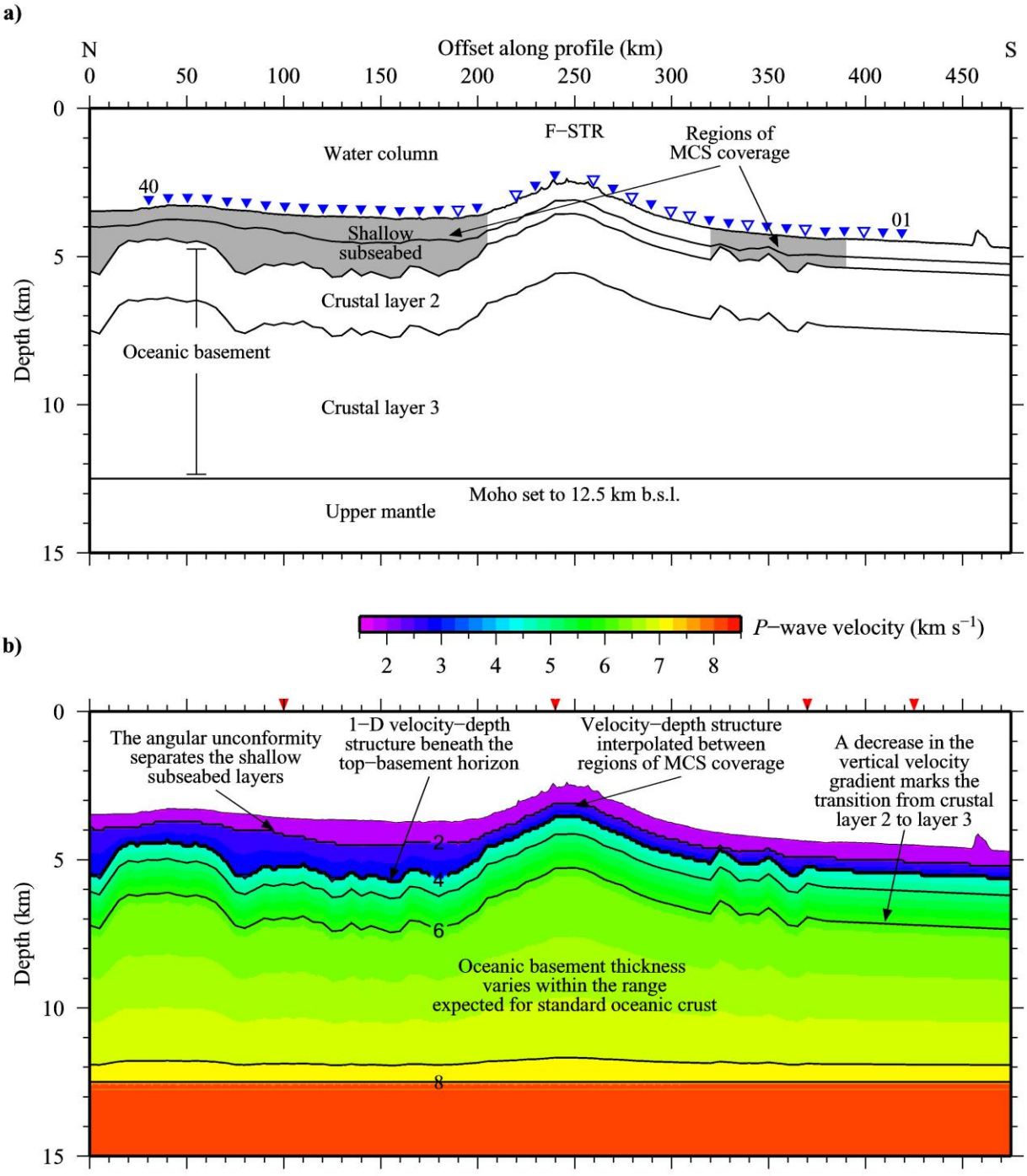

Figure 2.11 Layer and velocity-depth structure of the initial model. a) The boundary surfaces of the model are shown (black lines) together with the extent of coverage of the shallow subseabed from the MCS reflection data (grey region) of Line 3 from RRS *Charles Darwin* cruise CD8/85. The model layers, described in Section 2.6, are annotated. Filled/open blue inverted triangles mark OBS/OBH locations. b) The velocity-depth structure of the initial model. Iso-velocity contours (black lines) are annotated with a 1 km s^{-1} contour interval. Key features, as discussed in the text, are also annotated. The profile offset locations of the 1-D velocity-depth profiles plotted in Figure 2.13 are indicated with red arrowheads. The layering structure is summarised in Table 2.2.

Table 2.2 Layering structure of the initial 2-D velocity-depth model. The thicknesses of the shallow subseabed layers were acquired from the interpretation of the coincident MCS reflection data from RRS *Charles Darwin* cruise CD8/85, Line 3 (see Ali *et al.*, 2003). The oceanic basement and upper mantle structures represent averages of the structure of mature Atlantic oceanic crust from White *et al.* (1992). † The lower velocity of the water column quoted here has been calculated using the velocity gradient and the average seabed depth of 4 km b.s.l..

Model layer	Thickness (km)	Upper velocity (km s^{-1})	Lower velocity (km s^{-1})	Velocity gradient (s^{-1})
Water column	~4.0	1.49	1.51†	0.005
Shallow subseabed 1	0.5-1.0	1.75	2.00	0.25-0.50
Shallow subseabed 2	0.5-1.5	2.50	3.00	0.35-1.00
Upper oceanic basement	2.0	4.50	5.50	0.50
Lower oceanic basement	4.5-6.0	6.00	7.10	0.20-0.25
Upper mantle	-	8.00	-	<0.005

The seabed along profile P01 was extracted from the gridded shipboard swath bathymetry data and down-sampled to 1 km intervals to populate the highest density of nodes permitted by the parameterisation of the input model for *rayinvr* (Zelt & Smith, 1992). The seabed (top boundary surface of model layer 2) was assigned an uncertainty of ±30 m, based on the accuracy of the *HYDROSWEEP DS2* multibeam system (1% of the range; Grevemeyer *et al.*, 2004). This layer was assigned a velocity of 1.49 km s^{-1} at the top (sea level, 0 km depth) increasing with a vertical velocity gradient of 0.005 s^{-1}, to 1.51 km s^{-1} at 4 km b.s.l..

2.6.3 OBS positioning

The location of each OBS was converted from geographical coordinates to the profile offset reference framework outlined in Section 2.2.1. The depth of each OBS was calculated using the traveltime pick of the direct water wave arrival at zero-offset and the average velocity of sound in seawater (1.50 km s^{-1}). The calculated water depths for each OBS were checked against the seabed depth taken from the shipboard swath bathymetry at the corresponding profile offset. Small mismatches in the depth obtained from the traveltime data and the swath bathymetry data were recorded for some OBSs due to offline locations. In addition, where necessary, the seabed depth was adjusted, within the assigned uncertainty (Section 2.6.2), to place all instruments just above the seabed for consistency and to match the actual experiment geometry. It was also important to ensure that each OBS was not located

within 0.005 km of a depth node to prevent ray-tracing errors when using *rayinvr*. For example, the seabed node at 169.00 km was moved to 169.01 km to accommodate OBH26, located at 169.001 km profile offset.

Following these minor adjustments to the position of the seabed, the modelled velocity structure of the water column and geometry of the seabed were tested. Ray packages representing direct water waves and seabed-surface reflections were traced through the model to produce calculated traveltimes at all shot-receiver offsets for each OBS, for comparison with the observed traveltime picks (phases P_w and P_{wm}, respectively; Figure 2.12). The asymmetry of phase P_{wm} arrivals is controlled by the asymmetry of the seabed depth to either side of the OBS. This asymmetry can be used to confirm that the record sections are correctly orientated prior to traveltime modelling (Figure 2.12a).

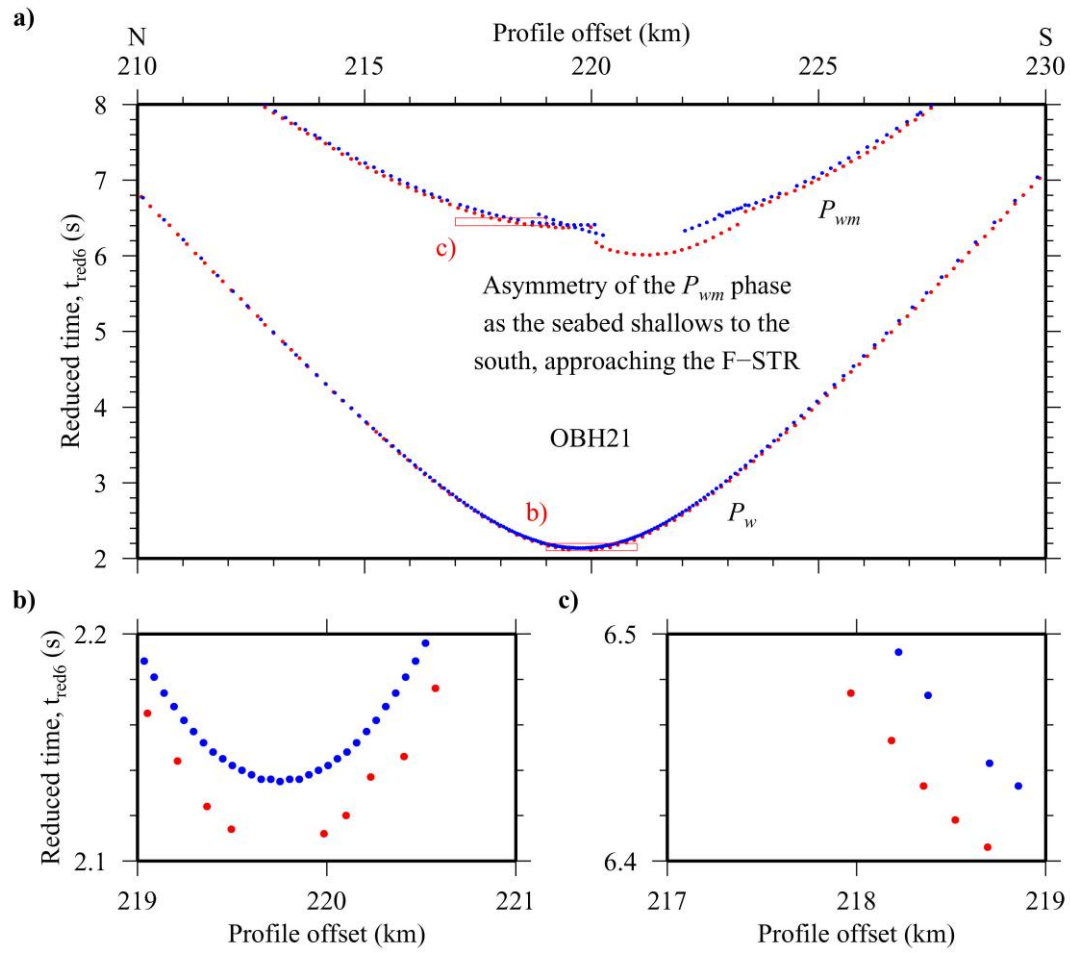

Figure 2.12 Ray-trace modelling of the water column to test OBS positioning and initial model seabed geometry. a) The asymmetry of the seabed-surface multiple reflection can be used to check the orientation of the record section and the arrival time of the traveltime picks. Red boxes indicate the regions shown in greater detail in b) and c). b) and c) Modelling revealed a systematic delay of ~30 ms between the traveltime picks (red) and the calculated traveltime data (blue). This delay was corrected by application of a static time shift of +30 ms to all traces.

At this stage of analysis it was discovered that all of the calculated traveltimes for phases P_w and P_{wm} arrived 30 ms later than the corresponding observed traveltime picks (Figure 2.12b & c). The cause of the misfit was attributed to a misassignment by the shipboard data processor of the delay between the shot trigger pulse and the maximum energy output from the source array used as the correct start time for each shot trace. This error was corrected by applying a bulk static time shift of +30 ms to all traces.

After small adjustments to the seabed and instrument locations, the only remaining misfits between calculated and observed traveltimes for phases P_w and P_{wm} are observed at near-offset for OBSs in the region of the F-STR. These minor misfits are attributed to short-wavelength seabed fluctuations that could only be modelled with a much finer node interval. The node spacing interval was not decreased in an attempt to reduce these minor misfits as the aim of this study is to investigate the large-scale 2-D velocity-depth structure of the whole oceanic crust and upper mantle, and, for this purpose, the current model definition provides adequate resolution within the modelling constraints embedded into *rayinvr* (Zelt & Smith, 1992) within the context of time-efficient modelling.

2.6.4 Shallow subseabed

The subseabed nodes of the initial 2-D velocity-depth model also need to be populated with informed estimates of the crustal and upper mantle velocity and depth to produce a working model for ray-tracing with *rayinvr*. Preliminary information about the velocity-depth structure of the shallow subseabed can be obtained using the TWTT horizons mapped from the MCS reflection data together with various *P*-wave velocity estimates from previous seismic experiments and direct observations.

2.6.4.1 Seismic stratigraphy

Originally, five horizons were mapped below the seabed on the MCS reflection data (Section 2.4; Figure 2.5c), separating the five sedimentary units that were categorised by Ali *et al.* (2003). As the purpose of this study is to produce a 2-D velocity-depth model of the oceanic crust and uppermost mantle to constrain 3-D modelling of 'whole plate' lithospheric flexure (Chapter 5), only the main units which demonstrate the load-related flexure are required.

Consequently, the sediment column was divided into two layers, separated by the angular unconformity interpreted as representing the onset of subsidence due to surface loading. Shallow subseabed layer 1 represents the Neogene sediments infilling the flexural moats formed by island-related plate loading, whereas shallow subseabed layer 2 represents the Mesozoic sediments derived from the West African margin.

2.6.4.2 Depth conversion

In order to convert the horizons representing the angular unconformity and the top basement surfaces from TWTT to depth for input to the initial 2-D velocity-depth model, information about the internal *P*-wave velocity of each shallow subseabed layer was required. The range of apparent velocities observed for the P_s phase is not directly applicable because this phase is only observed on record sections from OBSs deployed on the F-STR where no directly comparable seismic stratigraphy is observed on the MCS reflection data (Figure 2.5c). Consequently, interval velocities were sourced from a combination of standard sediment relationships (Hamilton, 1978), Ali *et al.* (2003)'s stacking velocities, Dash *et al.* (1976)'s 1-D model and DSDP drilling logs (Lancelot *et al.*, 1978b) (Figure 2.5d). Interval velocities of 1.90 and 2.75 km s^{-1} were used to convert the angular unconformity and the top-basement horizons, respectively, from TWTT to depth. In the initial 2-D velocity-depth model, these layers were assigned small 1-D vertical velocity gradients so that turning rays would be traced when modelling with *rayinvr*.

Although there are no directly observable primary refracted arrivals of seismic energy travelling exclusively through these layers, they need to be included in the forward modelling process (Section 2.7) because any change in the velocity-depth structure of the shallow subseabed has a direct impact on the ray path, and hence traveltime, of phase P_{g1}, P_{g2}, P_n and P_mP arrivals.

It is worth noting at this point that the shallow subseabed velocity structure in the 2-D velocity-depth model (Section 3.2) will ultimately be used to convert the TWTT picks of the regional MCS-derived flexural markers into layer thicknesses and depths below seabed (Section 3.3), and to best estimate bulk layer density (Chapter 5). In turn, these depths, thicknesses and densities will be used to calculate the 'background' upper plate (crustal) characteristics and, hence, the load input for 'whole plate' flexure modelling, the results of which will be presented in Chapter 5.

2.6.5 Oceanic basement and uppermost mantle

A simplified, 1-D, two-layered oceanic basement with an underlying lithospheric mantle, was incorporated beneath the top-basement surface to complete the initial model (Figure 2.11) using layer thicknesses, velocities and velocity gradients derived from White *et al*. (1992)'s model for standard, mature Atlantic oceanic crust (Figure 2.13).

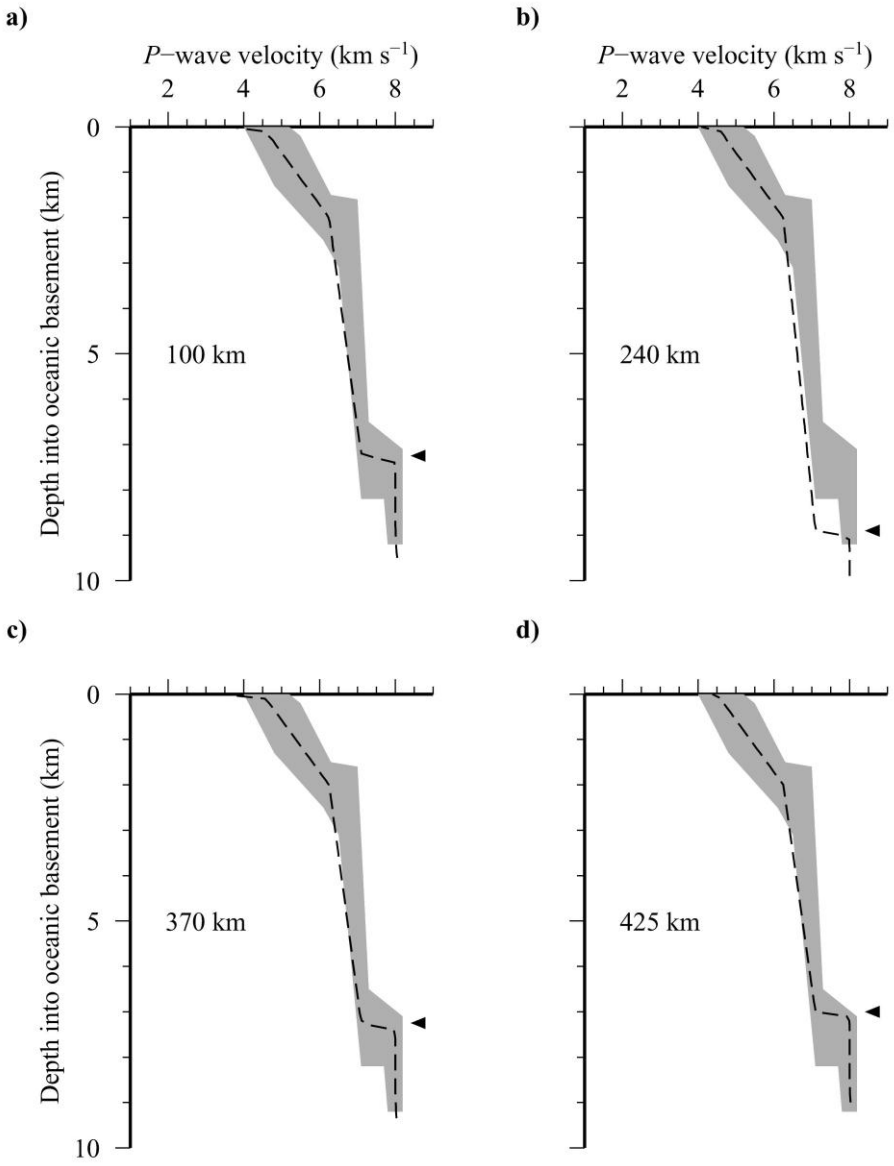

Figure 2.13 1-D velocity-depth profiles from the initial model (black dashed lines), see Figure 2.11 for locations. The expected range in velocity-depth structure for mature Atlantic oceanic basement is also included (grey shaded region; after White *et al.* 1992). The depth of the Moho in the initial model is also indicated (black arrowheads). a) 100 km profile offset. b) 240 km profile offset. c) 370 km profile offset. d) 425 km profile offset.

This starting velocity-depth structure is applicable here because the presence of magnetic anomaly isochrons M0 to M21, either side of the Cape Verde archipelago, suggests that this region of oceanic basement was accreted during the separation of the African continent from the Americas in the early Cretaceous, between 110 and 150 Ma.

2.7 Wide-angle seismic data modelling

Wide-angle modelling of the observed traveltime data aimed to produce a crustal model, accurate to ±1 km at the Moho, as a prerequisite for flexural modelling at an appropriate resolution (Chapter 5). The 2-D forward ray-tracing approach, *rayinvr* (Zelt & Smith, 1992), was used to obtain a velocity-depth model of the crustal and upper mantle structure at the Cape Verde mid-plate swell, along profile P01. The profile is approximately parallel to the MAR, which is where the oceanic crust throughout this region was accreted and, hence, the age of the crust along the entire profile is of a similar age. Additionally, the oceanic crust in the region of the Cape Verde Islands is mature (>110 Ma), implying that the velocity-depth structure of the crust immediately adjacent to the profile will be very similar, thus validating the 2-D approach to modelling.

2.7.1 Traveltime modelling

It is widely accepted that, as part of forward modelling any OBS data, rays are traced backwards from an OBS to each shot location, rather than from the shot to the OBS as the data were acquired. The result is a set of calculated traveltimes that can be compared to the observed traveltime picks (e.g. Figures 2.14, 2.15 & 2.16). A top-down approach was implemented for forward modelling, tracing rays through progressively deeper model layers to calculate arrivals at increasing shot-receiver offsets.

Figure 2.14 Summary of ray-trace modelling of traveltime picks from hydrophone data recorded by OBS08. See Figure 2.1 for OBS location. a) Bandpass filtered (0-5-70-80 Hz) record section plotted without the application of any amplitude corrections. Calculated traveltimes for all modelled subseabed phases are plotted at all offsets and coloured according to phase assignment. b) Observed traveltime picks (black vertical bars, representing the assigned uncertainties) and calculated traveltimes at corresponding shot-receiver offsets, coloured as for a). The χ^2 value gives an indication of the quantitative fit of the calculated traveltimes to the observed picks (χ^2 = 1: best achievable fit; χ^2 < 5: acceptable fit – see Section 2.7.1; Equation 2.3). c) Ray diagram showing the rays traced to produce the calculated arrivals in b). Record sections and traveltimes are plotted with a reduction velocity of 6 km s^{-1}.

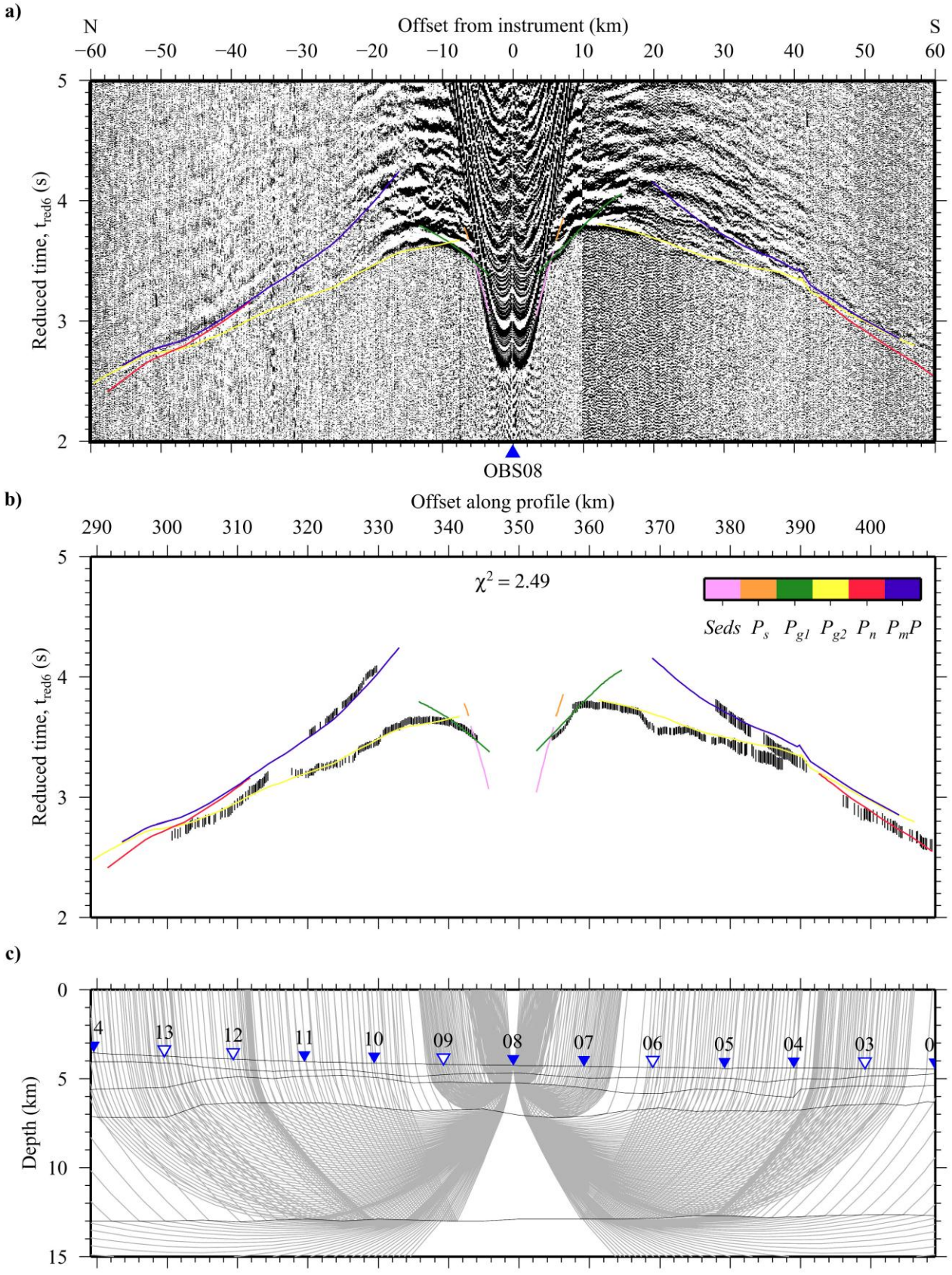
a)
N
Offset from instrument (km)
S
−60 −50 −40 −30 −20 −10 0 10 20 30 40 50 60
Reduced time, t_{red6} (s)
OBS08
b)
Offset along profile (km)
290 300 310 320 330 340 350 360 370 380 390 400
$\chi^2 = 2.49$
Seds P_s P_{g1} P_{g2} P_n P_mP
Reduced time, t_{red6} (s)
c)
Depth (km)
14 13 12 11 10 09 08 07 06 05 04 03 0

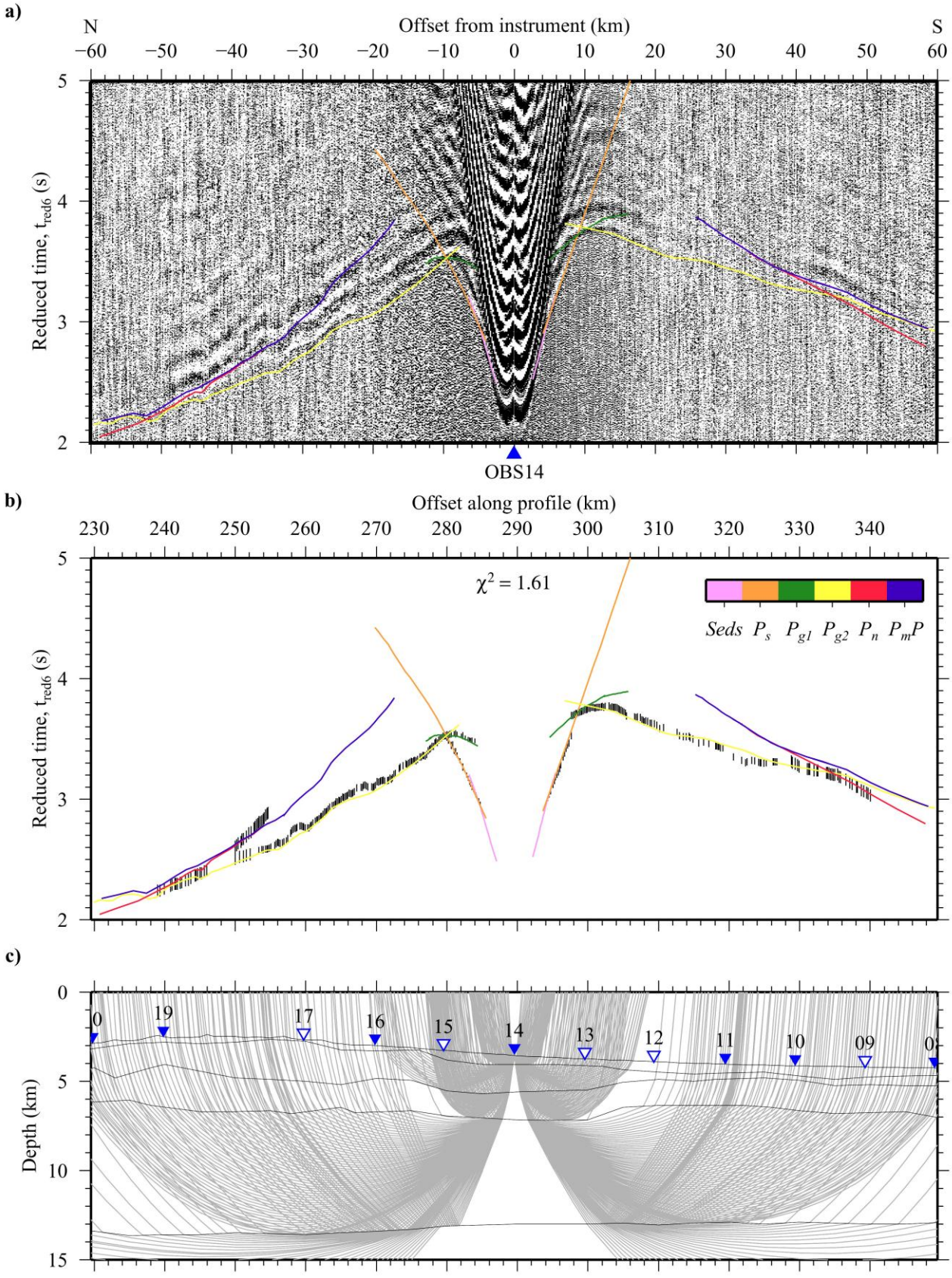

Figure 2.15 Summary of ray-trace modelling of traveltime picks from hydrophone data recorded by OBS14. See Figure 2.14 for details.

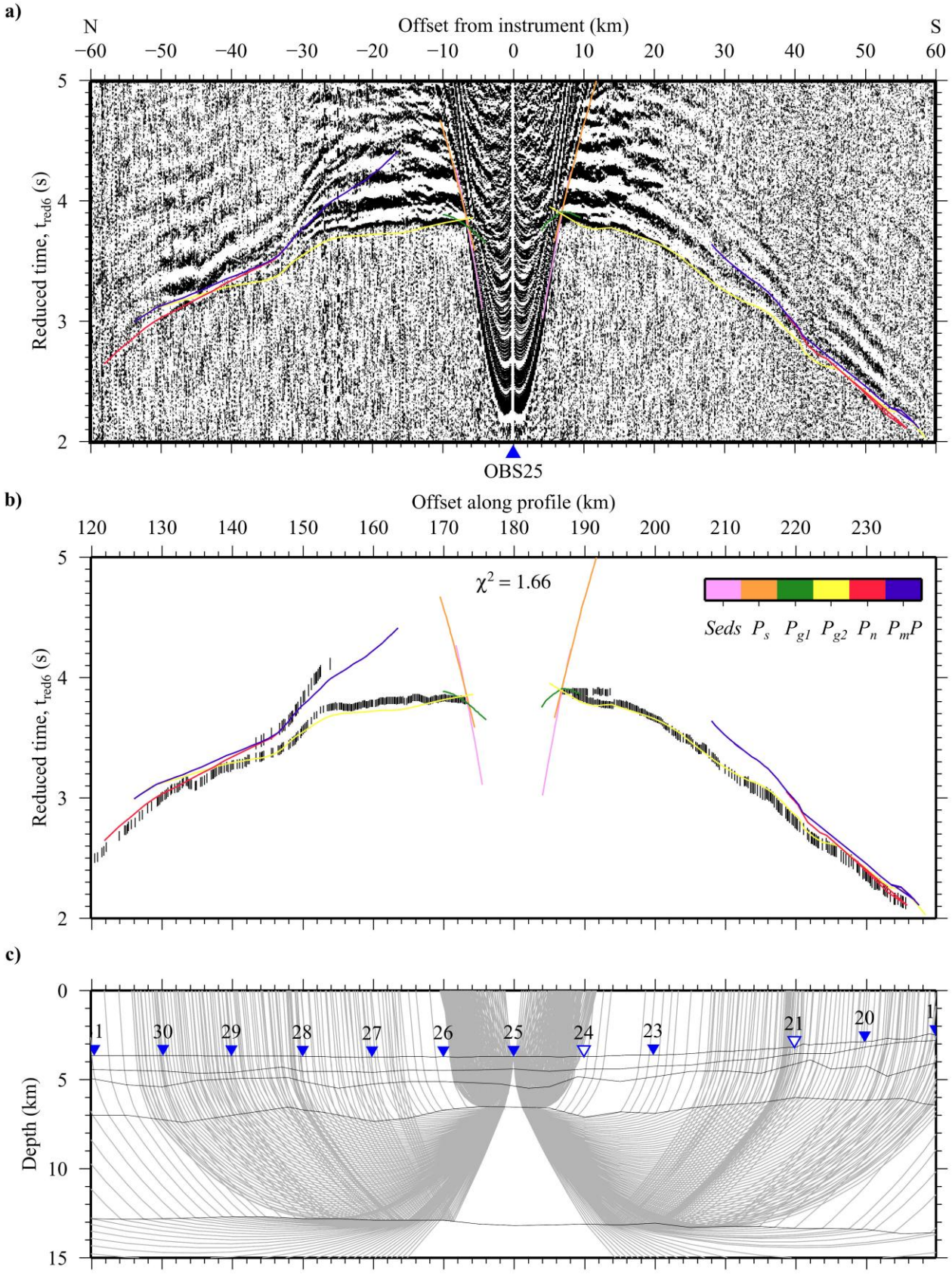

Figure 2.16 Summary of ray-trace modelling of traveltime picks from hydrophone data recorded by OBS25. See Figure 2.14 for details.

For each layer, the arrivals from a subset of four or five adjacent instruments were modelled simultaneously, starting at the northern end of the profile. A 'rolling window' technique was adopted to progressively incorporate additional instruments along the profile while maintaining an overlap with the previous subset. Rays are categorised into groups called ray packets and each packet contains all the rays which turn in the same layer or reflect off the same boundary surface. In this study, ray packet nomenclature follows the same labelling convention used for the phases observed on the WA refraction data record sections (Table 2.1).

Initially, the fit of calculated traveltimes to the observed was qualitatively assessed to produce a model that approximately satisfied the observed data. During this qualitative assessment, many different propagation scenarios were considered through all the layers of the model as part of the phase comparison process. Where there was a significant misfit in either the intercept time or the slope of the calculated traveltime curve, adjustments were made to the layer thicknesses or velocity gradients, respectively. In cases where it was impossible to match the calculated traveltimes to the observed traveltime picks by reasonable modification of the model layers, groups of picks were reassessed, and where necessary assigned to a different phase.

Once the assigned phases were considered to be an accurate representation of the ray packets tracing through the model space, two-point ray-tracing was conducted whereby arrival times are calculated only for those ray paths that will match the shot-receiver offsets of the observed picks. This two-point ray-tracing provided an opportunity for quantitative (statistical) assessment of the fit of the calculated traveltimes to the observed picks. Joint analysis of the root-mean-square (rms) traveltime misfit and the χ^2 parameter (Zelt & Smith, 1992):

$$\chi^2 = \frac{1}{n}\left[\sum_{i=1}^{n}\left(\frac{T_c - T_o}{T_u}\right)^2\right] \qquad \textbf{(2.3)}$$

where T_c is the calculated traveltime, T_o is the observed traveltime and T_u is the total traveltime uncertainty for each pick from i=1 to i=n, acted as a statistical indicator when making minor adjustments to further refine the fit of the velocity-depth model.

An example of the fit of the calculated traveltimes to the observed picks is shown for a representative selection of record sections in Figures 2.14, 2.15 and 2.16. The ray coverage in the model space is also plotted in order to highlight those areas of the

model that are best constrained by the traveltime data. A summary of the assigned uncertainties, number of picks, rms misfit and χ^2 values for each of the identified phases for the resulting model can be found in Table 2.3. For reference, a χ^2 of 1 is considered a good fit, while a χ^2 of <1 is an over-fit to the observed traveltime picks. In this study, a χ^2 of <5 is considered an acceptable fit. A complete set of pick comparison and ray coverage diagrams can be found in Appendix A.

Table 2.3 Quantitative fit of the 2-D velocity-depth model discussed in Section 3.2, to the observed traveltime data. Pick uncertainties, number of traveltime picks, rms misfit between calculated and observed traveltimes, and the χ^2 value for each numbered phase identified in the WA data set are included.

Phase	Traveltime uncertainty (ms)	Number of picks	Rms misfit (s)	χ^2 value
P_w	20	4079	0.013	0.447
P_{wm}	20	3773	0.027	1.889
P_s	20-30	272	0.045	4.437
P_{g1}	20-30	1252	0.040	2.591
P_{g2}	30-40	8235	0.053	2.783
P_n	40-50	1938	0.084	3.591
P_mP	50	1442	0.079	3.306

2.8 Summary

A detailed description of the geophysical data and the approach to analysis and forward modelling has been outlined and justified. In the following chapter, the 2-D velocity-depth model resulting from forward modelling is presented and a preliminary interpretation is given. The shallow subseabed layering structure is compared to the initial structure observed with the MCS reflection data and the sensitivity of the traveltime fit is assessed in terms of model uncertainty. Modelling of the 2-D Free-air gravity anomaly (FAA) is also undertaken as an independent evaluation of the model and to provide an insight into the subcrustal density structure of the lithosphere.

3. Seismic model, sensitivity, resolution and uniqueness testing

3.1 Introduction

In this chapter the 2-D velocity-depth model resulting from forward modelling (henceforth referred to as the *rayinvr* model) is presented together with a preliminary interpretation, and various tests of the model structure are undertaken to ascertain the resolution and uniqueness of the model. Shallow layer boundary surfaces from the *rayinvr* model are converted from depth b.s.l. back to TWTT, and compared to the MCS reflection data and horizons used to construct the initial model (Section 3.3). Following this re-examination of the shallow subseabed, the resolution limits of the *rayinvr* model were investigated and sensitivity testing was conducted to determine uncertainties in the model boundary layer depths and velocity structure (Section 3.4). A comparison of the FAA calculated from the equivalent 2-D velocity-density-depth model, with the observed shipboard FAA is used to provide an independent assessment of the uniqueness of the modelled crustal and upper mantle structure (Section 3.5).

3.2 Forward modelling results

The *rayinvr* model (Figure 3.1) can be summarised as a succession of two discrete sedimentary packages overlying typical two-layered, mature Atlantic oceanic basement with the upper mantle beneath (Table 3.1).

Figure 3.1 Layer and 2-D velocity-depth structure of the *rayinvr* model. a) The boundary surfaces of the model are shown (black lines). Blue shading on the Moho indicates the regions constrained by P_mP arrivals. Key structures, described in Section 3.2, are annotated. b) The 2-D velocity-depth structure of the *rayinvr* model. The *P*-wave velocity coloured shading is masked to show the extent of ray coverage. Iso-velocity contours (black lines) are plotted with a 1 km s^{-1} contour interval. The 7.25, 7.7 and 7.75 km s^{-1} contours (black dashed lines) highlight the velocity structure of the lower oceanic basement and uppermost mantle. c) Plot of ray density indicating areas of the model with a higher level of constraint. Key features, as discussed in the text, are annotated. The profile offset locations of the 1-D velocity-depth profiles plotted in Figure 3.2 are indicated with red arrowheads in b).

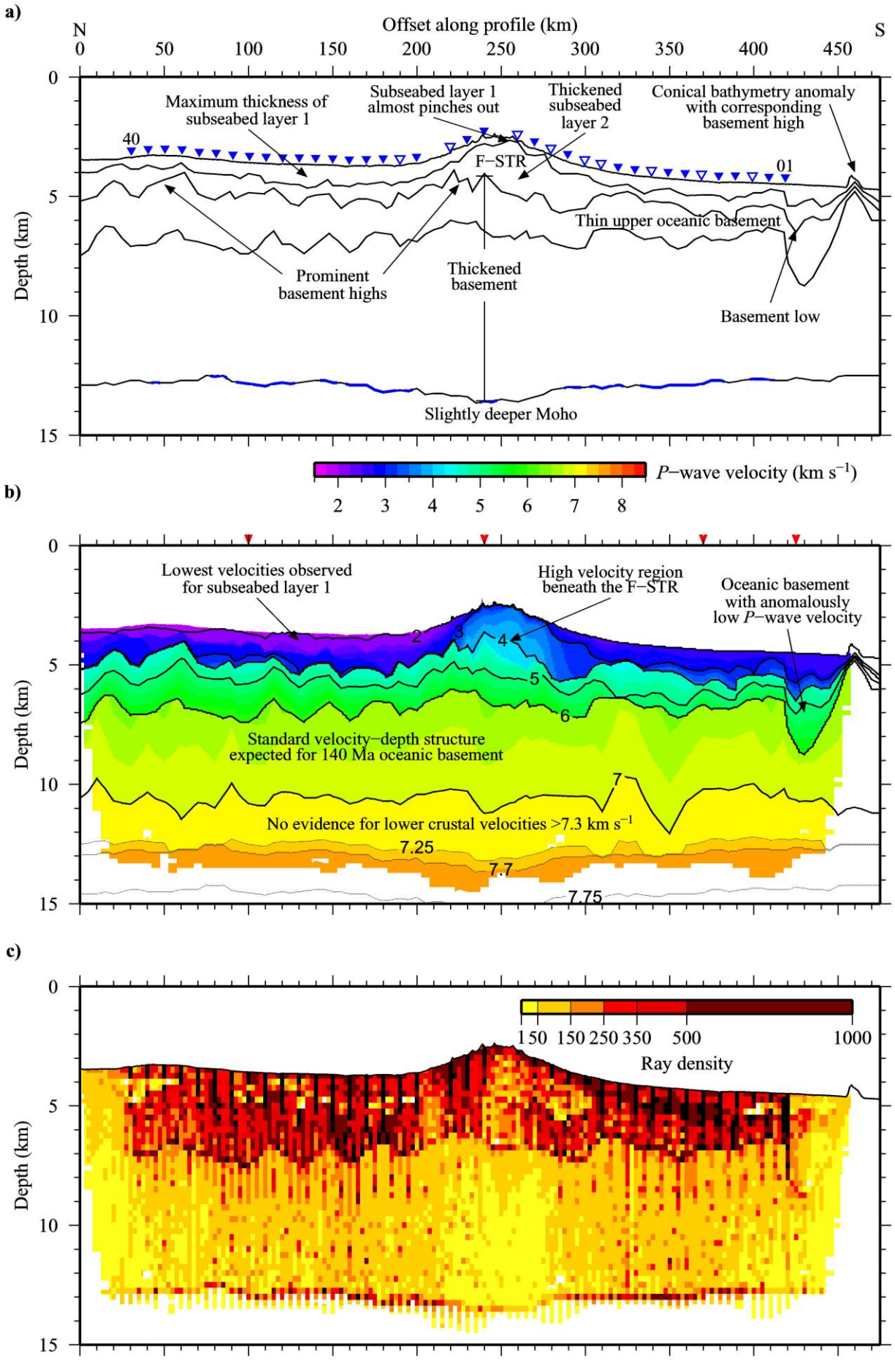
a)
N
Offset along profile (km)
S
0
50
100
150
200
250
300
350
400
450
Depth (km)
Maximum thickness of subseabed layer 1
Subseabed layer 1 almost pinches out
Thickened subseabed layer 2
Conical bathymetry anomaly with corresponding basement high
40
F–STR
01
Thin upper oceanic basement
Prominent basement highs
Thickened basement
Basement low
Slightly deeper Moho
P–wave velocity (km s−1)
2
3
4
5
6
7
8
b)
Lowest velocities observed for subseabed layer 1
High velocity region beneath the F–STR
Oceanic basement with anomalously low P–wave velocity
Standard velocity–depth structure expected for 140 Ma oceanic basement
No evidence for lower crustal velocities >7.3 km s−1
7.25
7.7
7.75
c)
150
150
250
350
500
1000
Ray density

Table 3.1 Layering structure of the *rayinvr* model. † The lower velocity of the water column quoted here has been calculated using the velocity gradient and the average seabed depth of 4 km b.s.l.. Values in brackets for shallow subseabed layer 2 are taken from 250 km profile offset, and are representative of the high-velocity region beneath F-STR.

Model layer	Thickness (km)	Upper velocity (km s^{-1})	Lower velocity (km s^{-1})	Velocity gradient (s^{-1})
Water column	~4.0	1.49	1.51†	0.005
Shallow subseabed 1	0.3-1.0	1.90-3.00	2.20-3.40	~0.50
Shallow subseabed 2	0.5-1.0 (2.0)	2.50-3.60	2.70-4.30	~0.75 (0.50)
Upper oceanic basement	1.0-2.0	4.30-4.80	4.90-6.10	~0.63
Lower oceanic basement	4.0-7.0	6.40-6.70	7.10-7.30	~0.11
Upper mantle	-	7.70	-	~0.03

The structure of the shallow subseabed and underlying oceanic basement is generally similar to that incorporated into the initial model. The most anomalous feature of the velocity-depth model is observed at the point where the F-STR intersects profile P01. In this region, high *P*-wave velocities are required in shallow subseabed layer 2, suggesting a structure that formed independently from standard oceanic basement accretion and subsequent sediment deposition. Several 1-D velocity-depth profiles through the *rayinvr* model are presented in Figure 3.2 and a detailed description of each model layer (except the water column) is given in the following subsections.

3.2.1 Shallow subseabed

The first, shallowest layer, subseabed layer 1, is present along the entire profile although it has slightly different characteristics either side of the F-STR. To the north, this layer has an average thickness of 0.7 km, reaching a maximum thickness of 1 km at ~150 km profile offset (Figure 3.1a), and exhibits *P*-wave velocities ranging from 2.0 to 2.5 km s^{-1} (Figure 3.1b). This range of velocities matches those recorded by Lancelot *et al.* (1978b) for the marls and claystone turbidites observed up to 1 km below the seabed at DSDP site 368. The layer appears to almost pinch out over the F-STR before returning to an average thickness of 0.6 km at profile offsets >320 km, where slightly higher velocities of 2.5 to 2.9 km s^{-1} are observed. The higher velocities observed to the south of the F-STR could be indicative of a greater

concentration of chert and porcellanite or even diabase sills (Lancelot *et al.*, 1978b). Based on the *P*-wave velocities required to satisfy the WA traveltime data, and the observation of a prominent angular unconformity in the MCS reflection data, this layer of the model is interpreted to represent a sequence of moat infill sediments that was deposited in the accommodation space resulting from the flexure of the lithospheric plate following the emplacement of the Cape Verde archipelago.

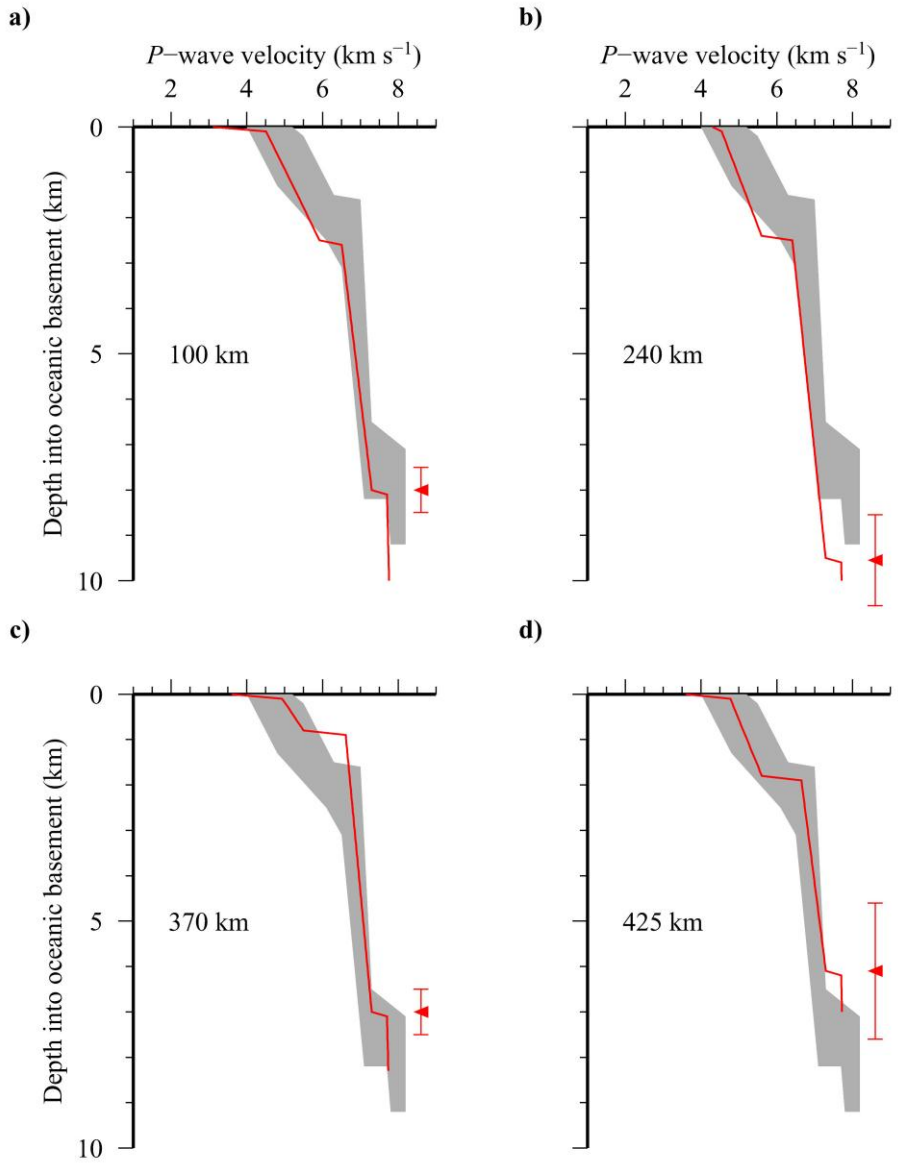

Figure 3.2 1-D velocity-depth profiles (red lines) from the *rayinvr* model, see Figure 3.1 for locations. The expected range in velocity-depth structure for mature Atlantic oceanic basement is also included (grey shaded region; after White *et al.*, 1992). The depth of the Moho in the *rayinvr* model is also indicated (red arrowheads with uncertainty bars). a) 100 km profile offset. b) 240 km profile offset. c) 370 km profile offset. d) 425 km profile offset.

The second layer, subseabed layer 2, generally exhibits a thickness of ~1 km and *P*-wave velocities ranging from 2.5 to 3.5 km s^{-1} (Figure 3.1b), which is more laterally consistent than the shallowest layer. This velocity range is similar to that used for this layer in the initial model and fits within the range expected for terrigenous sediments (Hamilton, 1978), matching Ali *et al.*'s (2003) interpretation. However, between 210 and 310 km profile offset, this layer thickens to a maximum of 2.2 km and exhibits velocities ranging from 3.5 to 4.3 km s^{-1}, which are constrained by the P_s phase observed on the mid-profile OBSs. This higher velocity region, coincident with the bathymetric high of the F-STR, suggests that either the emplacement of volcanic material at the Cape Verde mid-plate swell may not be localised entirely to the islands or that the F-STR is comprised of volcaniclastic material derived from flank collapse of the neighbouring islands (Section 2.3).

3.2.2 Oceanic basement

The oceanic basement was modelled as two layers to produce groups of arrivals to match the two distinct crustal phases, P_{g1} and P_{g2}, observed in the data. The intra-basement model boundary was required to accommodate a decrease in vertical velocity gradient, interpreted to represent the transition from the pillow basalt and dykes of layer 2 to the gabbros of layer 3 in the standard model of oceanic crust (White *et al.*, 1992).

The top-basement surface lies an average depth of 5.25 km b.s.l. and is coarsely uneven, with irregular undulations of amplitude 0.5 km and wavelength >15 km (Figure 3.1a). There are three prominent basement highs >1 km shallower than the average depth of the top-basement surface: the first is located between 10 and 60 km profile offset, where a peninsula of shallower bathymetry extends west from Sal (Figure 2.1a); the second is located beneath the northern edge of the F-STR, at 225 km profile offset; and the third basement high, at 460 km profile offset, is directly below a localised bathymetry anomaly (Figure 3.1a) that corresponds to the location of a volcanic cone of height ~1.5 km and diameter ~10 km that can be seen in the shipboard swath bathymetry data at 13° 16.00' N 24° 23.00' W (Figure 2.4a). Although the velocity-depth model is not directly constrained at this profile offset (Figure 3.1c), this cone is, most likely, an intermediate-sized seamount. A basement low, 1 km below the average depth of the top-basement surface, is located at 425 km profile offset.

There is little lateral variation in the velocity structure of the oceanic basement along the profile, with average values for the upper and lower layers of 5.1 and 6.9 km s^{-1} respectively (Figure 3.2). The interval velocities for the oceanic basement layers in the *rayinvr* model are similar to those input into the initial model, although the velocity of the lower layer ranges from ~6.60 to 7.25 km s^{-1} in the *rayinvr* model.

The total thickness of the oceanic basement increases from the north towards the F-STR as a consequence of the basement high and the slightly increased depth of the Moho (Section 3.2.3), reaching a maximum thickness of 9.5 km at 240 km profile offset (Figure 3.1a). The observed thickening of the oceanic basement is largely accommodated within the upper layer (interpreted as oceanic layer 2) and there is no evidence of high *P*-wave velocities (>7.3 km s^{-1}) at the base of the lower layer (interpreted as oceanic layer 3), which are associated with undercrustal material (e.g. Charvis *et al.*, 1999).

To the south of the F-STR, between 320 and 420 km profile offset, the oceanic basement thins to 7 km thickness, with most of the thinning accommodated in the upper basement layer, affecting the vertical velocity gradient (Figure 3.2c). At 425 km profile offset, the upper basement layer velocity structure reverts to the average structure of the model. As this transition coincides with the basement low and the depth to the Moho remains constant, the total thickness of the oceanic basement reduces to 6.0 km.

The maximum depth of penetration of rays traced through the lower crust (corresponding to arrivals from phase P_{g2}) is ~11 km b.s.l. which is, on average, 2 km shallower than the modelled Moho (Section 3.2.3; Figure 3.1c). The velocity structure of the deepest parts of the crust is, therefore, constrained by modelling the P_n and P_mP phases, the result of which is described in the next section.

3.2.3 Moho and upper mantle

The topography of the Moho is very subdued, with an average Moho depth of 12.9 km b.s.l., which increases slightly to 13.6 km beneath the F-STR, at ~250 km profile offset. The primary constraint on the depth to the Moho comes from arrivals reflected at the crust-mantle interface, the P_mP phase. Unfortunately, this phase is not clearly identifiable on all record sections, and is particularly difficult to identify in the centre of the profile where these arrivals are of a lower SNR than elsewhere. Also, without further control on the velocity structure of the lower crust (>10 km

depth), the uncertainty in the position of the Moho is large (±1.0 km), due to the trade-off between the interval velocity and thickness of the lower crustal layer.

On records with clear arrivals at shot-receiver offsets >35 km, the P_n phase can be identified and this provides further control on lower crustal velocities, allowing Moho depth to be independently modelled. The upper mantle velocity directly below the Moho is 7.7 km s^{-1} and a small positive velocity gradient in the mantle (~0.03 s^{-1}) is required in order to turn the P_n rays, with 8.5 km s^{-1} nominally assigned to the base of the model at 40 km depth. The absence of arrivals at >70 km shot-receiver offset throughout the dataset means that only the velocity of the upper mantle directly beneath the Moho is determined directly by this study.

3.2.4 Summary of the *rayinvr* model

The *rayinvr* model shows an igneous basement section that is 8.25 km thick on average, well within the range expected for standard mature Atlantic oceanic basement (White *et al.*, 1992), and similar to that observed in the pilot study conducted by Pim *et al.* (2008), although the crust does appear to slightly thicken towards the centre of the profile beneath the F-STR, to a maximum of 9.5 km. High shallow-crustal velocities suggest, however, that the thickening is accommodated within the upper crust either by extrusion as part of island emplacement or as a high velocity volcaniclastic debris deposit on top of the basement, a consequence of adjacent island failure. Analysis of the detailed swath bathymetry data in the area better supports the latter possibility, with evidence of mass transport from the adjacent island of Fogo (Day *et al.*, 1999; Masson *et al.*, 2008).

Receiver function analysis (Lodge & Helffrich, 2006) suggests that crustal thickening, perhaps by undercrustal magmatic emplacement, may be present beneath the islands, where Moho depths up to 20 km are inferred. There is no evidence from this study to suggest that such an enhanced crustal thickness exists regionally beneath the swell. Additionally, there is no direct evidence from the seismic data for lower crustal velocities >7.3 km s^{-1}, a common feature observed at oceanic islands which show significant volumes of undercrustal material (e.g. Caress *et al.*, 1995). However, it is possible that a thin layer of magmatically emplaced material exists at or within the base of the oceanic crust that is below the resolution and constraint provided by the WA seismic data alone.

3.3 Depth-time conversion and comparison with MCS data

The shallow subseabed structure of the initial model was determined using interval velocities (estimated from a range of sources) to convert the TWTT horizons interpreted from the MCS reflection data along RRS *Charles Darwin* cruise CD8/85 Line 3 into layer surface boundaries at depths b.s.l. (Section 2.6.4). Throughout forward modelling (Section 2.7.1), the seismic velocities and boundary geometries of the shallow subseabed layers required modification from their initial structure in order to match the calculated traveltimes to those observed. As a means of checking the geometry and velocity of the sedimentary layers in the *rayinvr* model, the depth of the unconformity and top-basement horizons have been converted back into TWTT using the model-derived layer velocities (Figure 3.3c) and compared with the MCS reflection data for consistency with the initial interpretation (Figure 3.3). The lateral spacing of depth nodes in the model, 1 km for the seabed and 5 km for all subseabed layers, limits the ability of the model-calculated horizons to exactly match observed features that have a wavelength >10 km so only the fit to the general trend at the appropriate TWTT is investigated.

Figure 3.3 Comparison of the key shallow subseabed horizons picked from the MCS reflection data Line 3, collected during RRS *Charles Darwin* cruise CD8/85 (Ali *et al.*, 2003), with the time-converted boundaries from the *rayinvr* model. a) Line 3 with the seabed, angular unconformity and top-basement horizons following the sediment stratigraphy defined by Ali *et al.* (2003). See Figure 2.5 and Section 2.4 for details. b) Time-converted boundaries from the *rayinvr* model. The model boundaries, although more coarsely sampled, correspond with the originally interpreted positions of the angular unconformity and the top-basement reflector and agree well with distinct changes in reflector characteristics, giving confidence in the shallow model structure. The locations of the 1-D velocity-depth profiles taken from the *rayinvr* model and plotted in part c) are indicated with red arrowheads. c) A comparison of 1-D velocity-depth profiles from the *rayinvr* model (red lines) with those used initially to convert the picked time horizons to depth: black line – stacking velocity from MCS Line 5, black dashed line – stacking velocity at DSDP site 368, blue line – 1-D seismic refraction model of Dash *et al.* (1976) (after Ali *et al.*, 2003).

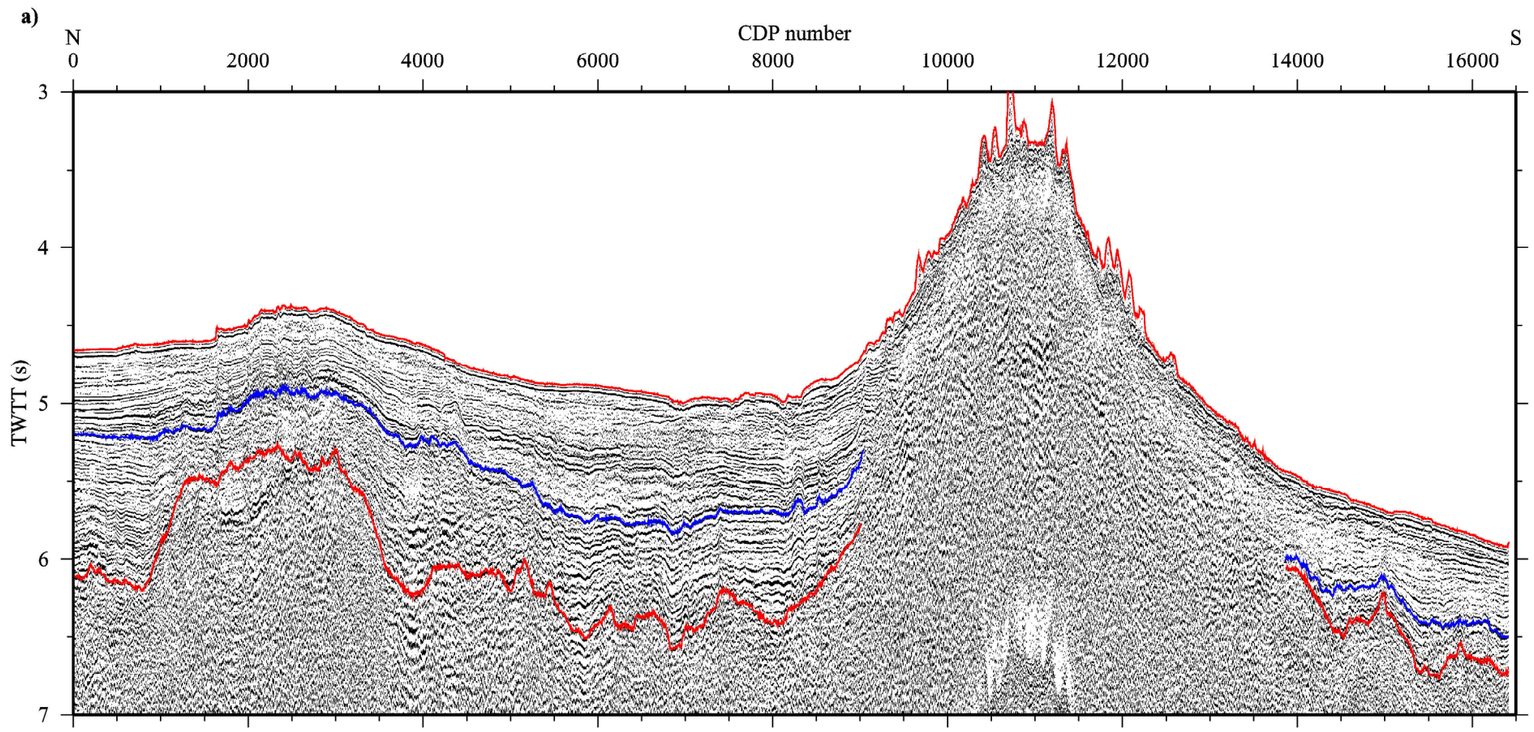
a)
N
CDP number
S
0
2000
4000
6000
8000
10000
12000
14000
16000
3
4
5
6
7
TWTT (s)

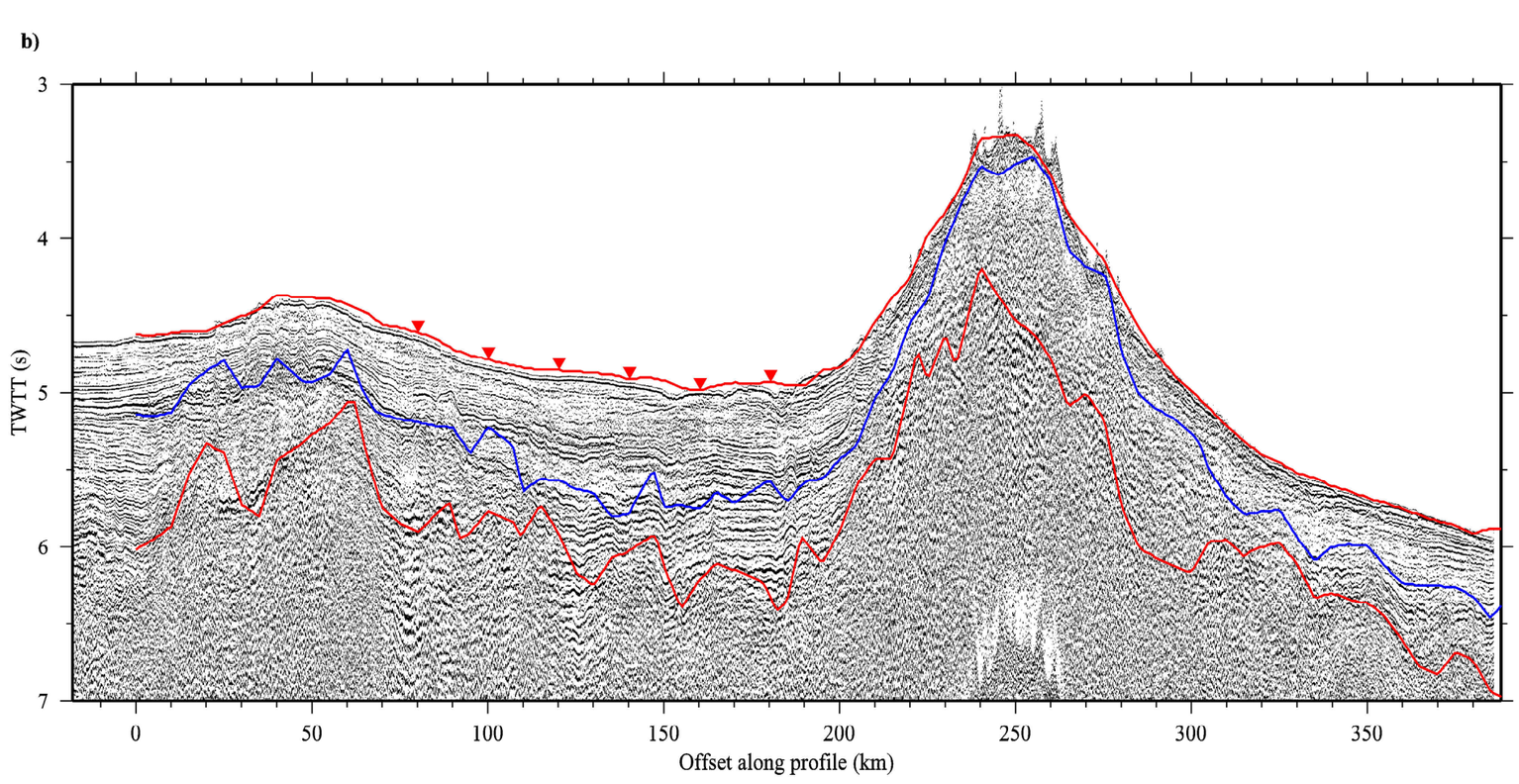
b)
3
4
5
6
7
TWTT (s)
0
50
100
150
200
250
300
350
Offset along profile (km)

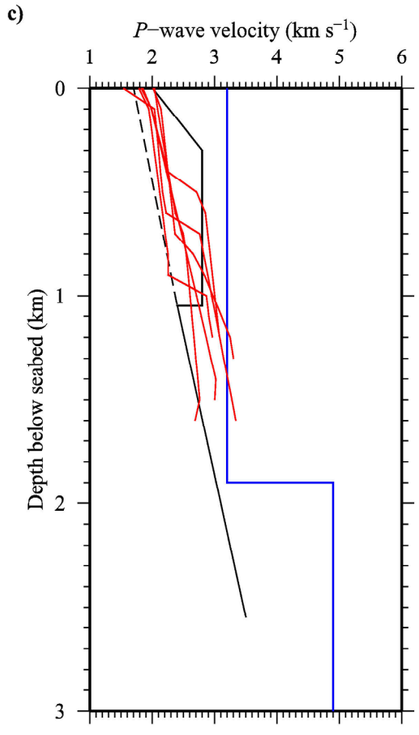
c)
P–wave velocity (km s−1)
1
2
3
4
5
6
0
1
2
3
Depth below seabed (km)

It is immediately apparent that the TWTT horizons calculated from the *rayinvr* model (Figure 3.3b) are not in perfect spatial agreement with those initially observed from the MCS data (Figure 3.3a). To the north of the F-STR, there appears to be a slight southward shift in the modelled seabed compared to the MCS reflection data. WA profile P01 and MCS Line 3 are close to one another but are not in identical positions and minor mismatches such as this may have arisen due to the slight differences in the location of data acquisition during the two separate geophysical cruises (MCS data - Line 3, RRS *Charles Darwin* 1985; WA data - profile P01, R/V *Meteor* 2004), as well as the adjustments that were made to the modelled seabed to account for offline OBS positions (Section 2.6.3).

The horizon calculated from the model boundary layer within the shallow subseabed correlates well with the angular unconformity observed in the MCS reflection data. Either side of the F-STR, this layer separates an upper, acoustically transparent layer containing occasional chaotic reflectors, from a lower, highly stratified package of moderate amplitude reflectors. It is not possible to appraise the intra-subseabed boundary layer between 200 and 300 km profile offset as there is a reduction in the SNR of the MCS reflection data due to the combined scattering effect of the steep slopes and rough bathymetry over the F-STR (e.g. Figure 2.4c).

The top-basement horizon calculated from the *rayinvr* model generally follows the lowest coherent, high-amplitude reflector and matches the location of the corresponding horizon in the initial interpretation. Beneath this surface, the characteristically uneven reflector pattern of the upper surface of the oceanic basement is evident. The model-calculated top-basement horizon is deeper than the initial interpretation between 25 and 40 km profile offset and, instead, correlates with a strong reflector that was not picked during the original analysis. Beneath the F-STR, where no initial picks were initially made from the MCS reflection data, the model-calculated top-basement horizon closely follows a discontinuous high amplitude reflector with similar characteristics to the one observed beneath the basement high at ~30 km profile offset.

Given the constraints imposed by data acquisition and modelling, and the error bounds on the interface depths of the *rayinvr* model, the shallow subseabed structure of the *rayinvr* model fits the horizons identified in the MCS reflection data.

3.4 Model limitations and sensitivity testing

The limitations of the model in terms of representing the true subseabed structure, is broadly constrained by the node spacing limitations of the *rayivnr* forward modelling technique, the shot point interval and the distance between OBSs. As outlined in Section 2.6.1, the subseabed model layers are only defined at 5 km intervals, thus providing limits on minimum size of anomalous structures that may be resolved.

The structure in areas of the model with a high ray density will be better constrained than areas where the ray density is lower. Figure 3.1c indicates the density of rays that have been traced through the *rayinvr* model, to shot-receiver offsets where there are traveltime picks for all OBSs. Each calculated traveltime datum is produced by summing the product of the velocity along each ray segment with the segment length. Approaching the maximum depth of ray penetration (>11 km b.s.l.), there is a low ray density coupled with longer total ray path length, meaning that the velocity-depth model is less well constrained and the solution is, therefore, non-unique.

To assess the resolution of the model, in terms of the *P*-wave velocity and boundary layer depth, a sensitivity testing approach was adopted whereby seismic velocities and boundary depths were systematically varied and the statistical and qualitatively observed fit reassessed. Firstly, layer velocities were tested by increasing or decreasing both the upper and lower velocities of all the nodes in each layer in turn (except the water column), keeping all other velocity nodes constant and all boundary positions fixed. Secondly, each layer boundary, with the exception of the seabed, was shifted shallower or deeper, keeping the rest of the model fixed.

During the forward modelling, the goodness of fit of the velocity-depth model was assessed using the rms traveltime misfit and χ^2 parameter (Section 2.7). For the sensitivity testing, a model was considered an acceptable fit as long as the difference in calculated and observed traveltimes did not exceed twice the standard error assigned to the picks. Table 3.2 displays the method of testing and the point at which the maximum allowable departure in layer boundary depth is reached for the Moho. The full results of this analysis show that *P*-wave velocities may differ by ± 0.1 km s^{-1} in the shallow subseabed layers, and by up to ± 0.2 km s^{-1} in lower basement layer and an acceptable fit is still achieved. On the same basis, the depth to

the top of the oceanic basement is estimated to lie within ±0.1 km of the *rayinvr* model interface at worst, and the depth to the Moho is estimated to lie within ±0.5 km. The ability of the traveltime data to resolve velocity perturbations is quantitatively assessed in Chapter 4 using the *FAST* inversion program.

Table 3.2 Summary of rms traveltime misfit values from sensitivity testing of the depth of the Moho model boundary. The assigned uncertainty and rms misfit of the *rayinvr* model are included for comparison. The maximum uncertainty (twice the assigned uncertainty) is the benchmark against which the models were tested. When the position of the Moho is adjusted by ±0.5 km, the maximum uncertainty is exceeded for the P_n and P_mP phases.

	Phase				
	P_s	P_{g1}	P_{g2}	P_n	P_mP
Assigned uncertainty (s)	0.030	0.030	0.040	0.050	0.050
Final model rms misfit (s)	0.045	0.040	0.053	0.084	0.079
Maximum uncertainty (s)	0.060	0.060	0.080	0.100	0.100
Moho - 0.25 km, rms misfit (s)	0.045	0.040	0.052	0.079	0.087
Moho + 0.25 km, rms misfit (s)	0.045	0.040	0.054	0.097	0.082
Moho - 0.50 km, rms misfit (s)	0.045	0.040	0.052	0.085	0.103
Moho + 0.50 km, rms misfit (s)	0.045	0.040	0.054	0.126	0.090

3.5 Gravity data

The uniqueness of the *rayinvr* model was also tested by calculating the gravity anomaly for a corresponding density-depth model and comparing this to both the Sandwell & Smith (1997) 1' global free-air gravity dataset and the higher-resolution shipboard data (Figure 3.4) acquired during seismic acquisition. In addition, gravity modelling also offers the potential of additional constraint on the deeper parts of the model not otherwise well constrained by seismic arrivals.

3.5.1 Data acquisition and processing

During the R/V *Meteor* cruise in 2004 (M62/3 – Grevemeyer *et al.*, 2004), a LaCoste & Romberg model "S" air-sea dynamic gravimeter (model number S84) recorded continuously along profile P01 at a sampling rate of 1 Hz, providing high spatial resolution gravity data with a precision of ±0.1 mGal (LaCoste & Romberg LLC, 1998). The raw data were tied to base station readings and corrected for drift (~0.038 mGal day^{-1}).

Figure 3.4 Free-air gravity anomalies calculated from the thin layer and block density models. a) Free-air gravity anomaly observed along profile P01 from the Sandwell & Smith (1997) 1' global satellite derived dataset (grey band including error) and the higher resolution shipboard data (blue line) compared to the calculated anomalies from b) the thin layer density model and c) the block density model, red and green lines respectively. Densities are annotated in kg m^{-3}.

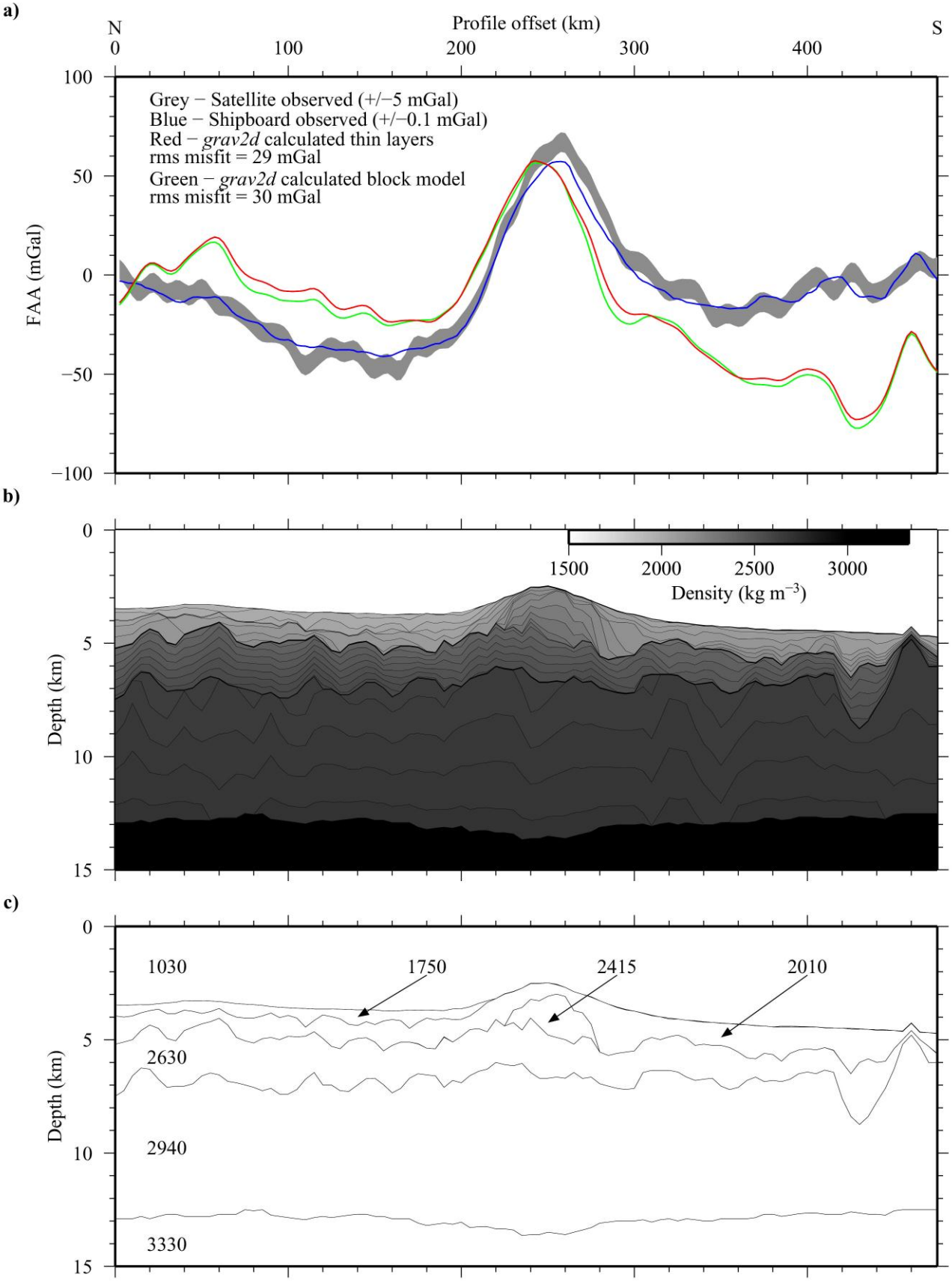
a)
N
Profile offset (km)
S
0
100
200
300
400
100
50
0
−50
−100
FAA (mGal)
Grey − Satellite observed (+/−5 mGal)
Blue − Shipboard observed (+/−0.1 mGal)
Red − grav2d calculated thin layers
rms misfit = 29 mGal
Green − grav2d calculated block model
rms misfit = 30 mGal
b)
0
5
10
15
Depth (km)
1500
2000
2500
3000
Density (kg m−3)
c)
0
5
10
15
Depth (km)
1030
1750
2415
2010
2630
2940
3330

The observed gravity data, g_{obs}, need to be corrected to account for the change in the Earth's radius, which varies with latitude, ϕ (Moritz, 1980):

$$g_{\phi} = 978032.68 \times \left(\frac{1 + 0.0019319 \sin^2 \phi}{\sqrt{\left(1 - 0.0066944 \sin^2 \phi\right)}} \right) \quad \textbf{(3.1)}$$

Additionally, in order to negate the effect of the motion of the research vessel, the Eötvös correction (EC) is calculated using the ship's heading, α, speed in knots, v, and current latitude, ϕ:

$$EC = 7.503v \sin\alpha \cos\phi + 0.004154v^2 \quad \textbf{(3.2)}$$

The application of these corrections to the observed gravity data enables the FAA to be calculated using the following equation:

$$FAA = g_{obs} - g_{\phi} + EC \quad \textbf{(3.3)}$$

A Gaussian filter of width 10 km was applied to the data in the space domain to remove high frequency variations in the gravity anomaly caused by short-wavelength (<10 km) structures that cannot be resolved given the limitations of the velocity-depth model (Section 3.4). A comparison of the shipboard FAA to the Sandwell & Smith (1997) 1' global FAA demonstrates that they are in good agreement (Figure 3.4a), although the shipboard data has a higher resolution. The most prominent feature in the FAA is the large amplitude (~60 mGal) peak centred at 250 km profile offset, coinciding with the location of the F-STR. There is also a long-wavelength gravity low of amplitude -35 mGal, centred at 150 km profile offset.

3.5.2 Two-dimensional modelling

A 2-D approach was adopted for gravity modelling which assumes that there is no change to the density-depth structure into and out of the plane of the profile. Figure 2.1 clearly shows this not to be the case, as the Cape Verde Islands lie to either side of profile P01. In Chapter 5, the initial 2-D interpretation will be compared to the results of 3-D modelling of the FAA, and out of plane effects will be reviewed and discussed.

3.5.2.1 *grav2d*

The 2-D gravity program, *grav2d*, written by J.H. Luetgert and based on the algorithm of Talwani *et al.* (1959), calculates gravity anomalies from a sequence of

layered blocks that are populated with interval densities. All of the models have been extended by 1000 km in the profile offset direction (to both the north and south) to minimise edge effects in the region where the model structure is to be tested. The 1-D vertical density-depth structure of the extended regions is replicated from the nearest end of the model.

3.5.2.2 Velocity-density conversions

In order to calculate the FAA along profile P01, a 2-D density-depth model was constructed from the *rayinvr* model (Figure 3.1). Experimental analysis of crustal rocks and sediments reveals a strong correlation between *P*-wave velocity and density (e.g. Christensen & Mooney, 1995). From similar experimental data, several standard velocity-density relationships have been derived for a range of sediments (Hamilton, 1978) and oceanic crustal rocks (Carlson & Raskin, 1984; Carlson & Herrick, 1990). Drilling log data from DSDP site 368 also indicate that the shallow subseabed in the region of the Cape Verde Islands is likely to be predominantly siliceous (Lancelot *et al.*, 1978b).

Layer interval velocities were converted into interval densities using the two-part velocity-density curve shown in Figure 3.5, which was used to provide a greater precision than the standard 'Nafe-Drake curve' (Nafe & Drake 1957; Ludwig *et al.*, 1970) which follows the average relationship for all lithologies. The first half of the curve, for *P*-wave velocities (v) $\leq$3.7 km s^{-1}, is described by Hamilton (1978)'s relationship for the density of siliceous rocks, ρ_s:

$$\rho_s = 1.124 + 0.347v - 0.0157v^2 \quad \textbf{(3.4)}$$

The second half of the curve, for *P*-wave velocities >3.7 km s^{-1}, is described by Carlson & Raskin (1984)'s relationship for the density of oceanic crustal rocks ρ_{oc}:

$$\rho_{oc} = 3.81 - \left(\frac{6.0}{v}\right) \quad \textbf{(3.5)}$$

Model layer boundaries and iso-velocity contours were used to divide the model into a succession of thin layers or blocks (Section 3.4.2.3). Each layer or block was assigned an interval velocity calculated from an average of the bounding velocity contours. An interval density was then attributed to each layer, ranging between 1750 and 3000 kg m^{-3}, according to the velocity-density relationships (Eq. 3.4 & Eq. 3.5). The densities of the water column and the upper mantle layers were held fixed to

values of 1030 and 3330 kg m^{-3}, respectively, which are widely adopted (e.g. Watts *et al.*, 2009).

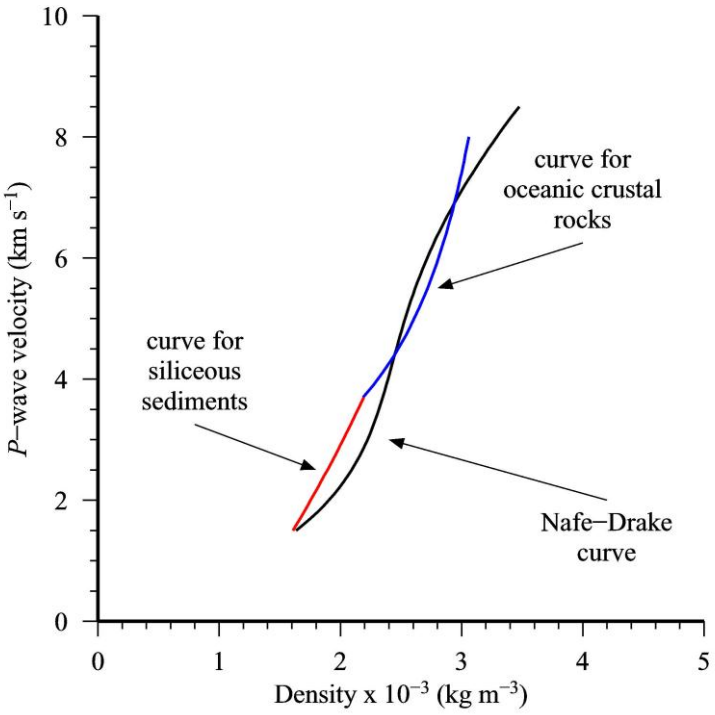

Figure 3.5 Two-part velocity-density curve used to convert the *rayinvr* model into a density model in preparation for 2-D gravity modelling. Curves showing the relationship between *P*-wave velocity and density for siliceous sediments (red line) of *P*-wave velocities ≤3.7 km s^{-1} (after Hamilton, 1978) and oceanic crustal rocks (blue line) for *P*-wave velocities >3.7 km s^{-1} (after Carlson & Raskin, 1984). Also shown for comparison is the 'Nafe-Drake curve' (black line; Nafe & Drake, 1957; Ludwig *et al.*, 1970).

3.5.2.3 Modelling

An initial density model was constructed using iso-velocity contours ranging between 1.6 and 7.4 km s^{-1}, with a contour interval of 0.2 km s^{-1}. This produced a 'thin layer' model, with an increase in density between adjacent layers of 30 to 80 kg m^{-3}. Density contrasts at the seabed and Moho were 590 and 330 kg m^{-3}, respectively (Figure 3.4b). A second, simplified density model was constructed using only the main iso-velocity contours in the shallow subseabed (2.2 and 3.7 km s^{-1}), and the top-basement and mid-basement surfaces from the *rayinvr* model. This 'block' approach reflects the main structure of the model using larger density contrasts of ~200 kg m^{-3} between adjacent layers (Figure 3.4c). The calculated FAAs from both the thin layer model and the block model are compared in Figure 3.4a. The rms misfit between the FAAs calculated using the thin layer model and block model

is only 3 mGal. It is apparent that the block model includes enough structure to produce a gravity anomaly that closely matches that calculated using the detailed thin layer model, and to simplify model construction during sensitivity testing (Section 3.5.4), the block model was, consequently, used as the basis of uniqueness testing.

3.5.2.4 Results

The FAA calculated using the block density model (red line, Figure 3.4a) shows a reasonable agreement with the short (<50 km) and medium wavelength (~100 km) features in the observed data (blue line and grey band including error). The small highs at 60 and 400 km profile offset and the low at 420 km match those observed, although the calculated anomalies have larger amplitudes. The main peak at 250 km profile offset is also matched by the calculated gravity anomaly. The calculated anomaly also contains an effectively linear trend of -0.1 mGal km^{-1} from north to south that results from the increase in water depth with increasing profile offset. Interestingly, the same trend is not present in the observed FAA. Instead, a long-wavelength (~300 km) negative anomaly is present with a peak of amplitude -35 mGal at ~150 km.

The long-wavelength anomaly may be a result of crustal thickness variations unconstrained by the seismic modelling. Assuming a density contrast between the lowermost oceanic basement and the mantle of 300 kg m^{-3}, this would require an increase in the depth of the Moho of 2.8 km between 80 and 220 km profile offset to produce an anomaly of amplitude -35 mGal. This is clearly larger than the seismic resolution at Moho depth (0.5 km; Section 3.4) and can be discounted. The long-wavelength anomaly must, therefore, be a result of deeper-seated density variation in the subcrustal, lithospheric mantle, a region which is largely unconstrained by the seismic data.

3.5.3 Long-wavelength misfit

In order to assess the likely origin of the long-wavelength mismatch, bathymetry and gravity data along a 2500 km extended profile centred on profile P01 were analysed (Figure 3.6; Figure 3.7a & b). Shipboard gravity data were not collected beyond the limits of profile P01, so for the purposes of analysing the long-wavelength mismatch, the Sandwell & Smith (1997) 1' global FAA was used (blue line, Figure 3.7b). The negative anomaly observed in the data, centred at 150 km profile offset, is still

prominent in the global FAA but there is also a positive anomaly of amplitude 20 mGal centred at -175 km. The largest density contrast is found at the seabed interface and, thus, long-wavelength trends in the FAA primarily reflect changes in water depth. Therefore, a simplified two-layer density model of the water column and the seabed was constructed (Figure 3.7a) to calculate the gravity anomaly due solely to changes in bathymetry (black line, Figure 3.7b).

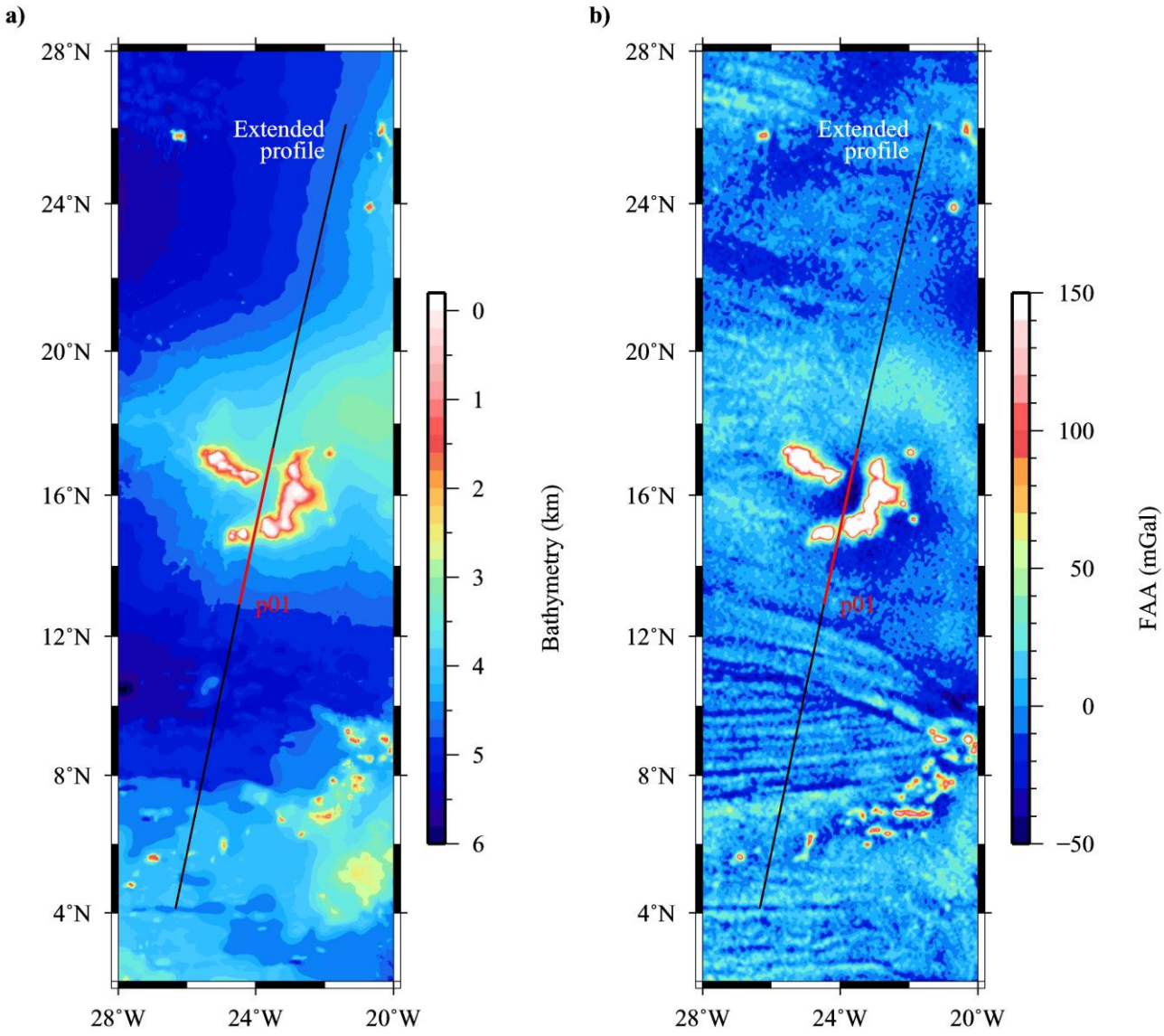

Figure 3.6 Bathymetry and gravity anomalies along a 2500 km extended profile (black line), centred on profile P01 (red portion). a) The GEBCO 1' (IOC, IHO & BODC, 2003) bathymetry clearly shows the extent of the Cape Verde Swell. b) The satellite-derived Free-air gravity anomaly (Sandwell & Smith, 1997) clearly shows the highs of the swell and the islands, as well as a large circular low anomaly concentrated at the southern edge of the swell, beneath the Cape Verde Islands.

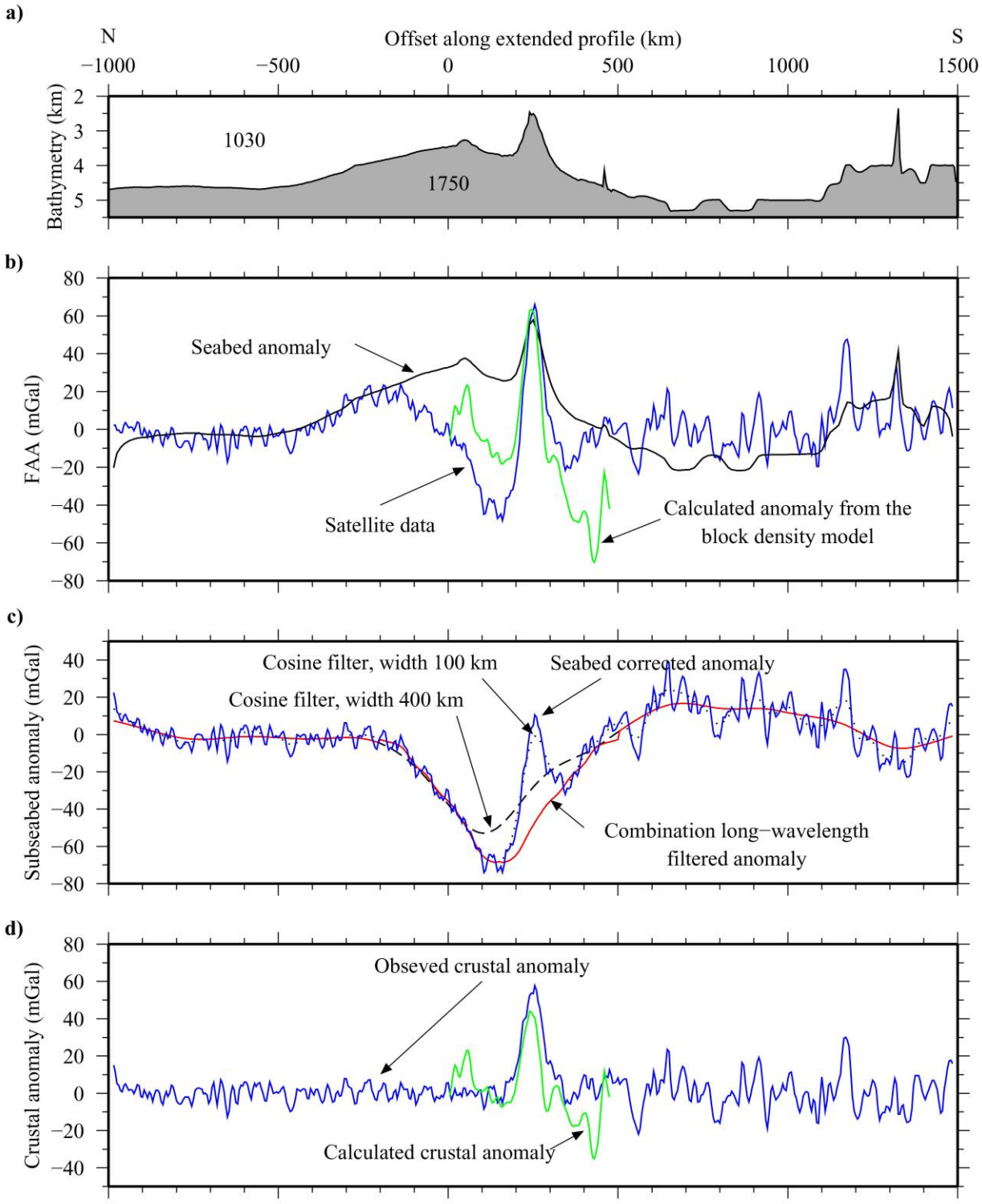

Figure 3.7 Isolating the long-wavelength component of the Free-air gravity anomaly. a) Bathymetry defined by the combination of GEBCO 1' (IOC, IHO & BODC, 2003) and shipboard swath bathymetry data with a simple two-layer density model (densities are annotated in kg m^{-3}) used to isolate the influence of the seabed topography on the Free-air gravity anomaly shown in part b). c) Deconstruction of the long-wavelength components in the subseabed gravity anomaly. A combination of filter widths was required to isolate the long-wavelength low at 150 km profile offset while retaining the medium-wavelength high at 250 km profile offset. d) Observed crustal gravity anomaly (blue line; Free-air gravity anomaly with the long-wavelength component removed), compared with the crustal gravity anomaly calculated from the block density model with the seabed anomaly removed (green line). Note that the calculated and observed anomalies are now in much closer agreement, except at the extremities of the model where the structure is less well constrained by the seismic data.

The density of the subseabed used in this model reflects the density of the shallowest layer in the block model (1750 kg m^{-3}). The calculated seabed anomaly (black line; Figure 3.7b) was then removed from the satellite-derived FAA to obtain the subseabed anomaly (blue line, Figure 3.7c), which is now dominated by a long-wavelength negative anomaly, the long-wavelength positive anomaly having been removed.

Various 2-D filters were applied, in the space domain, to the subseabed anomaly to match the long-wavelength low centred at 150 km profile offset (Wilson *et al.*, 2010; see Appendix B). It was not possible to isolate the long-wavelength signal south of 150 km due to the superposition of the medium-wavelength peak at 250 km profile offset. As a best approximation, a combination long-wavelength signal was created using a cosine filter of width 400 km (black dashed line, Figure 3.7c) at the flanks of the profile (<-200 km and >500 km) and a cosine filter of width 100 km (black dotted line, Figure 3.7c) between -200 and 150 km, with the filtered signal mirrored about 150 km to fit the long-wavelength trend between 150 km and 500 km, thus assuming it to be symmetrical (red line, Figure 3.7c). The long-wavelength signal was subsequently removed from the subseabed anomaly to reveal the 'crustal' anomaly, which has been compared to the anomaly calculated from the block model with the bathymetry anomaly removed (Figure 3.7d). The observed and calculated crustal anomalies show a reasonable agreement between 100 and 350 km profile offset but diverge at the extremities of the model.

Before testing the sensitivity of the crustal anomaly to subtle changes in the crustal density structure, the possible origin of the long-wavelength anomaly was investigated. Firstly, the block density model was modified to include lateral variations in the density of the lithospheric mantle by incorporating a region of low density (relative to 'normal' mantle) centred at 150 km profile offset. A range of density contrasts, compensation depths and low-density region widths were tested in an attempt to reproduce the amplitude of the long-wavelength anomaly. The subcrustal gravity anomaly calculated using a model with a region of low density (contrast -30 kg m^{-3}) 200 km wide, extending to a compensation depth 100 km (black lines, Figure 3.8b) matches the amplitude of the long-wavelength component (red line, Figure 3.8a). Its wavelength characteristics, however, are not well matched, suggesting that the low-density region may have a different shape or gradual lateral density transitions rather than the sharp boundaries modelled here. If the low-density

region extends laterally at shallow depths (<50 km), both the amplitude and the wavelength of the subcrustal gravity anomaly can be closely matched (blue dashed lines, Figure 3.8a & b). These example models are clearly non-unique but a compensation depth of >50 km b.s.l. matches estimates from other studies of the swell (e.g. McNutt, 1988) and the more regional-scale low density anomaly in the lithospheric mantle beneath the Cape Verde Islands which, in turn, better fits the passive seismological models of Lodge & Helffrich (2006).

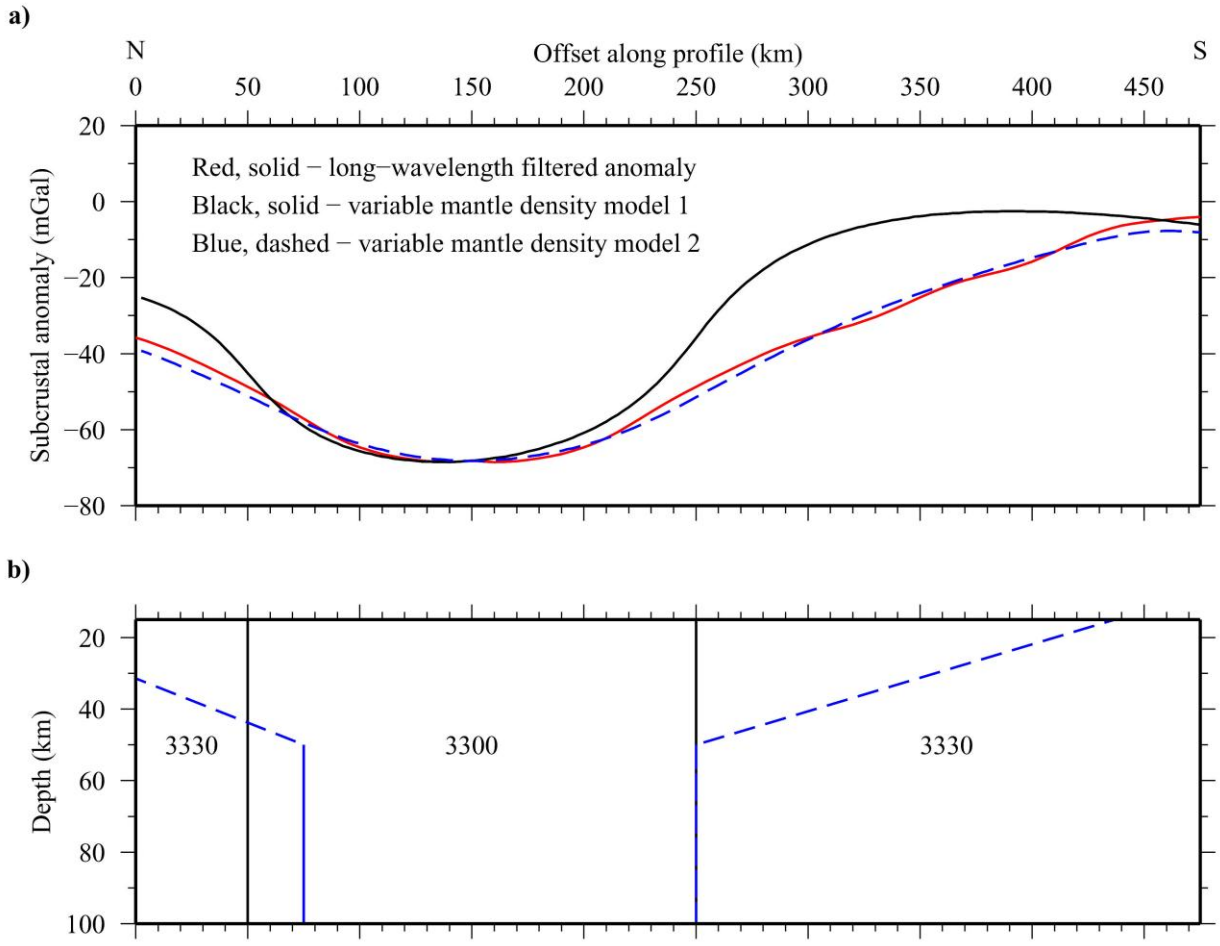

Figure 3.8 Modelling of the long-wavelength subcrustal gravity anomaly. b) Models incorporating lateral variation in mantle density with a compensation depth of 100 km (black and blue dashed lines) match the amplitude and wavelength characteristics of the observed long-wavelength anomaly (red line) in a). Densities are annotated in kg m^{-3}.

3.5.4 Crustal model sensitivity testing

The fit of the crustal gravity anomaly will now be considered. Modifications were made to the block density model within the constraints of the seismic modelling (Section 3.4) in an attempt to reduce the mismatch between the calculated and observed crustal gravity anomalies, assessed statistically using the rms gravity misfit.

3.5.4.1 Crustal thickness

Variations in the total crustal thickness were modelled in an attempt to account for the misfit at the extremities of the model (<50 and >350 km profile offset). A 1 km increase in the depth of the Moho between 0 and 60 km profile offset, and a gradual decrease of up to 2 km from 330 to 475 km profile offset, improved the fit of the flanking regions of the anomaly to the observed data (Figure 3.9a-c). The rms misfit of the calculated crustal anomaly to the observed is reduced from 13 mGal to 10 mGal. The adjustments made to the depth of the Moho exceed the uncertainties of the seismic modelling but this is concentrated mainly at the southern end of the profile, where the coverage of the WA data is much reduced. It is evident that changes in total crustal thickness could at least partly account for the regions of misfit at the ends of profile P01 where the velocity-density-depth model is under constrained.

3.5.4.2 Undercrustal material

As discussed in Section 3.4, the *rayinvr* model provides limited constraint on the lower crust, particularly in the central region of profile P01. A further series of tests was conducted to investigate whether the calculated gravity anomaly is sensitive to the presence of undercrustal magmatic material and, if so, to what extent. To undertake these tests, a series of modifications were made to the block density model to represent the presence of various thicknesses of undercrustal material beneath the crust and magmatic intrusion into the lower crust. These modifications were constrained to range from below to above the seismic resolution in velocity (hence density) and interface geometry at Moho depth.

Figure 3.9 Sensitivity testing of the crustal block density model. a) Comparison of the crustal gravity anomaly (grey band including error; see Figure 3.7) and shipboard data (blue line) with the gravity anomaly calculated from the block density models shown in b) to f). Note that the long-wavelength component of the Free-air anomaly (red line, Figure 3.7c) and the seabed anomaly (black line, Figure 3.7b) have been removed. The density constants used for the water column (1030 kg m^{-3}), shallow subseabed layer 2 (2010 kg m^{-3}), oceanic layer 2 (2630 kg m^{-3}) and layer 3 (2940 kg m^{-3}), and the mantle (3330 kg m^{-3}) are consistent for all models shown in b) to f). Other densities specific to isolated blocks are annotated in kg m^{-3}. For parts b) to f), the colour coding of the model corresponds to the colour coding of the associated calculated anomaly plotted in a). See text for discussion.

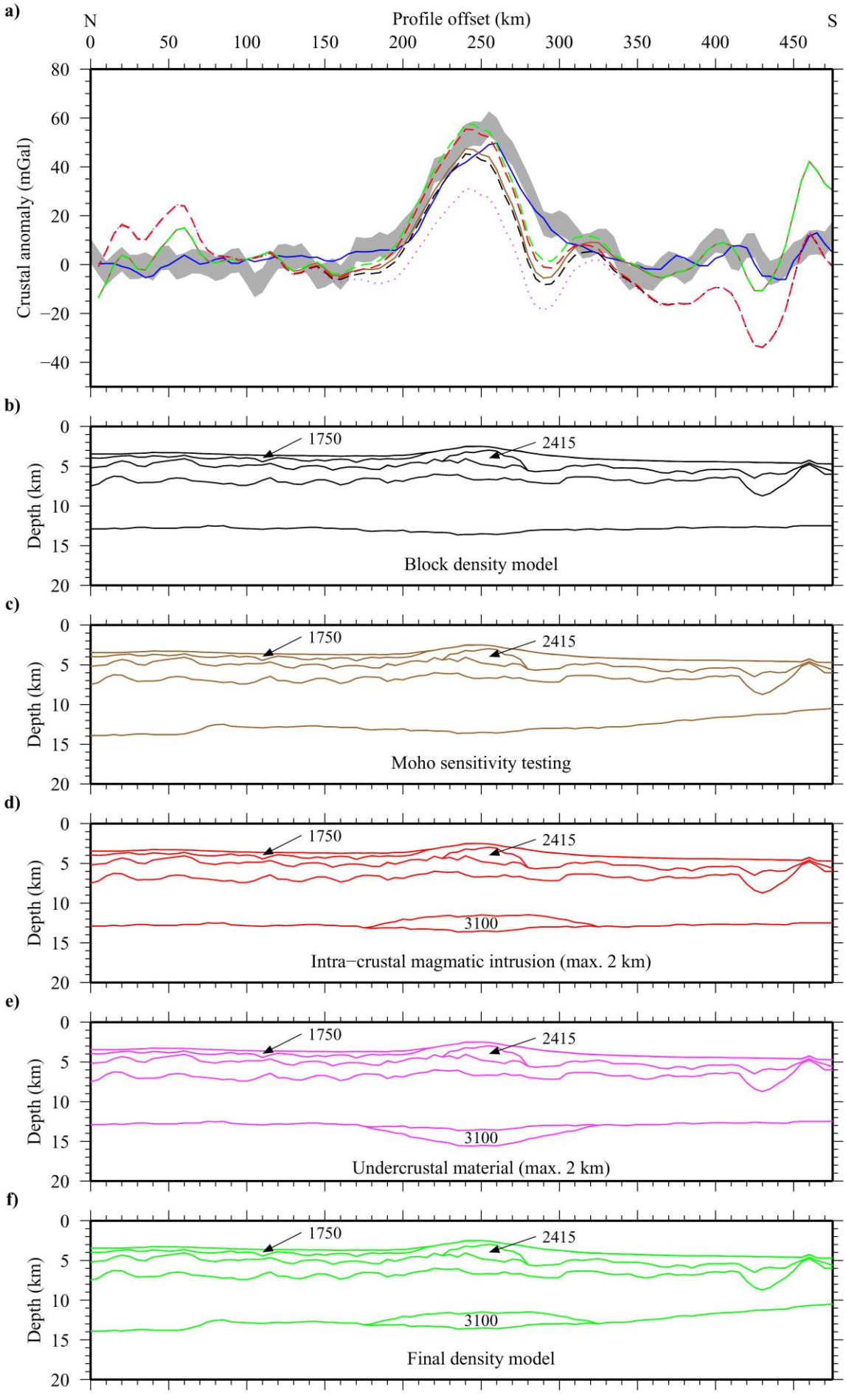
a)
N
Profile offset (km)
S
0
50
100
150
200
250
300
350
400
450
80
60
40
20
0
−20
−40
Crustal anomaly (mGal)
b)
1750
2415
Depth (km)
Block density model
c)
1750
2415
Depth (km)
Moho sensitivity testing
d)
1750
2415
3100
Depth (km)
Intra−crustal magmatic intrusion (max. 2 km)
e)
1750
2415
3100
Depth (km)
Undercrustal material (max. 2 km)
f)
1750
2415
3100
Depth (km)
Final density model
0
5
10
15
20

A range of velocity-depth models was created in which a layer of underplate or intra-crustal intrusion with *P*-wave velocities ranging from 7.3 to 7.5 km s^{-1} (e.g Morgan *et al.*, 1989) was incorporated below the Moho or within the lower crust, using a cosine function centred at 250 km profile offset with a width of 150 km, and with amplitudes ranging between ±3 km to control the additional model boundary surface. Following each modification, the fit to the seismic traveltime data was reassessed and the FAA recalculated to show the change in the crustal gravity anomaly, which is manifest mainly in the amplitude of the medium-wavelength peak at 250 km profile offset. Modelling shows that it is possible for a layer of intra-crustal intrusive material up to 2 km thick to be incorporated into the model to improve the fit to the peak FAA without significantly reducing the fit to the seismic data (Figure 3.9d). Conversely, the addition of a layer of undercrustal material below the Moho reduces the amplitude of the gravity anomaly peak, as the density contrast between the undercrustal material and the mantle that it effectively replaces is negative, and this increases the rms gravity misfit to the crustal anomaly (Figure 3.9e). A summary of the rms gravity anomaly misfit and the rms traveltime misfit of phases P_n and P_mP for each model used for sensitivity testing is given in Table 3.3.

Table 3.3 Quantitative fit of models used for sensitivity testing of the crustal block density model. The rms gravity misfit and the rms traveltime misfit of phases P_n and P_mP are provided for each model shown in Figure 3.9.

Model	Rms gravity misfit (mGal)	Rms traveltime misfit, P_n (s)	Rms traveltime misfit, P_mP (s)
Block density	13	0.084	0.079
Moho sensitivity	10	0.092	0.090
Intrusion (max. 2 km)	12	0.079	0.102
Underplate (max. 2 km)	16	0.087	0.157
Final density	10	0.088	0.102

Combining the changes in crustal thickness and the maximum extent of potential intra-crustal magmatic intrusion produces a final model (Figure 3.9f) that fits the main features of the observed crustal gravity anomaly, suggesting that a small amount (up to 2 km maximum thickness) of magmatic material may be present at the base of the oceanic crust, located beneath the F-STR. A similar feature is observed at the Louisville Guyot in the SW Pacific (Contreras-Reyes *et al.*, 2010). The likely

existence and extent of intra-crustal magmatic material will be discussed further in Chapter 5 in the context of 'whole plate' lithospheric flexure.

3.6 Summary

The shallow structure of the *rayinvr* model has been checked against the co-incident MCS data and sensitivity testing was undertaken to determine the full extent of the uncertainties on the interface depths and layer velocities. Independent 2-D gravity modelling was also used to investigate the uniqueness of the crustal model and to infer possible upper mantle density variations. It is also important to ensure that the structure of the *rayinvr* model is solely that required to fit the observed traveltime data and, hence, unaffected by any bias input by the modeller. To test the possibility of inherent modeller bias, in Chapter 4, two different inversion methods will be applied to simplified initial models, to produce velocity-depth models that fit the observed traveltime data. The models resulting from these inversions will be compared to the *rayinvr* model in order to assess whether the various structures identified and discussed in Section 3.2 are required by the data.

4. Inversion modelling and final seismic modelling results

4.1 Introduction

The main focus of this chapter is to ascertain the degree of uniqueness of the *rayinvr* model. A series of traveltime inversions, with largely unconstrained input models, was undertaken in order to model the observed traveltime data without the influence of any modeller bias (Section 4.2). The degree to which structures observed during the preliminary interpretation (Section 3.2) are reliably reproduced by the inversion methods will be used to define the uniqueness of the *rayinvr* model. The resolution limits of the models resulting from these inversions has also been tested, to allow direct comparisons to be made with the forward modelling method and to consider the implications for the FAA modelling presented in Section 3.4. The structure of the *final* 2-D velocity-depth model is described and interpreted in Section 4.3, including a comparison with the pilot study model of Pim *et al.* (2008) which was created using a subset of the traveltime data.

4.2 Inverse modelling of wide-angle data

The *rayinvr* model (Figure 3.1), fits all of the available WA seismic refraction and MCS reflection data within the assigned uncertainties. Calculation and modelling of the FAA provided an approach by which the model structure could be tested independently, and allowed estimation of the extent by which the depth and velocity nodes might be changed and still fit the observed data. Irrespective of the level of fit achieved, the *rayinvr* model is still inherently non-unique because of the trade-off between layer interval velocities and boundary depths. In order to gauge the impact of modeller bias on the outcome of the forward modelling, a series of modeller-independent inversions was completed using different starting models and smoothing parameters.

In this section, the *rayinvr* model is compared to a series of models produced by the modeller-independent inversion programs, *FAST* (Zelt, 1998) and *tomo2d* (Korenaga *et al.*, 2000), in order to assess the level of uniqueness of the forward modelling result. If the output model produced by an inversion is comparable to the forward modelling result then confidence can be placed in the uniqueness of its velocity-depth structure. The parameterisation and approach, synthetic testing, results and resolution testing of each method are discussed in the following two sub-sections. Finally, the conclusions drawn from the results of all of the inversions are summarised in Section 4.2.3.

4.2.1 First Arrival Seismic Tomography, *FAST*

The goal of the *FAST* inversion program is to reduce the misfit between calculated and observed traveltimes to a minimum, and the process is composed of two distinct stages. The forward modelling part of the method uses a finite-difference traveltime calculation (Vidale, 1988; 1990), modified to include head waves originating from large velocity contrasts (Hole & Zelt, 1995), to produce a grid of traveltimes to each model node from a given source location. Ray path geometries are recovered by following the steepest gradient in traveltime backwards from each receiver to the source. A regularised inversion then uses the ray path lengths to solve for slowness updates to the model based on the misfit between observed and calculated traveltimes, weighted according to the observed uncertainties. An objective function, which includes parameters outlining the desired model smoothness and the trade-off between minimising model updates and minimising traveltime misfit, prevents model updates above the resolution of the data that could prevent the inversion from reaching the true minimum in the traveltime misfit.

4.2.1.1 Parameterisation and approach

The finite-difference traveltime calculation works on a regular grid with the same grid node interval, h, in both the x and z dimensions. A forward grid node interval of 0.1 km in both the x and z dimension was chosen to allow accurate timing of ray propagation and to ensure that different rays were averaged to calculate each modelled traveltime, for comparison to observed traveltimes, at an average shot point spacing of 0.18 km.

Modifications to the velocity field during the inversion process were applied using a grid size that ensured the velocity updates were applied on a larger scale than the maximum vertical and horizontal resolution of the data, without spatially aliasing any detectable velocity anomalies. The inverse grid node interval was set to 2.0 km in the *x* dimension and 0.4 km in the *z* dimension. Smoothing and weighting parameter choices were based on the approach adopted by Zelt & Barton (1998) where *FAST* was applied to a 3-D dataset in an oceanic setting.

For each inversion, five non-linear iterations were completed whereby new ray paths and traveltime data were calculated through the current velocity-depth model. Following each non-linear iteration, a maximum of five potential model updates were tested, each with a decreased weighting applied for model smoothness and a corresponding increased weighting applied to reduce the data misfit. Searching for potential model updates ceased once a minimum in data fit was achieved, leading to the next non-linear iteration.

4.2.1.2 Synthetic inversion modelling

Prior to running an inversion to produce a model that fits the observed traveltime data, the subseabed imaging potential and the influence of the initial model must be tested by attempting to recover a known subseabed structure or 'target model' using synthetic traveltime data. Synthetic traveltime data, with the same spatial distribution as the observed data, were generated by forward ray-tracing the *rayinvr* model. A component of random noise was then added to the synthetic data, to reflect the variance of real data, with a standard deviation based on the uncertainties assigned to the observed traveltime data. Synthetic inversions, using different initial models, were then carried out against the synthetic traveltime data.

Preliminary trials incorporating synthetic first arrival traveltime data corresponding to all of the refraction phases (P_s, P_{g1}, P_{g2} and P_n) failed to produce a velocity-depth model that resembled the target model. With no ability with *FAST* to model traveltime data from the P_mP phase, there was also no direct constraint on the lower crustal velocity structure and, as a result, rays corresponding to the P_n phase were only traced to just below the maximum depth of P_{g2} coverage, leading to unusually large velocities (>7.1 km s^{-1}) at depths of ~10 km. All subsequent *FAST* inversions were, consequently, limited to incorporating first arrival traveltime data corresponding to the P_s, P_{g1} and P_{g2} phases and, therefore, this method is limited to

resolving the velocity-depth structure down to mid-crustal depths. Traveltime data from the P_n and P_mP phases were, thus, modelled using the inversion program *tomo2d* (Section 4.2.2) to provide an independent assessment of the uniqueness of the lower crustal and uppermost mantle velocity-depth structure.

The region of the target model that is sampled by forward ray-tracing during the generation of synthetic traveltime data (Figure 4.1a) demonstrates that the maximum imaging depth of the *FAST* inversion method is 10 km b.s.l.. A plot of the cell hit count (Figure 4.1b) illustrates that the target model is well sampled between 30 and 420 km profile offset. A lower than average count is evident beneath the F-STR, between 200 and 280 km, where there are fewer traveltime picks and it is expected that in this region, and at the edges of the model (<30 km and >420 km), the inversion program will have a lower resolving capability. It is also unlikely that the deepest velocity-depth structure will be recovered due to the reduced cell hit count at depths >8.5 km b.s.l. (Figure 4.1b).

In order to introduce as little bias as possible, a two-layer initial model, with a pseudo-1-D velocity-depth structure, was constructed (Figure 4.2a). The two layers represented the water column, with a velocity of 1.49 km s^{-1} at the sea surface increasing to 1.51 km s^{-1} at the seabed, and a subseabed layer with a velocity of 1.6 km s^{-1} just below the seabed increasing to 7.5 km s^{-1} at the base of the model, 20 km b.s.l.. The vertical velocity gradient (~0.35 s^{-1}) was chosen so that for any point in the subseabed, the velocity of the initial model is lower than the target model. Upper and lower velocity bounds (Table 4.1) were set in order to prevent unrealistically high or low velocities being introduced to the updated model throughout the inversion process, as occurred during preliminary trails when incorporating P_n phase traveltime data.

The results of the synthetic inversion of the pseudo-1-D initial model are summarised in Figure 4.2. The output model, masked to show only the areas of ray coverage (Figure 4.2b), reveals that the deepest turning rays reach a maximum depth of ~8.0 km b.s.l. between 30 and 420 km profile offset where there is good ray coverage. This depth of penetration is shallower than the maximum depth imaged during forward ray-tracing of the target model (Figure 4.1b) and it is possible that the very low shallow subseabed velocities in the initial model (Figure 4.2a) are causing the inversion to overcorrect, replacing them with high velocities (Figure 4.2d) that prevent rays from sampling to the expected depth. The main features in the target

model (Section 3.2) have been accurately reproduced by the inversion, including the high velocity region beneath the F-STR and the basement high at 50 km profile offset. Additionally, the 4 km s^{-1} and 6 km s^{-1} iso-velocity contours of the output model agree with the top-basement and mid-basement layer boundaries from the target model to within ±0.2 km, which is comparable to the uncertainties assigned during sensitivity testing (Section 3.4).

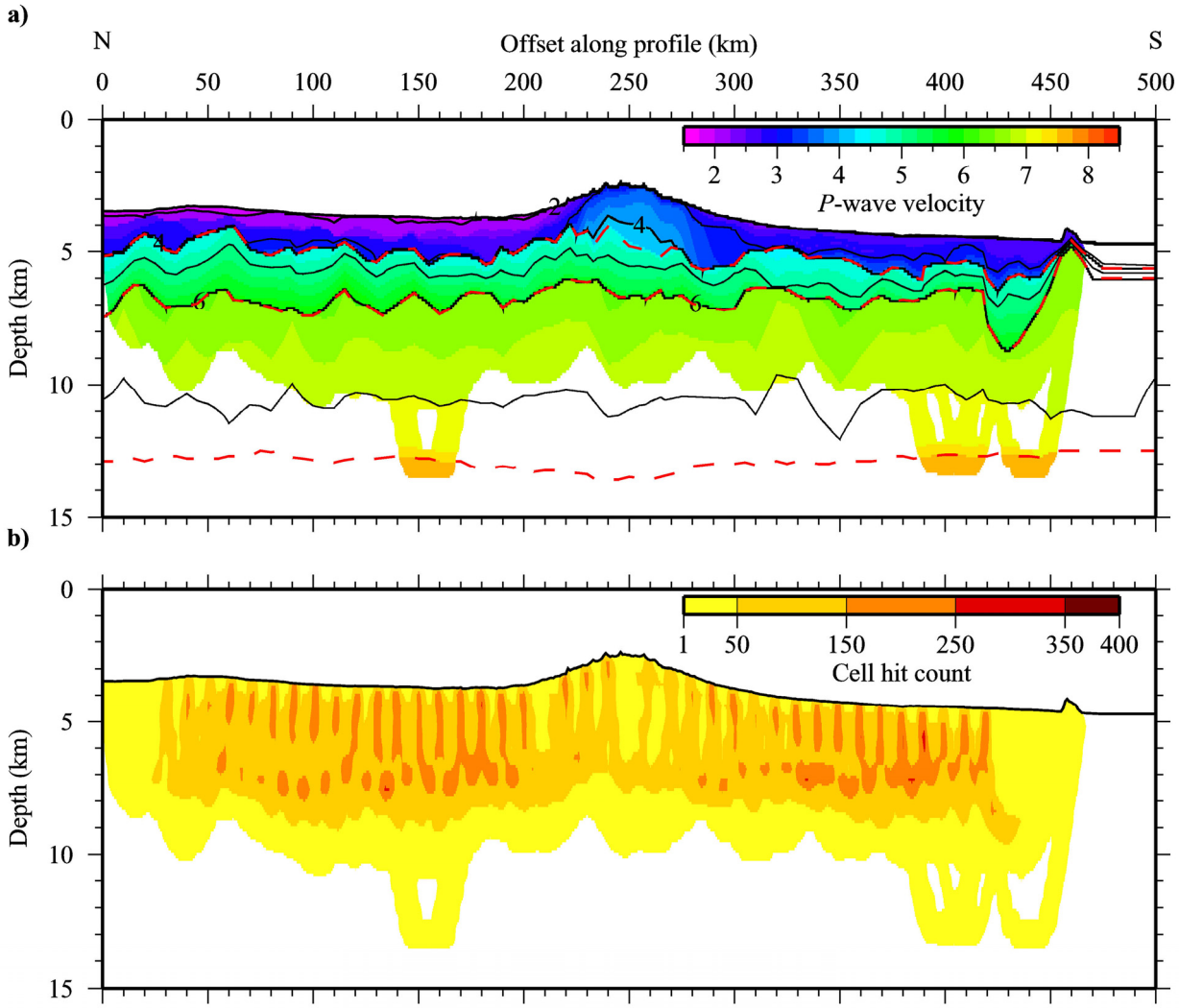

Figure 4.1 Region of the *rayinvr* model sampled by forward ray-tracing with the inversion program *FAST*. a) The velocity-depth structure masked to show cells that are sampled by traced rays. Iso-velocity contours (black lines) are annotated with a 1 km s^{-1} contour interval. The oceanic basement layer boundaries of the *rayinvr* model (red dashed lines) are also shown. b) A plot of cell hit count gives a representation of sampling density, revealing areas of the model that should be well and poorly resolved during inversion.

Table 4.1 Summary of upper and lower velocity bounds applied to all *FAST* inversions to prevent the introduction of unrealistically high or low *P*-wave velocities during model updates.

Current velocity (km s^{-1})	Lower update limit (km s^{-1})	Upper update limit (km s^{-1})
1.5	1.5	2.3
2.0	1.7	7.1
3.0	2.4	7.1
4.0	3.2	7.1
5.0	4.5	7.1
6.0	5.5	7.1
7.0	6.7	7.1
8.0	7.7	8.3
8.3	8.0	8.5

A plot of the cell hit count (Figure 4.2c) shows that there is a clear concentration of ray paths extending to depth beneath each OBS but this does not appear to have caused any significant vertical smearing of the velocity structure. At the maximum depth of ray coverage, 7.0 to 8.0 km b.s.l., the synthetic inversion recovers the large-scale velocity structure but a short-wavelength velocity undulation (~20 km, amplitude 0.3 km s^{-1}) is observed (Figure 4.2b) that results from the uneven ray sampling at depth (Figure 4.2c).

Analysis of the difference between the target model and the output model (Figure 4.2d) reveals that the velocity structure is generally recovered to within ±0.25 km s^{-1}, which is only marginally larger than the maximum variation found during sensitivity testing of the *rayinvr* model (Section 3.4), whilst still achieving an acceptable fit within error bounds.

Figure 4.2 *FAST* inversion of the two-layer, pseudo-1-D initial model using synthetic traveltime data. a) Velocity-depth structure of the initial model and b) the output model following the inversion, masked by ray coverage. Iso-velocity contours (black lines) are annotated with a 1 km s^{-1} contour interval. The boundary surfaces of the target (*rayivnr*) model (red lines) are shown for comparison. c) Cell hit count indicates the number of rays traced through each cell of the output model to provide the final solution. (d) Difference between the target (*rayinvr*) model and the output model. Velocity difference contours are included (black lines) at ±0.5 km s^{-1} intervals to highlight areas of significant mismatch. See text for discussion.

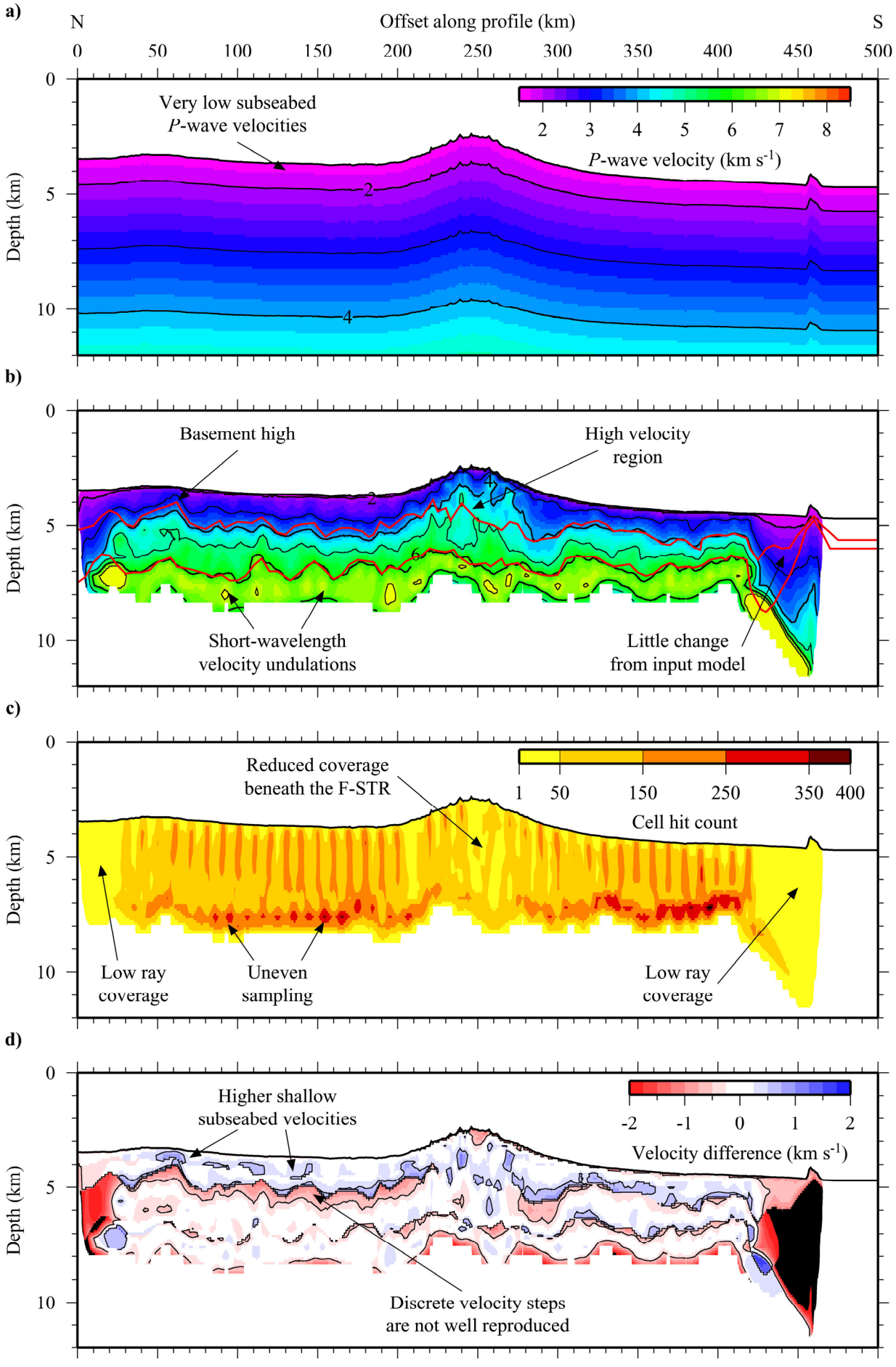
a)
N
Offset along profile (km)
S
0
50
100
150
200
250
300
350
400
450
500
Depth (km)
Very low subseabed
P-wave velocities
2
3
4
5
6
7
8
P-wave velocity (km s-1)
2
4
b)
Basement high
High velocity
region
Short-wavelength
velocity undulations
Little change
from input model
c)
Reduced coverage
beneath the F-STR
1
50
150
250
350
400
Cell hit count
Low ray
coverage
Uneven
sampling
Low ray
coverage
d)
Higher shallow
subseabed velocities
-2
-1
0
1
2
Velocity difference (km s-1)
Discrete velocity steps
are not well reproduced

Differences of up to ±1.00 km s^{-1} are observed in thin bands concentrated around the location of the target model layer boundaries. This feature is unsurprising given that the *FAST* inversion method is unable to incorporate discrete, incremental steps in the velocity-depth profile, such that only the best-fitting, smoothly varying velocity-depth model will be recovered. These thin bands can, thus, be regarded as reflecting discrete model layer boundaries. The inversion also incorporates higher velocities in the shallow subseabed, when compared to the target model (Figure 4.2d), causing the down-going rays to turn back towards the seabed more sharply, reducing the maximum depth of ray coverage (Figure 4.2c) and, therefore, the imaging potential.

At the edges of the ray coverage, the inversion fails to recover the velocity-depth structure of the target model due to too few rays sampling the model space (Figure 4.2c & d). Outside of the lateral limits of good cell hit count, <25 km and >425 km, velocity differences in excess of 1 km s^{-1} are observed and the velocity-depth structure of the synthetic inversion model is largely unchanged from the initial model. These lateral confidence boundaries are a direct limitation of the distribution of OBSs and are, therefore, independent of the initial model.

To increase the maximum depth of ray coverage, and thereby improve the model recovered by the inversion, further constraints need to be placed on the shallow subseabed of the initial model. The shallow subseabed structure of the *rayinvr* model has been corroborated by the depth-time conversion of the mid-sediment and top-basement layer boundaries and their comparison to the MCS reflection data (Section 3.3). A revised initial model was, therefore, constructed with a 2-D velocity-depth structure down to the top-basement surface, beneath which the velocities increase linearly to 7.5 km s^{-1} at the base of the model, 20 km b.s.l. (Figure 4.3a).

Figure 4.3 *FAST* inversion of the four-layer, 2-D initial model using synthetic traveltime data. a) Velocity-depth structure of the revised initial model and b) the output model following the inversion, masked by ray coverage. Iso-velocity contours (black lines) are annotated with a 1 km s^{-1} contour interval. The boundary surfaces of the target (*rayinvr*) model (red lines) are shown for comparison. c) Cell hit count indicates the number of rays traced through each cell of the output model to provide the final solution. d) Difference between the target (*rayinvr*) model and the output model. Velocity difference contours are included (black lines) at ±0.5 km s^{-1} intervals to highlight areas of significant mismatch. See text for discussion.

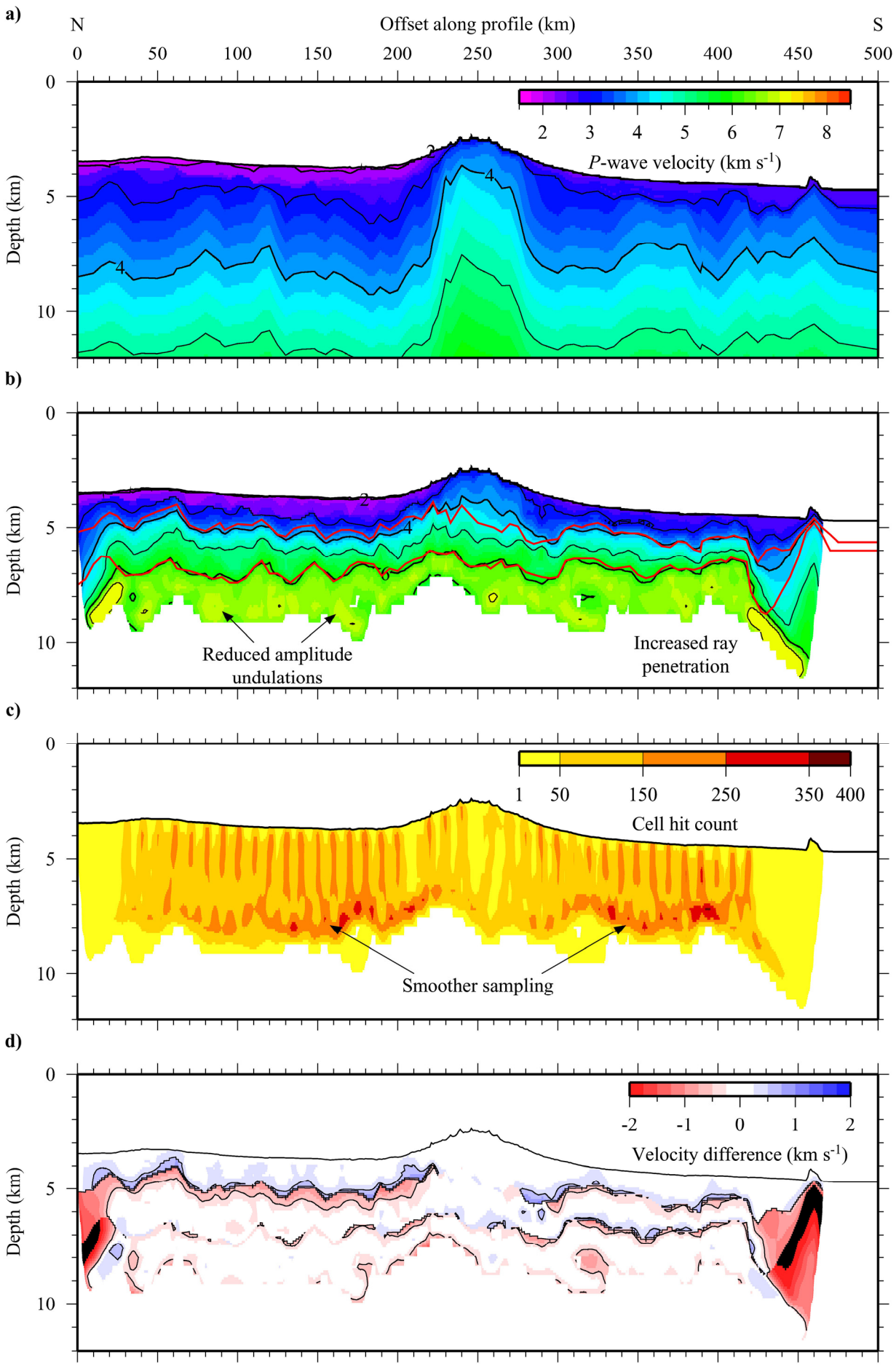
a)
N
Offset along profile (km)
S
0
50
100
150
200
250
300
350
400
450
500
Depth (km)
0
5
10
2
3
4
5
6
7
8
P-wave velocity (km s-1)
2
4
4
b)
Reduced amplitude undulations
Increased ray penetration
c)
1
50
150
250
350
400
Cell hit count
Smoother sampling
d)
-2
-1
0
1
2
Velocity difference (km s-1)

The results of the synthetic inversion of the 2-D initial model are summarised in Figure 4.3. The output model (Figure 4.3b) is notably smoother than the model obtained using the pseudo-1-D initial model (Figure 4.2b) and the main features of the target model are well defined. The deepest turning rays now reach a maximum depth of ~8.75 km b.s.l. between the lateral confidence boundaries. This improved depth of coverage corresponds to the lower limit of cells with a hit count >50 rays for the target model (Figure 4.1b). The increased ray penetration has, to some extent, resulted in a smoother sampling of the model space at depth (Figure 4.3c), thereby reducing the amplitude of the short-wavelength velocity undulations (Figure 4.3b).

Analysis of the difference between the target model and the output model (Figure 4.3d) reveals that the velocity structure is generally recovered to within ±0.25 km s^{-1}, and areas of mismatch are smaller and of reduced amplitude in comparison to those of the previous output model (Figure 4.2d). The misfit associated with the target model layer boundaries has been reduced to velocity differences of up to ±0.75 km s^{-1}. Despite the greater degree of initial constraint on the shallow subseabed structure, the output model still includes velocities higher than the target model and demonstrates that this modeller-introduced bias has little influence on the final result, other than improving the imaging potential of the inversion.

4.2.1.3 Real inversion modelling results

Following the results of the two synthetic inversions, the revised initial model, with 2-D structure down to the top-basement horizon, was chosen as the starting point for the real inversion using observed traveltime data, because it offers greater imaging potential and has a minimal biasing effect on the shallow subseabed structure. The observed first arrival traveltime data corresponding to the P_s, P_{g1} and P_{g2} phases were incorporated and it was expected that the maximum vertical imaging potential would closely resemble the extent of coverage reached during the synthetic inversion of the revised initial model (Figure 4.3c).

The results of the real inversion of the 2-D initial model are summarised in Figure 4.4. The output model (henceforth referred to as the *FAST* model), masked by areas of ray coverage (Figure 4.4b), resembles the *rayinvr* model (Figure 4.1a) within the lateral confidence boudaries, and the velocity-depth structure closely resembles that of mature Atlantic oceanic crust (White *et al.*, 1992).

As previously demonstrated for the output models from the synthetic inversions, the 4.0 and 6.0 km s^{-1} iso-velocity contours closely follow the top-basement and mid-basement layer boundaries from the *rayinvr* model (Figure 4.4b) and classification by velocity stratification divides the model into three layers:

1. A thin, shallow subseabed layer 1.0 to 1.5 km thick with velocities ranging from 1.9 to >3.0 km s^{-1}.
2. An intermediate layer that is 1.0 to 2.0 km thick with velocities ranging from 3.5 to 6.0 km s^{-1}.
3. A deep layer with an average *P*-wave velocity of 6.5 km s^{-1} that extends to the maximum depth imaged.

A significant departure from this standard classification is observed at the centre of the model, between 200 and 300 km profile offset, where the shallow subseabed layer has a higher average velocity and merges continuously with the intermediate layer.

Ray coverage through the *FAST* model (Figure 4.4c) shows that the deepest turning rays reach ~9.5 km, which is deeper than that reached during the synthetic inversions. The increase in the area of model space that is imaged results in a larger variation in the cell hit count at depth, causing short-wavelength velocity undulations (~20 km, amplitude 0.3 km s^{-1}) similar to those that were produced by the synthetic inversion of the pseudo-1-D initial model. There are also very short wavelength velocity undulations (~10 km, amplitude 0.2 km s^{-1}) concentrated between 5.0 and 8.0 km b.s.l., highlighted by the fluctuations of the 6 km s^{-1} iso-velocity contour in Figure 4.4b that are likely caused by vertical smearing due to ray path biasing beneath each of the OBSs (Figure 4.4c). There is no evidence of vertical smearing following the synthetic inversions as the increase in short-wavelength variations is due to a greater degree of variance in the observed traveltime picks. This variance may reflect small-scale structure that cannot be accurately modelled given the limitations of data coverage and model parameterisation.

Figure 4.4 *FAST* inversion of the four-layer, 2-D initial model using observed traveltime data. a) Velocity-depth structure of the revised initial model and b) the output (*FAST*) model following the inversion, masked by ray coverage. Iso-velocity contours (black lines) are annotated with a 1 km s^{-1} contour interval. The boundary surfaces of the *rayinvr* model (red lines) are shown for comparison. Vertical black lines in b) indicate the lateral confidence boundaries. c) Cell hit count indicates the number of rays traced through each cell of the output model to provide the final solution. d) Difference between the *rayinvr* model and the *FAST* model. Velocity difference contours are included (black lines) at ±0.5 km s^{-1} intervals to highlight areas of significant mismatch. See text for discussion.

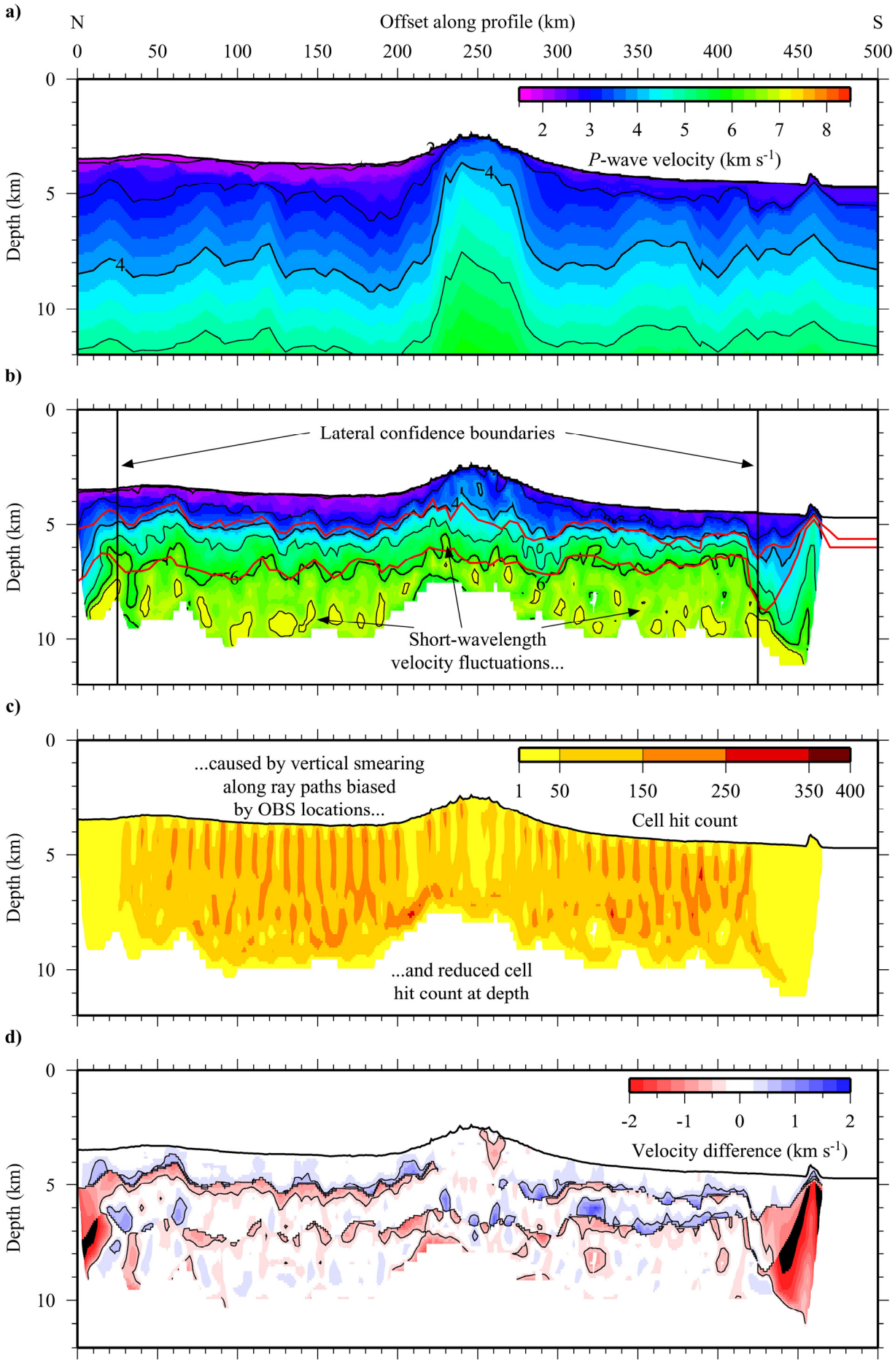
a)
N
Offset along profile (km)
S
0
50
100
150
200
250
300
350
400
450
500
Depth (km)
0
5
10
2
3
4
5
6
7
8
P-wave velocity (km s-1)
b)
Lateral confidence boundaries
Short-wavelength
velocity fluctuations...
c)
...caused by vertical smearing
along ray paths biased
by OBS locations...
1
50
150
250
350
400
Cell hit count
...and reduced cell
hit count at depth
d)
-2
-1
0
1
2
Velocity difference (km s-1)

Analysis of the difference between the *rayinvr* model and the *FAST* model (Figure 4.4d) confirms that the large-scale velocity structure of the two models is similar. Areas of misfit occur where there has been ray coverage biasing during the inversion or result from comparison of smooth vertical velocity gradients in the *FAST* model with discrete velocity steps in the *rayinvr* model, for example at the top-basement boundary.

4.2.1.4 Checkerboard resolution testing

The resolution limits of the *FAST* model were determined by testing the ability of the inversion program to recover velocity anomalies of various size and amplitude. The approach taken was similar to that used for the synthetic inversions. One of several checkerboard anomaly patterns (Table 4.2) was added to the *FAST* model, synthetic traveltime data were generated, a component of random noise was added and an inversion was completed using the revised initial model and the synthetic traveltime data. The output model can be directly compared to the 'anomaly-incorporated' *FAST* model, and the recovered anomaly pattern can be evaluated against both the input checkerboard pattern and the residual anomaly, to assess the recovery potential of the inversion.

Table 4.2 Summary of checkerboard anomaly patterns applied during resolution testing of the *FAST* model.

Test number	Checkerboard width, *x* (km)	Checkerboard height, *z* (km)	Maximum amplitude (± %)
1	50	4	5.0
2	100	2	5.0
3	25	2	5.0
4	75	1	5.0
5	50	4	2.5
6	100	2	2.5

A total of six checkerboard tests were conducted to define the limits of resolution. The first four tests comprise anomalies with maximum amplitudes of ±5 % of the *FAST* model. This amplitude corresponds to a velocity perturbation of ±0.10 km s^{-1} just below the seabed increasing to ±0.35 km s^{-1} at the base of the lower crust, and was chosen to match the resolution of the *rayinvr* model determined by model layer sensitivity testing (Section 3.3). The last two tests utilised the two large checkerboard patterns but with maximum amplitude of only ±2.5 % of the *FAST* model. These

final tests were designed to investigate the possibility that the *FAST* inversion method could accurately recover smaller velocity perturbations than the forward *rayinvr* modelling. The results of each checkerboard test are presented in Figures 4.5-4.10.

The first two checkerboard tests (Table 4.2) were intended to identify any regions where there is potential for particularly poor recovery. For both patterns the input anomalies are well recovered throughout the model space (Figures 4.5 & 4.6), except at the edges of lateral confidence, as discussed in the previous section.

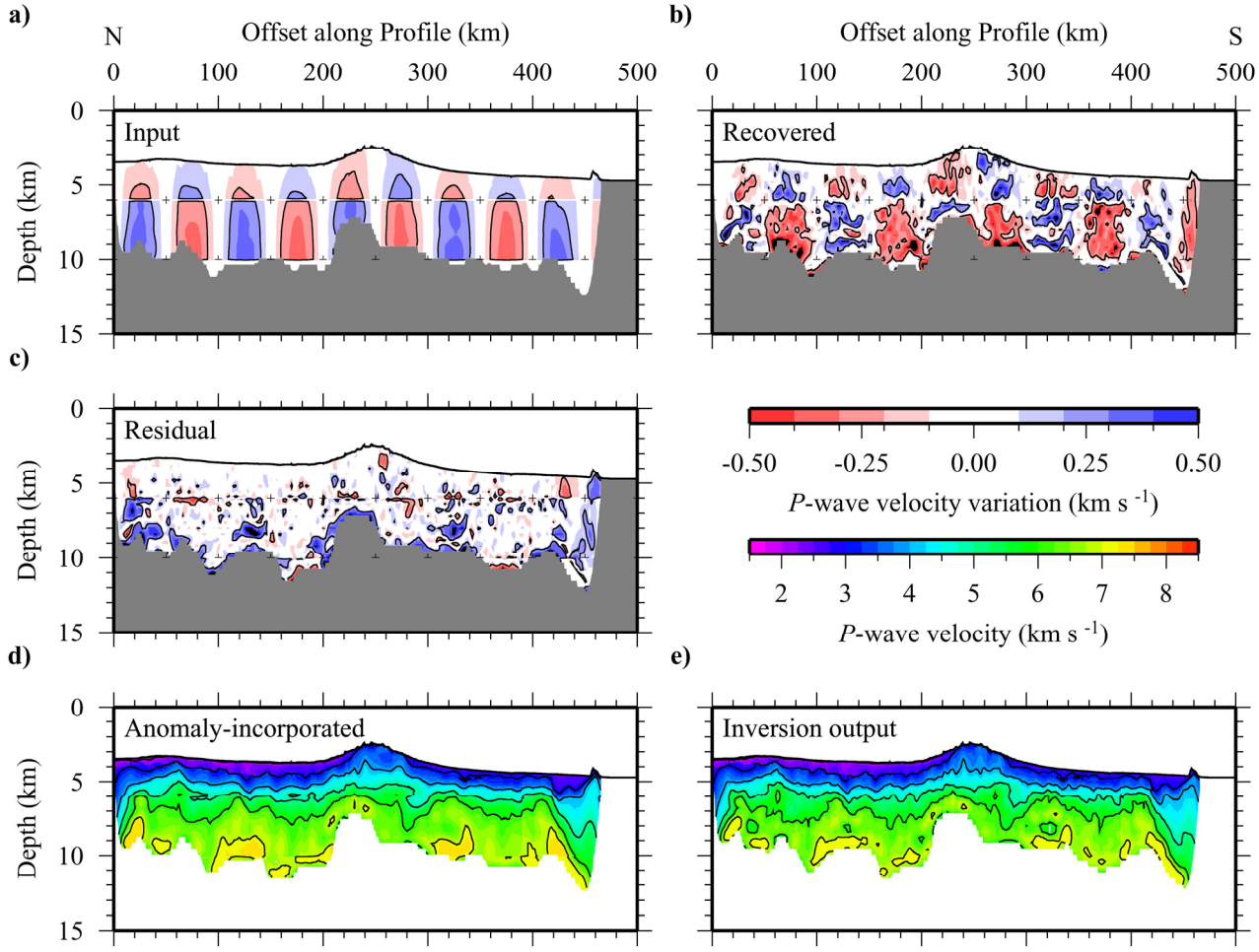

Figure 4.5 Resolution testing of the *FAST* model using a checkerboard size of 50 by 4 km with maximum anomaly amplitudes of ±5%. a) Input checkerboard anomaly pattern. b) Anomaly recovered by the inversion. c) Residual anomaly. d) Anomaly-incorporated *FAST* model used to generate synthetic traveltime data. e) Output model following an inversion of the revised initial model using the checkerboard synthetic traveltime data. Black crosses in parts a) to c) highlight the corners of the checkerboard regions and the anomalies are contoured at ±0.2 km s^{-1}. Iso-velocity contours are plotted in d) and e) with a 1 km s^{-1} contour interval. All plots are masked according to ray coverage.

There is some evidence of ray path biasing which leads to a distortion of the original checkerboard shapes and, in some cases, the amplitude of the recovered

anomaly exceeds that of the input anomaly pattern, but overall the input pattern has been well recovered and the residual anomalies are negligible (Figures 4.5c & 4.6c). These results demonstrate that the *FAST* inversion method is capable of resolving large-scale anomalies at a resolution that is comparable to the forward modelling technique.

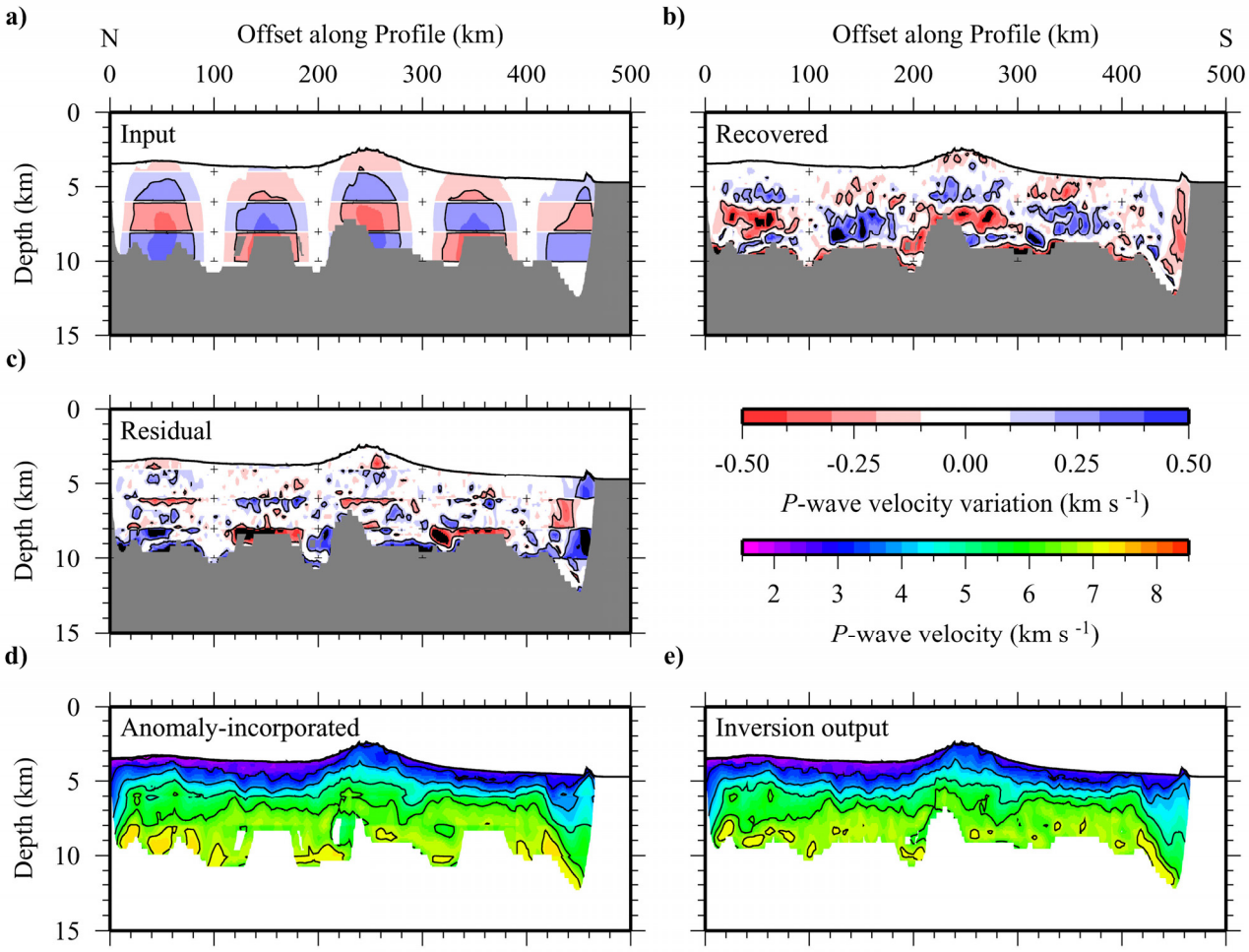

Figure 4.6 Resolution testing of the *FAST* model using a checkerboard size of 100 by 2 km with maximum anomaly amplitudes of ±5%. a) Input checkerboard anomaly pattern. b) Anomaly recovered by the inversion. c) Residual anomaly. d) Anomaly-incorporated *FAST* model used to generate synthetic traveltime data. e) Output model following an inversion of the revised initial model using the checkerboard synthetic traveltime data. Black crosses in parts a) to c) highlight the corners of the checkerboard regions and the anomalies are contoured at ±0.2 km s^{-1}. Iso-velocity contours are plotted in d) and e) with a 1 km s^{-1} contour interval. All plots are masked according to ray coverage.

The next objective was to determine the limits of spatial resolution using two smaller checkerboard anomaly patterns (Table 4.2). The results of the 25 by 2 km checkerboard test are summarised in Figure 4.7. The amplitudes are reasonably well recovered to depths of 8 km b.s.l. (Figure 4.7b), but below this depth the checkerboard shapes are too small to be resolved due to the limited ray coverage.

Ray path biasing has caused more distortion to the spatial distribution of the anomalies compared to the checkerboard test with a longer horizontal wavelength (Figure 4.5b).

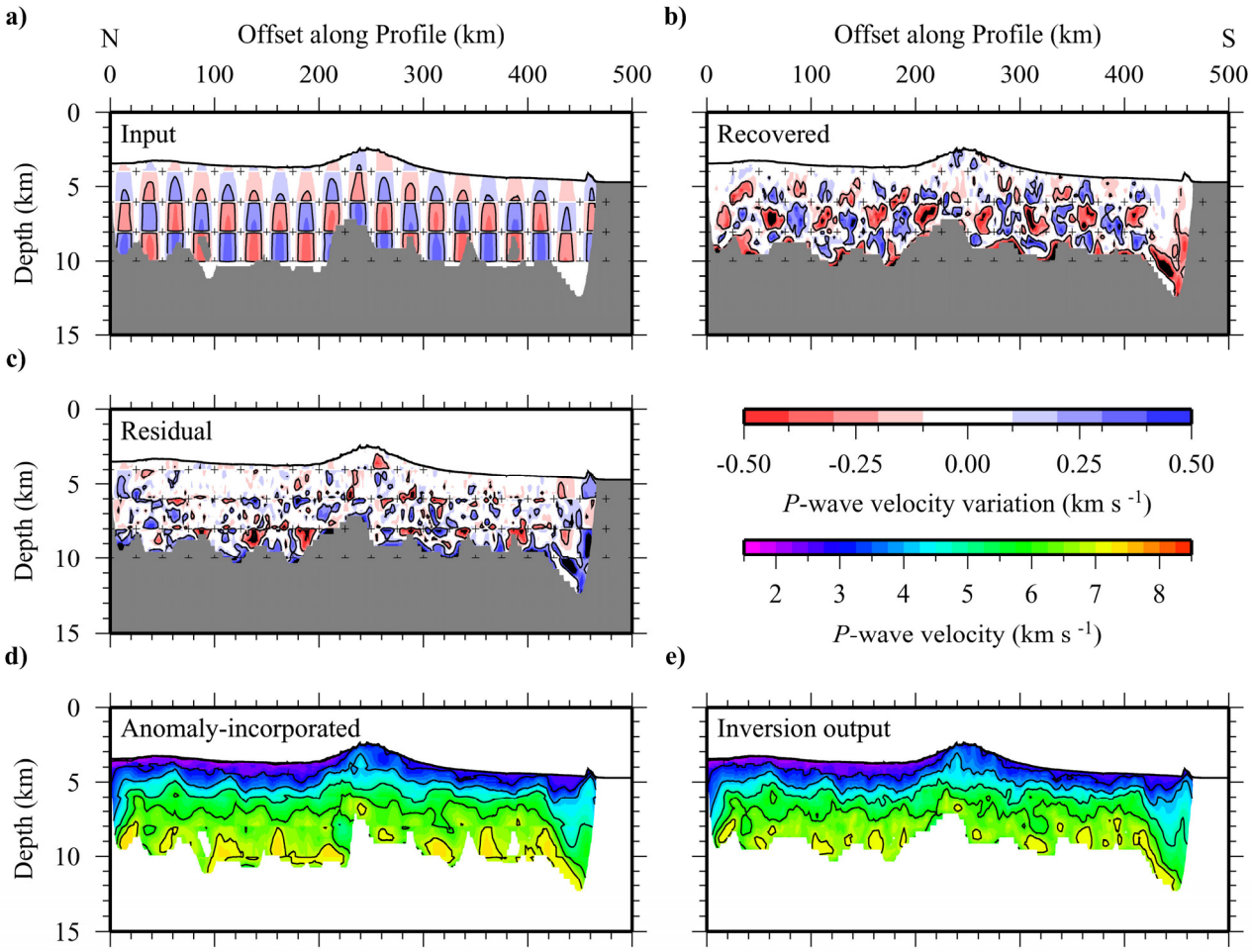

Figure 4.7 Resolution testing of the *FAST* model using a checkerboard size of 25 by 2 km with maximum anomaly amplitudes of ±5%. a) Input checkerboard anomaly pattern. b) Anomaly recovered by the inversion. c) Residual anomaly. d) Anomaly-incorporated *FAST* model used to generate synthetic traveltime data. e) Output model following an inversion of the revised initial model using the checkerboard synthetic traveltime data. Black crosses in parts a) to c) highlight the corners of the checkerboard regions and the anomalies are contoured at ±0.2 km s^{-1}. Iso-velocity contours are plotted in d) and e) with a 1 km s^{-1} contour interval. All plots are masked according to ray coverage.

Vertical resolution was assessed with a 75 by 1 km checkerboard test, the results of which are summarised in Figure 4.8. A direct comparison of the residual anomaly to the input checkerboard anomaly reveals that the inversion has failed to accurately recover the full amplitude of the pattern. A weak pattern has been recovered (Figure 4.8b) but without knowledge of the input pattern it would be difficult to interpret this result with any certainty.

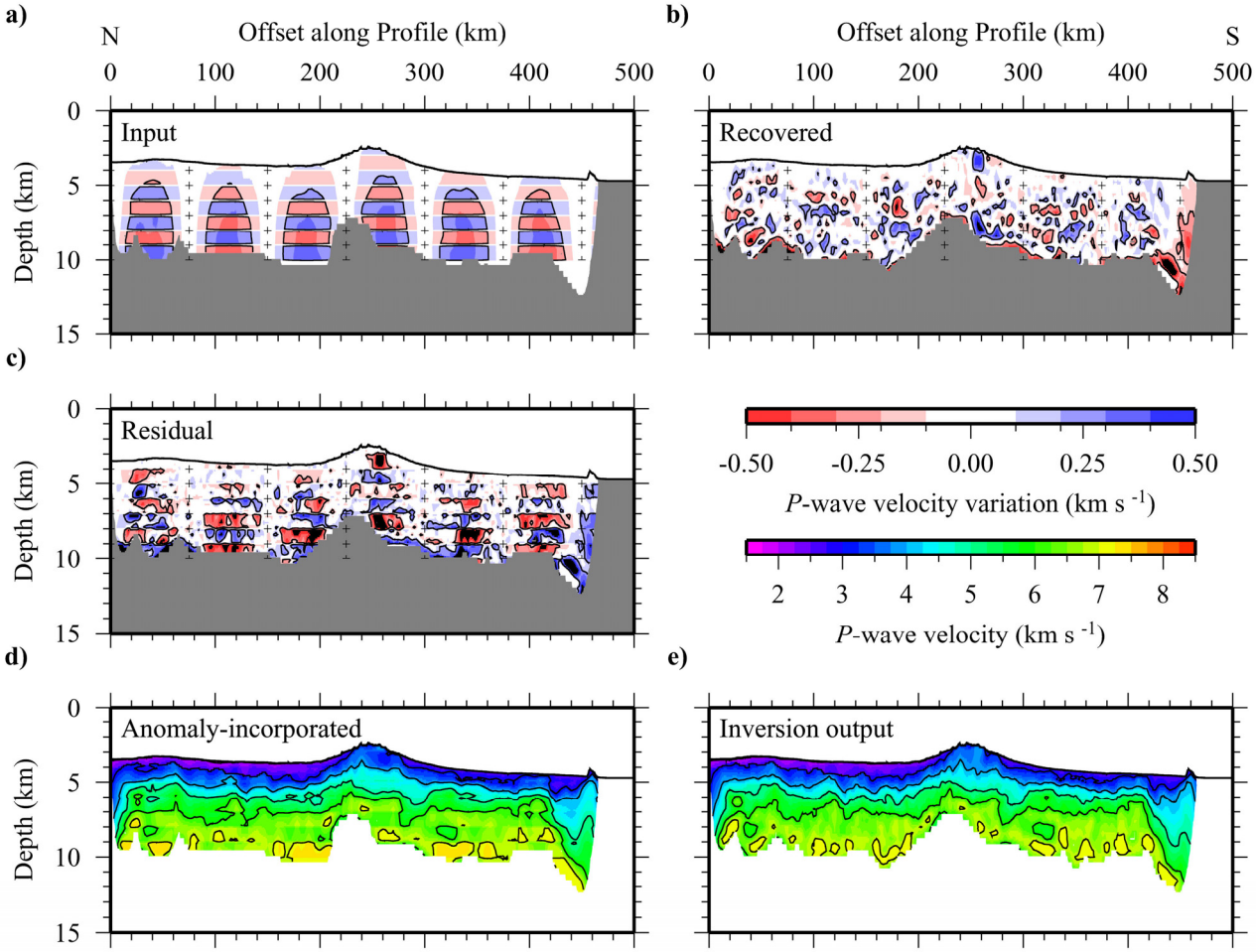

Figure 4.8 Resolution testing of the *FAST* model using a checkerboard size of 75 by 1 km with maximum anomaly amplitudes of ±5%. a) Input checkerboard anomaly pattern. b) Anomaly recovered by the inversion. c) Residual anomaly. d) Anomaly-incorporated *FAST* model used to generate synthetic traveltime data. e) Output model following an inversion of the revised initial model using the checkerboard synthetic traveltime data. Black crosses in parts a) to c) highlight the corners of the checkerboard regions and the anomalies are contoured at ±0.2 km s^{-1}. Iso-velocity contours are plotted in d) and e) with a 1 km s^{-1} contour interval. All plots are masked according to ray coverage.

The results of these tests define the horizontal and vertical resolution limits of the *FAST* inversion method to be 25 km and 1 km, respectively. These minimum resolvable lengths are smaller than the main features interpreted from the *rayinvr* model (Section 3.2), with velocity amplitudes in agreement with the results of sensitivity testing conducted using the forward modelling approach (Section 3.4).

The final two checkerboard tests (Table 4.2) involved the two large checkerboard patterns but with the maximum amplitude of the anomalies reduced by half, to ±2.5 % of the *FAST* model velocities. The results of both tests, summarised in Figures 4.9 & 4.10, demonstrate that the inversion struggles to recover a recognisable checkerboard anomaly. For both checkerboard sizes, the anomaly pattern is more

strongly recognisable in the recovered anomaly than in the residual anomaly, but the distortion caused by ray path biasing has had a greater effect than with the larger amplitude anomalies.

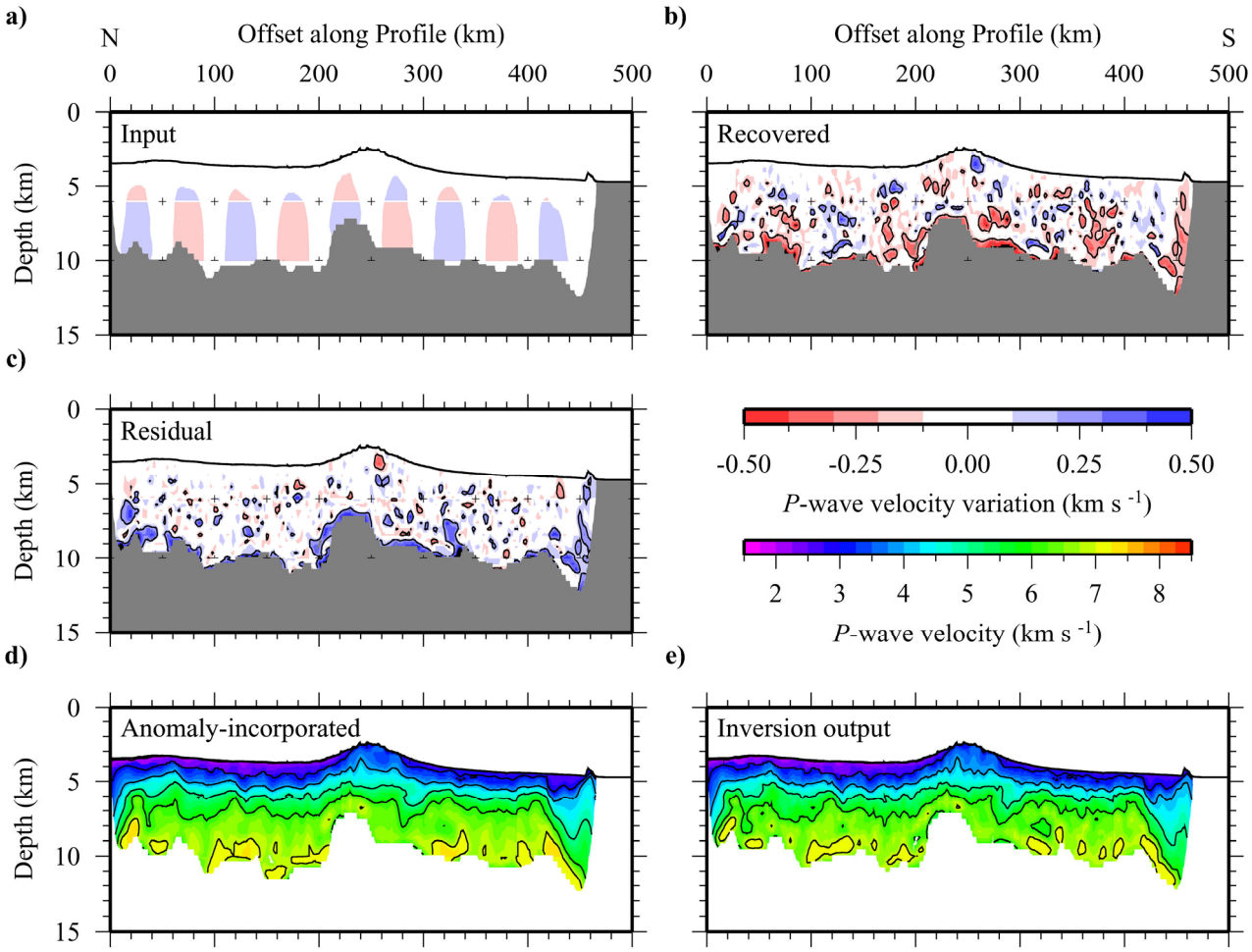

Figure 4.9 Resolution testing of the *FAST* model using a checkerboard size of 50 by 4 km with maximum anomaly amplitudes of ±2.5%. a) Input checkerboard anomaly pattern. b) Anomaly recovered by the inversion. c) Residual anomaly. d) Anomaly-incorporated *FAST* model used to generate synthetic traveltime data. e) Output model following an inversion of the revised initial model using the checkerboard synthetic traveltime data. Black crosses in parts a) to c) highlight the corners of the checkerboard regions and the anomalies are contoured at ±0.2 km s^{-1}. Iso-velocity contours are plotted in d) and e) with a 1 km s^{-1} contour interval. All plots are masked according to ray coverage.

Although the *FAST* inversion method can resolve slightly smaller amplitude anomalies at large scales (>50 km horizontal, > 2 km vertical), it suffers from ray path biasing, leading to the incorporation of very short wavelength anomalies (<20 km) that were apparent in the results of both the synthetic and the real inversions. The *FAST* inversion method is also limited to mid-crustal depths (~8 km) due to the inability to model P_mP and P_n phase traveltime data. In the next section these data will be incorporated using the inversion program *tomo2d* to assess the

uniqueness and resolution of the lower crust and uppermost mantle of the *rayinvr* model.

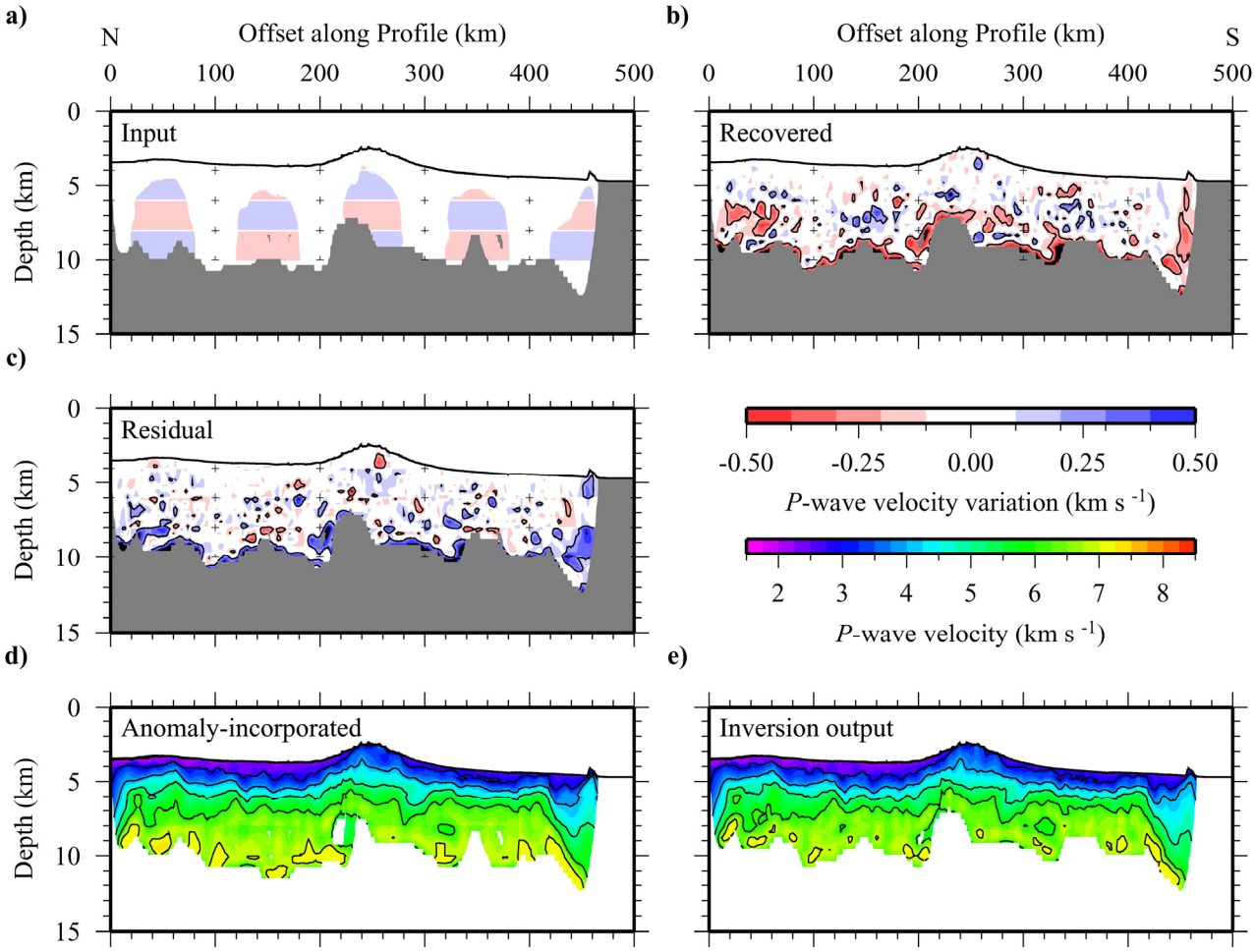

Figure 4.10 Resolution testing of the *FAST* model using a checkerboard size of 100 by 2 km with maximum anomaly amplitudes of ±2.5%. a) Input checkerboard anomaly pattern. b) Anomaly recovered by the inversion. c) Residual anomaly. d) Anomaly-incorporated *FAST* model used to generate synthetic traveltime data. e) Output model following an inversion of the revised initial model using the checkerboard synthetic traveltime data. Black crosses in parts a) to c) highlight the corners of the checkerboard regions and the anomalies are contoured at ±0.2 km s^{-1}. Iso-velocity contours are plotted in d) and e) with a 1 km s^{-1} contour interval. All plots are masked according to ray coverage.

4.2.2 Incorporating reflected arrivals, *tomo2d*

As with *FAST*, the *tomo2d* inversion program comprises a first stage for traveltime calculation and a second stage to apply updates to the velocity model. The forward calculation of Korenaga *et al.* (2000)'s inversion program, *tomo2d*, uses a hybrid of the graph and ray-bending methods. The graph method calculates the shortest traveltime from an origin node (in this case the OBS locations) to all other nodes (e.g. Moser, 1991). This method is limited by the possible node connections defined

by the modeller and as a result traveltimes may be overestimated. A ray-bending method (Moser *et al.*, 1992) is then implemented to improve accuracy for all node pairs connecting an OBS to a shot point.

The traveltime residuals are used to create a perturbational velocity model, with updates that are constrained by horizontal and vertical smoothing parameters, and this is then summed with the starting velocity model. When incorporating reflection traveltime data, a further parameter controls the relative weighting of velocity updates and reflector depth updates. The linearised inversion is applied iteratively until it converges on a model that fits all the available traveltime data.

4.2.2.1 Parameterisation and approach

Both the forward calculation and the inversion operate on a 'hanging mesh' model where the horizontal gridlines follow the bathymetry. A regular mesh was chosen with grid node intervals of 1.0 km in the *x* dimension and 0.1 km in the *z* dimension, to a maximum depth of 15 km below the seabed. As the velocity model is updated during an inversion it is also smoothed laterally and vertically to avoid the incorporation of velocity anomalies below the spatial resolution of the data, as discussed in Section 3.4 and Section 4.2.1.4. The horizontal smoothing lengths increased linearly with depth from 1.5 km immediately below the seabed to 15 km at the base of the mesh. Similarly, the vertical smoothing lengths increased from 0.15 to 1.5 km.

For each inversion, ten iterations were completed and the χ^2 parameter was used to assess the fit of the calculated traveltime data to the observed. A minimum was often reached before the tenth iteration, with further iterations attempting to over-fit the model to the data, resulting in unrealistic velocity updates. The iteration that reached the minimum χ^2 value, therefore, produced the best-fit model for each inversion.

4.2.2.2 Synthetic inversion modelling

Tests were conducted to assess the subseabed imaging potential and the influence of the initial model, using the same testing approaches adopted for the *FAST* inversion program (Section 4.2.1.2). Synthetic traveltime data were generated from the target model using the forward calculation of *tomo2d* and a component of noise, with a standard deviation based on the assigned uncertainties, was added using the *rayinvr* program subroutine *ttnoise*.

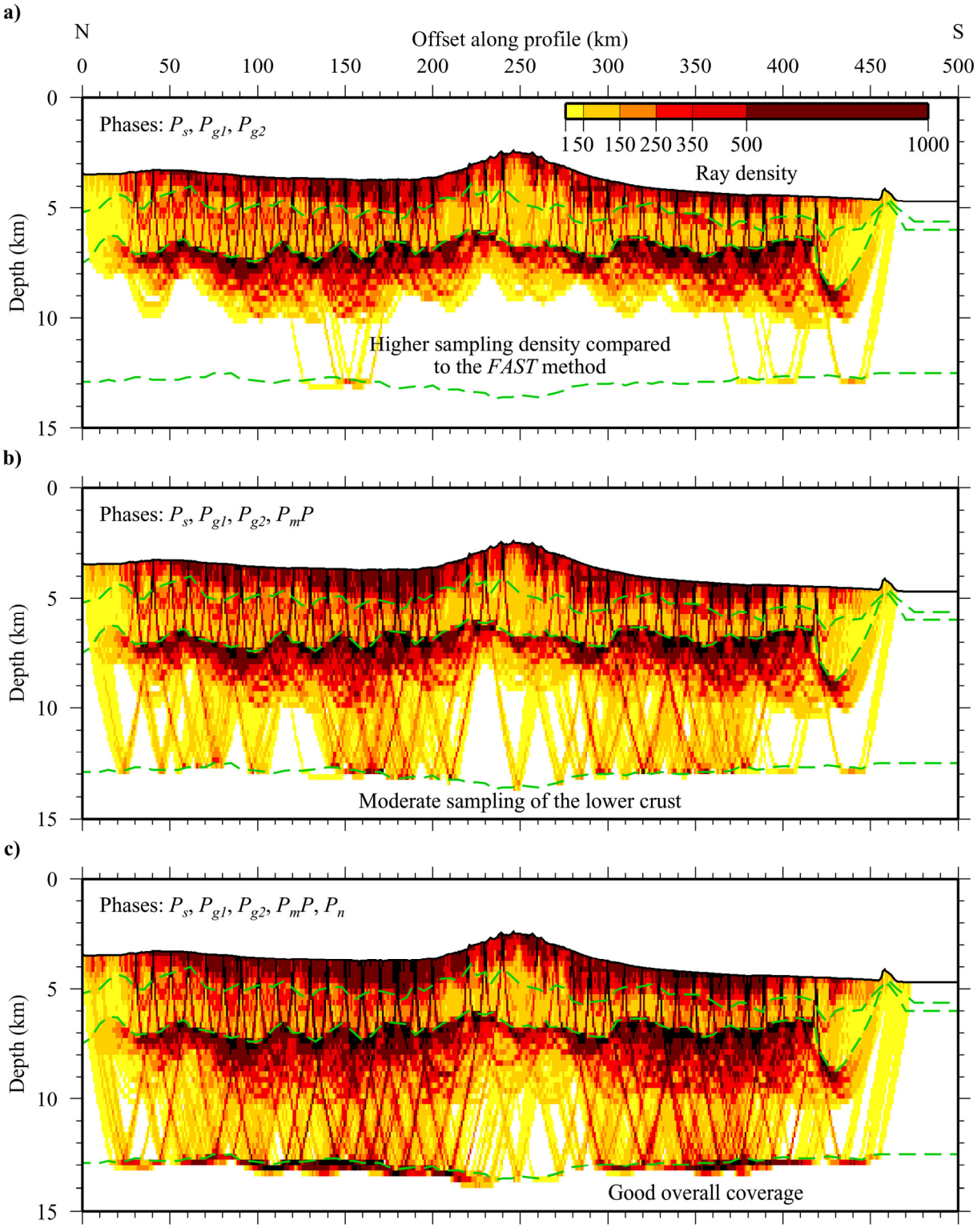

Figure 4.11 Region of the *rayinvr* model sampled by forward ray-tracing with the inversion program *tomo2d*. A plot of ray density gives a representation of sampling density, revealing areas of the model that should be well and poorly resolved during inversions using traveltime data from a) the P_s, P_{g1} and P_{g2} phases, b) with the addition of P_mP phase traveltime data and c) with the cumulative addition of P_n phase traveltime data. The oceanic basement layer boundaries of the *rayinvr* model (green dashed lines) are also shown.

The region of the target model that is sampled by forward ray-tracing during the generation of synthetic traveltime data (Figure 4.11), increases with the inclusion of traveltime data from the P_mP and P_n phases, as expected. The ray coverage experienced using traveltime data corresponding to the shallow subseabed and crustal phases, P_s, P_{g1} and P_{g2} (Figure 4.11a), is similar to that for the *FAST* method (Figure 4.1b) although there is a higher sampling density between 8 and 10 km b.s.l.. The addition of P_mP phase traveltime data marginally increases the ray density at shallow-to-mid-crustal depths and provides a moderate sampling of the model space down to the Moho (Figure 4.11b). Inclusion of P_n phase traveltime data provides ray coverage through the uppermost part of the upper mantle and also increases the ray density at lower crustal depths (Figure 4.11c). The limited sampling below the Moho should still be sufficient to determine large-scale lateral changes in the *P*-wave velocity of the shallow mantle and the vertical velocity gradient.

The reproducibility of the target model was first tested using traveltime data corresponding to the shallow subseabed and crustal phases, P_s, P_{g1} and P_{g2}. Results of the synthetic inversion of the same 2-D initial model used for the *FAST* inversions are summarised in Figure 4.12. The output model (Figure 4.12b) does not compare well to the target model and most noticeably contains several areas of unrealistically low *P*-wave velocities (<1.5 km s^{-1}) in the shallow subseabed. Additionally, the high velocity region beneath the F-STR has not been accurately reproduced and the maximum depth of ray coverage is significantly shallower than the maximum depth imaged during forward ray-tracing of the target model (Figure 4.11a). Based on the ray density (Figure 4.12c), the lateral confidence boundaries can be placed slightly closer to the edges of the model, at 20 and 430 km, than for the *FAST* inversion method. Analysis of the difference between the target model and the output model (Figure 4.12d) reveals mismatches of up to ±1.00 km s^{-1} at the target model top-basement layer boundary, similar to those produced by the *FAST* inversion method.

Figure 4.12 Inversion using *tomo2d* of the four-layer, 2-D initial model using synthetic traveltime data. a) Velocity-depth structure of the initial model and b) the output model following the inversion, masked by ray coverage. Iso-velocity contours (black lines) are annotated with a 1 km s^{-1} contour interval. The boundary surfaces of the target (*rayinvr*) model (red lines) are shown for comparison. c) Plot of ray density indicates areas of the model that are well and poorly constrained in the final solution. d) Difference between the target (*rayinvr*) model and the output model. Velocity difference contours are included (black lines) at ±0.5 km s^{-1} intervals to highlight areas of significant mismatch. See text for discussion.

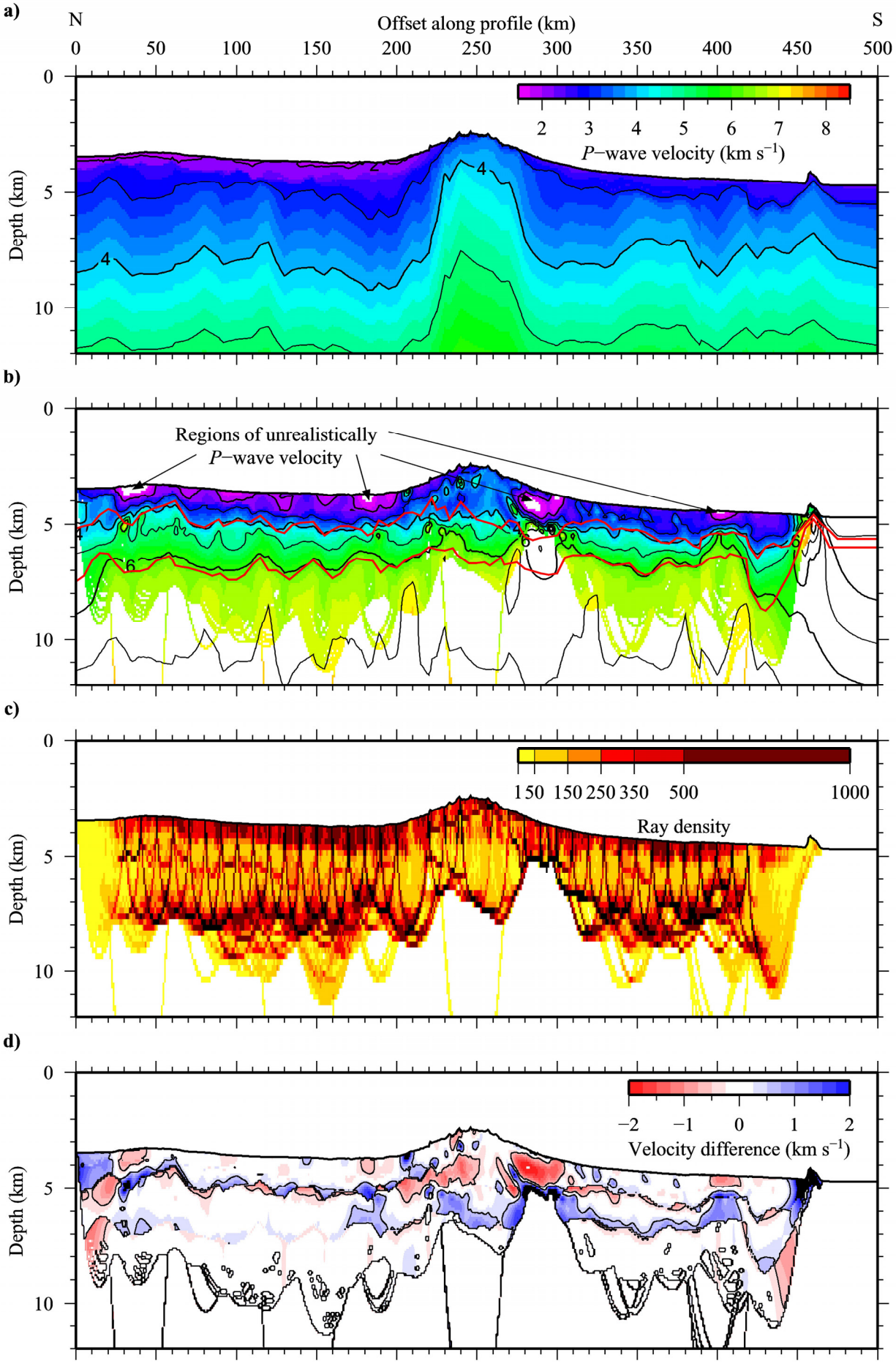
a)
N
Offset along profile (km)
S
0
50
100
150
200
250
300
350
400
450
500
Depth (km)
0
5
10
2
3
4
5
6
7
8
P–wave velocity (km s−1)
4
4
b)
Regions of unrealistically
P–wave velocity
4
6
6
c)
150
150
250
350
500
1000
Ray density
d)
−2
−1
0
1
2
Velocity difference (km s−1)

The uppermost section of the model is already well constrained by the MCS reflection data (Section 3.3) and corroborated by the results from the *FAST* inversion (Section 4.2.1.3). In order to suppress the production of areas of low velocity in the shallow subseabed, a revised initial model was created. The revised 2-D initial model differs from the original 2-D initial model from the top-basement boundary downwards, where the velocity now increases from 4.5 km s^{-1} to 8.3 km s^{-1} at the base of the model (20 km b.s.l.).

The results of the synthetic inversion of the revised 2-D initial model are summarised in Figure 4.13. The output model (Figure 4.13b) is now very similar to the output model from the *FAST* synthetic inversion of the original 2-D model (Figure 4.3b). Ray coverage now reaches a maximum depth beneath the F-STR that agrees with the results of the forward ray-tracing through the target model (Figure 4.11a) and the ray density pattern is well matched (Figure 4.13c). The difference between the target model and the output model (Figure 4.13d) has been reduced throughout. A clear misfit still exists, however, around the mid-basement layer boundary of the target model at >150 km profile offset.

Figure 4.13 Inversion using *tomo2d* of the revised four-layer, 2-D initial model using synthetic traveltime data. a) Velocity-depth structure of the revised initial model and b) the output model following the inversion, masked by ray coverage. Iso-velocity contours (black lines) are annotated with a 1 km s^{-1} contour interval. The boundary surfaces of the target (*rayinvr*) model (red lines) are shown for comparison. c) Plot of ray density indicates areas of the model that are well and poorly constrained in the final solution. d) Difference between the target (*rayinvr*) model and the output model. Velocity difference contours are included (black lines) at ±0.5 km s^{-1} intervals to highlight areas of significant mismatch. See text for discussion.

Figure 4.14 Inversion using *tomo2d* of the revised four-layer, 2-D initial model using synthetic traveltime data. a) Velocity-depth structure of the revised initial model and b) the output model following the inversion, masked by ray coverage. Iso-velocity contours (black lines) are annotated with a 1 km s^{-1} contour interval. Black dashed lines mark the initial and final locations of the reflector. The boundary surfaces of the target (*rayinvr*) model (red lines) are shown for comparison. c) Plot of ray density indicates areas of the model that are well and poorly constrained in the final solution. d) Difference between the target (*rayinvr*) model and the output model. Velocity difference contours are included (black lines) at ±0.5 km s^{-1} intervals to highlight areas of significant mismatch. See text for discussion.

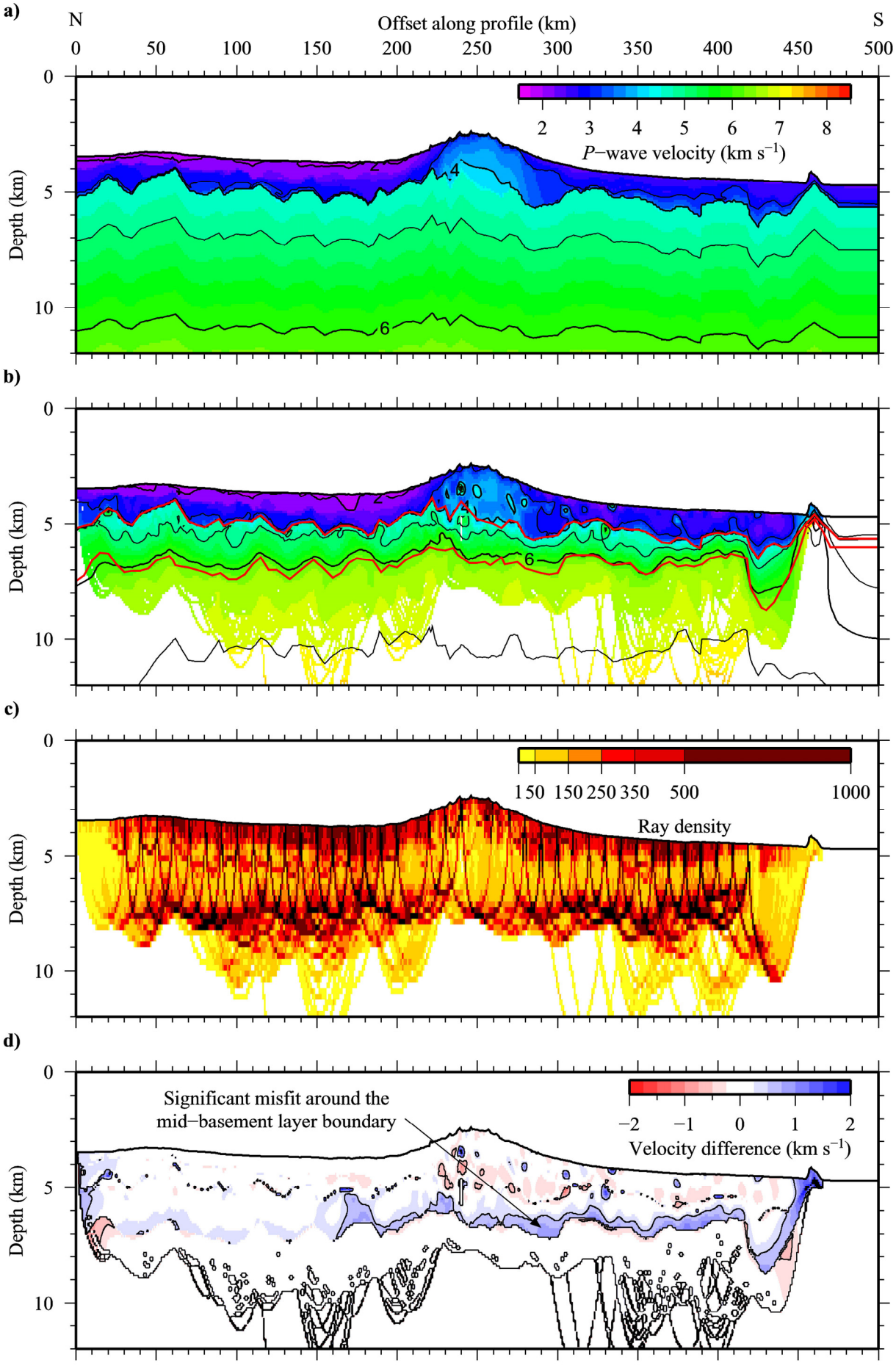
a)
N
Offset along profile (km)
S
0
50
100
150
200
250
300
350
400
450
500
Depth (km)
0
5
10
2
3
4
5
6
7
8
P–wave velocity (km s−1)
4
6
b)
c)
150
150
250
350
500
1000
Ray density
d)
Significant misfit around the
mid–basement layer boundary
−2
−1
0
1
2
Velocity difference (km s−1)

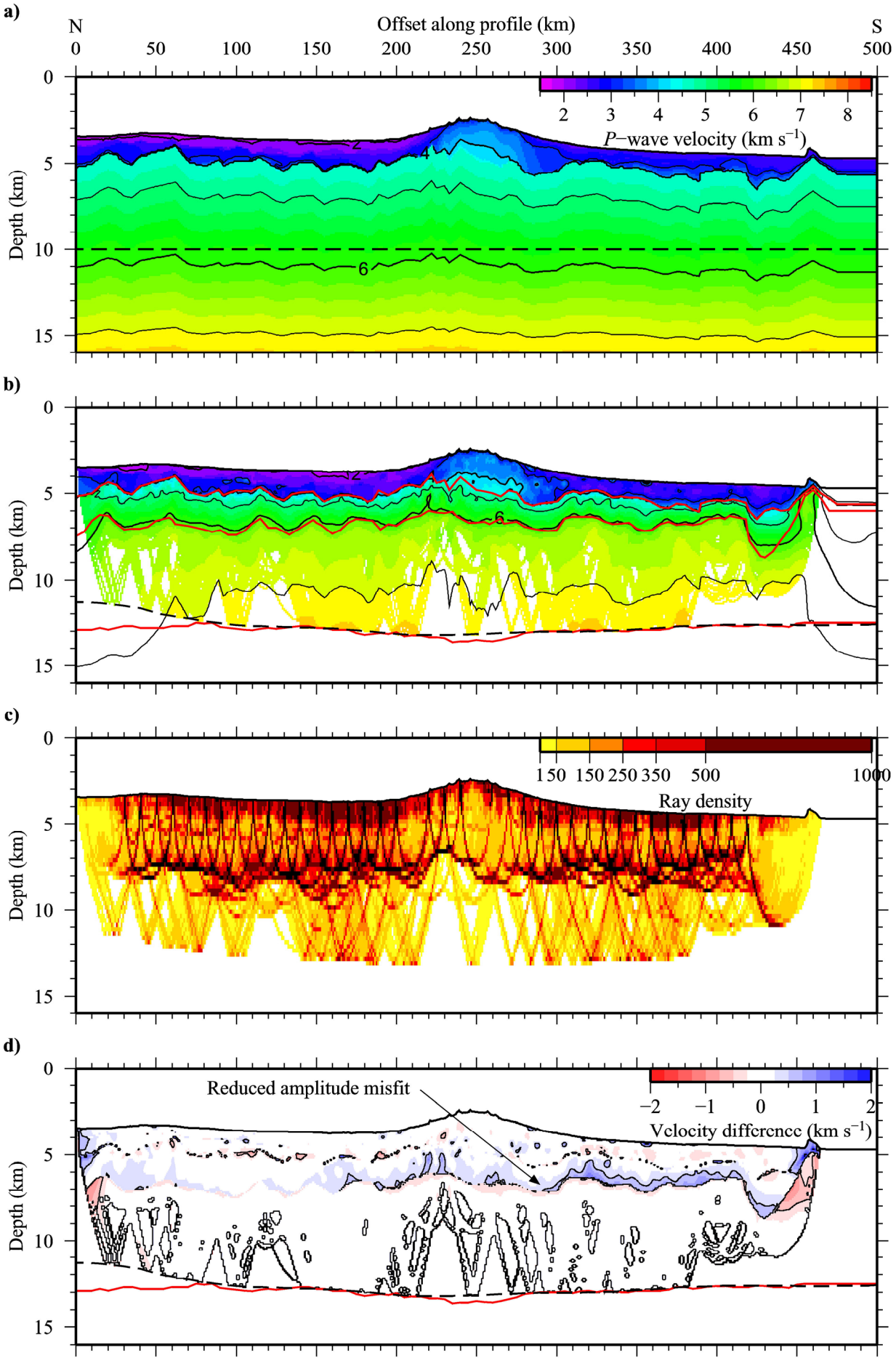
a)
N
Offset along profile (km)
S
0
50
100
150
200
250
300
350
400
450
500
2
3
4
5
6
7
8
P–wave velocity (km s−1)
Depth (km)
0
5
10
15
2
4
6
b)
c)
150 150 250 350 500 1000
Ray density
d)
Reduced amplitude misfit
−2 −1 0 1 2
Velocity difference (km s−1)

This testing has shown that, starting with the new 2-D initial model, the *tomo2d* inversion can recover the target model to mid-crustal depths with results equal to the *FAST* inversion. Subsequently, the P_mP phase traveltime data were incorporated into a joint inversion of both the velocity structure and a reflection generating boundary, which is hereafter referred to as a reflector. A final synthetic inversion was conducted with the revised 2-D initial model and a reflector that started as a horizontal boundary at a depth of 10 km b.s.l. along the entire length of the model. The results, summarised in Figure 4.14, demonstrate the excellent recovery of both the velocity-depth structure, between 20 and 430 km profile offset, and of the Moho reflector between 70 and 380 km profile offset (Figure 4.14b), even beneath the F-STR where there is reduced ray coverage (Figure 4.14c). Towards the edge of the model, where ray coverage is reduced (<50 km), the recovered Moho is more than 1 km shallower than the target due to the lower velocities in the oceanic basement of the final model that have changed little from the input model (Figure 4.14a & b).

The increased ray density in the upper 8 km of the model (Figure 4.14c) has reduced the amplitude of the misfit observed at the depth of the mid-crustal layer boundary of the target model. The result from this final synthetic test gives confidence that, using the observed traveltime data, the *tomo2d* method can accurately produce a model of the crustal structure down to the Moho (Figure 4.14d) when given some guidance in the input model to reduce the uncertainty resulting from shallow subseabed variations at a scale that is above the resolution of the data.

It is apparent that *tomo2d* requires a significant amount of modeller input, especially when compared to *FAST* (Section 4.2.1), to produce a model that fits the traveltime data. However, given that *FAST* is limited to inversions using only first arrival traveltime data, the application of *tomo2d* to a model with pre-constrained shallow subseabed structure is necessary to test the Moho depth and sub-Moho velocities obtained using the forward modelling approach.

4.2.2.3 Real inversion modelling results

A total of three inversions were made using the observed traveltime data. Two of these inversions used the revised 2-D initial model as a starting point, with the first incorporating traveltime data from the P_s, P_{g1} and P_{g2} phases to produce an output model directly comparable to the result of the *FAST* inversion. The second included traveltime data from the P_mP phase to produce a model that was constrained down to

the Moho reflector. The final inversion started with the output model from the second inversion and incorporated traveltime data from the P_n phase to recover the velocity structure of the uppermost mantle.

The output model produced by the first inversion (Figure 4.15b) is very similar to the result of the *FAST* inversion (Figure 4.4b), and appears to be smoother at the maximum depth of ray coverage. Analysis of the difference between the *rayinvr* model and the output model (Figure 4.15d) shows that throughout the majority of the model space the velocities are consistent to ±0.25 km s^{-1}. There is a band of misfit to the south of the F-STR at ~6 km b.s.l., where the output model contains higher velocities than the *rayinvr* model by up to 1 km s^{-1}, similar to that seen in the *FAST* model comparison (Figure 4.4d). Also, there are small areas of misfit within the top 2.5 km of the shallow subseabed, between 230 and 340 km profile offset, that result from ray path biasing due to the sparse data over the F-STR and the short smoothing lengths at these depths (<5 km laterally, <0.5 km vertically).

Inclusion of traveltime data from the P_mP phase does not lead to an output model that is significantly different down to mid-crustal depths (Figure 4.16b). It does, however, give rise to a result which is different to the *rayinvr* model. The velocities at the base of the lower crust are up to 0.3 km s^{-1} higher and the final Moho position is deeper by at least 1 km at profile offsets ranging from 70 to 220 km and from 290 to 375 km. The final geometry and depth of the Moho reflector resulting from the inversion was the same regardless of the initial depth (Figure 4.16a & b).

Figure 4.15 Inversion using *tomo2d* of the revised four-layer, 2-D initial model using the observed traveltime data from phases P_s, P_{g1} and P_{g2}. a) Velocity-depth structure of the revised initial model and b) the output model following the inversion, masked by ray coverage. Iso-velocity contours (black lines) are annotated with a 1 km s^{-1} contour interval. The boundary surfaces of the *rayinvr* model (red lines) are shown for comparison. Vertical black lines in part b) indicate the lateral confidence boundaries. c) Plot of ray density indicates areas of the model that are well and poorly constrained in the final solution. d) Difference between the *rayinvr* model and the output model. Velocity difference contours are included (black lines) at ±0.5 km s^{-1} intervals to highlight areas of significant mismatch. See text for discussion.

Figure 4.16 Inversion using *tomo2d* of the revised four-layer, 2-D initial model using the observed traveltime data from phases P_s, P_{g1}, P_{g2} and P_mP. a) Velocity-depth structure of the revised initial model and b) the output model following the inversion, masked by ray coverage. Iso-velocity contours (black lines) are annotated with a 1 km s^{-1} contour interval. Black and grey dashed lines mark the initial and final locations of the reflector using two different starting depths. The boundary surfaces of the *rayinvr* model (red lines) are shown for comparison. c) Plot of ray density indicates areas of the model that are well and poorly constrained in the final solution. d) Difference between the *rayinvr* model and the output model. Velocity difference contours are included (black lines) at ±0.5 km s^{-1} intervals to highlight areas of significant mismatch. See text for discussion.

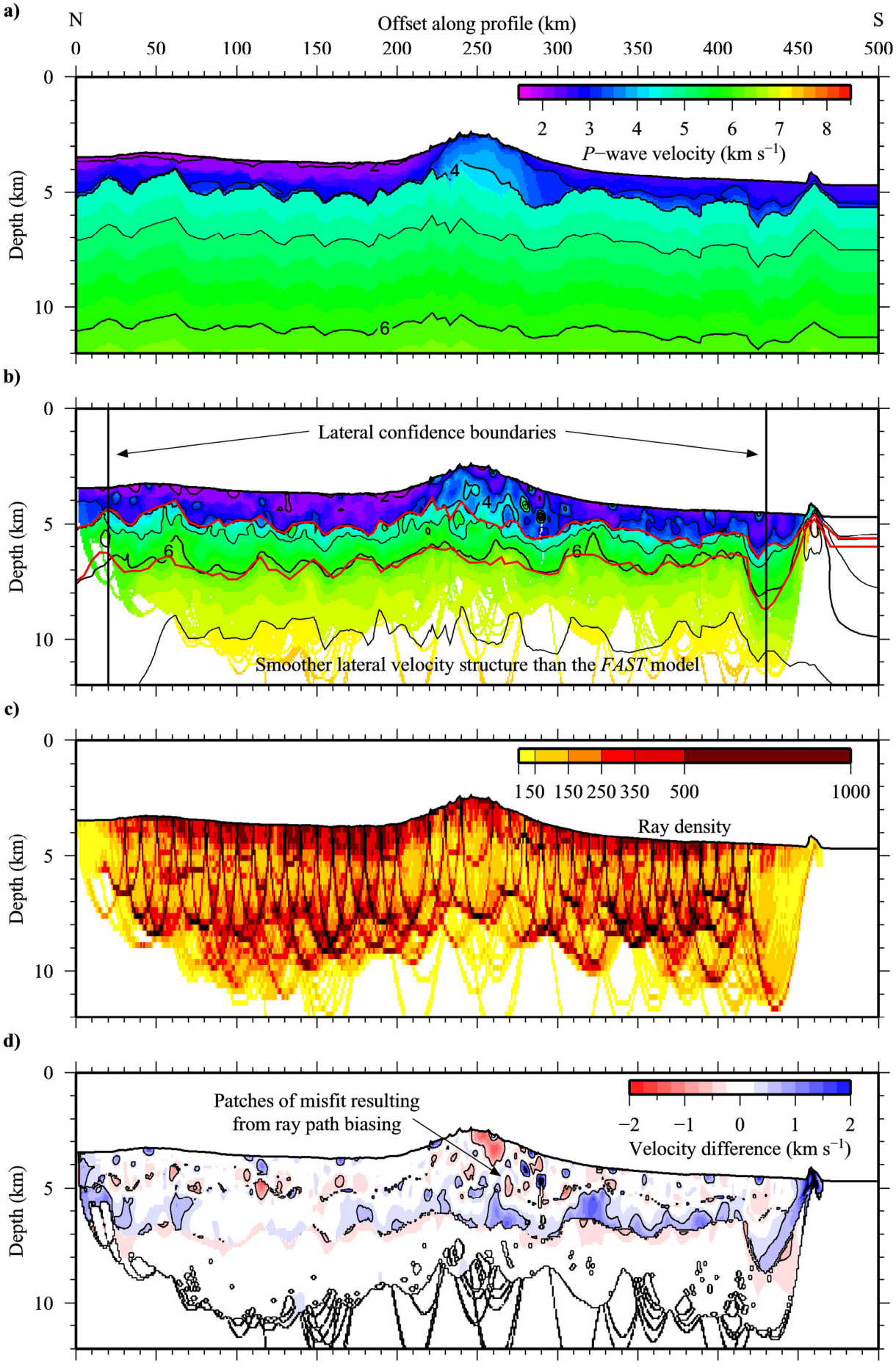
a)
N
Offset along profile (km)
S
0
50
100
150
200
250
300
350
400
450
500
Depth (km)
0
5
10
2
3
4
5
6
7
8
P–wave velocity (km s−1)
4
6
b)
Lateral confidence boundaries
Smoother lateral velocity structure than the FAST model
c)
150
150
250
350
500
1000
Ray density
d)
Patches of misfit resulting
from ray path biasing
−2
−1
0
1
2
Velocity difference (km s−1)

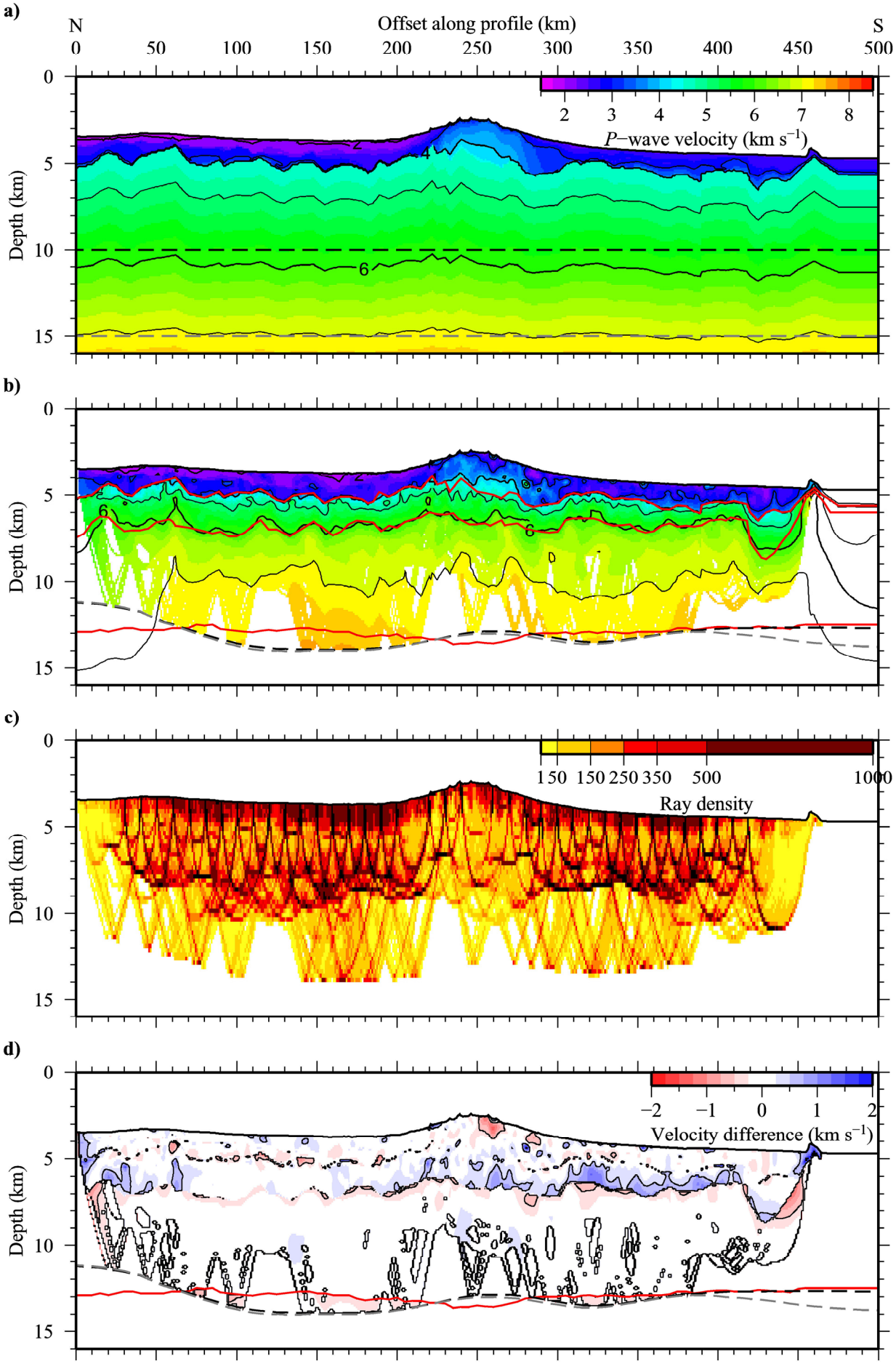
a)
N
Offset along profile (km)
S
0
50
100
150
200
250
300
350
400
450
500
2
3
4
5
6
7
8
P–wave velocity (km s−1)
Depth (km)
b)
c)
150
150
250
350
500
1000
Ray density
d)
−2
−1
0
1
2
Velocity difference (km s−1)

Analysis of the difference between the *rayinvr* model and the *tomo2d* output model (Figure 4.16d) shows that the velocities agree to within 0.25 km s^{-1} except around the *rayinvr* model layer boundaries and the regions of overlap between the two different Moho solutions. These results imply that the uncertainty in the depth of the Moho could be up to ±1.2 km, which is notably larger than the value obtained using the sensitivity testing approach in Section 3.4.

To ensure that rays were traced to sub-Moho depths when incorporating traveltime data for the P_n phase into the inversion, the output model of the second inversion, modified to set all sub-Moho *P*-wave velocities to 8.0 km s^{-1}, was used as the starting point. The results of the final inversion are summarised in Figure 4.17. The output model (Figure 4.17b), henceforth referred to as the *tomo2d* model, shows the same crustal velocity structure as the result from the previous inversion, and is better constrained due to the increased ray density at mid-to-lower crustal depths (Figure 4.17c). The average velocity of the uppermost mantle in the *tomo2d* model is 7.8 km s^{-1}, which agrees with the *rayinvr* model (7.7 km s^{-1}) to within the uncertainties defined in Section 3.4. The vertical velocity gradient in the mantle ranges from 0.03 to 0.04 s^{-1} (Figure 4.17b), which is significantly smaller than the gradient in the *rayinvr* model (0.11 s^{-1}). This large difference most likely arises from differences in Moho geometry and, because the shallow depth of penetration of P_n ray paths beneath the Moho (Figure 4.17c) provides limited constraint, the vertical velocity gradients derived from the both the forward modelling and the inversion remain largely uncertain.

Figure 4.17 Inversion using *tomo2d* using observed traveltime data from phases P_s, P_{g1}, P_{g2}, P_mP and P_n. a) The initial model is modified from the output model shown in Figure 4.16b to set sub-Moho *P*-wave velocities to 8.0 km s^{-1}. b) The output (*tomo2d*) model following the inversion, masked by ray coverage. Iso-velocity contours (black lines) are annotated with a 1 km s^{-1} contour interval. Black dashed lines mark the initial and final locations of the reflector. The boundary surfaces of the *rayinvr* model (red lines) are shown for comparison. c) Plot of ray density indicates areas of the model that are well and poorly constrained in the final solution. d) Difference between the *rayinvr* model and the output model. Velocity difference contours are included (black lines) at ±0.5 km s^{-1} intervals to highlight areas of significant mismatch. See text for discussion.

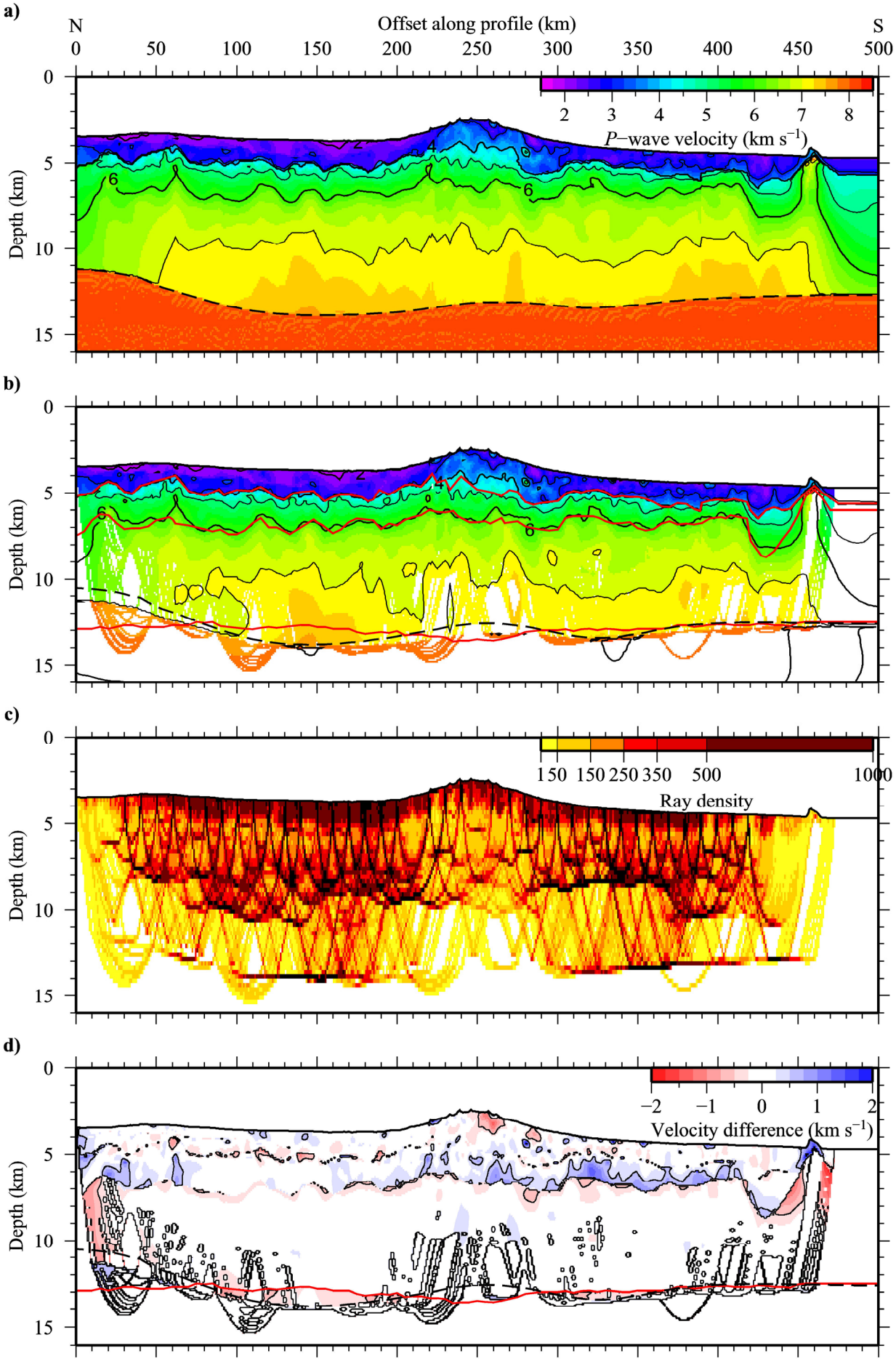
a)
N
Offset along profile (km)
S
0
50
100
150
200
250
300
350
400
450
500
Depth (km)
0
5
10
15
2
3
4
5
6
7
8
P–wave velocity (km s−1)
6
6
b)
Depth (km)
c)
150
150
250
350
500
1000
Ray density
Depth (km)
d)
−2
−1
0
1
2
Velocity difference (km s−1)
Depth (km)

4.2.2.4 Checkerboard and lower crust resolution testing

The resolution of the *tomo2d* model was tested at the limits determined for the *FAST* model using the 25 by 2 km checkerboard pattern with maximum anomaly amplitudes of ±5%. This test was intended to determine whether or not the increased ray density, provided by the inclusion of the P_mP phase traveltime data, leads to any improvement in the recovery of velocity perturbations. The results, summarised in Figure 4.18, reveal that the ability of *tomo2d* to recover the anomaly pattern is limited to mid-crustal depths of ~10 km b.s.l., similar to *FAST* (Section 4.2.1.4).

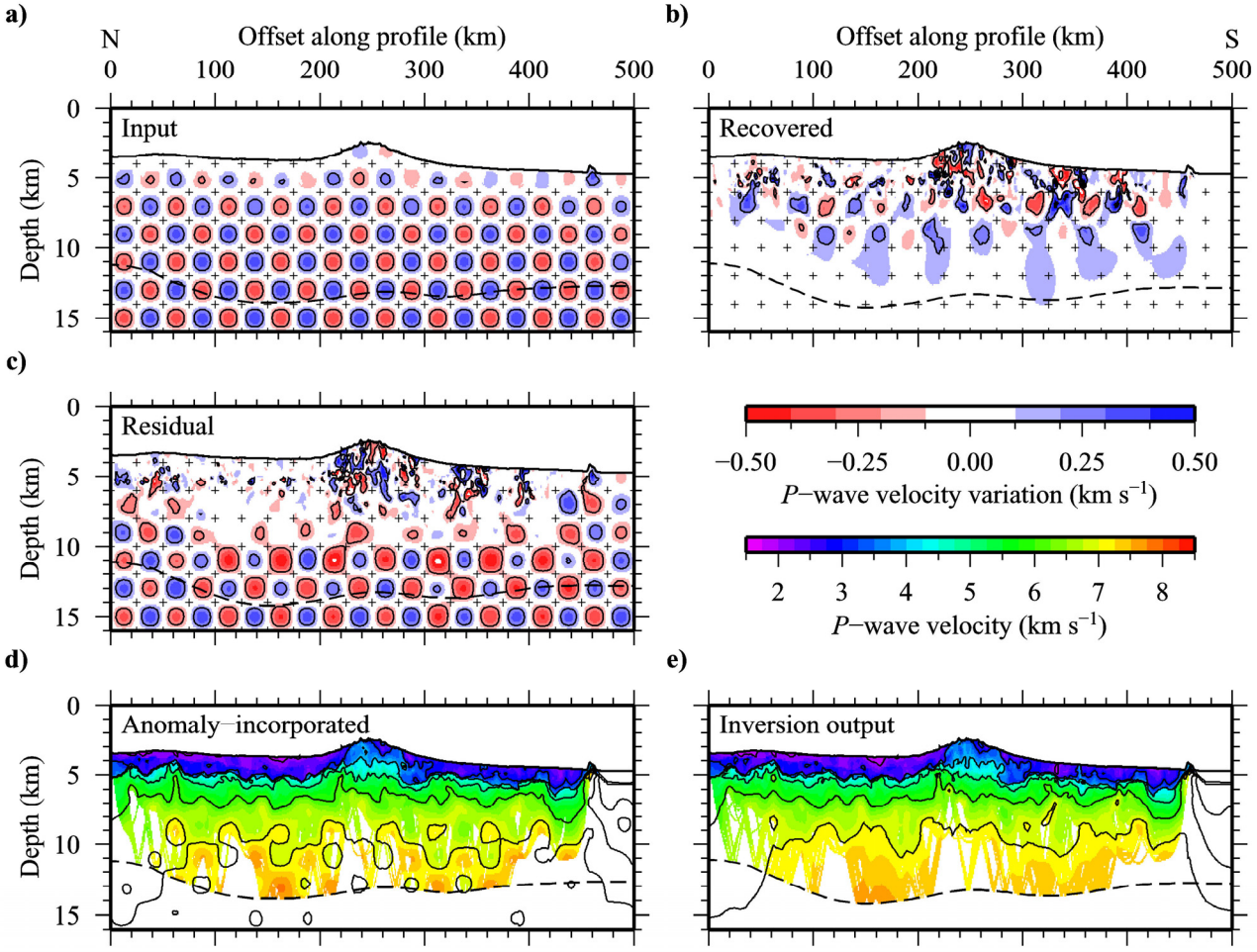

Figure 4.18 Resolution testing of the *tomo2d* model using a checkerboard size of 25 by 2 km with maximum anomaly amplitudes of ±5%. a) Input checkerboard anomaly pattern. b) Anomaly recovered by the inversion. c) Residual anomaly. d) Anomaly-incorporated *tomo2d* model used to generate synthetic traveltime data. e) Output model following an inversion of the new initial model using the checkerboard synthetic traveltime data. Black dashed lines mark the initial and final locations of the reflector. Black crosses in parts a) to c) highlight the corners of the checkerboard regions and the anomalies are contoured at ±0.2 km s^{-1}. Iso-velocity contours are plotted in d) and e) with a 1 km s^{-1} contour interval. Parts b), d) and e) are masked according to ray coverage.

At lower crustal depths between 10 km b.s.l. and the Moho, there is a great degree of vertical smearing of the anomaly pattern and the inversion program tends towards the inclusion of positive anomalies (Figure 4.18b). The inclusion of P_mP phase traveltimes allows the velocity structure of the lower crust to be determined but the resolution is much lower and only large-scale structure can be accurately interpreted with any certainty.

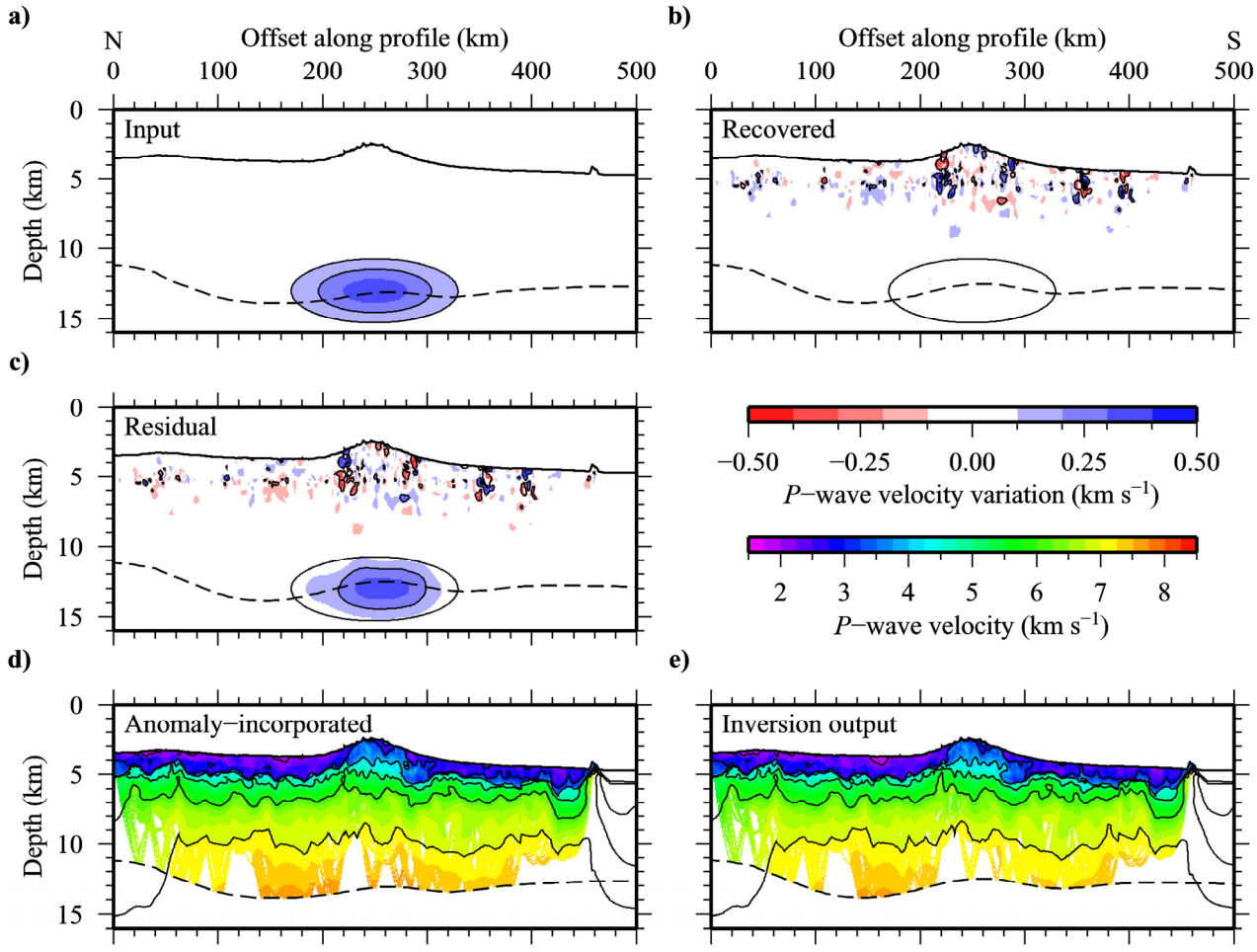

Figure 4.19 Resolution testing of the *tomo2d* model using a large positive anomaly (maximum amplitude +5%) centred at 250 km profile offset. a) Input anomaly. b) Anomaly recovered by the inversion. c) Residual anomaly. d) Anomaly-incorporated *tomo2d* model used to generate synthetic traveltime data. e) The output model following an inversion of the new initial model using the checkerboard synthetic traveltime data. Black dashed lines mark the initial and final locations of the reflector. The black oval in parts a) to c) highlights the outline of the input anomaly and the anomalies are contoured at ±0.2 km s^{-1}. Iso-velocity contours are plotted in d) and e) with a 1 km s^{-1} contour interval. Parts d) and e) are masked according to ray coverage.

In order to assess the resolution of the lower crustal velocity structure and, hence, the potential depth uncertainty of the Moho reflector, two further anomaly tests were conducted. The first introduced a large positive velocity anomaly (amplitude +5%),

centred at 250 km profile offset (Figure 4.19a), that was intended to test the ability of the inversion method to detect a region of higher velocities, that could indicate a body of intra-crustal intrusion or undercrustal material of similar size and magnitude considered during the 2-D FAA modelling (Section 3.5). The second included two medium-sized negative velocity anomalies (amplitude -5%), centred at 170 and 330 km profile offset (Figure 4.20a), that were intended to assess the ability of the inversion program to discriminate between velocities of <7.0 km s^{-1} and >7.3 km s^{-1} at the base of the lower crust.

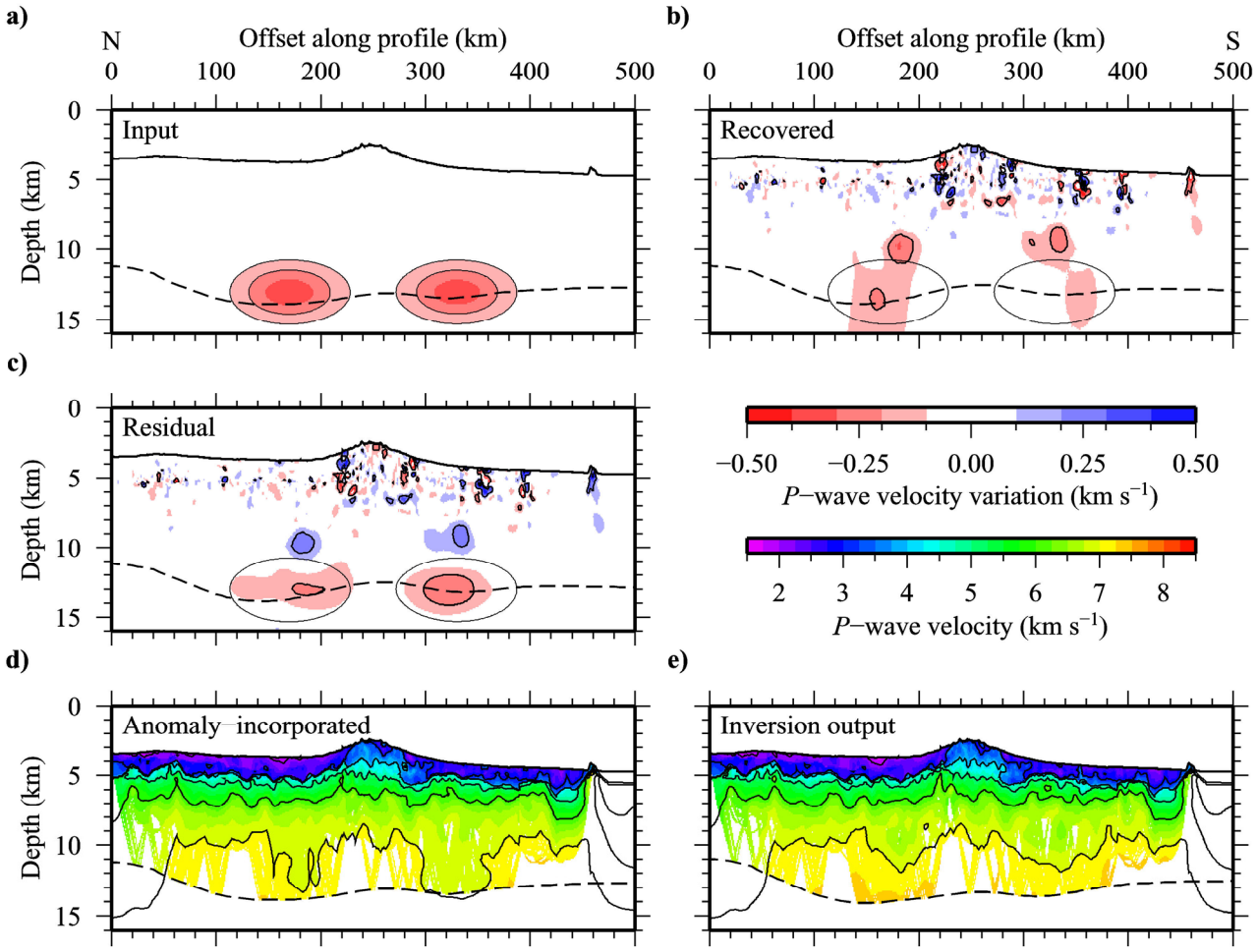

Figure 4.20 Resolution testing of the *tomo2d* model using two medium-sized negative anomalies (maximum amplitude -5%) centred at 170 and 330 km profile offset. a) Input anomaly pattern. b) Anomaly recovered by the inversion. c) Residual anomaly. d) Anomaly-incorporated *tomo2d* model used to generate synthetic traveltime data. e) Output model following an inversion of the new initial model using the checkerboard synthetic traveltime data. Black dashed lines mark the initial and final locations of the reflector. The black ovals in parts a) to c) highlight the input anomaly pattern and the anomalies are contoured at ±0.2 km s^{-1}. Iso-velocity contours are plotted in d) and e) with a 1 km s^{-1} contour interval. Parts d) and e) are masked according to ray coverage.

The results from both of these resolution tests (Figures 4.19 & 4.20) demonstrate that *tomo2d* is almost entirely insensitive to ±5% velocity perturbations at the base of the lower crust. In the case of the positive anomaly, there is no evidence of any significant recovery (>0.1 km s^{-1}; Figure 4.19b). Instead, small positive and negative anomalies are incorporated into the shallow subseabed region of the model <7 km b.s.l. (Figure 4.19b) in an attempt to fit the synthetic traveltime data. A marginally better result is observed for the negative anomalies, although there is a high degree of vertical smearing (Figure 4.20b). The anomalies are less than 50% recovered, as evidenced by the strong correlation between the residual anomaly (Figure 4.20c) and the input anomaly (Figure 4.20a).

These results indicate that the velocity uncertainty within the lower crust is up to ±0.4 km s^{-1}. An equivalent traveltime solution would be reached if the lower crustal velocities included in the *tomo2d* model (between 100 and 230 km profile offset and between 360 and 440 km profile offset) were lower by ~0.3 km s^{-1} given a corresponding shift of the Moho to shallower depth. Similarly, a region of high velocities at the base of the lower crust beneath the F-STR could be included, with a corresponding shift of the Moho to a greater depth.

4.2.3 Assessment of modeller bias

The velocity-depth models resulting from the forward modelling with *rayinvr* and the inversions using both *FAST* and *tomo2d* are compared in Figure 4.21. Disregarding minor differences due to the limitations imposed by each of the individual methods, it is apparent that the results agree to within the uncertainties previously discussed.

All three models demonstrate a three-layer crustal structure comprising sediments and/or shallow subseabed material (beneath the F-STR) overlying a two-layer oceanic basement. A comparison of 1-D velocity-depth profiles through the oceanic basement from the three output models is shown in Figure 4.22. These profiles confirm that the models are in good agreement where there is constraint provided by ray coverage, and that the velocities are generally within the range expected for mature Atlantic oceanic basement (White *et al.*, 1992).

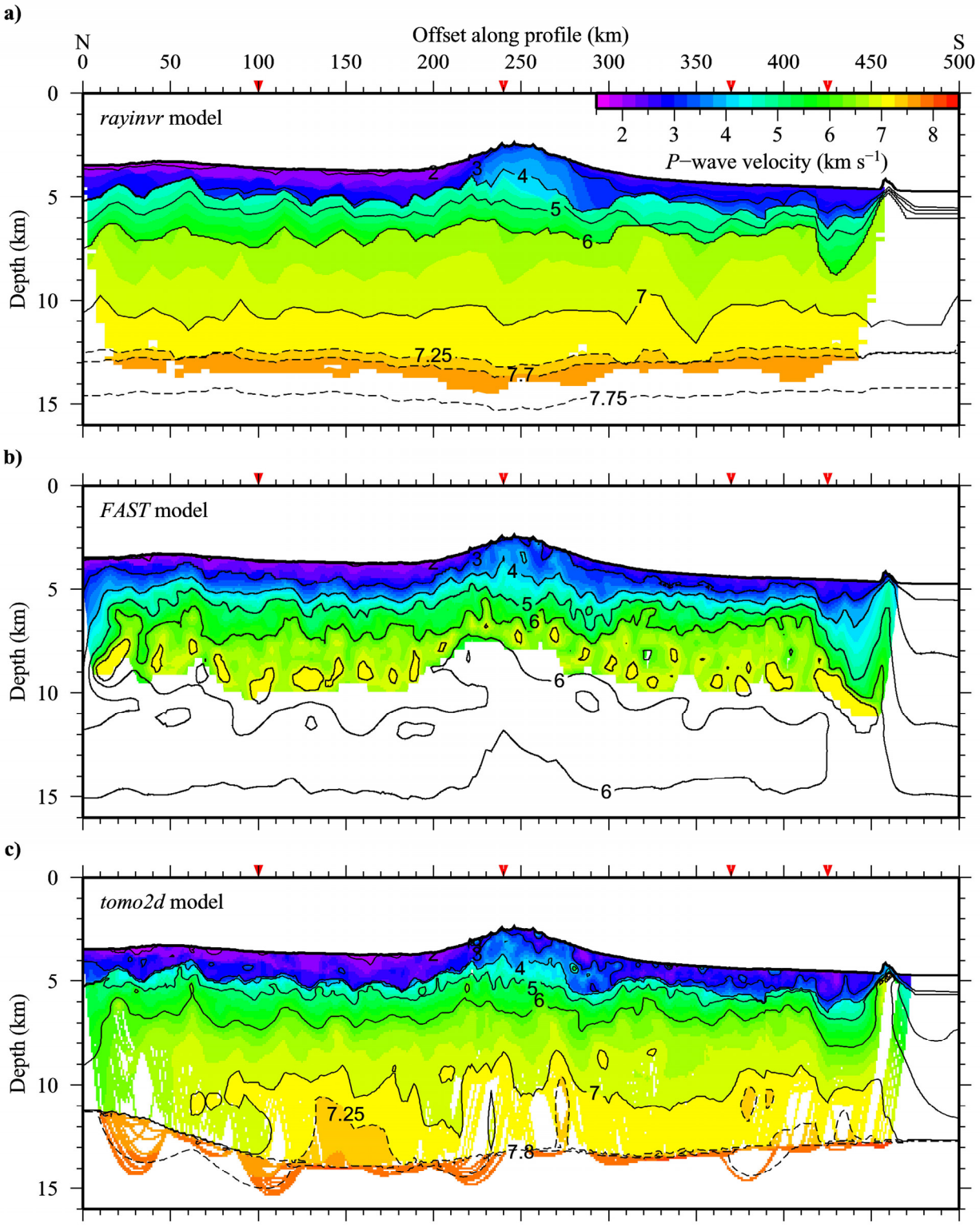

Figure 4.21 Comparison of velocity-depth models resulting from forward modelling with *rayinvr*, a), and from the inversions with *FAST*, b), and *tomo2d*, c). The *P*-wave velocity coloured shading is masked to show the extent of ray coverage. Iso-velocity contours (black lines) are plotted with a 1 km s^{-1} contour interval. The 7.25, 7.7 and 7.75 km s^{-1} contours in part a) and the 7.25 and 7.8 km s^{-1} contours in part c) (black dashed lines) highlight the velocity structure of the lower oceanic basement and uppermost mantle. The profile offset locations of the 1-D velocity-depth profiles plotted in Figure 4.22 are indicated with red arrowheads.

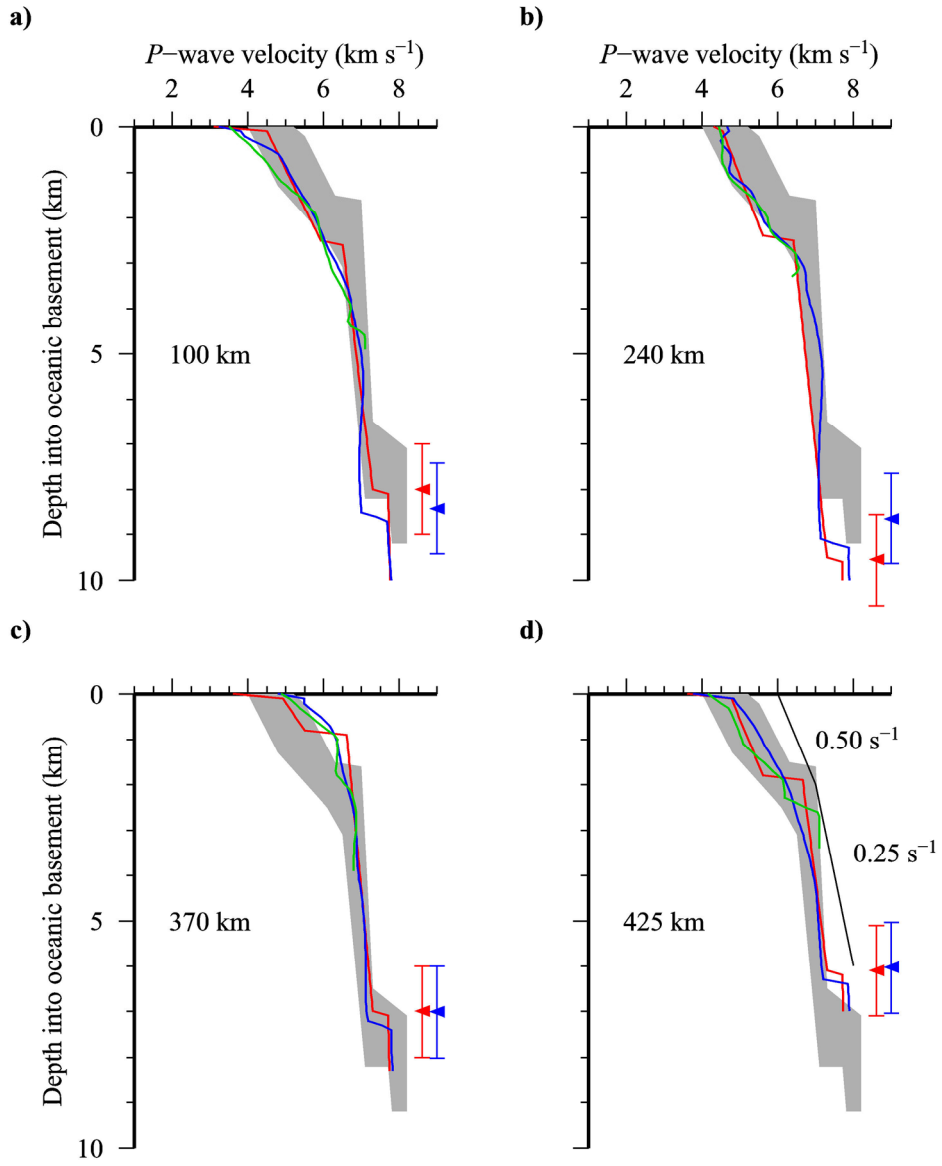

Figure 4.22 Comparisons of 1-D velocity-depth profiles taken from the *rayinvr* model (red lines), the *FAST* model (green lines) and the *tomo2d* model (blue lines). The expected range in velocity-depth structure for mature Atlantic oceanic basement is also included (grey shaded region; after White *et al.*, 1992). The depth of the Moho in the *rayinvr* and *tomo2d* models is also indicated (red and blue arrowheads with uncertainty bars, respectively). a) 100 km profile offset. b) 240 km profile offset. c) 370 km profile offset. d) 425 km profile offset. The black line shows an example of the subtle change in vertical velocity gradient between oceanic layers 2 and 3 that is often observed in the *tomo2d* model.

During the forward modelling process, modeller bias, in particular related to the expected layering structure of the oceanic basement, has resulted in a large degree of lateral smoothness, even in regions of low ray density. The *rayinvr* model has not had any unnecessarily complex lateral velocity variations incorporated as the overall aim of the modelling was to obtain the large-scale velocity structure and the location of layer boundaries for application to 3-D 'whole plate' lithospheric flexure

modelling (Chapter 5). In contrast, the inversion methods tend to incorporate variation that is below the resolution of the traveltime data due to ray path biasing. Variations to the velocity model were often applied to initially satisfy only a local reduction in traveltime misfit, but further iterations concentrated model updates in these areas, resulting in structures that were not considered geologically realistic.

The main difference between the *rayinvr* model and both the *FAST* and *tomo2d* models lies at the boundary between layer 2 and layer 3 in the oceanic basement. During the forward modelling a velocity increase of up to 1.0 km s^{-1} was included at this boundary in order to produce calculated traveltime data to match the observed P_{g2} phase traveltime data. Such an intra-basement velocity discontinuity was not similarly required by either of the two inversion methods to produce a comparable fit to the data, and instead this 'boundary' is only perceived as a decrease in the vertical velocity gradient from >0.50 s^{-1} to <0.25 s^{-1} (Figure 4.22d). Additionally, the position of the Moho and the velocity of the uppermost mantle, determined by the forward approach and with the final *tomo2d* inversion, can be considered a good match to within the uncertainties.

The *rayinvr* model was chosen as the ultimate, best-fit, 2-D velocity-depth model (henceforth referred to as the *final* model) because it was the simplest model which satisfies the data and the results of the independent inversions have confirmed that it is largely unique and free from modeller bias. Furthermore, the velocity and boundary depth uncertainties of the model are at least as low as those determined during the initial sensitivity testing (Section 3.4), except for the Moho which should now be considered to lie within ±1.0 km.

4.3 Final seismic modelling results

The seismic modelling has revealed that the oceanic crust at the Cape Verde Swell has a very similar structure to that expected of standard mature Atlantic oceanic crust (White *et al.*, 1992). The oceanic basement is, on average, 8.25 km thick and there is no direct evidence for additional undercrustal material beneath the Moho.

It is at this point worth directly comparing the *final* model with that from the pilot study of Pim *et al.* (2008) (henceforth referred to as the *Pim* model; Figure 4.23), which included the data from just nine of the OBSs.

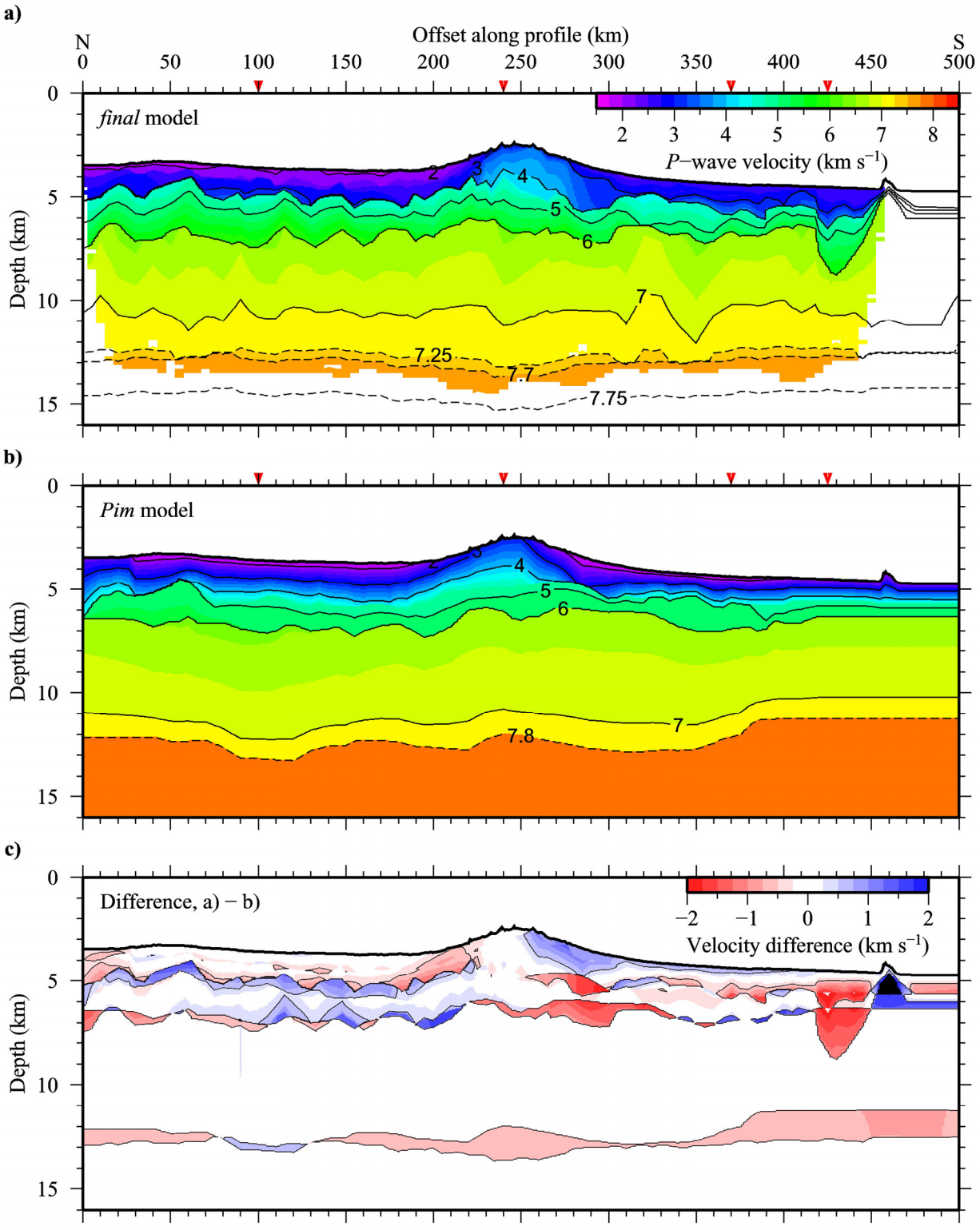

Figure 4.23 Comparison of the *final* velocity-depth model, a), with that of Pim *et al.* (2008), the *Pim* model b). Iso-velocity contours (black lines) are plotted with a 1 km s^{-1} contour interval. The 7.25, 7.7 and 7.75 km s^{-1} contours in a) and the 7.8 km s^{-1} contour in b) (black dashed lines) highlight the velocity structure of the lower oceanic basement and uppermost mantle. The profile offset locations of the 1-D velocity-depth profiles plotted in Figure 4.24 are indicated with red arrowheads. c) Difference between the *final* model and the *Pim* model. Velocity difference contours are included (black lines) at ±0.5 km s^{-1} intervals to highlight areas of significant mismatch. See text for discussion.

Figure 4.23c shows the difference between the *Pim* model and the *final* model. In general, the models are similar which in one sense is reassuring, but in another sense is somewhat surprising given the significantly fewer and more widely spaced OBSs used to derive the *Pim* model. The main differences between the two models are as follows:

1. The trade-off between the shallow subseabed and oceanic layer 2 thicknesses and velocity-depth profiles. The *Pim* model has a thicker shallow subseabed layer with a comparatively high vertical velocity gradient coupled with a thinner oceanic layer 2 with a relatively low vertical velocity gradient (Figure 4.24).
2. The roughness of the top-basement and mid-basement layer boundaries. The *final* model includes more nodes to permit a greater control on structural and lateral velocity variations that were required to fit all of the traveltime data.
3. The incorporation of all 38 OBS datasets leads to, on average, a 1-2 km deeper but less vertically varying Moho, although the vertical velocity gradient in oceanic layer 3 in both models is effectively equivalent (Figure 4.24).
4. The velocity-depth structure on the margins of the F-STR is aliased in the *Pim* model towards the locations of the two OBS that constrain its shallow subseabed structure.

Although the simpler and smoother *Pim* model is likely to be more geologically realistic considering the resolution versus depth capabilities of the various methods used to acquire and analyse the data, the denser subseabed sampling achieved by the entire dataset results in, statistically, a better fit, especially when considering layer interface geometries and velocity transitions across interfaces. Also, given the limited depth of signal penetration subseabed, the depth and geometry of the Moho in the *final* model is likely to be a more accurate representation not only of the lower crust and uppermost mantle velocity structure (and hence more definitive in terms of likely existence of lower crustal underplate/intrusion) but also Moho geometry.

A further, and probably obvious, conclusion that can be drawn is that in regions of rapid change in seabed bathymetry or likely significant lateral change in velocity and layer thickness, it is better to deploy more closely spaced instruments over and either side of such features, while for more subdued or strike-line type profiles, more

widely spaced instruments may provide more than adequate subseabed imaging and resolution at all crustal depths.

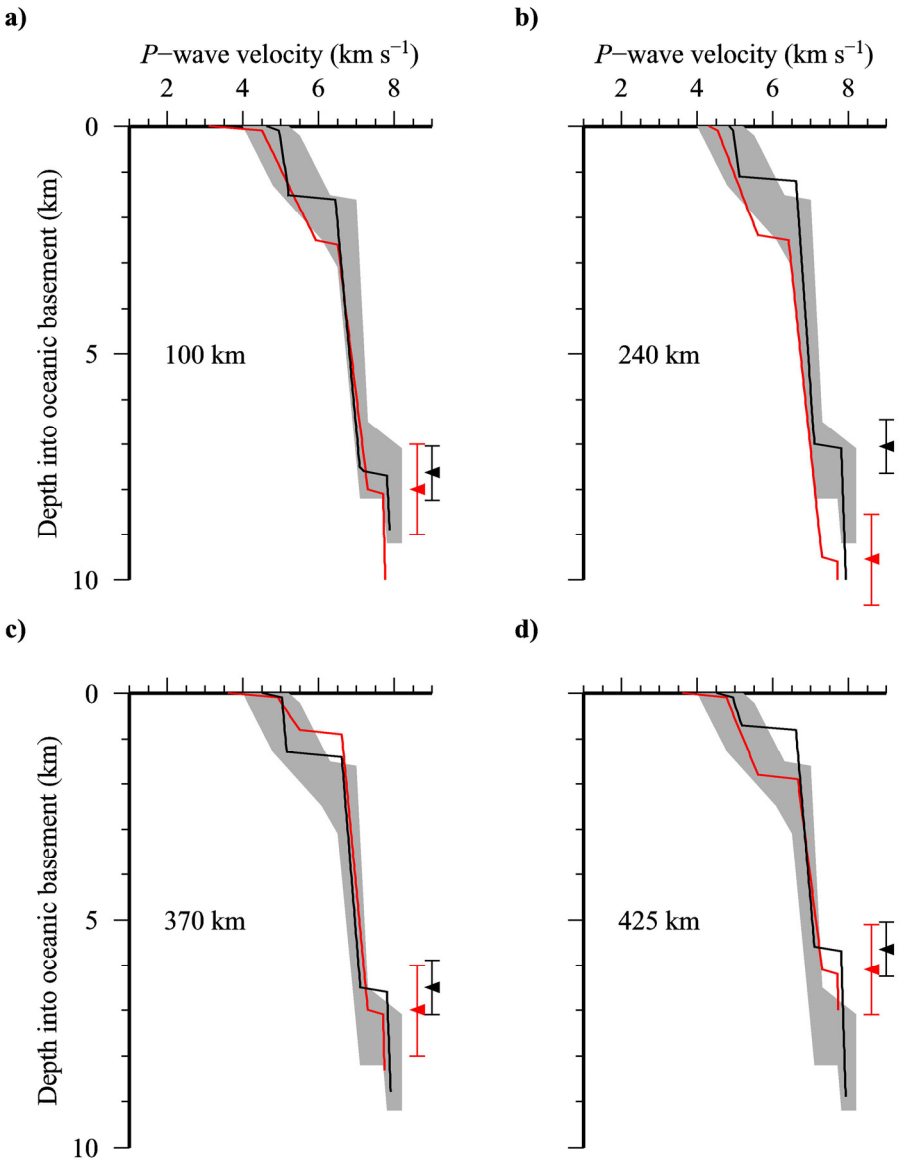

Figure 4.24 Comparisons of 1-D velocity-depth profiles taken from the *final* model (red lines) and the *Pim* model (black lines). The expected range in velocity-depth structure for mature Atlantic oceanic basement is also included (grey shaded region; after White *et al.*, 1992). The depth of the Moho in the *final* and *Pim* models is also indicated (red and black arrowheads with uncertainty bars, respectively). a) 100 km profile offset. b) 240 km profile offset. c) 370 km profile offset. d) 425 km profile offset.

4.4 Summary

Two inversion approaches have been tested and applied to the traveltime data using initial models which introduced limited modeller bias. Both the *FAST* model and the *tomo2d* model, each resulting from a series of inversions, have confirmed that the *rayinvr* model is unique and that the features that have been interpreted are clearly resolved by the observed data. The *rayinvr* model, chosen as the *final* 2-D velocity-depth model, will be used as the basis of all other modelling in this thesis. In the following chapter the *final* model will be used to constrain the results from 3-D 'whole-plate' lithospheric flexure modelling, in order to determine the rheological properties of the lithosphere, and ultimately provide an insight into the mechanism for the support of the Cape Verde Swell.

5. Modelling lithospheric flexure and gravity in 3-D

5.1 Introduction

The rheology of the oceanic lithosphere is strongly temperature dependent and as the age of the oceanic lithosphere increases, it cools, thickens and becomes stronger. A single parameter, the effective elastic thickness (T_e) is used as a proxy for the long-term (>0.1 Ma) strength of a lithospheric plate (Watts, 2001). The effective elastic thickness is roughly equivalent to the 450 °C isotherm (Watts, 2001; Figure 1.3). For oceanic lithosphere, T_e increases with age from 0 km at the mid-ocean ridge to ~40 km adjacent to the passive continental margin. The expected T_e can, thus, be predicted if the age of the plate is known. The flexural response of the lithosphere to external loading, such as by islands or seamounts, can also be analysed to reveal the apparent T_e. Any disagreement between the apparent and expected T_e would imply that the strength of the plate has been altered by a process independent of the standard mode of evolution of oceanic lithosphere (Watts & Burov, 2003).

In the region of the Cape Verde Islands the lithosphere is 120-140 Myrs old, according to the correlation of magnetic lineations with the reversal timescale of the Earth's magnetic field (Müller *et al.*, 2008). The age of the islands ranges from >20 to <3 Ma (Mitchell *et al.*, 1983; Plesner *et al.*, 2003; Duprat *et al.*, 2007; Holm *et al.*, 2008; Dyhr & Holm, 2010; Madeira *et al.*, 2010). At the time of first loading, the ~120 Ma lithosphere would be expected to have a corresponding T_e of 25-35 km, assuming a plate cooling model (Parsons & Sclater, 1977; Stein & Stein, 1992) with no external thermal influences. Two-dimensional modelling along profile P01 (Section 3.5) required a region of low density in the lithospheric mantle to reconcile the calculated gravity anomaly with the observed FAA. It is likely that such a region would result from a thermal anomaly (e.g. Robinson, 1988), which would also

reduce the T_e of the lithosphere in the region through the process of thermal rejuvenation.

In this chapter, the *final* 2-D velocity-depth model (Figure 4.23a) is used as a fixed crustal reference to constrain modelling of the 3-D flexural response of the lithosphere to the loading of the Cape Verde Islands. The flexural surfaces calculated from a suite of 3-D flexure models are compared to the crustal structure interpreted from the WA and MCS data, to determine the apparent T_e of the lithosphere in the region (Sections 5.2 & 5.3). Subsequently, as a test of the preferred flexure model, the crustal component of the FAA is calculated from a background 1-D density model and suitable load and infill densities, for comparison with the observed FAA (Section 5.4). These results will be analysed and compared to those obtained using the 2-D method to provide some insight into the mechanism that supports the anomalous bathymetry of the Cape Verde Swell (Section 5.5).

5.2 Modelling three-dimensional flexure

Before the strength of the lithosphere can be determined by a forward modelling approach, the pattern of observed subsidence must be ascertained and the volume and spatial distribution of the load must be accurately known. In the following subsections, the observed moat infill sediment thickness is determined for comparison to calculated flexural surfaces, the geometry of the driving load is obtained by filtering the bathymetry to remove the long-wavelength swell component and suitable fixed values and testable ranges are selected for the density parameters.

5.2.1 Flexural markers

The amplitude and wavelength of lithospheric flexure in response to loading is recorded by horizons in the shallow and deep subsurface, such as unconformities in the sediment column and the Moho. By assuming that the shapes of these key horizons within the seismic model are governed solely by the flexural response of the lithosphere to loading by the Cape Verde Islands, it is possible to determine the apparent T_e, and, therefore, the apparent strength of the lithospheric plate.

5.2.1.1 Angular unconformity

When the oceanic lithosphere undergoes surface loading, a flexural moat develops that acts as a depositional basin for sediments and volcaniclastic material derived

from the islands and their edifices during erosional and mass wasting processes. At the Cape Verde Islands, an angular unconformity marks the base of a succession of Miocene-to-Recent moat infill sediments and acts as a marker of the flexural subsidence that has occurred since the time of loading. The moat infill sediments correspond to the shallowest subseabed layer in the velocity-depth model for WA profile P01 (Figures 3.1 & 3.3). Although the flexural marker within the sediment column is well constrained along profile P01, by both the forward seismic modelling and the subsequent traveltime inversions, this provides only a limited, 2-D control on the amplitude and wavelength of the regional 3-D flexure.

Ali *et al.* (2003) mapped the TWTT thickness of the moat infill sediments along all available seismic reflection data in the region of the Cape Verde Islands (Figure 5.1a). Fitting a surface to these data reveals the approximate amplitude and wavelength of the basin into which the sediments were deposited (Figure 5.1b). The TWTT data were converted to true thickness using the average *P*-wave velocity of the shallowest layer in the *final* 2-D velocity-depth model, 2.1 km s^{-1}. Ali *et al.* (2003) used a larger interval velocity of ~2.8 km s^{-1}, obtained from a combination of MCS stacking velocities and DSDP site 368 velocity measurements, resulting in a greater thickness of the moat infill sediments. The thickness of the sediments presented here is considered a more reliable estimate because the interval velocity used to depth convert the TWTT map is independently constrained by the *final* 2-D velocity-depth model along profile P01.

The thickness of the moat infill sediments generally increases towards the islands (Figure 5.1c). The main depositional basin was roughly circular, centred halfway between the eastern islands of Maio and Boa Vista where the sediment thickness reaches a maximum of ~1.2 km. A secondary area of thicker deposition extends to the northwest and correlates with the location of São Nicolau, São Vicente and Santo Antão. Although the island of Fogo reaches the highest elevation in the archipelago, the infill sediments do not show a strong pattern of thickening around it. The lack of a strong flexural signature around Fogo and Brava may be due to a combination of the limited lateral extent of the submarine edifice and their young age (<3 Ma eruption ages for Brava; Madeira *et al.*, 2010) compared to the other islands.

Figure 5.2a demonstrates that the flexural marker, extracted from the moat infill sediment thickness map, is consistent with the unconformity layer boundary in the *final* 2-D velocity-depth model, except beneath the F-STR. The mismatch occurs

where the sediment thickness has been interpolated over the F-STR due to a lack of TWTT data (Figure 5.1). Additionally, the velocity-depth model indicates a high velocity region beneath the F-STR, consistent with the interpretation that it is part of the submarine edifice (Figure 3.1), giving confidence in the overall suitability of the sediment thickness map to reflect regional flexure.

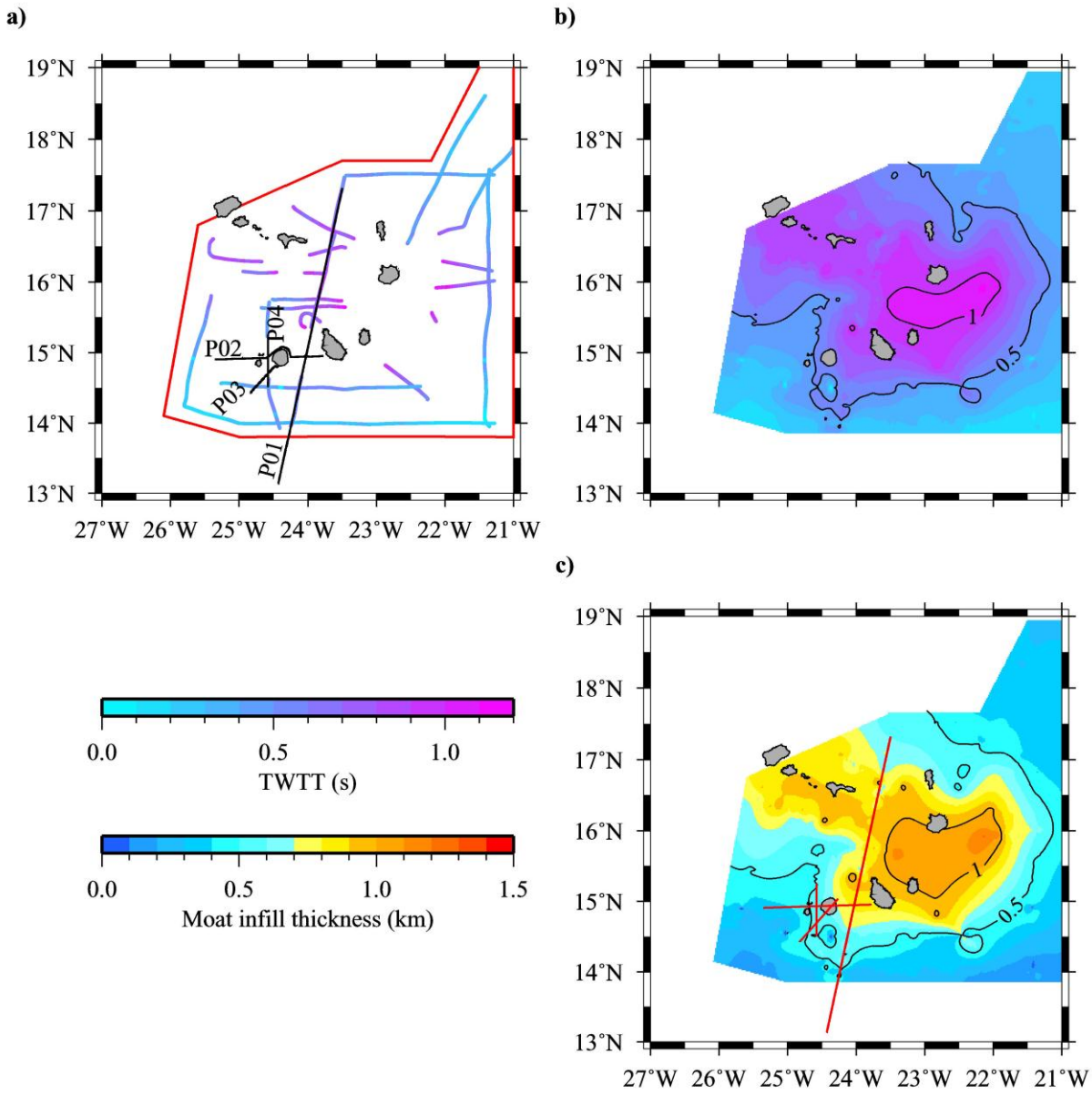

Figure 5.1 Calculation of regional moat infill sediment thickness from TWTT data. a) Distribution of the raw TWTT data for the moat infill sediments along all available seismic reflection profiles, as interpreted by Ali *et al.* (2003). Black lines show the ship track between the shot points of profiles P01, P02, P03 and P04. Red polygon indicates the area cropped after fitting a smooth surface to these data. b) Fitting a surface to the TWTT data reveals the approximate shape of the basin into which the sediments were deposited. TWTT contours (black lines) have a 0.5 s contour interval. c) The true moat infill thickness, converted from the TWTT surface using an interval velocity of 2.1 km s^{-1} obtained from the *final* 2-D velocity-depth model. Thickness contours (black lines) have a 0.5 km contour interval. Red lines show the locations of velocity-depth models for profiles P01, P02, P03 and P04. Note that for profile P02, the data recorded for shot-receiver pairs from around the north of Fogo have been modelled after projection into an east-west trending plane beneath the island.

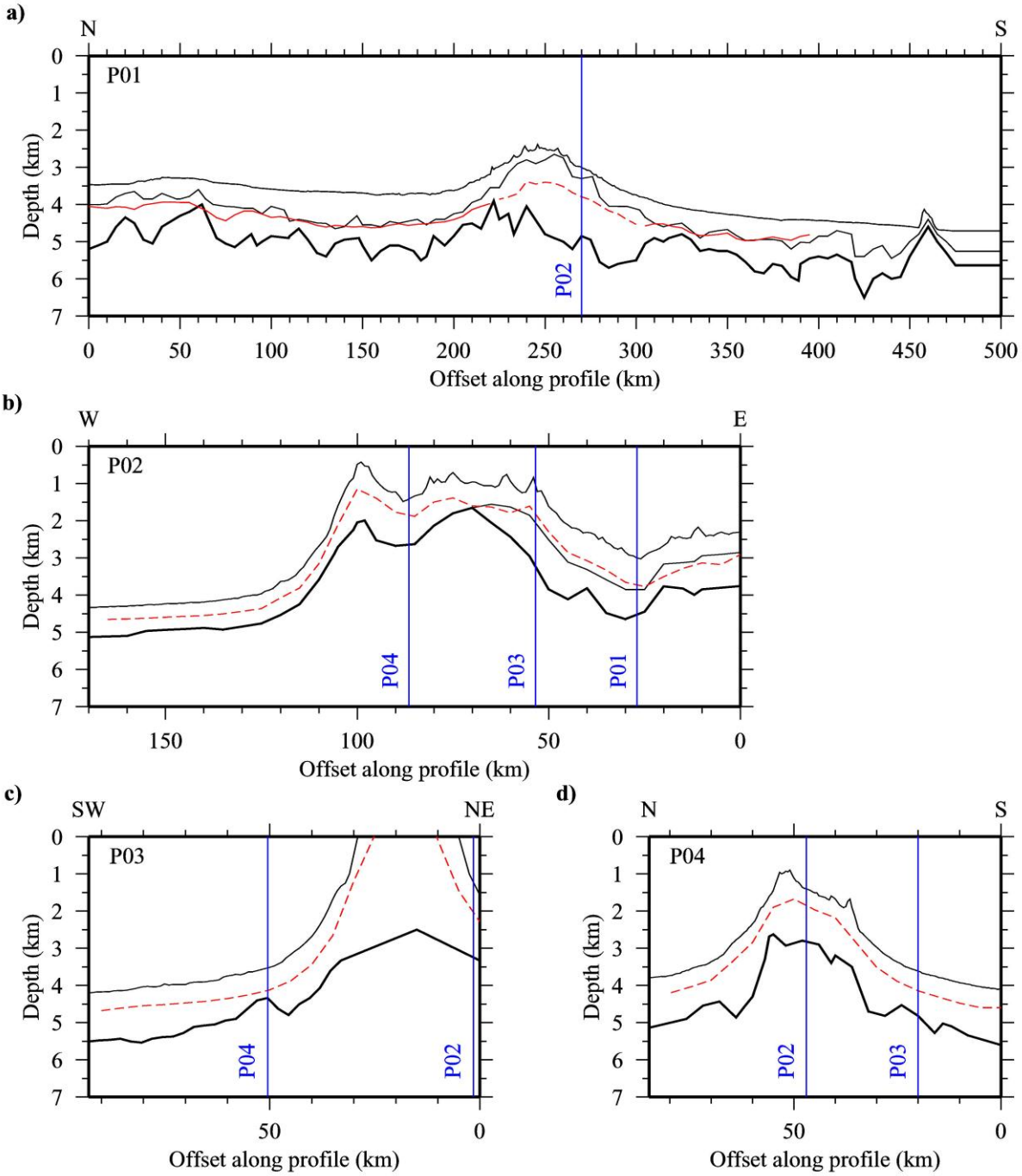

Figure 5.2 Comparison of the base of moat infill sediments flexural marker, calculated from the TWTT picks of Ali *et al.* (2003), with the corresponding layer boundaries from the velocity-depth models along profiles P01, P02, P03 and P04. Each plot shows model layer boundaries (black lines) including the top basement surface (thick black line), intersections with other profiles, as labelled (vertical blue lines) and the depth of the flexural marker below the seabed (red line, dashed where the raw TWTT data has been interpolated, Figure 5.1). a) Along profile P01 there is good agreement between the calculated flexural marker and the modelled unconformity except beneath the F-STR where sediment thickness has been interpolated. For parts b) to d), showing the shallow structure along profiles P02, P03 and P04 (modelled by Wiebke Brunn and others at IFM-GEOMAR; pers. comm.), the whole succession of sediments (including those deposited prior to island building) has been modelled as a single layer, and can only be used to demonstrate that the depth of the flexural marker does not exceed the depth of the top-basement surface.

The flexural marker was also compared to the velocity-depth models along profiles P02, P03 and P04, modelled by Wiebke Brunn and others at IFM-GEOMAR (pers. comm.; Figure 5.2b-d). These three models were created with a single subseabed layer overlying the igneous part of the oceanic crust, so they can only be used to check that the depth of the flexural marker does not exceed the total sediment thickness. The only exception to this occurs at the eastern end of profile P02, between 0 and 70 km profile offset, where the sediment column has been modelled as two layers and, in this case, the mid-sediment boundary correlates well with the flexural marker (Figure 5.2b).

5.2.1.2 Moho

If there has been no addition of undercrustal material to the base of the oceanic crust during island formation, then the Moho may act as a secondary marker of lithospheric flexure. This relies on the assumption that the thickness of the oceanic crust does not vary significantly on a regional scale and, hence, the pre-flexure Moho was at a constant depth below the seabed. The velocity-depth models for profiles P01, P02, P03 and P04 (Figure 5.3) reveal that the Moho lies between 11 and 13 km depth b.s.l. and the igneous part of the oceanic crust is ~7 km thick. An increase in the thickness of the upper crust is observed where profiles P02, P03 and P04 intersect the submarine edifice of Fogo and Brava. These areas of thicker upper crust show similarities to the high velocity region evidenced beneath the F-STR on profile P01 and reflect the influence of island building on the overall crustal structure.

In Figure 5.4, subseabed velocity-depth curves are compared for profiles P01, P02, P03 and P04 at the locations where the profiles intersect. In general, there is good agreement in Moho depth between pairs of models at their intersection. At the intersection of profiles P01 and P02 the modelled Moho depth differs by ~2.5 km. Attributing suitable uncertainties to the depth of the Moho for each model, determined following the resolution testing of the *final* 2-D velocity-depth model of profile P01, does not produce any possibility for agreement (Figure 5.4a). Given that fewer traveltime data with larger uncertainties were used to fit the Moho along profile P02, the depth of the Moho along profile P01 is considered more robust. Additionally, the Moho depth along profile P02 increases by ~2 km within 15 km of the intersection with profile P01 and, although a sharp increase in Moho depth is not geologically unrealistic, the Moho depth along profile P01 varies by < 1 km over

~500 km and is constrained by more data, giving a greater confidence in this model. Considering also that elsewhere along profile P02 the Moho is predominantly deeper by ~2 km, it seems that the depth observed along profile P01 is most consistent with all the available data.

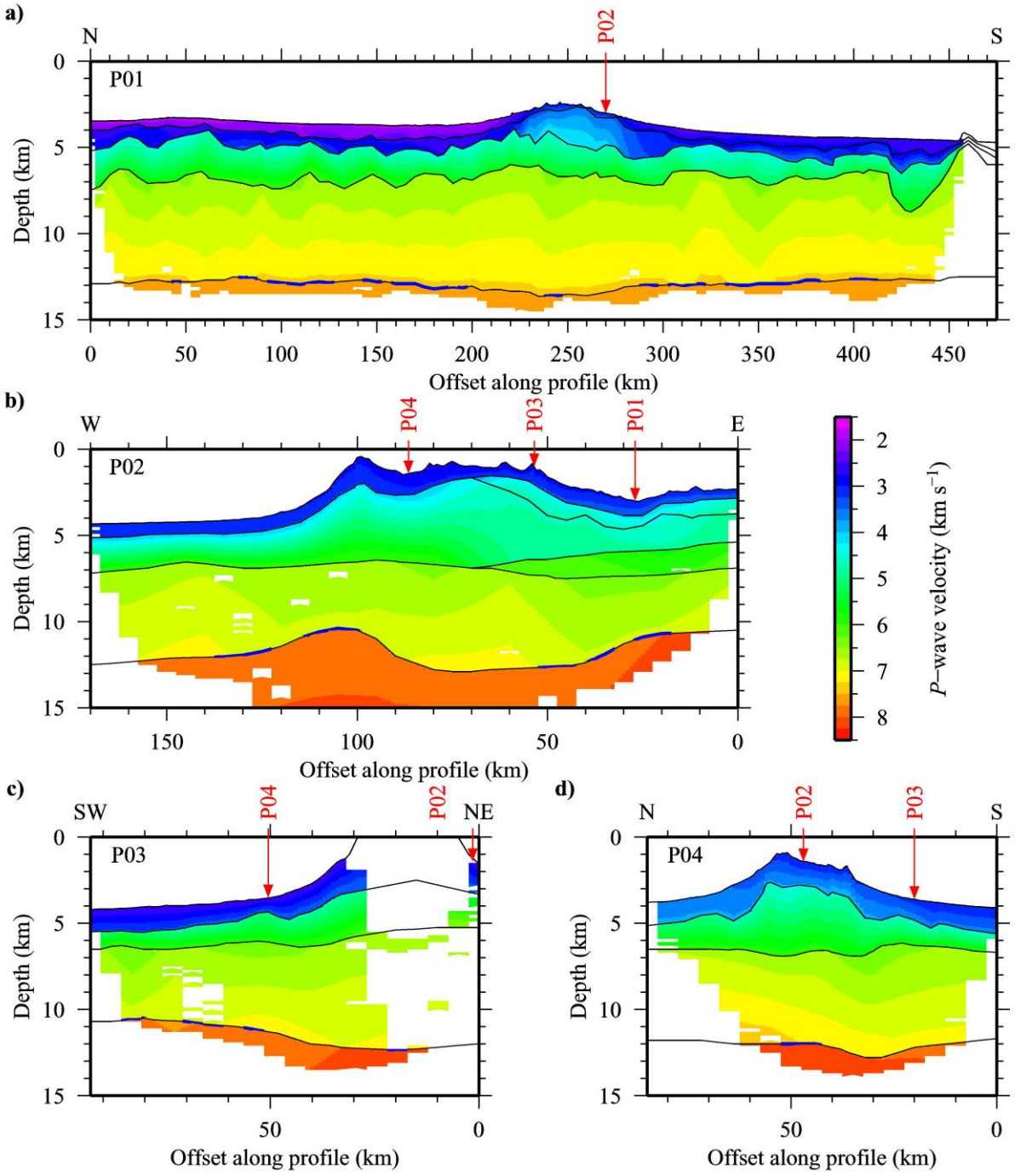

Figure 5.3 Combined layer and 2-D velocity-depth structure for WA profiles P01, P02, P03 and P04. The boundary surfaces of the models are shown (black lines). The *P*-wave velocity (coloured shading) is masked to show the extent of ray coverage. Blue shading on the Moho indicates the regions constrained by P_mP arrivals. Intersections with other profiles, as labelled, are also indicated (red arrows). a) Profile P01. b) Profile P02. c) Profile P03. d) Profile P04. The models shown in parts b) to d) were produced by Wiebke Brunn and others at IFM-GEOMAR (pers. comm.).

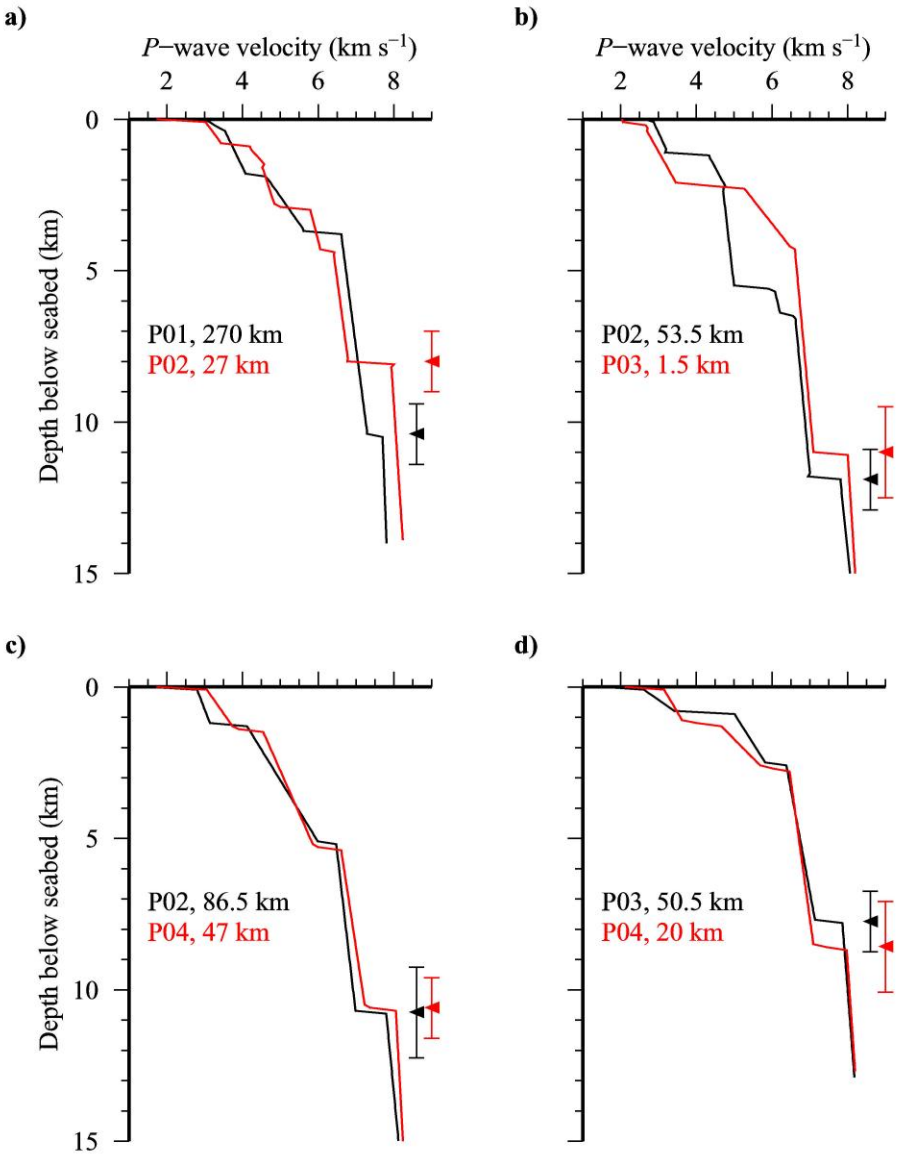

Figure 5.4 1-D velocity-depth profiles from the intersections between 2-D velocity-depth models. See Figure 5.3 for the locations of intersections. a) Comparison of the velocity structure of profile P01 at 270 km profile offset (black line) with that of profile P02 at 27 km profile offset (red line). Arrowheads with error bars represent the modelled Moho depth and associated uncertainties for profile P01 (black) and P02 (red). b) Profile P02 at 53.5 km profile offset (black line) and profile P03 at 1.5 km profile offset (red line). c) Profile P02 at 86.5 km profile offset (black line) and profile P04 at 47 km profile offset (red line). d) Profile P03 at 50.5 km profile offset (black line) and profile P04 at 20 km profile offset (red line).

There are also some discrepancies in the crustal velocity structure at the intersection of P02 and P03 (Figure 5.4b). These differences may result from the modelling of out-of-plane traveltime data that were picked from off-line shots where the ship track for profile P02 was diverted to the north around Fogo, between 51 and 87 km profile offset (Figure 5.1a).

Although there is significant variation in the total crustal thickness, large increases are concentrated along profiles P02, P03 and P04 in the vicinity of the islands, where the addition of undercrustal material may have occurred during island growth. Such modification to the depth of the Moho since loading prevents these models from being used to constrain the pattern of modelled flexure. The thickness of the crust along profile P01 shows comparatively little variation (Section 3.2) and so the Moho along profile P01 will be used a secondary assessment of the flexure calculated during modelling. Figure 5.3a shows that the Moho along profile P01 is almost horizontal, suggesting that there has been very little flexure. Low amplitude flexure would be expected if the lithosphere is anomalously strong or if the subsidence due to surface loading has been partially counteracted by uplift attributed to an opposing, upwards-acting force.

5.2.2 Defining the load

In order to accurately define the volume and spatial distribution of the load driving flexure, it is necessary to isolate the Cape Verde Islands and their submarine edifices from the regional bathymetric swell by removing the long-wavelength signature from the observed bathymetry. Ali *et al.* (2003) tested a range of median filters and found that a filter of width 500 km best described the swell. A directional median filter that removes short-wavelength bathymetric features from long-wavelength regional gradients has since been developed (Kim & Wessel, 2008), for the specific application of separating volcanic islands from regional swells.

In order to determine the optimum filter to separate the short-wavelength driving load from the long-wavelength regional swell, both the median filter and the directional median filter were tested using a series of filter widths, following the method detailed by Kim & Wessel (2008). The filter was applied over a large region, extending beyond the area of interest containing the flexural markers by half of the maximum filter width (250 km) to avoid the introduction of edge effects caused by uneven sampling. After removing the long-wavelength regional bathymetric swell determined by each filter, the ratio of driving load volume to footprint area was calculated and plotted against filter width (Figure 5.5b). The peak on each curve, the maximum ratio of load volume to footprint area, occurs at the optimum filter width. A median filter of width 300 km and a directional median filter of width 240 km were found to be the optimum filter widths. Both filters achieve the best statistical

separation of regional swell from island load and are similar on a large scale (Figure 5.5c & d), showing a slight curve in the swell peak towards the southwest. However, the shape of the swell differs at medium wavelengths of 50-100 km. This mismatch is most apparent at 16° 00' N 23° 30' W, where the median filter has extracted a dome with amplitude ~0.5 km but the directional median filter has produced no such feature. The swell described by each optimum filter is compared in Figure 5.5e to the observed bathymetry along a north-south profile at 23° 30' W. The directional median filter of width 240 km has accounted for the regional swell throughout, but the median filter of width 300 km has overestimated the swell height in the proximity of the islands. Application of a longer wavelength median filter, for example a width of 500 km as used by Ali *et al.* (2003), reduces the effect of the islands on the maximum swell amplitude but does not accurately reproduce the shape of the swell (see Ali *et al.*, 2003, Figure 9). Following this assessment, a directional median filter of width 240 km was chosen to represent the long-wavelength regional bathymetry of the Cape Verde Swell.

Figure 5.5 Extraction of the long-wavelength component of bathymetry on a regional scale. For parts a), c) and d): the bathymetry along a north-south trending profile (black line A-A') is shown in part e); bathymetry contours in the range 3.0 to 5.5 km (black lines) with a 0.5 km contour interval. a) The GEBCO 1' (IOC, IHO & BODC, 2003) bathymetry of the region encompassing the Cape Verde Swell. b) Determination of optimum filter widths, from peaks on the curves of the ratio of residual load volume to footprint area for a median filter (red line and triangles) and a directional median filter (blue line and circles). c) Bathymetry of the long-wavelength regional swell using a median filter of width 300 km. d) Bathymetry of the long-wavelength regional swell using a directional median filter of width 240 km. e) Comparison of the raw and filtered bathymetry for each of the optimum filter widths at 23° 30' W. The directional median filter of width 240 km (blue line) makes an excellent interpolation of the long-wavelength component of the raw bathymetry (black line) beneath the submarine edifice between Santiago and Maio. In comparison, the median filter of width 300 km is still heavily influenced by the topography of the islands and their edifices and the swell height at 16° 00' N is overestimated by >0.5 km.

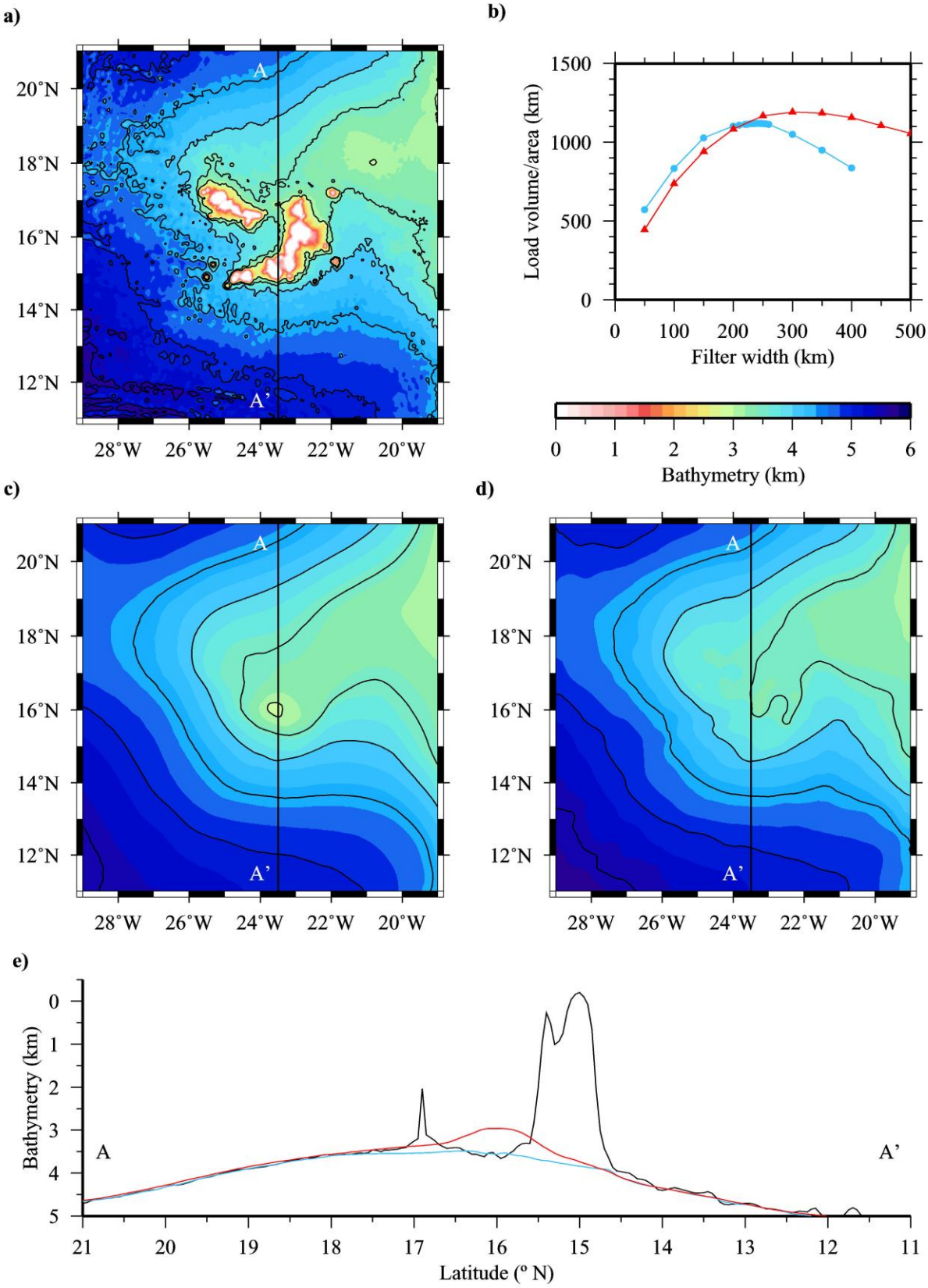
a)
b)
c)
d)
e)
A
A'
20°N
18°N
16°N
14°N
12°N
28°W
26°W
24°W
22°W
20°W
Load volume/area (km)
1500
1000
500
0
0
100
200
300
400
500
Filter width (km)
0
1
2
3
4
5
6
Bathymetry (km)
Bathymetry (km)
Latitude (° N)
21
20
19
18
17
16
15
14
13
12
11

Figure 5.6a reveals the topography of the island load after the swell has been removed from the bathymetry. Where the topography of the load was <0 m it was clipped to 0 m to prevent small loads with positive buoyancy from influencing the calculated pattern of downwards flexure. The 300 m contour, which was used to test the ratio of load volume to footprint area, as described above, provides an outline of the driving load, which comprises the islands and their submarine edifices. The two distinct components of the load, the linear chain of islands to the northwest and the curved chain to the east, are situated over the areas of thickest moat infill sediments (Figure 5.6b). Interestingly, the sediments appear to be slightly offset to the east, and also to the south in the case of the northwest chain, in comparison to the island distribution suggesting that there have been additional external influences to the shape of the flexural basin.

As a final preparation, the model was shifted downwards by 3.9 km, corresponding to the average bathymetry of the swell in the sub-region where the island load is concentrated (Figure 5.6c). Inside the region of interest, the difference between load bathymetry and observed bathymetry is generally <0.5 km, except to the southwest at the edge of the swell crest where the observed bathymetry increases towards 5 km b.s.l. while the load bathymetry remains constant at 3.9 km b.s.l. (Figure 5.6d). Setting the load to its average depth has greatest effect on the aerial extent of the islands, and it should be noted that over the islands to the southwest the calculated gravity anomaly (Section 5.4) will subsequently be slightly overestimated (by up to 15 mGal), and similarly underestimated for those to the northeast, as the extent to which they emerge above sea level is larger and smaller than in reality, respectively.

Figure 5.6 Definition of the driving load, comprising the Cape Verde Islands and their submarine edifices, and preparation of the load for subsequent flexure modelling. a) Topography of the driving load following the removal of the long-wavelength regional swell derived by the directional median filter of width 240 km. The footprint area of the load is described by the 0.3 km contour (black line). The subregion used when considering the results of flexure modelling is also shown (red box). b) The footprint area of the driving load (black line) is situated over the areas of highest moat infill sediment thickness. c) The bathymetry of the driving load as prepared for input to the flexural modelling program, *topo2grv*, by incorporating a static shift of -3.9 km, corresponding to the average bathymetry of the swell in the sub-region. The load footprint area (black line) and sub-region for flexure modelling (red box) are shown. d) Difference between the actual swell bathymetry and the average depth (3.9 km b.s.l.) used for the input for *topo2grv*. For most of the driving load, (grey shaded region) the average depth fits the observed to ±0.5 km.

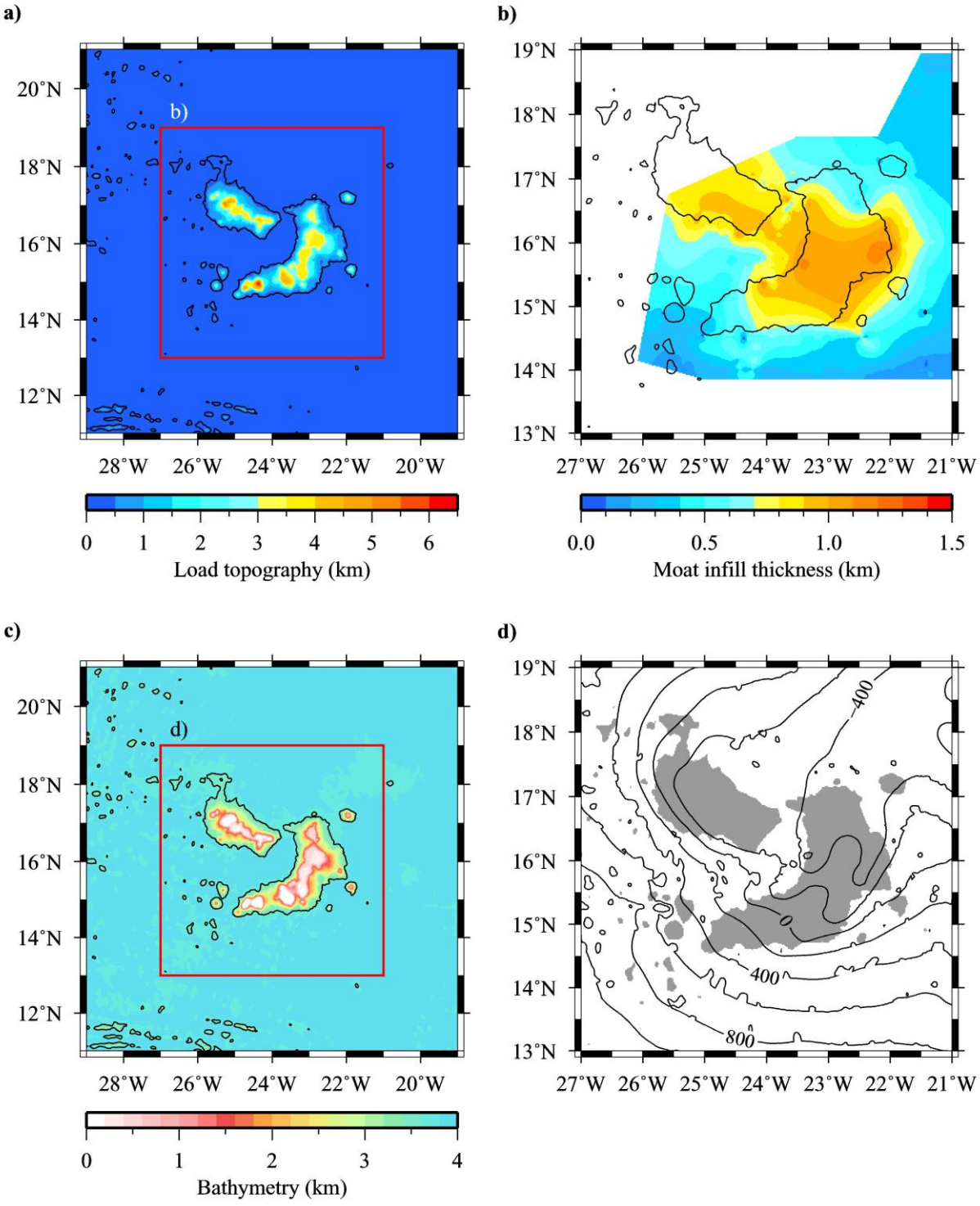

5.2.3 Modelling flexure with *topo2grv*

The 3-D flexural and gravity calculations were made using *topo2grv*, which was modified by Tony Watts in 2005 and is based on earlier versions of the program (mprg2 – J.R. Cochran, 1982; g3dgrid – W.H.F. Smith, 1986). The program calculates the amplitude and spatial distribution of subsidence caused by a load of

known shape, volume and density emplaced upon a lithospheric plate of specified strength. Following the flexural calculation, the gravity anomaly of the resulting model is determined (Section 5.4) using an array of densities specified for the water column, the mantle, a two-layer crustal model and the material that infills the basin created during flexure.

5.2.3.1 Density of the crust

A 1-D density model was constructed, following the method used to create the block density model of Section 3.5, to represent the average oceanic crust in the region prior to loading and flexure. Due to modelling constraints, the density model was further simplified into a two-layer crust. The first layer has a thickness of 0.65 km and a density of 2200 kg m^{-3}, and represents the pre-existing Cretaceous-to-Miocene sediments. The second layer has a thickness of 7.60 km and a density of 2850 kg m^{-3}, and represents the entire igneous section of the crust.

5.2.3.2 Driving load density

The load is predominantly composed of medium-to-high density igneous material that was magmatically emplaced onto the crust during island building. The density of the igneous part of the oceanic crust ranges from 2500 to 3000 kg m^{-3}, with an average value in this region of 2850 kg m^{-3}, and the core component of the load is expected to have a similar density. During island growth, particularly in a subaerial environment, erosional processes rework material derived from the volcanic edifices, depositing it down-slope. Such erosional and mass wasting deposits also contribute to the total load driving flexure, although this material would have a lower bulk density as porosity increases during reworking. Overall, the load is expected to have an intermediate density of ~2700 kg m^{-3}. A range of load densities from 2200 to 2900 kg m^{-3} were, therefore, tested for each value of T_e to determine the best-fit.

5.2.3.3 Sediment and moat infill densities

During flexural modelling, the primary load driving the flexure of the lithospheric plate comprises the islands and their edifices, as defined in Section 5.2.2. Additionally, the material that fills the flexural moat created by the primary load acts as a secondary load and will, itself, contribute to the total flexure. Hence, the density of the infill material must be well constrained to accurately model the flexure. In the *final* 2-D velocity-depth model, the moat infill sediments have an average *P*-wave

velocity of ~2.1 km s^{-1}, which corresponds to a density of ~2000 kg m^{-3} using the velocity-density relationship described in Section 3.5.2.2.

For *topo2grv*, the density of the infill material may only be defined by a constant value. In reality, the material filling the flexural depression beneath the surface expression of the load will also be part of the driving load with a density matching that of the load itself, whereas elsewhere this material will have a much lower density, matching that of the moat sediments. If the density of the infill material is set to match the load density then the calculated flexure will be an overestimate. Conversely, if the density of the infill material is set to match the density of the moat sediments then the total load beneath the islands and the resulting flexure will be underestimated. These two methods consequently represent end-member cases, and for a set load density and plate strength, will predict the minimum and maximum amount of flexure. Assessing the ratio of the volume of infill material beneath the load to the total volume of infill material, will allow a representative intermediate density to be assigned to the moat infill leading to the best-estimate of the flexural response of the lithosphere to loading.

5.2.4 Flexure results

For each of the three methods of infill density parameterisation, the amplitude and wavelength of flexure in response to the driving load was calculated for a range of different load densities (every 100 kg m^{-3}, from 2200 to 2900 kg m^{-3}) and plate strengths defined by the T_e parameter (every 10 km, from 0 to 70 km) with limits chosen to reflect the range expected for oceanic lithosphere. The calculated flexure was compared to the observed thickness of moat infill sediments and the rms misfit was assessed to determine the best-fit load density and T_e parameter pair. Additionally, the calculated flexural surface along profile P01 was compared to the shape of the seismically determined Moho to ensure a fit within the uncertainties.

5.2.4.1 Constant load and infill density

For the first suite of flexure calculations the density of the infill material was equated to the density of the load. This choice of infill density will produce the maximum possible flexure for a given T_e and load density combination and will allow a comparison to be made with the results of Ali *et al.* (2003) where constant values for both the load and infill densities were also used. Analysis of the rms misfit between

modelled flexure and observed moat infill thickness (Figure 5.7a) reveals a minimum for load densities of 2200 to 2400 kg m^{-3}, coupled with a high T_e of 40 to 50 km. The rms misfit between the modelled and observed Moho along profile P01 (Figure 5.7b) is also lowest at similarly low values of load density, but shows no clear distinction between values of T_e.

The spatial variation in calculated flexure for the best-fit parameter pair, a load density of 2300 kg m^{-3} and a T_e of 50 km (Figure 5.7c), reaches a maximum of ~1 km in a roughly circular area of maximum flexure that is offset slightly to the west compared to the observed moat infill thickness (Figure 5.1c). The difference between the modelled flexure and observed moat infill thickness (Figure 5.7d) is <0.2 km over most of the region, within twice the seismic uncertainties (criteria used for model sensitivity testing, see Section 3.4) of this boundary along profile P01. Larger amplitude mismatches (0.2-0.5 km) occur to the east and the west of the area of maximum flexure and are due to the offset mentioned above. Ali *et al.* (2003) also found that a high T_e (~50 km) was necessary to produce a fit to the observed moat infill thickness using a model solely incorporating downwards-acting loads. The implications of a high apparent T_e are discussed further in Section 5.3.

Figure 5.7e compares the top and base of the crust resulting from the calculated flexure to the seismically determined unconformity and Moho along profile P01. For the best-fit load density–T_e pair of 2300 kg m^{-3} and 50 km, there is a good level of agreement in the shape of the calculated and observed surfaces. In comparison, calculation using a load density–T_e pair based on the expected properties of the load and the lithosphere (2700 kg m^{-3} and 30 km), shows the resulting flexure is up to 2 km greater than the observed model layers.

Figure 5.7 Summary of flexure calculated using a constant load and infill density. a) Rms misfit between observed moat infill sediment thickness and calculated flexure within the range of tested load densities and values of T_e. Misfit contours (black lines) with a 0.05 km interval. The best-fit and expected parameter pairs are indicated (blue and red dots, respectively). b) Rms misfit between the seismically determined Moho and the base of the flexed crust along profile P01. Misfit contours (black lines) with a 0.05 km interval. c) Regional flexure calculated for the best-fit parameter pair. Flexure contours (black lines) with a 0.5 km contour interval. The location of profile P01 (black line) is also shown. d) Difference between observed moat infill sediment thickness and the best-fit calculated flexure masked according to the presence of observed data. Positive values indicate areas where the calculated flexure underestimates the observed thickness. Difference contours (black lines) with a 0.2 km contour interval. e) Comparison of the flexure calculated crust with the seismically determined layer boundaries along profile P01. The seabed (black line), unconformity and Moho (grey bands including uncertainty) from the *final* 2-D velocity-depth model are compared to the driving load (orange shading) and the top and base of the 1-D model of the crust resulting from the flexure calculation for the best-fit and expected (based on plate age) parameter pairs (blue and red lines respectively). See text for discussion.

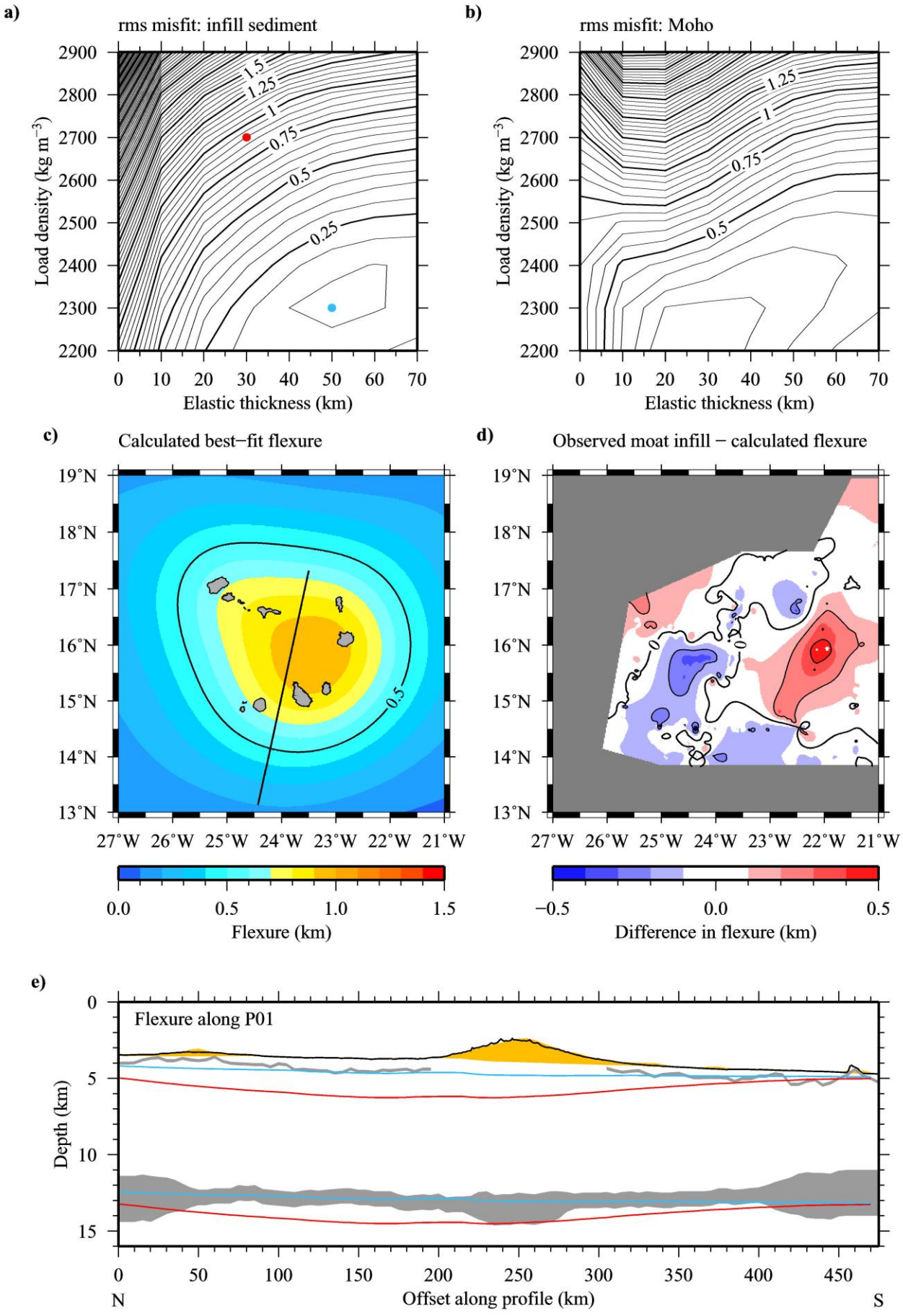
a)
rms misfit: infill sediment
Load density (kg m^{-3})
Elastic thickness (km)
b)
rms misfit: Moho
Load density (kg m^{-3})
Elastic thickness (km)
c)
Calculated best−fit flexure
Flexure (km)
d)
Observed moat infill − calculated flexure
Difference in flexure (km)
e)
Flexure along P01
Depth (km)
N
Offset along profile (km)
S

Using this method, a low load density is necessary to reduce the mass of the total load (islands plus infill material) and, hence, the amplitude of flexure but this is inconsistent with petrological studies of the composition of the islands (e.g. Stillman *et al.*, 1982). Considering that the best-fit load density (2300 kg m^{-3}) is closer to the sediment density (2000 kg m^{-3}) than that of the expected load density (2700 kg m^{-3}; e.g. Minshull & Charvis, 2001) it appears that a model with low density infill material may provide a more appropriate solution.

5.2.4.2 Low density infill material

During the second suite of flexure calculations a density of 2000 kg m^{-3} was assigned to the infill material, according to the density of the infill moat sediments determined from the *final* 2-D velocity-depth model. The rms misfit between modelled flexure and observed moat infill thickness (Figure 5.8a) is generally reduced and shows a broader minimum zone, demonstrating a correlation between increasing load density and increasing T_e that favours values of T_e >40 km and load densities between 2500 and 2900 kg m^{-3}. In contrast, the rms misfit between the modelled and observed Moho along profile P01 (Figure 5.8b) is largely insensitive to both the T_e and the load density, and does not reduce the range of model parameter pairs that are acceptable within the seismic uncertainties.

The spatial variation in calculated flexure for the best-fit parameter pair, a load density of 2800 kg m^{-3} and a T_e of 60 km (Figure 5.8c), is very similar to the best-fit result using the previous method as is the corresponding difference to the observed moat infill sediment thickness. Flexure is accommodated over a broader area and reaches a slightly larger maximum amplitude of ~1.1 km due to the higher values of T_e and load density compared to the result obtained using the previous method.

A load density of 2800 kg m^{-3} fits within the range of densities expected for the islands, but the T_e is twice as large as predicted, based on the age of the lithosphere at the time of loading. As the infill density is much lower, there is less difference in the flexure produced by the best-fit and the expected parameter pairs. Along profile P01 (Figure 5.8e) the expected parameter pair (2700 kg m^{-3}, 30 km) only overestimates the flexure by up to 0.5 km compared to the best-fit pair (2800 kg m^{-3}, 60 km).

Figure 5.8 Summary of flexure calculated using a low density for the infill material, matching the density of the moat sediments. See Figure 5.7 for details.

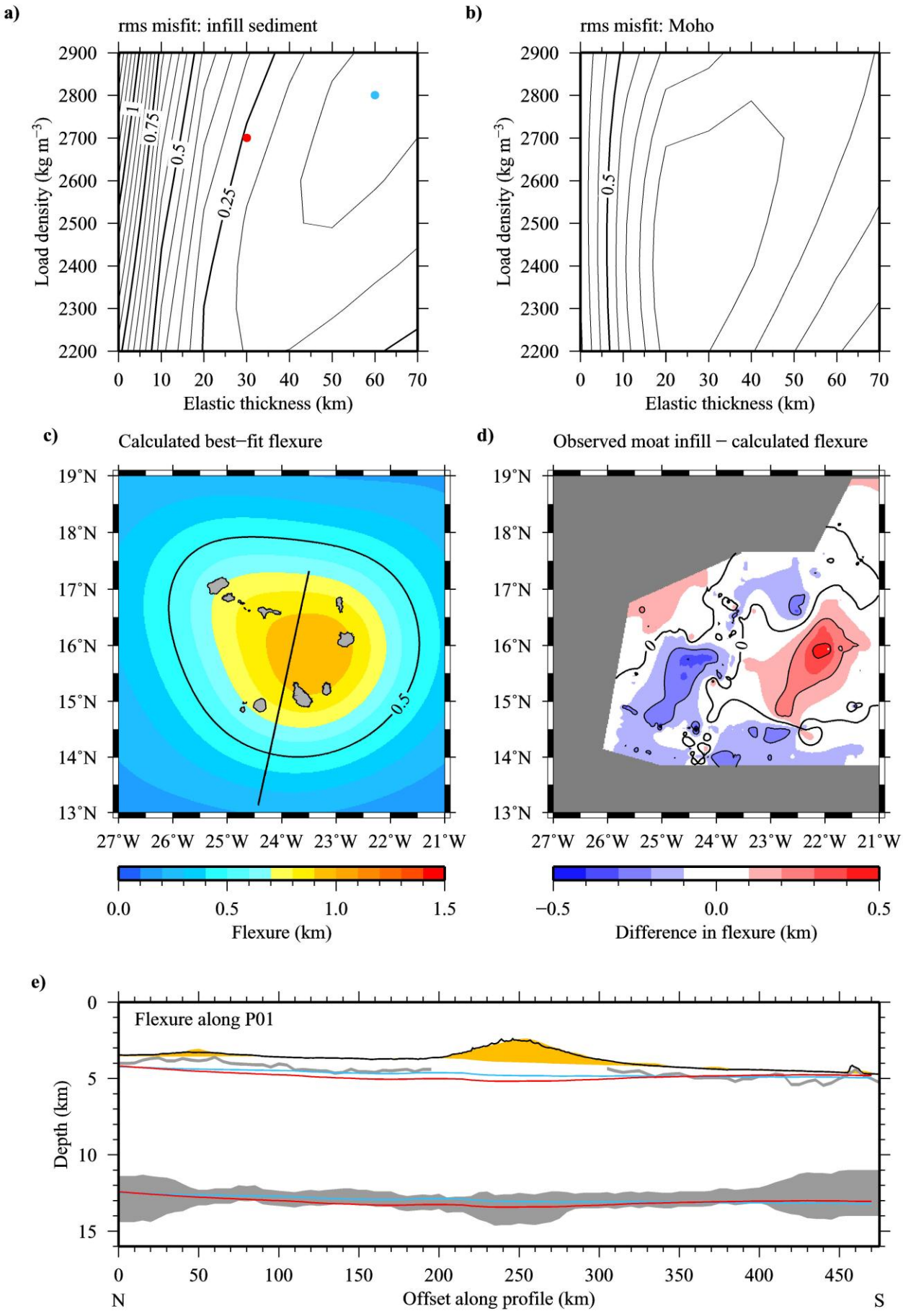
a)
rms misfit: infill sediment
Load density (kg m^{-3})
Elastic thickness (km)
b)
rms misfit: Moho
c)
Calculated best−fit flexure
Flexure (km)
d)
Observed moat infill − calculated flexure
Difference in flexure (km)
e)
Flexure along P01
Depth (km)
Offset along profile (km)
N
S

The results obtained using this method represent the minimum flexure associated with each parameter pair because the overall magnitude of the load is underestimated. Prior to the final suite of flexure calculations, an intermediate infill density will be determined to produce the best representation of the total magnitude of the load.

5.2.4.3 Intermediate density infill material

It is not possible to incorporate spatial variation of the density of the infill material within *topo2grv*. Instead, the proportion of infill material beneath the footprint of the driving load was calculated, as a fraction of the total volume, in order to set an intermediate density that would better reflect the mass of the total load. The fraction of infill material situated directly beneath the load is controlled by the strength of the lithosphere and a summary is presented in Table 5.1. When the lithosphere is weaker, high-amplitude, short-wavelength flexure is concentrated below the driving load, and in this case it is appropriate to set the infill density to a value that is similar to the density of the load. For stronger lithosphere, low-amplitude, long-wavelength flexure occurs over a broad region with the infill material predominantly consisting of sediments, and hence a low density, similar to that of the moat infill sediments, is more representative of the infill material as a whole.

Table 5.1 Summary of the fraction of infill material located beneath the footprint of the surface load for each value of T_e used to determine the intermediate density of the infill material.

T_e (km)	Fraction of infill beneath load, F_{load}
0	0.80
10	0.59
20	0.43
30	0.35
40	0.30
50	0.27
60	0.24
70	0.23

Up to this point, only the flexural response to end-member total load masses has been calculated for each value of T_e. In this third suite of flexure calculations the infill density is set to an intermediate value between each load density and the moat infill sediment density determined from the *final* 2-D velocity-depth model. For each

choice of T_e, the infill density (ρ_{infill}) was calculated using the fraction (by volume) of infill material beneath the driving load (F_{load}) to control the relative contribution from the load and sediment densities (ρ_{load} and ρ_{seds}) according to the following equation:

$$\rho_{\text{infill}} = \rho_{seds} + F_{load}(\rho_{load} - \rho_{seds}) \quad \textbf{(5.1)}$$

The rms misfit between modelled flexure and observed moat infill thickness (Figure 5.9a) shows a correlation between increasing load density and increasing T_e, similar to that found using a low density for the infill material, and reaches a minimum at a T_e of 60 km and a load density of 2600 kg m^{-3}, corresponding to an infill density of 2144 kg m^{-3}. Also, the rms misfit between the modelled and observed Moho along profile P01 (Figure 5.9b) again fails to provide any further constraint on the range of parameter pairs that produce an acceptable fit.

As the best-fit load density of 2600 kg m^{-3} is slightly lower than expected (Section 5.2.3.2), the preferred model, chosen to match the observed flexure within the broad minimum zone of rms misfit, is for a load density of 2700 kg m^{-3}, representing basaltic ocean island material, coupled with a T_e of 60 km.

5.3 Elastic thickness of the lithosphere

The preferred model of flexure, and all of the best-fit models produced using the three different parameterisation methods for the density of the infill material, required a T_e of 50-60 km that greatly exceeds the expected range of 25 to 35 km, based on the age of the lithospheric plate at the time of loading. Ali *et al.* (2003) obtained a similar result using a constant load and infill density method, which was necessary in order to produce sufficiently large amplitudes of flexure to match their greater thickness of moat infill sediments that had been calculated using a larger interval velocity.

Figure 5.9 Summary of flexure calculated using an intermediate density for the infill material, determined from a weighted average of the density of the moat sediments and the density of the load (see Table 5.1). See Figure 5.7 for details. Note that in c) the regional flexure is that calculated for the preferred parameter pair. Additionally, the parameter pair and flexure calculated crust for the preferred model (green dot and lines, respectively) are shown in parts a) and e).

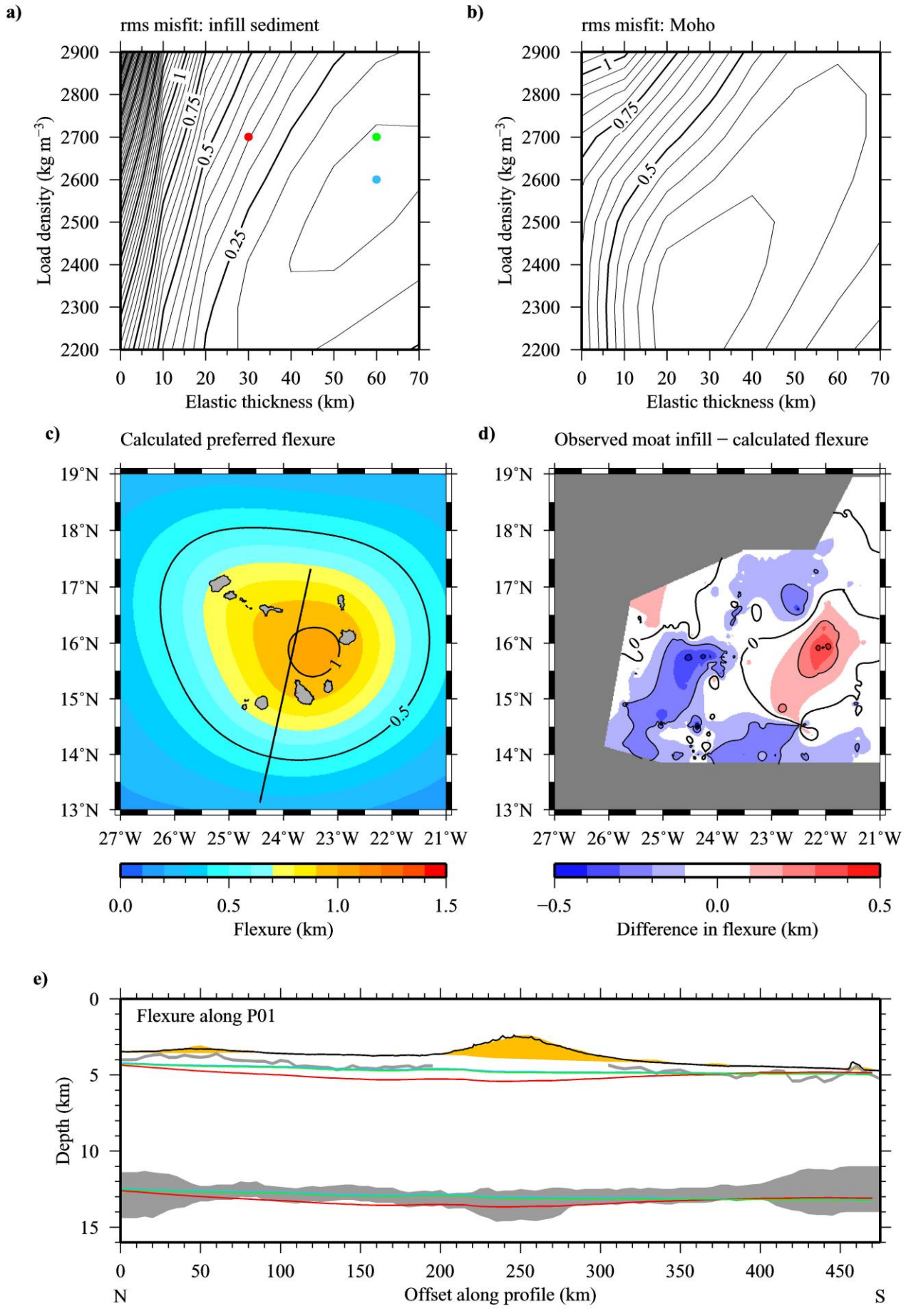
a)
rms misfit: infill sediment
Load density (kg m^{-3})
Elastic thickness (km)
b)
rms misfit: Moho
Load density (kg m^{-3})
Elastic thickness (km)
c)
Calculated preferred flexure
Flexure (km)
d)
Observed moat infill − calculated flexure
Difference in flexure (km)
e)
Flexure along P01
Depth (km)
N
Offset along profile (km)
S

It is not possible for the inherent strength of the plate to have reached a higher value than predicted by conductive cooling alone, as the lithosphere is unable to cool and thicken beyond the generally accepted rate (Stein & Stein, 1992). Instead, the high apparent strength, greater than that expected based on the plate age, could be attributed to external, sub-crustal or sub-lithospheric forces that provide buoyant support to the surface load.

5.3.1 Constant T_e

If it is assumed that the T_e of the lithosphere was 30 km at the time of loading, as predicted from plate cooling models (Parsons & Sclater, 1977; Stein & Stein, 1992), the excess flexure calculated using the surface loading models could be counteracted by subcrustal, upwards acting loads. Ali *et al.* (2003) developed a model based on this assumption and concluded that the observed moat infill thickness could be matched using a constant load and infill density of 2700 kg m^{-3} by incorporating an upwards acting load with 20 % of the mass of the surface load.

Adhering to this predicted value of a T_e of 30 km, a similar result is reached for the intermediate density infill material parameterisation. It is apparent that the flexure calculated using a load density of 2700 kg m^{-3} and a T_e of 30 km (Figure 5.10a) is too high in amplitude to match the observed moat infill thickness (Figure 5.1c). For a scenario of synchronous surface and undercrustal load emplacement, whereby the undercrustal load has the same spatial distribution as the surface load, the magnitude of uplift relative to downward flexure is directly proportional to the mass of the undercrustal load as a fraction of the surface load.

Figure 5.10 Flexure calculated from a model incorporating an upwards acting load at the base of the crust, assuming the expected value of a T_e of 30 km. a) Regional flexure calculated using the intermediate density infill material, load density of 2700 kg m^{-3} and a T_e of 30 km. Flexure contours (black lines) with a 0.5 km contour interval. b) The uplift (negative flexure) expected for an undercrustal load, with a subcrustal load fraction of 0.3. Uplift contours (black lines) with a 0.1 km contour interval. c) Total deflection (sum of flexure and uplift) for the best-fit subcrustal load fraction of 0.3. Flexure contours (black lines) with a 0.5 km contour interval. The location of profile P01 (black line) is also shown. d) Difference between observed moat infill sediment thickness and the best-fit total deflection masked according to the presence of observed data. Positive values indicate areas where the calculated flexure underestimates the observed thickness. Difference contours (black lines) with a 0.2 km contour interval. e) The seabed (black line), unconformity and Moho (grey bands including uncertainty) from the *final* 2-D velocity-depth model are compared to the driving load (orange shading) and the top and base of the 1-D model of the crust resulting from the flexure calculation for the best-fit parameter pair (blue lines). Note that the calculated base of crust includes the undercrustal load. See text for discussion.

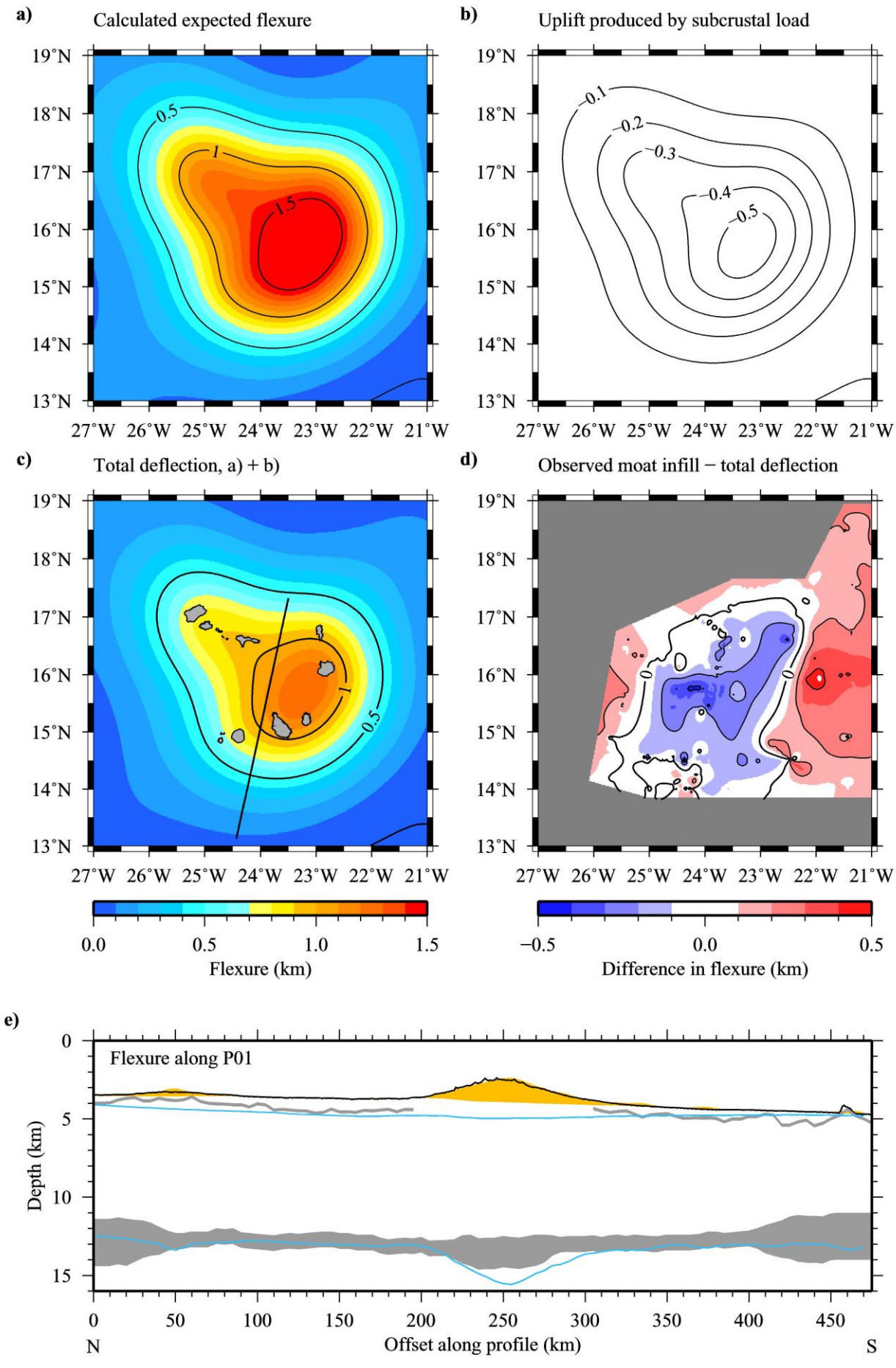
a)
Calculated expected flexure
b)
Uplift produced by subcrustal load
c)
Total deflection, a) + b)
d)
Observed moat infill − total deflection
19°N
18°N
17°N
16°N
15°N
14°N
13°N
27°W 26°W 25°W 24°W 23°W 22°W 21°W
0.0 0.5 1.0 1.5
Flexure (km)
−0.5 0.0 0.5
Difference in flexure (km)
e)
Flexure along P01
Depth (km)
0 5 10 15
0 50 100 150 200 250 300 350 400 450
N
Offset along profile (km)
S

A range of subcrustal load fractions, from 0 to 1, were tested by comparing the total deflection (the sum of downward flexure and uplift) to the observed moat infill thickness and determining the rms misfit. The best-fit total deflection was obtained for a fraction of 0.3 and the results are summarised in Figure 5.10. This result is comparable to that presented by Ali *et al.* (2003), where an undercrustal load mass fraction of 0.2 was found to produce the best-fit total deflection.

The difference between the total deflection and the observed moat infill thickness (Figure 5.10d) is still generally <0.5 km and predominantly <0.2 km. However, there is a larger area where the calculated flexure is too low that shows a direct relationship with increasing distance from the driving load, implying that a long-wavelength component of flexure is absent from the solution.

The volume of the undercrustal load can be determined from the best-fit mass fraction, a similarly determined density ratio and the modelled volume of the load driving surface flexure. Applying a density of 3000 kg m^{-3} for the undercrustal load, which is representative of the high density igneous material that may be accumulated at the base of the crust during island building magmatism, gives rise to a negative density contrast with the surrounding mantle material of -300 kg m^{-3}. The majority of the driving load is submarine and has a positive density contrast with the water column of 1700 kg m^{-3}, resulting in a density ratio of ~0.2. By conservation of mass, the undercrustal load must have a volume that is 1.5 times that of the surface load in order to provide enough uplift to partially counteract the flexure. Figure 5.10e compares the basal surface of the best-fit undercrustal load, after the lithosphere has undergone flexure, to the seismically determined Moho along profile P01 from the WA seismic data, and demonstrates that this amount of undercrustal material exceeds the maximum uncertainties of the WA seismic data.

The basal surface of the undercrustal load is also compared, in Table 5.2, to the Moho depth estimates of Lodge & Helffrich (2006) at the locations of the land-based recording stations located on seven of the Cape Verde Islands. As with the Moho along profile P01, there is a significant discrepancy (>2 km) between the depths calculated from analysis of receiver functions (Lodge & Helffrich, 2006) and those required by the model. The northwest chain of islands and Fogo require a larger undercrustal load in the flexure model than the 1-D receiver function tomography suggests, while the islands of Sal and Maio require less. Santiago is the only island beneath which the two estimates are in close agreement, with a difference of just

0.6 km. While the WA seismic data do not preclude the occurrence of undercrustal material beneath the islands, the flexure modelling implies that there is not a large enough volume of material to partially counteract the surface loading and match the observed moat infill thickness if the lithosphere has a constant T_e of 30 km.

Table 5.2 Comparison of the depth to the Moho beneath the Cape Verde Islands determined using receiver function analyses (Lodge & Helffrich, 2006) with those calculated during flexure modelling with an undercrustal load.

Island	Station latitude (N)	Station longitude (W)	Moho depth from receiver functions (km)	Moho depth undercrustal load (km)
Santo Antão	16° 59'	25° 12'	~10	18.9
São Vicente	16° 52'	24° 56'	~15	18.7
São Nicolau	16° 37'	24° 21'	~10	19.5
Sal	16° 44'	22° 56'	~20	17.7
Maio	15° 14'	23° 11'	~23	18.8
Santiago	14° 58'	23° 36'	~19	19.6
Fogo	14° 55'	24° 23'	~13	22.5

5.3.2 Variable T_e

Models that are parameterised with a constant value of T_e do not result in a pattern of flexure that adequately matches the observed moat infill thickness data at all wavelengths. Instead, models with both a high and low apparent T_e partially explain the observed flexure, suggesting that the effective rigidity of the lithosphere may vary either spatially or temporally during loading. To test the hypothesis of temporal variation, an approximation of the flexural response was made by combining a fraction of the total flexure that occurs for the expected T_e of 30 km (Figure 5.11a) with the remaining fraction of flexure that occurs for the best-fit T_e of 60 km (Figure 5.11b).

Figure 5.11 An estimate of the flexure associated with a variable T_e. a) Regional flexure calculated using the intermediate density infill material, load density of 2700 kg m^{-3} and a T_e of 30 km. Flexure contours (black lines) with a 0.5 km contour interval. b) Regional flexure calculated using the intermediate density infill material, load density of 2700 kg m^{-3} and a T_e of 60 km. Flexure contours (black lines) with a 0.5 km contour interval. c) The expected flexure for a combined model with variable T_e (30% at 30 km, 70% at 60 km). Flexure contours (black lines) with a 0.5 km contour interval. The location of profile P01 (black line) is also shown. d) Difference between observed moat infill sediment thickness and the calculated flexure for the variable T_e model, masked according to the presence of observed data. Positive values indicate areas where the calculated flexure underestimates the observed thickness. Difference contours (black lines) with a 0.2 km contour interval. e) Comparison of the flexure calculated crust with the seismically determined layer boundaries along profile P01. The seabed (black line), unconformity and Moho (grey bands including uncertainty) from the *final* 2-D velocity-depth model are compared to the driving load (orange shading) and the top and base of the 1-D model of the crust resulting from the flexure calculation for the variable T_e model (blue lines).

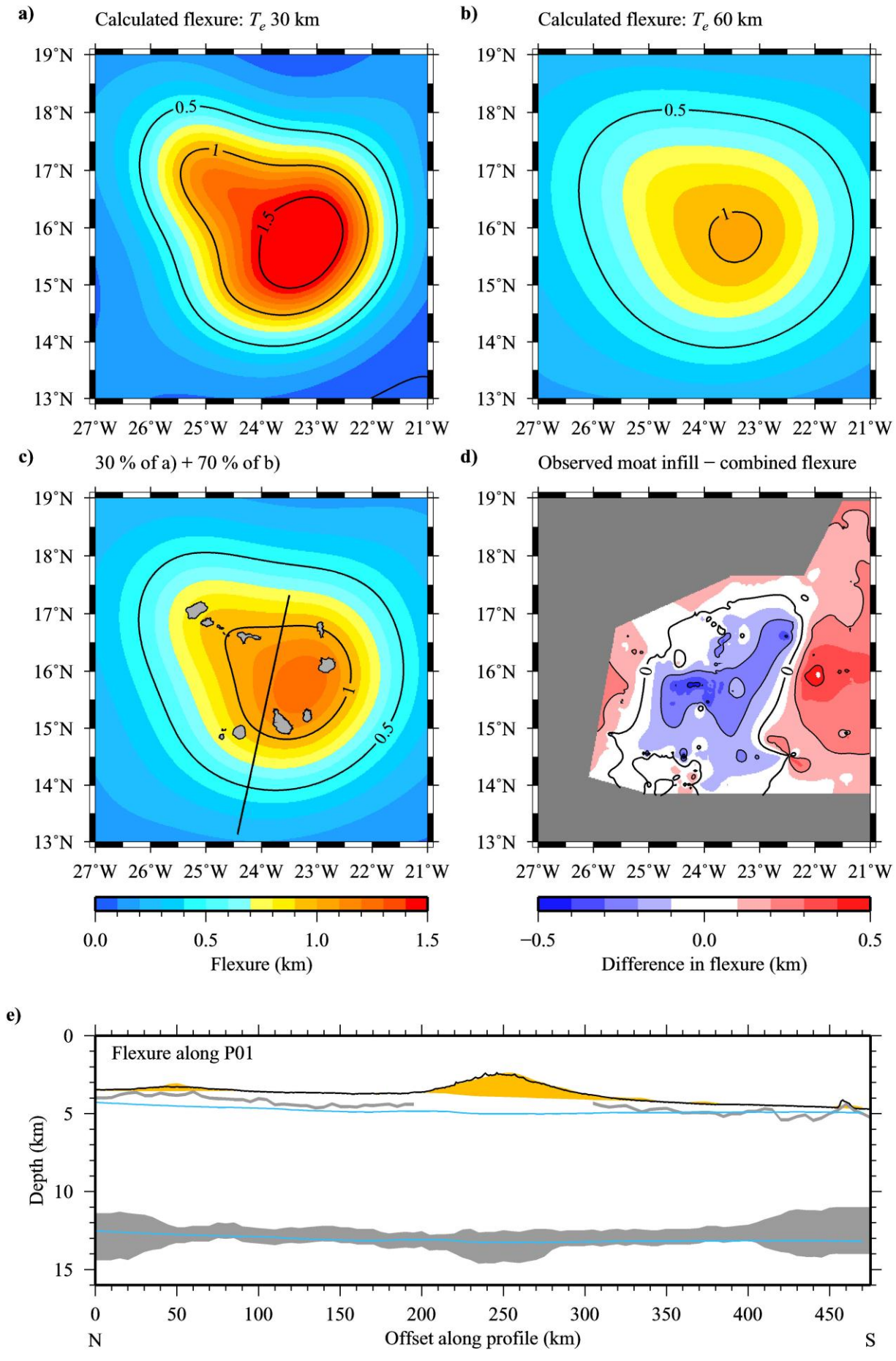
a)
Calculated flexure: T_e 30 km
b)
Calculated flexure: T_e 60 km
c)
30 % of a) + 70 % of b)
d)
Observed moat infill − combined flexure
19°N
18°N
17°N
16°N
15°N
14°N
13°N
27°W 26°W 25°W 24°W 23°W 22°W 21°W
0.5
1
1.5
0.0 0.5 1.0 1.5
Flexure (km)
−0.5 0.0 0.5
Difference in flexure (km)
e)
Flexure along P01
Depth (km)
0 5 10 15
0 50 100 150 200 250 300 350 400 450
N
Offset along profile (km)
S

A combined model incorporating 30% of the total flexure associated with a T_e of 30 km and 70% of the total flexure associated with a T_e of 60 km (Figure 5.11c) generated the best statistical fit to the observed moat infill sediment thickness. This combined model produces an overall pattern of flexure with the potential to explain magnitudes observed at all wavelengths. However, comparing the difference between calculated flexure and the observed moat infill thickness (Figure 5.11d) to that of the preferred model (Figure 5.9d) shows that this results overestimates the flexure by >0.2 km over a much larger region.

Much more likely is a model in which T_e varies spatially, something that cannot be modelled with *topo2grv* in its current form, whereby the strength of the lithosphere may be affected on a smaller scale by shallow features such as fracture zones or thermal rejuvenation of the lithosphere directly associated with island load emplacement.

5.4 Three-dimensional gravity anomaly

As an independent test of the preferred flexure model, the crustal component of the FAA was calculated with *topo2grv* from the 1-D density model and the chosen densities of the load and infill material. The calculated crustal component of the FAA was then compared to the observed FAA, using an assessment of the residual anomaly to determine any areas where the misfit is larger than the uncertainties.

5.4.1 Removing the regional

The observed FAA (Figure 5.12a) can be considered as the sum of three distinct components, each with a different characteristic wavelength. The first component consists of short-wavelength (<100 km), positive anomalies associated with the islands and their edifices. The second component is a medium-wavelength (100-550 km), negative anomaly that is related to the sediment accumulation in the flexural moat. Over a larger region, a third component can be observed that has a low positive amplitude and a very long-wavelength (>550 km).

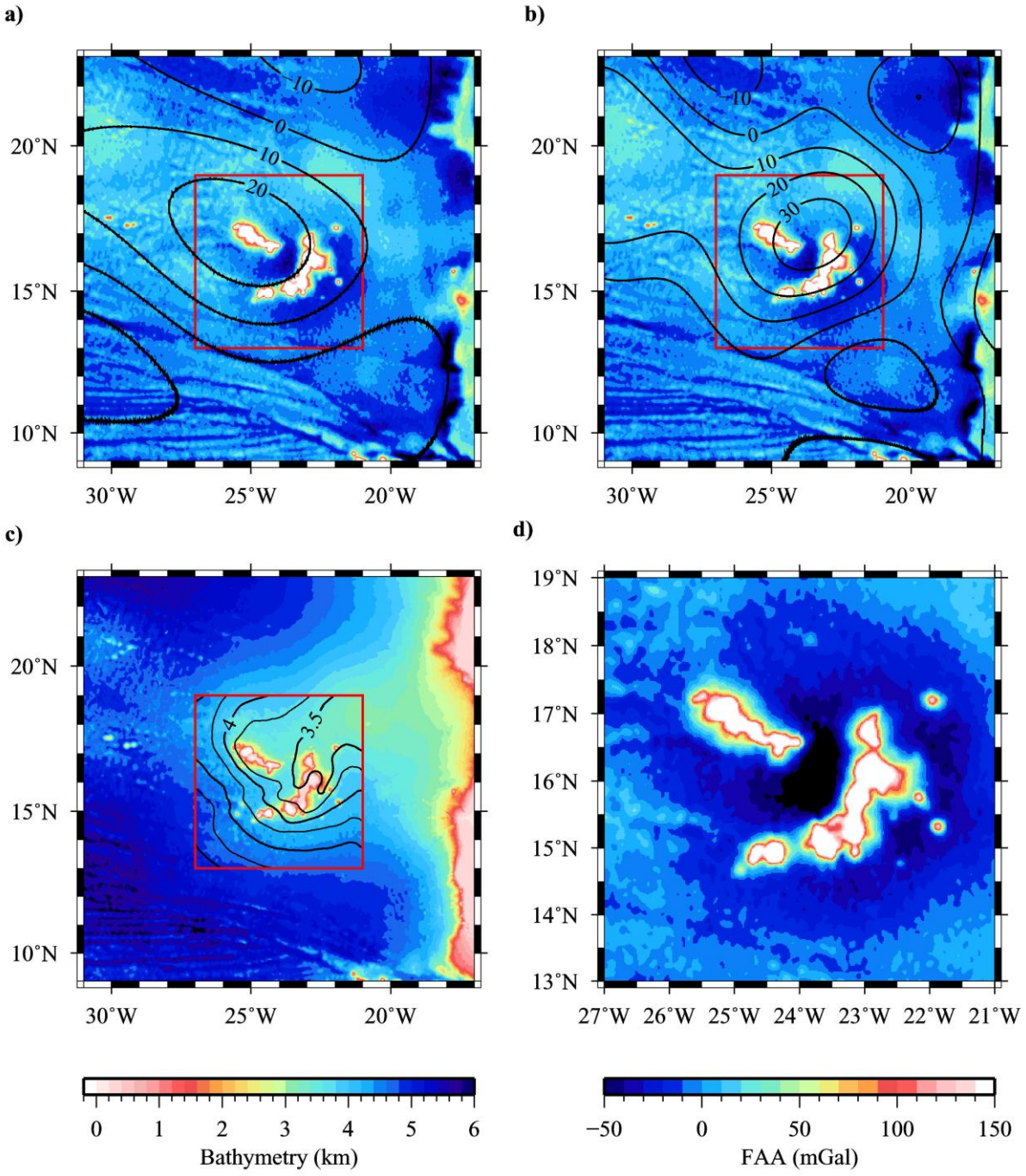

Figure 5.12 Determination of the long-wavelength component of the FAA, representing the regional topographic swell and its compensation. a) Comparison of the OSU91A (Pavlis & Rapp, 1990) satellite-derived gravity anomaly complete to degree and order n=m=40, including anomalies with wavelengths >1000 km (black contours with a 10 mGal contour interval) with the observed FAA. The area used for comparison with results from *topo2grv* is also shown (red box). b) As for a) but complete to degree and order n=m=72, including anomalies with wavelengths >550 km. The long-wavelength gravity anomaly contoured in b) has a distinct, approximately circular shape that shows a good spatial correlation with the bathymetry of the swell, c). Swell bathymetry contours (black lines) with a 0.25 km contour interval. d) The observed FAA with the long-wavelength component in b) removed will be used to assess the fit of the gravity anomalies calculated from the flexure models. The short-wavelength positive anomalies of the islands are superimposed on a medium-wavelength negative anomaly that is approximately centred beneath the load.

It is necessary to remove the long-wavelength component of the observed FAA, representative of the bathymetric swell and its regional compensation, in order to make a direct comparison with the gravity anomaly calculated from the preferred flexure model. The spherical harmonic of the observed satellite gravity field complete to degree and order 40 (Figure 5.12a) was chosen by Ali *et al.* (2003) to represent deep-seated gravity anomalies, with wavelengths >1000 km, that are unrelated to plate flexure. However, the spherical harmonic of the observed satellite gravity field to degree and order 72 (Figure 5.12b), representing wavelengths >550 km, shows a positive anomaly that is more clearly recognised as an independent feature, unrelated to the regional bathymetric high to the northeast, and shows a better spatial correlation to the swell bathymetry (Figure 5.12c), and, hence, can be regarded as characteristic of the 'swell anomaly'. This swell anomaly can be removed from the observed FAA to produce the crustal gravity anomaly (Figure 5.12d), against which the gravity anomalies calculated from the flexure models can be compared.

5.4.2 Residual gravity anomalies

The calculated gravity anomaly for the preferred flexure model of Section 5.3.3 (Figure 5.13a) is similar to the observed data (Figure 5.12d) and a plot of the residual anomaly (Figure 5.13b) shows that the observed crustal gravity anomaly is generally matched to ±30 mGal. Around the eastern islands, where the highest amplitude flexure occurs (see Figure 5.9c), the resulting gravity low is under-calculated by up to ~40 mGal, suggesting that the modelled plate is too rigid and does not flex sufficiently to accommodate a large enough volume of low density infill material to produce the negative gravity anomaly.

Figure 5.13 Summary of gravity anomalies calculated using an intermediate density for the infill material for the preferred model, a), the expected model, c), and the variable T_e model, e). Difference between the observed FAA with the long-wavelength swell component removed (Figure 5.12d) and the preferred, expected and variable T_e models are shown in b), d) and f), respectively. The 0.5 km bathymetry contour (black line) encloses the islands and their steep submarine flanks where the observed FAA is inaccurate and, hence, omitted from the statistical analysis. See text for discussion.

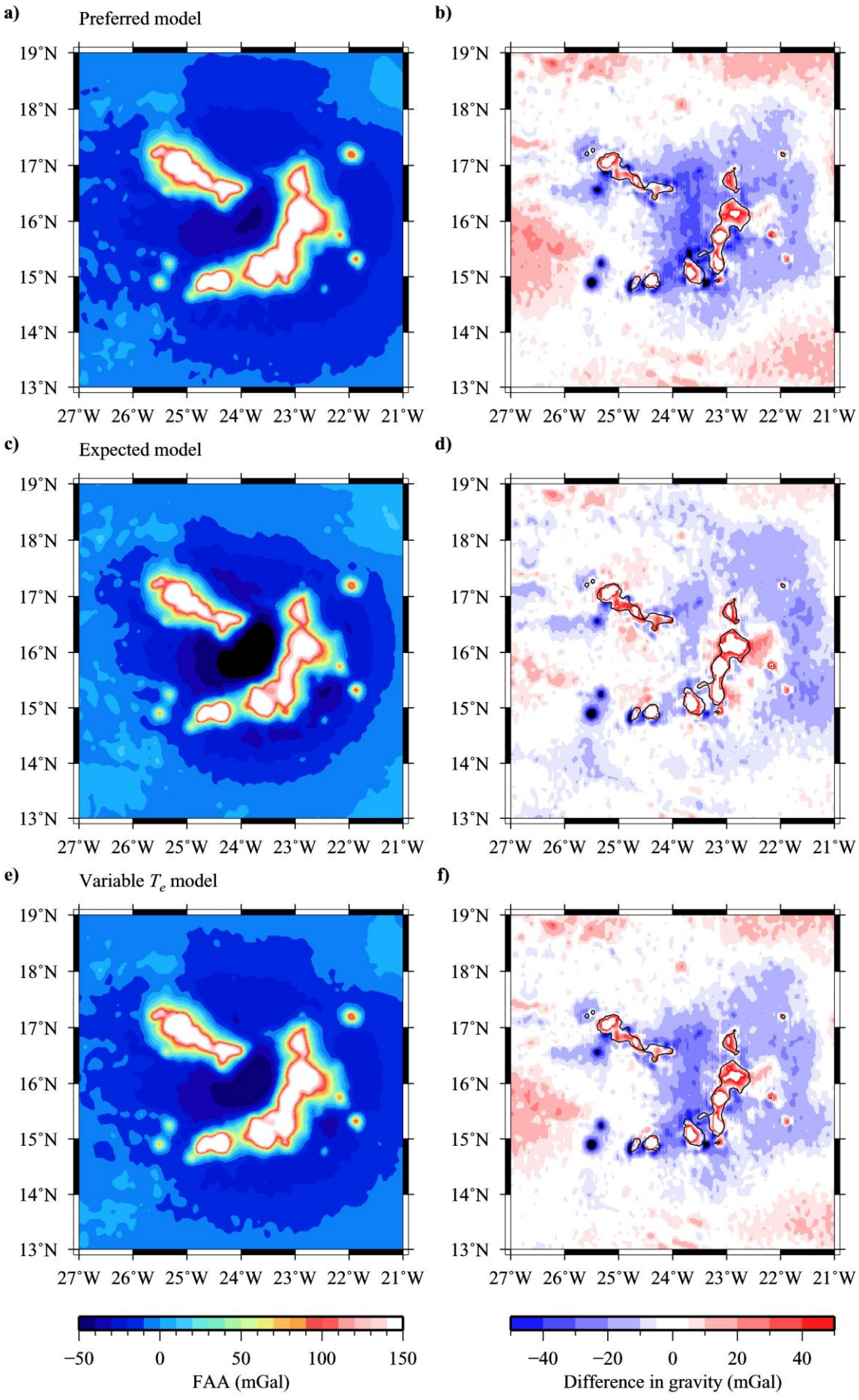
a)
Preferred model
b)
c)
Expected model
d)
e)
Variable T_e model
f)
19°N
18°N
17°N
16°N
15°N
14°N
13°N
27°W 26°W 25°W 24°W 23°W 22°W 21°W
−50 0 50 100 150
FAA (mGal)
−40 −20 0 20 40
Difference in gravity (mGal)

Over the islands and their edifices, the gravity calculated from the flexure model is considerably less than the observed, in some cases by >50 mGal. Increasing the density of the infill material directly beneath the load, where it is underestimated due to the limitation of the model parameterisation, would account for <10 mGal of the mismatch. Additionally, the observed gravity data is known to be inaccurate and has a lower spatial resolution over land and regions of shallow bathymetry, particularly for short-wavelength features such as ocean islands and seamounts (Sandwell & Smith, 1997; Marks & Smith, 2007; Sandwell & Smith, 2009). It is evident that the 0.5 km bathymetric contour outlines the large amplitude highs in the residual anomaly (Figure 5.13b). Excluding the areas proximal to the islands, the overall rms misfit between the calculated gravity anomaly for the preferred flexure model and the observed data is 12 mGal.

In comparison, the calculated gravity anomaly for the flexure model with a T_e of 30 km, as expected based on the age of the lithospheric plate at the time of loading (Figure 5.13c), shows a closer match to the observed crustal gravity anomaly (Figure 5.13d). If the areas within the 0.5 km bathymetric contour are excluded, the rms misfit is only 9 mGal. This model clearly explains the observed gravity anomaly but as demonstrated in Figure 5.9e, the calculated amplitude of flexure is too high and does not match the observed moat infill sediment thickness.

A basic estimate of the gravity anomaly produced by the variable T_e model was also determined by summing the equivalent fractions of the end-member anomalies (Figure 5.13e). The rms misfit between the calculated anomaly and the observed crustal gravity anomaly is 10 mGal (Figure 5.13f). Compared to the result from the preferred flexure model (Figure 5.13b), the gravity mismatch is reduced where the highest amplitude of flexure occurs, and fits equally well over the rest of the region. In areas distal to the load, the gravity mismatch is comparable to that observed for the model with a T_e of 30 km (Figure 5.13d). This variable T_e model, representing temporal variation in the strength of the lithospheric plate during loading is, hence, regarded as the best-fit model, considering the fit to both the observed moat infill thickness and the crustal gravity anomaly. However, a negative anomaly of amplitude -40 mGal and wavelength ~350 km, located beneath the eastern islands, is unaccounted for by the variable T_e model. This may be caused by a thermal or compositional anomaly in the lithosphere. If this negative anomaly is caused by a region of elevated temperature within the lithosphere, the plate should be

mechanically weakened. This is inconsistent with the results of 3-D flexure modelling, which suggest that the plate is actually 'strengthened'. To reconcile these conflicting results, the geophysical signature of the swell will be analysed separately to determine the depth at which its anomalous topography is compensated.

5.5 The Cape Verde Swell

Results of the three-dimensional flexure and gravity modelling suggest that, during loading or some time subsequently, an upwards acting force has 'strengthened' the lithosphere and caused flexure over longer wavelengths than expected based solely on the age of the plate. The volume of undercrustal material necessary to produce a sufficient magnitude of uplift to reduce the calculated flexure produced by surface loads given a T_e of 30 km is too large to fit within the uncertainties of the *final* 2-D velocity-depth model and other estimates of crustal thickness in the region. These results imply that the mechanism causing uplift originates at greater depth, either within the lithosphere, at the lithosphere-asthenosphere boundary, or some combination of the two. The long-wavelength topography of the swell can be related to long-wavelength gravity and geoid anomalies that result from density variations in the lithosphere and asthenosphere. If the region is in isostatic equilibrium, analysis of the gravity-topography slope (e.g. Watts, 1976) or the geoid-topography ratio (e.g. Cazenave *et al.*, 1988) can provide insight into the depth of the density variation.

The total long-wavelength gravity anomaly is the sum of two components, a positive anomaly resulting from the elevated swell topography and a negative anomaly due to the causative low density region. If the causative region is closer to the reference datum (sea level), a low gravity-topography slope would be expected. In contrast, if the low density region is at a greater depth, the positive anomaly from the swell topography would be dominant, resulting in a high gravity-topography slope. Using the gravity-topography slope (gravitational admittance), $Z(k)$, it is also possible to calculate the expected compensation depth (D_c) of the swell using the following formula (Watts, 2001):

$$D_c = \frac{Z(k)}{2\pi G(\rho_m - \rho_w)k} \qquad \textbf{(5.2)}$$

where G is the gravitational constant, k is the wavenumber ($2\pi/\lambda$) where λ is the characteristic swell wavelength of 2000 km, and ρ_m and ρ_w are the densities of the mantle (3330 kg m^{-3}) and the water column (1030 kg m^{-3}), respectively.

Similarly, long-wavelength positive deflections of the geoid are reduced if the compensation is close to the Earth's surface. Sandwell & MacKenzie (1989) summarised that low geoid-topography ratios (0-2 m km^{-1}) were indicative of shallow Airy compensation and intermediate ratios (2-6 m km^{-1}) provide evidence of average compensation depths of between 50 and 80 km, while high ratios (>6 m km^{-1}) represent dynamic support by convective stress at the lithosphere-asthenosphere boundary. A global analysis of the geoid-topography ratio at oceanic plateaus and swells (Marks & Sandwell, 1991) revealed a maximum of just 4.7 m km^{-1}, apparently excluding the possibility of a dynamic support mechanism. Using the geoid-topography ratio (ΔN / Δh) it is possible to obtain a more precise estimate the compensation depth of the swell using the following formula, based on Pratt isostasy (Haxby & Turcotte, 1978):

$$\frac{\Delta N}{\Delta h} = \frac{\pi G}{g}(\rho_m - \rho_w)D_c \qquad \textbf{(5.3)}$$

where G is the gravitational constant and g is the mean surface gravity.

The bathymetry of the swell, described by the directional median filter of width 240 km (Section 5.2.2), was converted into anomalous topography (Figure 5.14a) above the expected bathymetry for the age of the lithosphere based on the GDH1 model of cooling and subsidence (Stein & Stein, 1992). The long-wavelength, regional gravity anomaly that was removed in Section 5.4.1 is further reduced by removing the spherical harmonic component of the satellite gravity field complete to degree 10, which includes gravity anomalies with characteristic wavelengths >4000 km that arise from deep-seated density variations in the lower mantle (Bowin, 1983; Figure 5.14b). Similarly, the long-wavelength positive geoid anomaly associated with the swell (Figure 5.14c), complete to spherical harmonic degree and order 10<n=m<72, was extracted from the EGM96 model (Lemoine *et al.*, 1998) to reflect the signature of the swell and its compensation (wavelengths between 550 and 4000 km).

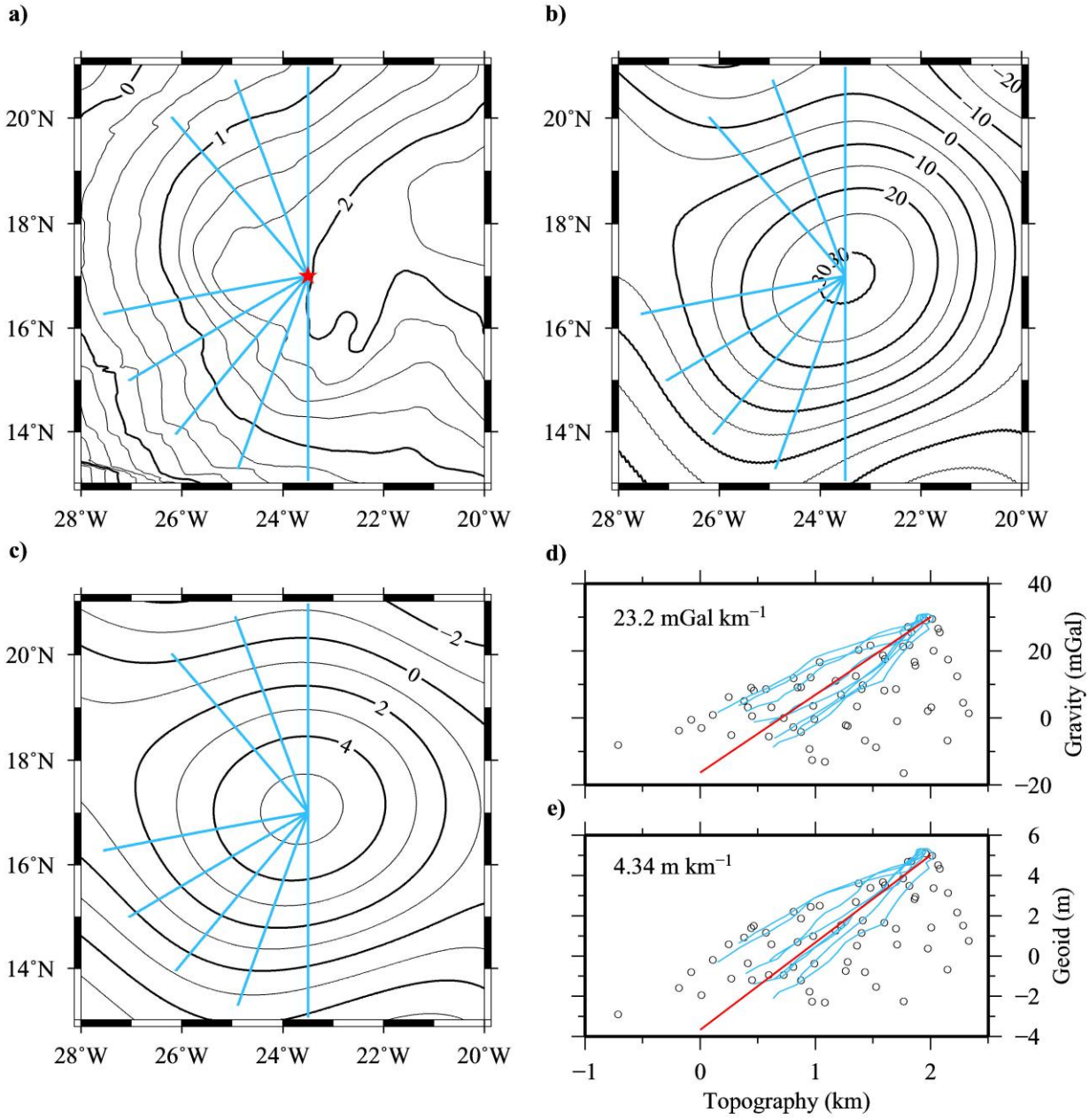

Figure 5.14 Calculation of the gravity-topography slope and the geoid-topography ratio of the Cape Verde Swell. a) Anomalous swell topography contours (black lines) with a 0.25 km contour interval. Data were extracted every 20 km along eight radial profiles (blue lines) diverging from the swell crest (red star). Long-wavelength spherical harmonic components of the satellite-derived gravity field (OSU91A, Pavlis & Rapp, 1990), b), and geoid (EGM96, Lemoine *et al.*, 1998), c), complete to degree and order 10<n=m<72 (including anomalies with wavelengths between 550 and 4000 km). Data were extracted every 20 km along eight radial profiles (blue lines) diverging from the swell crest (red star). d) Plot of gravity against topography, showing 1° x 1° averages (black circles), individual profiles (blue lines) and the average of all eight profiles (red line). The average gravity-topography slope is 23.2 mGal km^{-1}. e) Plot of geoid against topography, showing 1° x 1° averages (black circles), individual profiles (blue lines) and the average of all eight profiles (red line). The average geoid-topography ratio is 4.34 m km^{-1}.

It is possible to obtain estimates of the gravity-topography slope or geoid-topography ratio using linear regression on the spatial averages of these data (e.g. Watts, 1976; Sandwell & MacKenzie, 1989). The spatial average of swell topography, gravity and geoid anomalies was calculated for 1°x1° bins over the area shown in Figure 5.14. Plots of both gravity and geoid anomalies against topography for these averages reveal a large amount of scatter and there is no clear correlation between the data. A second method was employed, similar to that used by Monnereau & Cazenave (1990), which involved the analysis of the gravity-topography slope and geoid-topography ratio along radial profiles extending from the swell crest at 17° 00' N 23° 30' W. Profiles were generated at an angular increment of 20°. Profiles heading east were excluded due to the influence of the continental margin on the topographic anomaly and two profiles to the northwest (280° and 300°) were also excluded due to the presence of long-wavelength gravity and geoid signals that appear unrelated to the Cape Verde Swell. Data were extracted from the grids every 20 km along these profiles and the results are plotted in (Figure 5.14d & e). Although there is some variability in the gravity-topography and geoid-topography gradients, both along individual and between all the profiles, the results show average gravity-topography slope and geoid-topography ratio of 23.2 mGal km^{-1} and 4.34 m km^{-1}, respectively, that match the overall trend, particularly where the topographic anomaly is <1 km. The calculated gravity-topography slope matches the estimate of Crosby *et al.* (2006) who reported a slope of between 20 and 27 mGal km^{-1} for the Cape Verde Swell and the average geoid-topography ratio is in agreement with the value of 4.4 m km^{-1} obtained by Grevemeyer (1999).

Substituting the values obtained for the gravity-topography slope and geoid topography ratio into Equations 5.2 and 5.3 produces estimates for the compensation depth of the swell of 77 km and 88 km, respectively. The expected lithospheric plate thickness is between 95 and 125 km, depending on the heat flow model used (95 km – Parsons & Sclater, 1977; 125 km – Stein & Stein, 1992) with an intermediate depth, based on a model incorporating the temperature dependence of thermal conductivity (McKenzie *et al.*, 2005), of ~105 km. These results can be interpreted in terms of two models:

1. The compensation of the swell is entirely contained within the lithosphere as an anomalous region of low density extending to 80-90 km.

2. There is a component of thermal compensation within the lithosphere with an additional component of dynamic upwelling impinging on the base of the lithosphere that is ~25 ±20 km shallower than expected.

The second model is favoured given the observations of very long wavelength flexure that require the plate to be regionally 'strengthened' by an upwards-acting load.

5.6 Summary

The apparent strength of the lithosphere is estimated using 3-D calculations of flexure in response to surface loads. It is not possible, using a single rheological parameter, to exactly match the complex observed patterns of subsidence that are recorded by marker horizons in the shallow subseabed. Instead, there is evidence for spatial variations in T_e and 'strengthening' of the lithosphere by an upwards-acting 'load'. Analysis of long-wavelength gravity and geoid anomalies provide an estimate of the compensation depth of the swell that is only slightly shallower than the expected base of the lithosphere. The implications of these results for the support mechanism at the Cape Verde Swell will be discussed in Chapter 6.

6. Discussion and implications

6.1 Introduction

The Cape Verde archipelago is located in the middle of the slow moving-to-stationary African Plate (e.g. Pollitz, 1991) and is situated on the crest of the largest observed mid-plate oceanic swell on Earth. The Cape Verde Swell is >1500 km in diameter, with a crest >2 km higher than expected based on plate cooling and subsidence models (Parson & Sclater, 1977; Stein & Stein, 1992), and has long-wavelength gravity and geoid anomaly highs of ~30 mGal and ~5 m (Figure 5.14), respectively, making it the ideal location to conduct a detailed geophysical investigation of proposed swell and plate load support models.

The mechanisms that have been proposed to explain how the large-scale topographic swells associated with hotspot volcanism are sustained over geological timescales can be summarised as (Figure 1.7):

1. Shallow support within the crust (e.g. Morgan *et al.*, 1995),
2. Support within the upper mantle (e.g. Detrick & Crough, 1978; Robinson, 1988), and
3. Dynamic mantle upwelling (e.g. Sleep, 1995).

It is possible that these mechanisms are entirely independent or work in combination to produce the observed large-scale topographic anomalies.

WA seismic refraction data, collected in 2004 (CHARISMA experiment, R/V *Meteor* cruise M62/3 – Grevemeyer *et al.*, 2004) to supplement an existing MCS reflection data set, have been modelled to produce a 2-D velocity-depth model of the crustal structure along a radial transect through the swell. The crustal model has also provided additional constraint for 3-D 'whole plate' flexure modelling, which, coupled with a revised analysis of swell topography, gravity and geoid anomalies, has provided an insight into the deeper structure of the lithosphere.

In this chapter, the results presented in Chapters 3, 4 & 5 will be integrated with the existing studies of the Cape Verde Swell to evaluate the evidence for each of the

three mechanisms in turn (Sections 6.2, 6.3 & 6.4). Comparisons will also be made with the evidence for support mechanisms at other well-studied swells.

These individual evaluations will then be combined in Section 6.5 to develop a model for the subsurface structure beneath the Cape Verde Swell. Finally, in Section 6.6, a number of experiments will be proposed that could be developed in order to further explore or test the implied model for mid-plate swell support.

6.2 Undercrustal magmatic emplacement

Shallow crustal support would be evidenced by a thicker than average oceanic basement, originating either at the time of formation at a mid-ocean ridge due to above average magmatic accretion, or during island building by the synchronous addition of magmatic material into or underneath the base of the crust. These two processes are expected to result in a different crustal structure, distinguishable based on *P*-wave velocities. For igneous crustal thickening occurring as part of the accretion process, the range of velocities observed will fit within the range expected for standard oceanic basement (4.0 to 7.3 km s^{-1} – White *et al.*, 1992; Mutter & Mutter, 1993). However, undercrustal material that has been added as a part of a late stage process, possibly associated with oceanic island construction, is generally associated with *P*-wave velocities in excess of 7.3 km s^{-1} (e.g. Grevemeyer *et al.*, 2001a).

Prior to the CHARISMA experiment, estimates of the crustal thickness in the region of the Cape Verde Swell were limited in resolution and spatial extent to 1-D slope-intercept interpretations from four refraction profiles acquired using a marine source and land-based recording stations (Dash *et al.*, 1976) and from 1-D receiver function analysis of teleseismic waves recorded at stations on seven of the islands (Lodge & Helffrich, 2006). The results of these analyses positioned the Moho between 10 and 23 km b.s.l., indicating a significant degree of crustal thickening for many of the islands, given the expected Moho depth of ~12 km b.s.l. assuming standard Atlantic crustal thickness of 7 km (White *et al.*, 1992). However, this evidence of a thickened crust is heavily biased by the land-based recording stations, and does not provide a clear depiction of the lateral extent or internal structure of the thickened crust; it is entirely possible that the thickening is related to island growth and flexure of the pre-existing oceanic crust and does not extend laterally away from

the islands and their edifices. Interestingly, the 2-D velocity-depth models for profiles P02, P03 and P04 (Figure 5.3; produced by Wiebke Brunn and others at IFM-GEOMAR, pers. comm.), which traverse regions of the most recent volcanic activity in the Cape Verde archipelago at the islands of Fogo and Brava (<3 Ma), show no clear evidence for an unusually thickened crust or any emplacement of undercrustal magmatic material.

The *final* velocity-depth model along profile P01 (Figure 4.23a), shows no evidence for a thicker than average lower crust. A comparable result was also obtained from independent forward modelling using a subset of the WA refraction data (Pim *et al.*, 2008; Figure 4.23b). Although the depth of the Moho increases from 12.5 to 13.5 km b.s.l. from the profile edges to the centre, there is no evidence for a clear undercrustal body >2 km thick and >100 km wide as evidenced at Hawaii (Watts & ten Brink, 1989; Figure 6.1a), Marquesas (Caress *et al.*, 1995; Figure 6.1b), La Réunion (Charvis *et al.*, 1999), Ninetyeast Ridge (Grevemeyer *et al.*, 2001a) and Josephine Seamount (Peirce & Barton, 1991). Instead, the slight curve of the Moho is interpreted as a small downward deflection of the oceanic crust in response to surface loading.

The crustal velocity structure and range in observed Moho depth are comparable to those obtained by a similar WA seismic refraction experiment conducted over Tenerife (Canary Islands – Watts *et al.*, 1997; Figure 6.1c). Although also located on the African Plate, the Canary Islands are located on slightly older Atlantic lithosphere (~140 Ma) ~1500 km to the northeast. An unusual, and yet almost identical, step in velocity is observed at the upper crust-to-lower crust boundary (Table 6.1), which suggests that the crust onto which these two island groups are emplaced is very similar and that their formation at the Mid-Atlantic Ridge some 120 to 140 Myrs ago was by a similar process. In the lowermost oceanic crust *P*-wave velocities do not exceed 7.25 km s^{-1} in both cases (Table 6.1), which is less than that usually ascribed to bodies of undercrustal magmatic material (7.3 to 7.8 km s^{-1}, e.g. Caress *et al.*, 1995). For profile P01, the vertical uncertainty in the position of the Moho between 50 and 400 km profile offset is ±0.5 km and increases to ±1.0 km where there is limited data from phases P_n and P_mP beneath the F-STR. Similarly, at the base of the crust the seismic resolution limits the certainty in the *P*-wave velocities to ±0.2 km s^{-1}. Within the range of uncertainties attributed to the model, it is possible that a thin layer of intra-/undercrustal magmatic material does exist

beneath the Cape Verde Swell and that this may contribute to the swell topography. The possible existence of a thin layer of high velocity material was also considered, given similar data resolution limitations, in the study of Tenerife (Watts *et al.*, 1997), and it is possible that the structure of the lowermost crust is similar to that observed beneath the Louisville Guyot (Contreras-Reyes *et al.*, 2010).

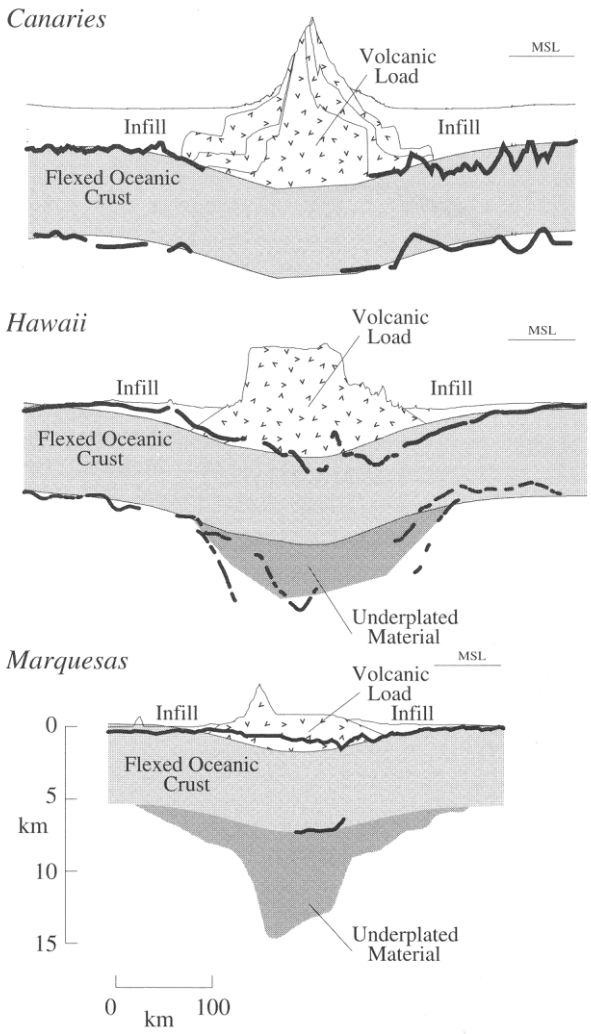

Figure 6.1 Crustal structure of the Hawaiian (Watts & ten Brink, 1989), Marquesas (Caress *et al.*, 1995) and Canary (Watts *et al.*, 1997) Islands (after Watts, 2001) predicted by simple elastic plate models and determined using seismic data (black lines). Both the Hawaiian and Marquesas Islands show evidence for a thick body of undercrustal material that is not observed beneath Tenerife (Canary Islands).

In addition to evidence from seismic experiments, modelling of the FAA provided an independent assessment of the likely presence of intra-/undercrustal material (Chapter 3). Anomalous bodies of varying thickness, with an intermediate density (3100 kg m^{-3}) between lower crustal gabbro (2940 kg m^{-3}) and uppermost mantle (3330 kg m^{-3}), were added to the seismically determined crustal model to simulate

the presence of either intra-crustal or undercrustal material. Incorporating any amount of undercrustal material to the model lessened the fit of the calculated gravity anomaly to the observed. In contrast, the gravity anomalies calculated from block density models that incorporated an intra-crustal magmatic intrusion up to 2 km in thickness and 150 km in width, centred beneath the F-STR, produced an acceptable level of fit to the crustal component of the observed FAA. However, an intra-crustal body such as this, with a higher density than the gabbroic material of the lower oceanic crust at the same depth, would have negative buoyancy and so, rather than supporting the Cape Verde Swell, would result in a reduced (less elevated) topography.

Table 6.1 Comparison of the velocity-depth structure of the oceanic basement at Tenerife (Canary Islands – Watts *et al.*, 1997) with that at the Cape Verde Swell.

Attribute	Tenerife	Cape Verdes
Upper basement thickness (km)	≤2.0	1.0-2.0
Upper basement velocity (km s^{-1})	4.8-5.8	4.3-6.1
Lower basement thickness (km)	≤5.0	4.0-7.0
Lower basement velocity (km s^{-1})	6.7-7.3	6.4-7.3
Moho depth (km)	12.5-15.0	12.5-13.5

Similarly, during 3-D flexure modelling (Chapter 5) a series of models was tested that incorporated varying amounts of positively buoyant undercrustal load in order to counteract the excess flexure caused by the surface loads. The observed thickness of moat infill sediments was closely matched using an undercrustal load with an equivalent sub-Moho thickness of up to 2.0 km directly beneath the F-STR. Such a model was discounted as the crustal thickness exceeded that obtained along profile P01 and those modelled directly beneath the islands from receiver function analyses (Lodge & Helffrich, 2006). Alternatively, if the volume of undercrustal material was modified to match the Moho depths recorded by Lodge & Helffrich (2006), the overall effect was that the uplift would be significantly less, and certainly would not significantly contribute to the observed height of the swell.

The short-wavelength component of the residual FAA calculated from the variable T_e flexure model comprises high amplitude positive anomalies beneath all of the islands. Data and modelling errors increase the uncertainty in the amplitude of these residual anomalies, thus preventing an unequivocal interpretation, but it is possible that a low amplitude residual positive anomaly is real. A positive anomaly would require a high density body, relative to background crust. This suggests that there may be intra-crustal material below the resolution of the seismic modelling, which must, therefore, be supported by a mechanism other than shallow crustal support given the lack of evidence for any significant volume of regional emplacement of undercrustal material.

It has been suggested that the extent of undercrustal magmatic material at oceanic plateaus and oceanic islands may depend on the residence time of the hotspot, and that large bodies take >30 Ma to form (Ito & Clift, 1998). If this hypothesis is correct, then given that the Cape Verde Swell is thought to have formed between 40 and 20 Ma and that there has been little movement (~215 km, ENE) of the African Plate in this region in the last 30 Ma (Pollitz, 1991), a significant body of undercrustal material should have accumulated. Evidence from seismic data suggests that if undercrustal material is present at the Cape Verde archipelago it is entirely localised beneath the islands and calculations demonstrate that it would not provide sufficient buoyancy to fully support the islands, and certainly has a negligible contribution to the regional topographic swell. Instead, swell support must originate deeper either within the lithosphere, at the lithosphere-asthenosphere boundary or as a combination of the two.

6.3 Anomalous lithosphere

Models of swell support that involve thermal rejuvenation of the lithosphere (e.g. Crough, 1978) and those which incorporate an accumulation of low density, depleted residual material associated with melting within or at the base of the lithosphere (e.g. Robinson, 1988; Morgan *et al.*, 1995) can be tested by considering the effect these processes have on the mechanical properties of the lithosphere and the corresponding long-wavelength geophysical signature. A region of anomalously low density material in the lithosphere would cause a negative gravity anomaly. If the density

variation is due to elevated temperature as opposed to a change in geochemical composition, then a heat flow anomaly will also be observed.

A low density region, ~200 km in width and extending from the base of the crust to the base of the lithosphere (~100 km b.s.l.), with a density contrast of -30 kg m^{-3} compared to 'standard' lithospheric mantle, was proposed during 2-D gravity modelling (Chapter 3) as a plausible model for the causative body of the medium-wavelength negative anomaly that was filtered from the observed data to obtain the crustal component of the FAA. The residual gravity anomaly from flexure modelling with the variable T_e model (Figure 5.13f) is dominated by a negative anomaly ~350 km in diameter with amplitude of up to -40 mGal.

It is possible to produce an estimate for the size, shape and density contrast of a low density body in the lithospheric mantle that would be required to reconcile the observed negative gravity anomaly. Several basic shapes were considered, including an infinite horizontal slab, a buried sphere and a vertical cylinder, because they best represent the likely shape of a mantle-based, low-density region caused by melting or thermal rejuvenation. Using the formula for the gravity anomaly ($\Delta\rho$) associated with an infinite horizontal slab (e.g. Nettleton, 1976):

$$\Delta g = 2\pi G \Delta \rho t \qquad \textbf{(6.1)}$$

where G is the gravitational constant, it is possible to obtain an estimate of the minimum density contrast ($\Delta\rho$) assuming a thickness (t) of 90 km, reflecting the entire subcrustal lithospheric mantle. Substituting the known values gives a density contrast of 10.5 kg m^{-3}.

The equivalent formula for the gravity anomaly produced by a buried sphere (e.g. Telford *et al.*, 1990) of radius, r and depth to centre, z is:

$$\Delta g = \frac{4\pi G r^3 \Delta \rho z}{3\left(x^2 + z^2\right)^{3/2}} \qquad \textbf{(6.2)}$$

where x is the horizontal distance of the observation point form the centre of the sphere and other parameters are as previously defined. A radius of 45 km and a depth of 55 km defines a sphere that extends from the base of the crust to the base of the lithosphere. Such a sphere requires a density contrast of -48 kg m^{-3} to produce the maximum amplitude of the observed negative anomaly.

Finally, the gravity, at a point off its axis, of an outcropping vertical cylinder is defined by the following equation (e.g. Dobrin & Savit, 1988):

$$\Delta g = 2\pi G\Delta\rho\left[\sqrt{L^2+(x-r)^2}-\sqrt{L^2+(x+r)^2}-2r\right]\frac{r}{4x} \qquad \textbf{(6.3)}$$

where L is the height of the cylinder and other parameters are as previously defined. Using a radius of 50 km and height 90 km, a density contrast of -20 kg m^{-3} is required to produce a gravity anomaly of -30 mGal at a distance of 50 km from the axis of the cylinder, similar to that observed (Figure 5.13f). The slab and sphere formulas produce minimum and maximum estimates of the density contrast, assuming the low density region extends throughout the lithosphere. Assuming that the anomalous body has a shape intermediate between an infinite slab and a sphere, biased towards that of a vertical cylinder, the density contrast of the anomalous low density region in the lithosphere required to fit the observed gravity anomaly is estimated to be -25 ±10 kg m^{-3}, which would equate to a temperature anomaly of ~250 °C.

Lodge & Helffrich (2006) also suggested the presence of a low-density depleted swell root beneath the Cape Verde Islands in order to explain the observed traveltimes of *P*-to-*S* mode conversion phases. In this instance, the swell root, which was calculated to be 65 km thick with a circular cross-section of radius ~600 km, required a density contrast of -670 kg m^{-3} compared to 'standard' mantle. Considering the order of magnitude difference between the density contrasts required by this model and the simplistic geometric estimations above, together with the magnitude of the observed negative anomaly in the FAA, the model of Lodge & Helffrich (2006) is improbable.

Courtney & White (1986) observed a positive heat flow anomaly with peak amplitude of +16 mW m^{-2} over the Cape Verde Swell using a series of heat flow measurements. The magnitude of this heat flow anomaly was found to be smaller than would be expected if the observed swell uplift is solely the result of the thermal rejuvenation of the lithosphere. Using the GDH1 model of Stein & Stein (1992), the heat flow anomaly is even lower, peaking at just +10 mW m^{-2}. Applying a mean value for the compensation depth (80 km; Chapter 5), along with an anomalous heat flow of 10-15 mW m^{-2}, the constant thinning model of Courtney & White (1986) predicts a swell crest height of 1.0 ±0.1 km and an initiation of thermal rejuvenation of between 50 and 100 Ma (Figure 6.2). This model does not account for the full

height of the swell (2.2 km), but an initiation time of 50 Ma or earlier is not ruled out by the more recent dates of island volcanism (<20 Ma) and is consistent with a gradual construction of the volcanic platform upon which the older islands to the east are situated. A gradual swell formation is supported by evidence from DSDP site 368 and the regional unconformity, that both suggest a long period of non-deposition or rapid erosion from ~100 to ~20 Ma (Lancelot *et al.*, 1978b; Ali *et al.*, 2003).

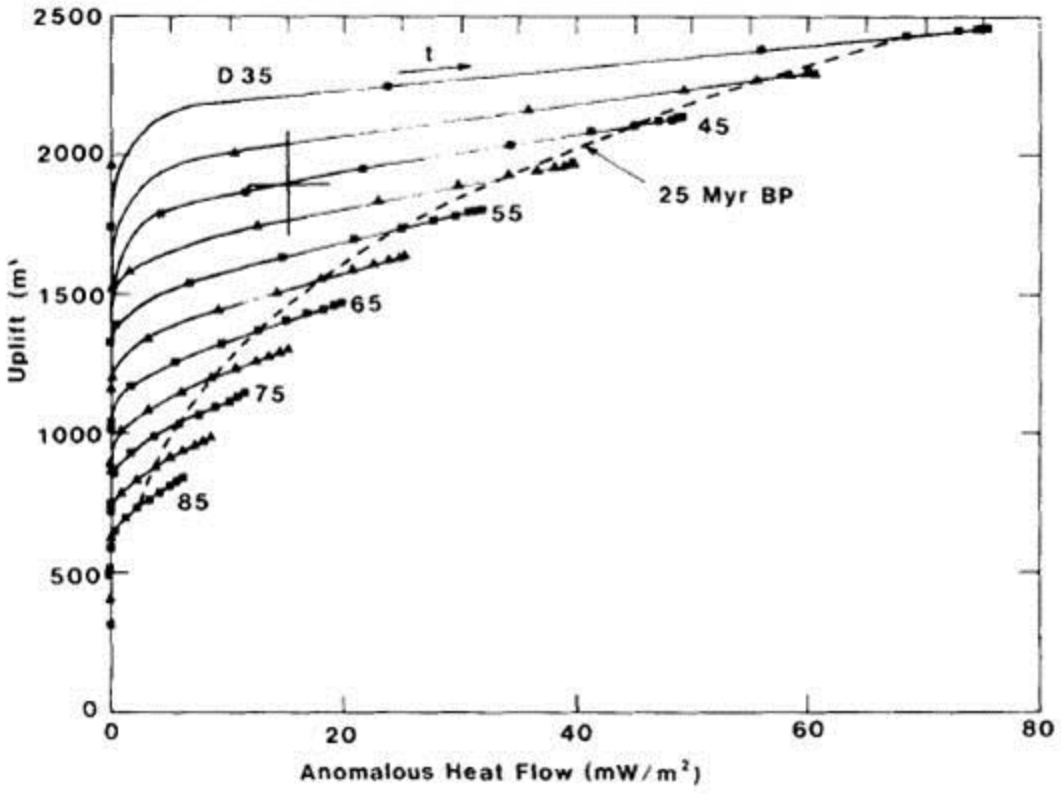

Figure 6.2 Thermal rejuvenation of the lithosphere by constant thinning (after Courtney & White, 1986). Each curve shows the change in surface uplift and heat flow with time since initial injection of hot material reaching depths b.s.l. of between 35 and 85 km. Symbols are plotted at 5 Ma time steps and the arrow shows the direction of increasing time since injection. Both observed uplift and heat flow anomalies are shown to increase with time and are dependent on the compensation depth. Assuming a compensation depth of 80 km and an anomalous heat flow of between 10 and 15 mW m^{-2} for the Cape Verde Islands, an initiation time for the thermal episode of between 50 and 100 Ma is predicted.

Feighner & Richards (1994) propose that thermal conduction from a plume of hot material rising through the asthenosphere may have weakened a central region beneath the Galápagos archipelago. The total height of the Galápagos Swell is estimated to be between 0.6 and 0.7 km (Monnereau & Cazenave, 1990; Canales *et al.*, 2002), with a corresponding geoid anomaly of 0.5 m. A low density region within the lithospheric mantle, located at a depth of <100 km, was also invoked by

Canales *et al.* (2002) to explain the residual 0.35 km amplitude, long-wavelength topography of the swell and the corresponding negative gravity anomaly, that were not explained by the ~2.3 km of crustal thickening constrained by WA seismic data.

If oceanic lithosphere has been thermally rejuvenated, then the plate should appear to be weaker than expected based solely on its age determined from magnetic anomalies (Müller *et al.*, 2008). Early estimates of the strength of the oceanic lithosphere at the Cape Verde Islands calculated the T_e to be between 15 and 30 km (Young & Hill, 1986; Calmant *et al.*, 1990), less than predicted for lithosphere that was ~120 Ma old at the time of loading (~30 km), suggesting that the plate is weaker than expected. Interestingly, there is no direct evidence from more recent 3-D whole plate flexure modelling at the Cape Verde Islands that the underlying plate has a T_e less than expected (Ali *et al.*, 2003) and, conversely, there is a strong argument for spatial variations in T_e that reflect high inherent plate strength (Chapter 5). Generally, in the Cape Verdes region the lithosphere demonstrates a rigid response, equivalent to a T_e of 60 km, but in some areas around the islands there is evidence for short-wavelength high amplitude flexure, suggesting that locally the plate may have a T_e of 30 km, matching the expected value.

At the Canary Islands, where there is evidence of a topographic swell of amplitude ~1.5 km (Monnereau & Cazenave, 1990; Crosby & McKenzie, 2009), results from 3-D flexure modelling imply that the lithosphere is weaker than expected for its predicted thermal age (Watts *et al.*, 1997). A coherence analysis of bathymetry and gravity data (Canales & Dañobeitia, 1998) revealed a compensation depth of 40-65 km with a small negative density constrast of ~33 kg m^{-3} in the lithosphere, corresponding to an increased temperature of ~325 °C. Canales & Dañobeitia (1998) advocate the model of Robinson & Parsons (1988), which involves a low viscosity region in the uppermost asthenosphere reheating the lower lithosphere without affecting the thermal structure of the upper lithosphere; thereby the plate retains most of its mechanical strength.

The density contrast invoked for the Canary Swell is similar in magnitude to that proposed to account for the negative gravity anomaly observed at the Cape Verde Swell. However, there is no evidence for thermal rejuvenation and weakening of the lithospheric plate at the Cape Verdes. It is possible that a combination of localised weakening, consistent with the observed negative gravity anomaly discussed above, and regional apparent strengthening, perhaps by dynamic upwelling, results in the

observation of a plate which is generally stronger than expected but with localised areas that have a lower strength, similar to that predicted based on its age.

6.4 Dynamic upwelling

A lack of evidence for a significant body of undercrustal material and less uplift than would be expected if associated with thermal rejuvenation, implies that dynamic mantle upwelling most likely plays a significant role in supporting the Cape Verde Swell. In this model, positively buoyant material rises through the asthenospheric mantle until it reaches the base of the lithosphere (e.g. Ribe & Christensen, 1994). At this point, the upwelling column exerts an upward-acting load on the base of lithosphere and, if there is a low degree of thermal rejuvenation, the lithosphere retains its long-term strength and flexural deformation associated with this upward-acting load is transferred to the surface. In simple terms, the downward flexure associated with surface loading is unbent by an upwards-acting buoyancy force.

McNutt (1988) calculates, using forward filtering and admittance techniques, that the depth of compensation for the topographic anomaly of the Cape Verde Swell is 69 ±10 km. This result is in close agreement with those obtained in Chapter 5 (77 and 88 km) where forward filtering and linear regression techniques were used to determine the gravity-topography slope and the geoid-topography ratio, respectively. Consequently, this calculated compensation depth is located within the lower lithosphere, suggesting that there may be a dual compensation mechanism involving a region of low density within the lithosphere, at an average depth of 50 km below the surface, coupled with an upwards-acting dynamic load impinging on the base of the lithosphere at ~100 km depth.

Applying both linear filters and admittance techniques to geoid and bathymetry data, Sheehan & McNutt (1989) estimated the T_e of the lithosphere and the compensation depth of the anomalous swell topography at the Bermuda Swell to be ~30 km and ~55 km, respectively, implying a model involving significant reheating of the lithosphere. Although convective support was not entirely ruled out (Sheehan & McNutt, 1989), a model in which the swell is maintained exclusively by dynamic upwelling was not permitted by the observed data. A compensation depth of 55 km is shallower than observed at the Cape Verde Swell and the corresponding topographic

anomaly is also less, peaking at ~1.0 km, indicating that there may be an absence of dynamic support beneath Bermuda.

Comparison of the flexural response of the lithosphere with the observed moat infill sediment thickness at the Cape Verde Islands (Chapter 5) reveals a complex pattern that suggests that the T_e of the plate varies spatially and is equal to or greater than the value expected (30 km) based on the age of the lithosphere at the time of loading (~120 Ma). Overall, the plate appears to respond to loading with low-amplitude, long-wavelength flexure representative of a T_e between 50 and 60 km. However, beneath the eastern islands and the northwest chain the observed amplitude of flexure is higher and of shorter wavelength, characteristic of a T_e of ~30 km. McKenzie (2010) investigated the influence of dynamic support on estimates of plate strength made using elastic plate models on a continental scale, and found that T_e was significantly overestimated in dynamically supported areas. This effect would explain why the apparent T_e at the Cape Verde Swell is twice that expected, and larger than would be expected even for the oldest oceanic lithosphere.

Global tomographic modelling (e.g. Zhao, 2001; 2004; Montelli *et al.*, 2004; 2006) reveals the presence of negative *P*-wave and *S*-wave velocity perturbations extending beneath oceanic mid-plate swells into the lower mantle. An anomalous region was detected beneath the Cape Verde Swell reaching depths in excess of 650 km with a minimum radius of 300 km, indicating a columnar region of low density material (Montelli *et al.*, 2006; Figure 6.3a). Resolution is limited in the deep mantle due to reduced ray density, but the results suggest that anomalous columns of material with relatively low seismic velocities extend beneath many of the world's hotspots to depths in excess of 1000 km. Recent 3-D spherical mantle convection modelling (Davies & Davies, 2009) has been successful in reproducing a variety of different dynamic upwellings with similar features to those observed using a seismic tomography approach (Montelli *et al.*, 2006).

The dimensions of the low density region beneath Hawaii are similar to that beneath the Cape Verde Swell, allowing a direct comparison to be made (Montelli *et al.*, 2006; Figure 6.3b). Geodynamic modelling of thermal upwelling beneath a moving lithosphere was conducted by Ribe & Christensen (1994) to determine the buoyancy flux necessary to produce the amplitude of uplift observed at the Hawaiian Swell. The best-fit model required the temperature of the upwelling column (180 km in diameter) to be 300 °C hotter than that of the surrounding mantle. In this model

the topography associated with thermal rejuvenation of the lithosphere, determined from uplift of isotherms, did not produce significant swell topography compared to that from pure dynamic upwelling (Figure 6.4).

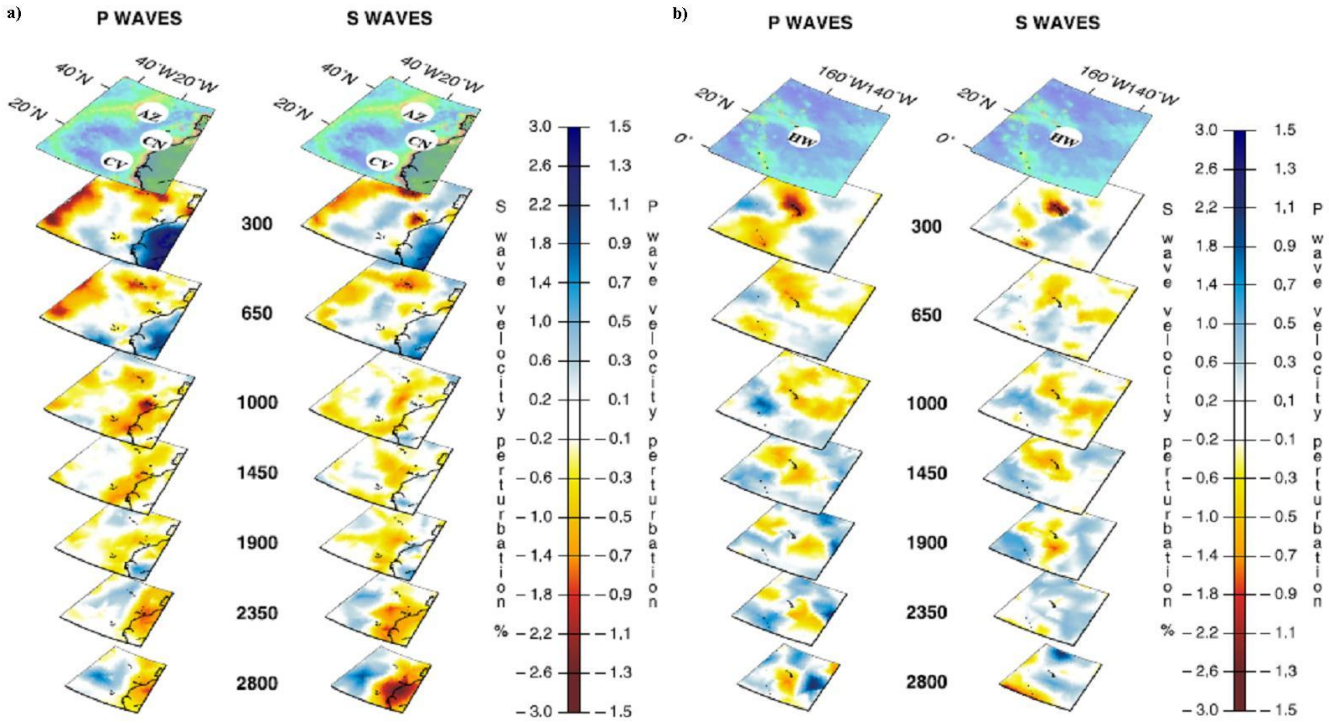

Figure 6.3 Perturbation of *P*-wave and *S*-wave tomographic models beneath a) the Cape Verde and b) Hawaii Swells (after Montelli *et al.*, 2006). Negative anomalies of similar dimensions can be observed beneath both swells to depths >650 km.

Relative to the underlying asthenospheric mantle, the Pacific Plate in the region of the Hawaiian Islands moves roughly an order of magnitude faster than the African Plate in the region of the Cape Verde Islands (e.g. Gripp & Gordon, 2002). Assuming a similar buoyancy flux for a dynamic upwelling beneath the Cape Verde Swell, which is reasonable given the comparable tomographic observations of Montelli *et al.* (2006), this would produce a topographic swell with a height of ~1.0 km. The remaining anomalous topography could be produced by thermal rejuvenation of the lithosphere, which is also plausible given that the African Plate has remained almost stationary for at least 30 Myrs (Pollitz, 1991).

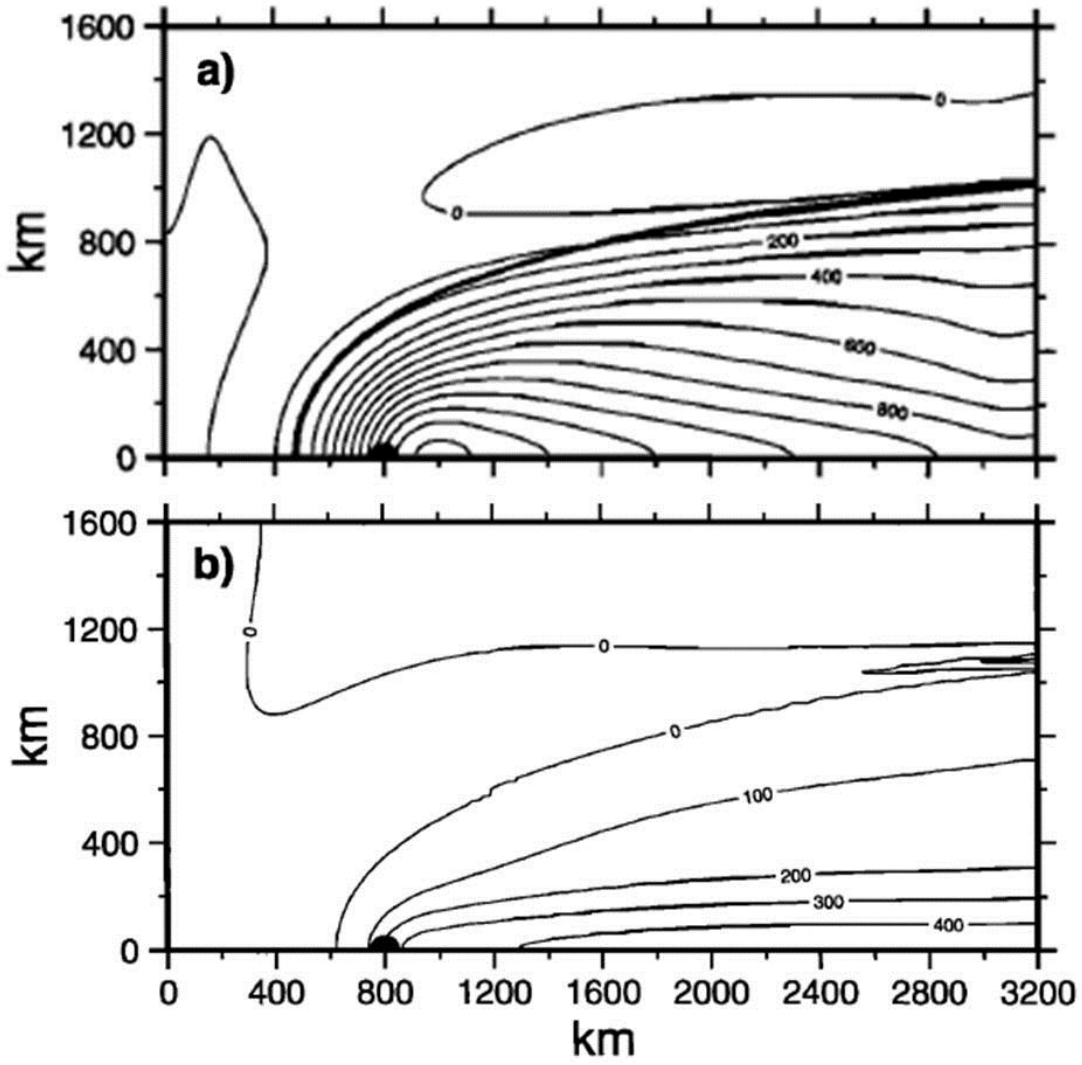

Figure 6.4 Modelled topographic anomalies produced by dynamic asthenospheric upwelling beneath a moving lithospheric plate (after Ribe & Christensen, 1994). Images are in plan view and show half of the swell extent. The location of the upwelling is marked by the black semi-circle and plate motion is to the right. a) Anomalous topography (black contours) created by dynamic upwelling acting as a load on the base of the lithosphere. b) Anomalous topography (black contours) created by thermal reheating of the lithosphere. The topography in b) is calculated from the uplift of the 1250 °C isotherm.

6.5 Support of the Cape Verde Swell

It is possible that undercrustal material is present either isolated beneath the Cape Verde Islands or elsewhere beneath the swell, that has not been sampled by the WA profiles. Considering that a layer of undercrustal material up to 9 km thick would be necessary to produce up to 0.5 km of uplift, the amount necessary to support the full swell topography of 2.2 km would be on the order of ~20 km thick, assuming a similar lateral extent and density of the undercrustal body. If crustal thickening

related to island formation is assumed to be directly linked to regional swell topography, the maximum height of the swell is expected to occur at the centre of the Cape Verde archipelago. Instead, the islands are located to the southwest of the swell crest and there is no clear explanation for why the buoyant influence of magmatically emplaced undercrustal material would be offset to the northeast. Assuming that the residual mantle Bouguer anomaly over the North Atlantic is caused by variations in crustal thickness, Wang *et al.* (2011) suggest that the crust beneath the entire Cape Verde Swell is anomalously (>7 km) thick. An above average crustal thickness is not supported by the *final* velocity-depth model. Instead, the anomalies must reflect a region of low density in the lithospheric mantle or deeper.

A significant residual negative gravity anomaly of amplitude -40 mGal and wavelength ~350 km can be seen in the plot of the difference between the observed FAA and the gravity anomaly produced by the variable T_e model of lithospheric flexure (Figure 5.13f – Chapter 5). The location of this anomaly, offset to the east of the centre of the archipelago, indicates that the variation in T_e is likely to have a complex spatial pattern with a low T_e present beneath the northwest chain of islands and beneath the oldest islands to the east. This may indicate localised thermal rejuvenation of the plate, which is supported by observations of positive heat flow anomalies (Courtney & White, 1986) and which could produce up to 50% of the total swell height.

The results of 3-D flexure modelling indicate that the lithospheric plate responds to surface loading with a mechanical strength greater than would be expected based on its age alone. In order to counteract the surface load, an upwards-acting load must be present either within or below the lithosphere. There is no evidence to suggest the presence of an undercrustal body with sufficient buoyancy to support the entire swell and analysis of the gravity-topography slope and the geoid-topography ratio implies that the swell is compensated at a depth of ~80 km. This is close to the base of the lithospheric plate, ~100 km, and provides an indication that dynamic upwelling impinging on the base of a rigid lithosphere may transfer regional uplift to the plate surface.

Other large mid-plate swells that are not linked to individual island groups or chains include the African Superswell (Nyblade & Robinson, 1994) and the South Pacific Superswell (McNutt & Fischer, 1987). The explanations provided for the mechanism(s) that supports the anomalous topography of these superswells (e.g.

McNutt, 1998) are equally contentious, with evidence for both thermal rejuvenation of the lithosphere (e.g. Nyblade & Robinson, 1994) and dynamic upwelling in the asthenosphere (e.g. Adam & Bonneville, 2005; Tanaka *et al.*, 2009). Given that a thermal origin is often invoked for the buoyancy that drives the observed columnar asthenospheric upwellings, it becomes apparent that in areas where absolute plate motion is slow, anomalous swell height should initially be supported dynamically and that over time, support from thermal rejuvenation should also contribute. Conversely, where absolute plate motion over a fixed asthenospheric source is rapid, support should be almost entirely dynamic.

A combined synthesis of the results reveals that the Cape Verde Swell is almost certainly supported by a combination of mechanisms. The evidence for shallow crustal support is weak but cannot be entirely discounted. Dynamic support is invoked to explain the apparent regional strength of the lithosphere, which greatly exceeds the strength expected from the standard plate cooling model. Thermal rejuvenation may occur beneath the archipelago, although the evidence for this is indirect given that flexure modelling shows that the plate is not weakened beyond its expected strength. Thus, any support from thermal rejuvenation must act in conjunction with regional dynamic support which adds 'strength' to the plate.

6.6 Further work

This section contains suggestions of further geophysical investigations that could be conducted to test various aspects relating to the hypothesised dual compensation mechanism of the Cape Verde Swell.

More extensive mapping of the moat infill sediment thickness is crucial in order to constrain the results of 3-D lithospheric flexure. Although the available TWTT data covers a large area throughout the archipelago, knowledge of the shallow subseabed velocities is limited to direct measurements at DSDP site 368 (Lancelot *et al.*, 1978b) and those obtained from the *final* 2-D velocity-depth model along profile P01 (Figure 4.23a). A more widespread knowledge of the sediment thickness could be gained by additional MCS reflection profiles located to the east of the archipelago where current sediment thickness maps suggest a large accumulation of sediment that, in turn, requires spatial variations of T_e. The new data could be used to improve the current interpretations of the existing reflection data

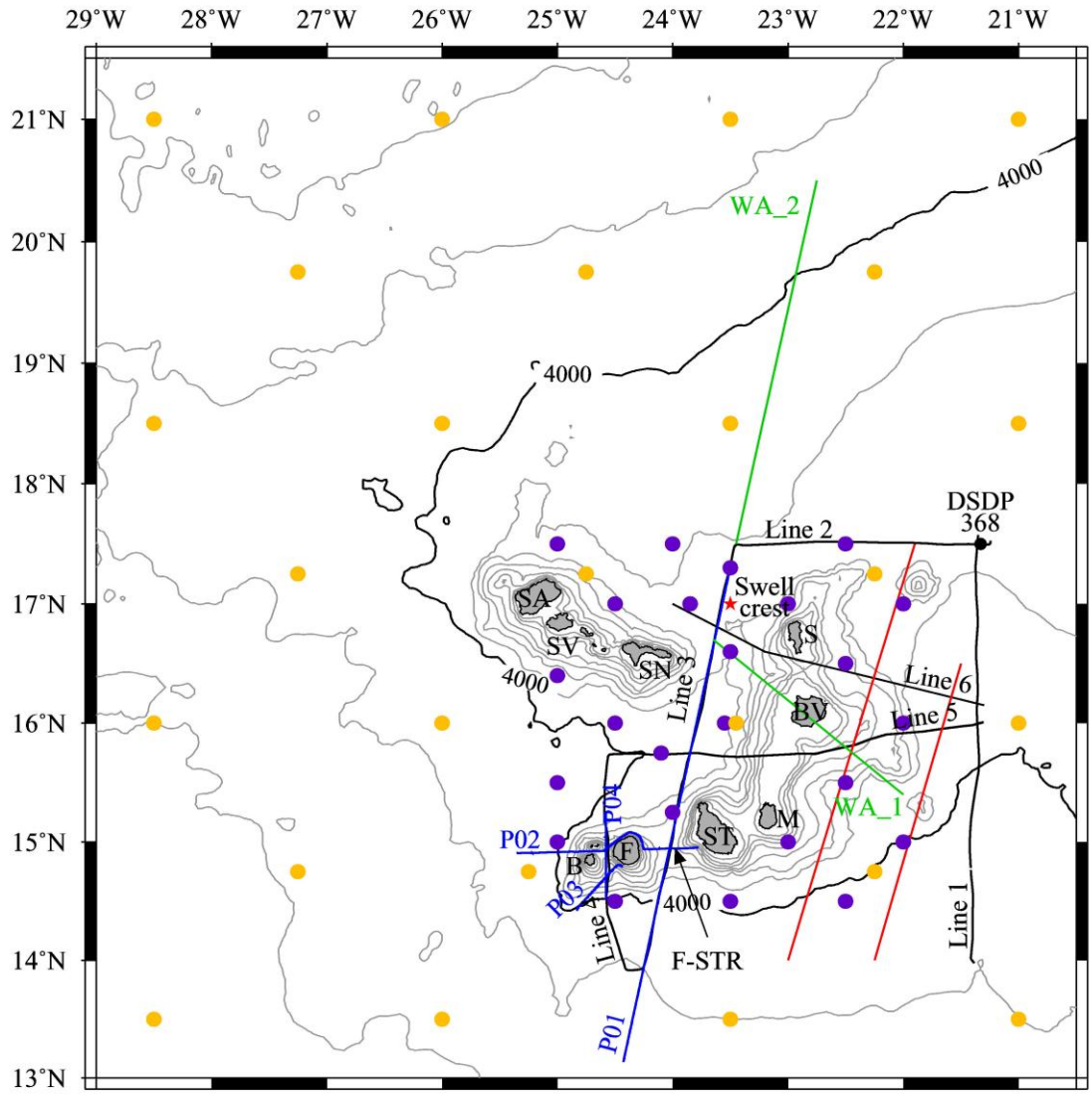

Figure 6.5 Further data acquisition at the Cape Verde Swell. The 4000 m bathymetric contour is used to outline the extent of the swell and the red star indicates the location of the swell crest. Bathymetric contours (grey) are plotted with a 500 m contour interval. a) Location of existing MCS profiles from RRS *Charles Darwin* cruise CD8/85 (black lines), see Ali *et al.* (2003), and WA profiles from R/V *Meteor* cruise M62/3 (blue lines). DSDP site 368 is indicated with a black dot. Proposed locations of MCS profiles (red lines), co-located MCS and WA profiles (green lines) and OBS locations for the long-term passive seismic experiments (deployment 1 – purple dots; deployment 2 – orange dots). Islands: SA, Santo Antão; SV, São Vicente; SN, São Nicolau; S, Sal; BV, Boa Vista; M, Maio; ST, Santiago; F, Fogo; B, Brava. F-STR, Fogo-Santiago Ridge. See text for discussion.

Additional WA profiles would provide greater constraint on the position of the Moho (Figure 6.5). Two profiles that have the potential to provide data to enable a critical evaluation of the current model of swell support would be:

1. Across one of the islands (e.g. Boa Vista), including both land and ocean-bottom recording instruments and sea shots, to test the possibility of highly localised undercrustal magmatic material.

2. Extending radially from the swell crest to the north, an area unaffected by island construction, to further examine the regional crustal structure.

Although there is no evidence of any undercrustal material beneath profile P01, results from receiver function analysis of teleseismic arrivals recorded at land-based stations (Lodge & Helffrich, 2006) suggest that crustal thickening only occurs locally beneath the islands. Additionally, the results presented in this thesis suggest that the Cape Verde Swell is supported by a combination of lithospheric thermal rejuvenation and dynamic upwelling in the asthenosphere. These hypotheses could be tested by completing a large-scale passive seismic experiment involving the long-term deployment of OBSs in two networks, one located around the archipelago and a second extending coverage to the north where the lithosphere has been unaffected by island building magmatism and the associated swell (Figure 6.5). Such deployments would be used to acquire a dataset comparable to that of the Hawaiian Plume-Lithosphere Undersea Mantle Experiment (PLUME – Leahy *et al.*, 2010; Wolfe *et al.*, 2011), and a combination of techniques, including body and surface wave tomographic imaging and receiver function analyses would be applied to investigate the whole lithospheric structure over the entire Cape Verde Swell.

It has been suggested that the topographic anomaly observed at Bermuda is the conjugate pair of the Cape Verde Swell, affecting lithosphere of a similar age (~120 Ma) on the opposite side of the Atlantic, and that they may have formed by the same process (Vogt, 1991). Figure 6.6 shows the topographic anomaly of the Bermuda Swell, together with the long-wavelength components of the satellite gravity field and the geoid. If the Bermuda and Cape Verde swells were created simultaneously at the MAR, together forming an 'Atlantic Superswell', and since the formation have individually remained isostatically compensated, then a relatively shallow mechanism for support is implied (either crustal or lithospheric). Although a synthesis of the results presented in this study with those available in the literature favour a more recent formation of the Cape Verde Swell, by a combination of thermal rejuvenation and dynamic upwelling, the two features are of similar lateral extent (although the amplitude of topographic anomaly at Bermuda is half that seen at the Cape Verde Swell) and the absolute plate motion of the North American Plate is also relatively low (less than twice the speed of the African Plate; Gripp & Gordon, 2002). The Bermuda Swell, therefore, presents an ideal location to conduct

an equivalent geophysical investigation to compare with the results obtained for the Cape Verde Swell.

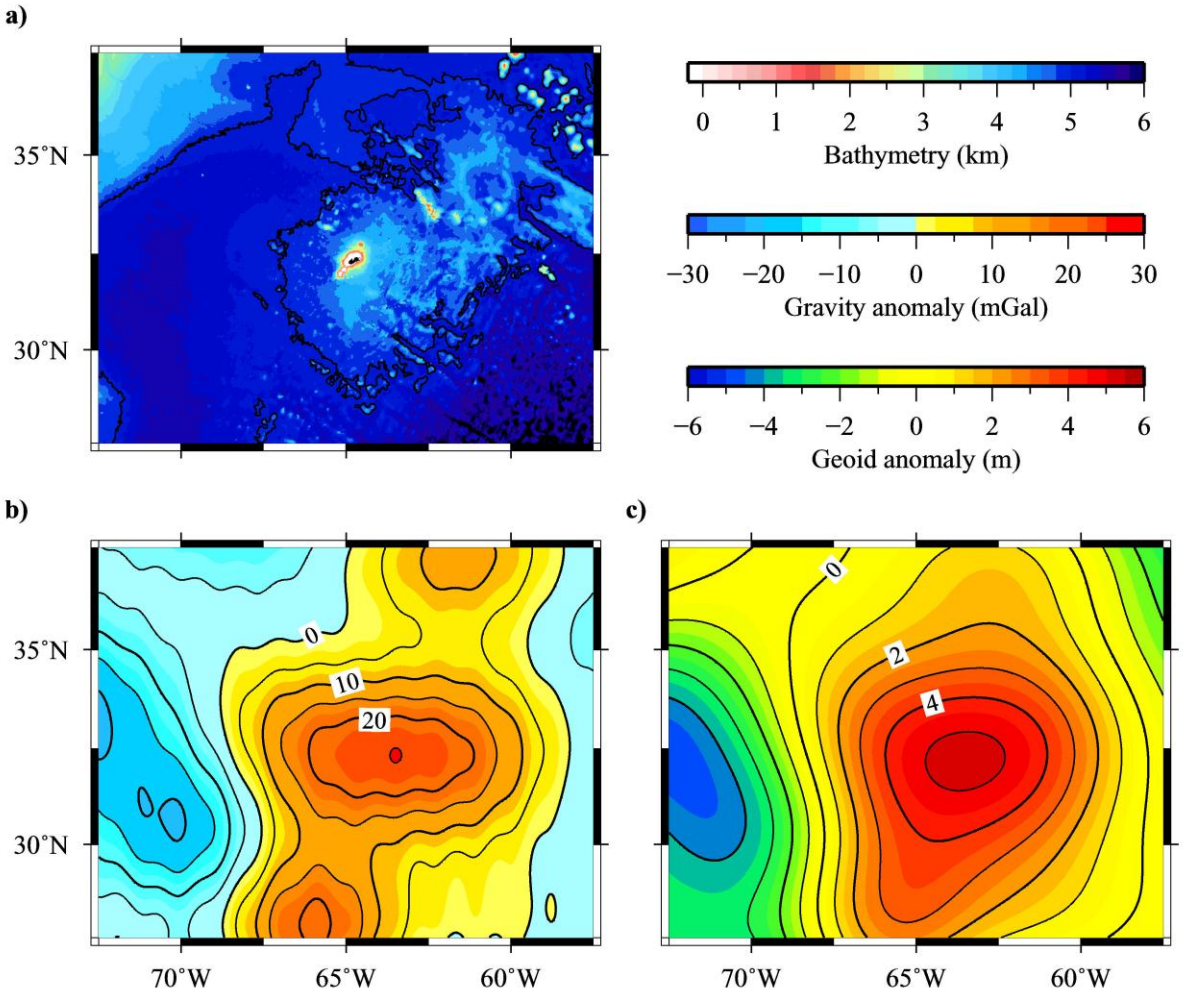

Figure 6.6 Geophysical characteristics of the Bermuda Swell. a) Bathymetry of the swell outlined by the 5 km bathymetric contour. b) Long-wavelength satellite-derived Free-air gravity field complete to degree and order 10<n=m<72 (OSU91A, Pavlis & Rapp, 1990) showing a positive anomaly of ~25 mGal. Gravity contours plotted (black lines) with a contour interval of 5 mGal. c) Long-wavelength geoid anomaly complete to degree and order 10<n=m<72 (Lemoine *et al.*, 1998) showing a positive anomaly of ~5 m. Geoid contours plotted (black lines) with a contour interval of 1 m. As with the Cape Verde Swell there is good spatial correlation between the observed bathymetry, gravity and geoid anomalies.

7. Conclusions

This thesis has documented an investigation of the crustal structure in the region of the Cape Verde archipelago, providing insight into the flexural response of the lithosphere to loading and the support mechanism of the Cape Verde Swell. The aim of this investigation was to test the proposed support mechanism hypotheses by ascertaining the structure and mechanical properties of the oceanic lithosphere. A range of analysis and modelling techniques were applied to the geophysical dataset and the results are summarised in the following conclusions:

- The average thickness and velocity structure of the igneous basement beneath the Cape Verde Swell is consistent with that of the standard definition of mature Atlantic oceanic crust of White *et al.* (1992). There is no evidence to support a significantly thickened crust and, consequently, that the swell is supported by a thickened crustal root.
- Although there is no direct evidence of lower crustal velocities exceeding 7.3 km s^{-1}, indicative of undercrustal magmatic material, a thin layer of high velocity material may exist within the resolution limits of the seismic and gravity data (<2 km).
- Flexure modelling implies that the lithosphere is stronger than expected from its magnetic anomaly-derived age. Regional 'strengthening' and swell support by undercrustal loads is ruled out by the seismic data, but this does not preclude the possibility of thicker crust to the northeast of the study area, beneath the crest of the swell. Synthesising the results of this study with those in the literature, for both the Cape Verde Swell and other swells, supports a model of dynamic upwelling within the asthenosphere.

- The residual medium-wavelength, negative gravity anomaly observed during both 2-D and 3-D modelling could be caused by reheating of the lithosphere. Heating reduces the strength of the lithospheric plate, increasing the amplitude of flexure due to surface loading, which, in turn, leads to a larger accommodation space for moat infill sediments.
- Analysis of the gravity-topography slope and the geoid-topography ratio indicates a compensation depth for the swell of ~80 km, within the lower lithosphere. This could represent the mean compensation depth between anomalous lithosphere (centred at ~50 km depth) and the impingement of hot, low-density upwelling material on the base of the lithosphere (at ~100 km depth)
- The results of this study imply that the mechanism that results in the observed topographic swell, is a column of hot upwelling material impinging on the base of the lithosphere. This upwelling column produces the observed anomalous topography, gravity and geoid anomalies through a combination of dynamic support and significant, but localised, thermal rejuvenation of the lithosphere.

References

Adam, C. & Bonneville, A., 2005. Extent of the South Pacific Superswell, *J. Geophys. Res.*, **110,** B09408, doi: 10.1029/2004JB003465.

Ali, M.Y., 2003. A geophysical study of lithospheric flexure in the vicinity of the Cape Verde Islands. Ph.D. thesis (unpublished), University of Oxford, pp255.

Ali, M.Y., Watts, A.B. & Hill, I., 2003. A seismic reflection profile study of lithospheric flexure in the vicinity of the Cape Verde Islands, *J. Geophys. Res.*, **108,** 2239, doi:10.1029/2002JB002155.

Avouac, J.P. & Burov, E.B., 1996. Erosion as a driving mechanism of intracontinental mountain growth, *J. Geophys. Res.*, **101,** 17747–17769.

Barry, K.M., Cavers, D.A. & Kneale, C.W., 1975. Report on recommended standards for digital tape formats, *Geophysics,* **2,** 344–352.

Bijwaard, H. & Spakman, W., 1999. Tomographic evidence for a narrow whole mantle plume below Iceland, *Earth Planet. Sci. Lett.*, **166,** 121–126.

Bowin, C., 1983. Depth of principle mass anomalies contribution to the Earth's geoidal undulations and gravity anomalies, *Mar. Geodesy*, **7,** 61–100.

Calmant, S., Francheteau, J. & Cazenave, A., 1990. Elastic layer thickening with age of the oceanic lithosphere: a tool for prediction of the age of volcanoes or oceanic crust, *Geophys. J. Int.*, **100,** 59–67.

Canales, J.P. & Dañobeitia, J.J., 1998. The Canary Islands swell: a coherence analysis of bathymetry and gravity, *Geophys. J. Int.,* **132,** 479–488.

Canales, J.P., Ito, G., Detrick, R.S. & Sinton, J., 2002. Crustal thickness along the western Galápagos Spreading Center and the compensation of the Galápagos hotspot swell, *Earth Planet. Sci. Lett.*, **203,** 311–327.

Cande, S.C. & Kent, D.V., 1992. A new geomagnetic polarity time scale for the Late Cretaceous and Cenozoic, *J. Geophys. Res.*, **97,** 13917–13951.

Cande, S.C. & Kent, D.V., 1995. Revised calibration of the geomagnetic polarity timescale, *J. Geophys. Res.*, **100,** 6093–6095.

Caress, D.W., McNutt, M.K., Detrick, R.S. & Mutter, J.C., 1995. Seismic imaging of hotspot-related crustal underplating beneath the Marquesas Islands, *Nature*, **373,** 600–603.

Carlson, R.L. & Herrick, C.N., 1990. Densities and porosities in the oceanic crust and their variations with depth and age, *J. Geophys. Res.*, **95,** 9153–9170.

Carlson, R.L. & Raskin, G.S., 1984. Density of the ocean crust, *Nature*, **311,** 555–558.

Cazenave, A., Dominh, K., Rabinowicz, M. & Ceuleneer, G., 1988. Geoid and depth anomalies over ocean swells and troughs: evidence of an increasing trend of the geoid to depth ratio with age of plate, *J. Geophys. Res.*, **93,** 8064–8077.

Charvis, P., Laesanpura, A., Gallart, J., Hirn, A., Lépine, J-C., de Voogd, B., Minshull, T.A., Hello, Y. & Pontoise, B., 1999. Spatial distribution of hotspot material added to the lithosphere under La Réunion, from wide-angle seismic data, *J. Geophys. Res.*, **104,** 2875–2893.

Christensen, N.I. & Mooney, W.D., 1995. Seismic velocity structure and composition of the continental crust: a global view, *J. Geophys. Res.*, **100,** 9761–9788.

Cohen, J. & Stockwell, J., 2000. *CWP/SU: Seismic Unix release 34: a free package for seismic research and processing*, Centre for Wave Phenomenon, Colorado School of Mines.

Collier, J.S. & Watts, A.B., 2001. Lithospheric response to volcanic loading by the Canary Islands: constraints from seismic reflection data in their flexural moat, *Geophys. J. Int.,* **147,** 660–676.

Contreras-Reyes, E., Grevemeyer, I., Watts, A.B., Planert, L., Flueh, E.R. & Peirce, C., 2010. Crustal intrusion beneath the Louisville hotspot track, *Earth Planet. Sci. Lett.,* **289,** 323–333, doi:10.1016/j.epsl.2009.11.020.

Courtney, R.C. & White, R.S., 1986. Anomalous heat flow and geoid across the Cape Verde Rise: evidence for dynamic support from a thermal plume in the mantle, *Geophys. J. R. Astr. Soc.,* **87,** 815–867.

Crosby, A.G. & McKenzie, D., 2009. An analysis of young ocean depth, gravity and global residual topography, *Geophys. J. Int.,* **178,** 1198–1219, doi:10.1111/j.1365-246X.2009.04224.x.

Crosby, A.G., McKenzie, D. & Sclater, J.G., 2006. The relationship between depth, age and gravity in the oceans, *Geophys. J. Int.,* **166,** 553–573, doi:10.1111/j.1365-246X.2006.03015.x.

Crough, S.T., 1978. Thermal origin of mid-plate hot-spot swells, *Geophys. J. R. Astr. Soc.,* **55,** 451–469.

Crough, S.T., 1983. Hotspot swells, *Ann. Rev. Earth Planet. Sci.,* **11,** 165–193.

Crough, S.T. & Jurdy, D.M., 1980. Subducted lithosphere, hotspots and the geoid, *Earth Planet. Sci. Lett.,* **48,** 15–22.

Dash, B.P., Ball, M.M., King, G.A., Butler, L.W. & Rona, P.A., 1976. Geophysical investigation of Cape Verde archipelago, *J. Geophys. Res.,* **81,** 5249–5259.

Davies, D.R. & Davies, J.H., 2009. Thermally-driven mantle plumes reconcile multiple hot-spot observations, *Earth Planet. Sci. Lett.,* **278,** 50–54, doi:10.1016/j.epsl.2008.11.027.

Davis, E.E. & Lister, C.R.B., 1974. Fundamentals of ridge crest topography, *Earth Planet. Sci. Lett.,* **21,** 405–413.

Day, S.J., da Silva, S.I.N.H. & Fonseca, J.F.B.D., 1999. A past giant lateral collapse and present-day flank instability of Fogo, Cape Verde Islands, *J. Volc. Geotherm. Res.*, **94,** 191–218.

Detrick, R.S. & Crough, S.T., 1978. Island subsidence, hot spots, and lithospheric thinning, *J. Geophys. Res.*, **83,** 1236–1244.

Dewey, J.F. & Bird, J.M., 1970. Mountain belts and the new global tectonics, *J. Geophys. Res.*, **75,** 2625–2647.

Dobrin, M.B. & Savit, C.H., 1988. *Introduction to geophysical prospecting fourth edition,* McGraw-Hill Inc., U.S.A.

Duncan, R.A. & Keller, R.A., 2004. Radiometric ages for basement rocks from the Emperor Seamounts, ODP Leg 197, *Geochem. Geophys. Geosyst.,* **5,** Q08L03, doi:10.1029/2004GC000704.

Duncan, R.A. & Richards, M.A., 1991. Hotspots, mantle plumes, flood basalts, and true polar wander, *Rev. Geophys.,* **29,** 31–50.

Duprat, H.I., Friis, J., Holm, P.M., Grandvuinet, T. & Sørensen, R.V., 2007. The volcanic and geochemical development of São Nicolau, Cape Verde Islands: constraints from field and $^{40}Ar/^{39}Ar$ evidence, *J. Volc. Geotherm. Res.*, **162,** 1–19, doi:10.1016/j.jvolgeores.2007.01.001.

Dyhr, C.T. & Holm, P.M., 2010. A volcanological and geochemical investigation of Boa Vista, Cape Verde Islands; $^{40}Ar/^{39}Ar$ geochronology and field constraints, *J. Volc. Geotherm. Res.,* **189,** 19–32, doi:10.1016/j.jvolgeores.2009.10.010.

Feighner, M.A. & Richards, M.A., 1994. Lithospheric structure and compensation mechanisms of the Galápagos Archipelago, *J. Geophys. Res.,* **99,** 6711–6729.

Filmer, P.E. & McNutt, M.K., 1989. Geoid anomalies over the Canary Islands group, *Mar. Geophys. Res.*, **11,** 77–87.

Filmer, P.E., McNutt, M.K. & Wolfe, C.J., 1993. Elastic thickness of the lithosphere in the Marquesas and Society Islands, *J. Geophys. Res.,* **98,** 19565–19577.

Grevemeyer, I., 1999. Isostatic geoid anomalies over mid-plate swells in the Central North Atlantic, *Geodynamics,* **28,** 41–50.

Grevemeyer, I., Weigel, W. & Jennrich, C., 1998. Structure and ageing of oceanic crust at 14° S on the East Pacific Rise, *Geophys. J. Int.,* **135,** 573–584.

Grevemeyer, I., Flueh, E.R., Reichert, C., Bialas, J., Klaschen, D. & Kopp, C., 2001a. Crustal architecture and deep structure of the Ninetyeast Ridge hotspot trail from active-source ocean bottom seismology, *Geophys. J. Int.,* **144,** 414–431.

Grevemeyer, I., Weigel, W., Schüssler, S. & Avedik, F., 2001b. Crustal and upper mantle seismic structure and lithospheric flexure along the Society Island hotspot chain, *Geophys. J. Int.,* **147,** 123–140.

Grevemeyer, I. & the Shipboard Scientific Party, 2004. *Meteor report, Equatorial and South Atlantic, Part 3, Cruise no. M62, Leg 3, CHARISMA – Cape Verde Hotspot: A Seismic Refraction study of ISostasy and MAgmatic underplating.* Cruise report (unpublished), IFM-GEOMAR.

Grevemeyer, I., Helffrich, G., Faria, B., Booth-Rea, G., Schnabel, M. & Weinrebe, W., 2010. Seismic activity at Cadamosto seamount near Fogo Island, Cape Verdes – formation of a new ocean island?, *Geophys. J. Int.,* **180,** 552–558, doi:10.1111/j.1365-246X.2009.04440.x.

Gripp, A.E. & Gordon, R.G., 2002. Young tracks of hotspot and current plate velocities, *Geophys. J. Int.,* **150,** 321–361.

Hamilton, E.L., 1978. Sound velocity-density relations in sea-floor sediments and rocks, *J. Acoust. Soc. Am.,* **63,** 366–377.

Haxby, W.F. & Turcotte, D.L., 1978. On isostatic geoid anomalies, *J. Geophys. Res.,* **83,** 5473–5478.

Hayes, D.E., 1988. Age-depth relationships and depth anomalies in the Southeast Indian Ocean and South Atlantic Ocean, *J. Geophys. Res.,* **93,** 2937–2954, doi:10.1029/JB093iB04p02937.

Hayes, D.E. & Rabinowitz, P.D., 1975. Mesozoic magnetic lineations and the magnetic quiet zone off northwest Africa, *Earth Planet. Sci. Lett.*, **28,** 105–115.

Heirtzler, J.R., Dickson, G.O., Herron, E.M., Pitman, W.C. & Le Pichon, X., 1968. Marine magnetic anomalies, geomagnetic field reversals, and motions of the ocean floor and continents, *J. Geophys. Res.*, **73,** 2119–2136.

Heleno da Silva, S.I.N., Day, S.J. & Fonseca, J.F.B.D., 1999. Fogo Volcano, Cape Verde Islands: seismicity-derived constraints on the mechanism of the 1995 eruption, *J. Volc. Geotherm. Res.*, **94,** 219–231.

Hill, I.A., 1985. *R.R.S. Charles Darwin cruise report 8/85: geophysical studies of the Cape Verde archipelago.* Cruise report (unpublished), University of Leicester.

Hole, J.A. & Zelt, B.C., 1995. 3-D finite-difference reflection traveltimes, *Geophys. J. Int.*, **121,** 427–434.

Holm, P.M., Wilson, J.R., Christensen, B.P., Hansen, L., Hansen, S.L., Hein, K.M., Mortensen, A.K., Pedersen, R., Plesner, S. & Runge, M.K., 2006. Sampling the Cape Verde mantle plume: evolution of melt compositions on Santo Antão, Cape Verde Islands, *J. Petrology*, **47,** 145–189, doi:10.1093/petrology/egi071.

Holm, P.M., Grandvuinet, T., Friis, J., Wilson, J.R., Barker, A.K. & Plesner, S., 2008. An $^{40}Ar/^{39}Ar$ study of the Cape Verde hot spot: temporal evolution in a semistationary plate environment, *J. Geophys. Res.*, **113,** B08201, doi:10.1029/2007JB005339.

I.O.C., I.H.O. & B.O.D.C., 2003. Centenary Edition of the GEBCO Digital Atlas, published on CD-ROM on behalf of the Intergovernmental Oceanographic Commission and the International Hydrographic Organisation as part of the General Bathymetric Chart of the Oceans: British Oceanographic Data Centre, Liverpool.

Ito, G. & Clift, P.D., 1998. Subsidence and growth of Pacific Cretaceous plateaus, *Earth Planet. Sci. Lett.*, **161,** 85–100.

Jones, S.M., 2003. Test of a ridge-plume interaction model using oceanic crustal structure around Iceland, *Earth Planet. Sci. Lett.*, **208,** 205–218, doi:10.1016/S0012-821X(03)00050-5.

Kim, S.-S. & Wessel, P., 2008. Directional median filtering for regional-residual separation of bathymetry, *Geochem. Geophys. Geosys.*, **9,** Q03005, doi:10.1029/2007GC001850.

Koppers, A.A.P. & Watts, A.B., 2010. Intraplate seamounts as a window into deep Earth processes, *Oceanography*, **23,** 42–57.

Koppers, A.A.P., Duncan, R.A. & Steinberger, B., 2004. Implications of a nonlinear $^{40}Ar/^{39}Ar$ age progression along the Louisville seamount trail for models of fixed and moving hot spots, *Geochem. Geophys. Geosyst.*, **5,** Q06L02, doi:10.1029/2003GC000671.

Korenaga, J., Holbrook, W.S., Kent, G.M., Kelemen, P.B., Detrick, R.S., Larsen, H.C., Hopper, J.R. & Dahl-Jensen, T., 2000. Crustal structure of the southeast Greenland margin from joint refraction and reflection seismic tomography, *J. Geophys. Res.*, **105,** 21591–21614.

LaBrecque, J.L., Kent, D.V. & Cande, S.C., 1977. Revised magnetic polarity time scale for Late Cretaceous and Cenozoic time, *Geology*, **5,** 330–335, doi:10.1130/0091-7613(1977)5<330:RMPTSF>2.0.CO;2.

LaCoste & Romberg LLC, 1998. *Model "S" air-sea dynamic gravity meter*. Instruction manual (unpublished), LaCoste & Romberg LLC, Texas.

Lancelot, Y. & the Shipboard Scientific Party, 1978a. Site 367: Cape Verde Basin, in *Init. Rep. DSDP*, **Vol. 41,** 163–232, eds. Lancelot, Y., Seibold, E. & Gardner, J.V., US Government Printing Office, Washington, DC.

Lancelot, Y. & the Shipboard Scientific Party, 1978b. Site 368: Cape Verde Rise, in *Init. Rep. DSDP*, **Vol. 41,** 233–326, eds. Lancelot, Y., Seibold, E. & Gardner, J.V., US Government Printing Office, Washington, DC.

Leahy, G.M., Collins, J.A., Wolfe, C.J., Laske, G. & Solomon, S.C., 2010. Underplating of the Hawaiian Swell: evidence from teleseismic receiver functions, *Geophys. J. Int.*, **183,** 313–329, doi:10.1111/j.1365-246X.2010.04720.x.

Lemoine, F.G., Kenyon, S.C., Factor, J.K., Trimmer, R.G., Pavlis, N.K., Chinn, D.S., Cox, C.M., Klosko, S.M., Luthcke, S.B., Torrence, M.H., Wang, Y.M., Williamson, R.G., Pavlis, E.C., Rapp, R.H. & Olson, T.R., 1998. *The development of the joint NASA, GSFC and the National Imagery and Mapping Agency (NIMA) geopotential model EGM96,* NASA technical report, NASA/TP-1998-206861.

Lindwall, D.A., 1988. A two-dimensional seismic investigation of crustal structure under the Hawaiian Islands near Oahu and Kauai, *J. Geophys. Res.*, **93,** 12107–12122.

Lodge, A. & Helffrich, G., 2006. Depleted swell root beneath the CapeVerde Islands, *Geology*, **34,** 449–452, doi:10.1130/G22030.1.

Ludwig, J.W., Nafe, J.E. & Drake, C.L., 1970. Seismic refraction, in *The Sea,* **Vol. 4,** 53–84, ed. Maxwell, A.E., Wiley, New York.

Madeira, J., Mata, J., Mourão, C., da Silveira, A.B., Martins, S., Ramalho, R. & Hoffmann, D.L., 2010. Volcano-stratigraphic and structural evolution of Brava Island (Cape Verde) based on $^{40}Ar/^{39}Ar$, U-Th and field constraints, *J. Volc. Geotherm. Res.*, **196,** 219–235, doi:10.1016/j.jvolgeores.2010.07.010.

Marks, K.M. & Sandwell, D.T., 1991. Analysis of geoid height versus topography for oceanic plateaus and swells using nonbiased linear regression, *J. Geophys. Res.*, **96,** 8045–8055.

Marks, K.M. & Smith, W.H.F., 2007. Some remarks on resolving seamounts in satellite gravity, *Geophys. Res. Lett.*, **34,** L03307, doi:10.1029/2006GL028857.

Marty, J.C. & Cazenave, A., 1989. Regional variations in subsidence rate of oceanic plates: a global analysis, *Earth Planet. Sci. Lett.*, **94,** 301–315.

Masson, D.G., Le Bas, T.P., Grevemeyer, I. & Weinrebe, W., 2008. Flank collapse and large-scale landsliding in the Cape Verde Islands, off West Africa, *Geochem. Geophys. Geosyst.*, **9,** Q07015, doi:10.1029/2008GC001983.

McKenzie, D., 2010. The influence of dynamically supported topography on estimates of T_e, *Earth Planet. Sci. Lett.*, **295,** 127–138, doi:10.1016/j.epsl.2010.03.033.

McKenzie, D., Jackson, J. & Priestley, K., 2005. Thermal structure of oceanic and continental lithosphere, *Earth Planet. Sci. Lett.*, **233,** 337–349, doi:10.1016/j.epsl.2005.02.005.

McNutt, M., 1988. Thermal and mechanical-properties of the Cape Verde Rise, *J. Geophys. Res.*, **93,** 2784–2794.

McNutt, M.K., 1998. Superswells, *Rev. Geophys.*, **36,** 211–244.

McNutt, M. & Fischer, K., 1987. The South Pacific Superswell, in *Seamounts, Islands, and Atolls, Geophys. Monogr. Ser.*, **43,** 25–34, eds. Keating, B.H. *et al.*, AGU, Washington, D.C.

Minshull, T.A. & Charvis, P., 2001. Ocean island densities and models of lithospheric flexure, *Geophys. J. Int.*, **145,** 731–739.

Mitchell, J.G., Le Bas, M.J., Zielonka, J. & Furnes, H., 1983. On dating the magmatism of Maio, Cape Verde Islands, *Earth Planet. Sci. Lett.*, **64,** 61–76.

Monnereau, M. & Cazenave, A., 1990. Depth and geoid anomalies over oceanic hotspot swells: a global survey, *J. Geophys. Res.*, **95,** 15429–15438.

Monnereau, M., Rabinowicz, M. & Arquis, E., 1993. Mechanical erosion and reheating of the lithosphere: a numerical model for hotspot swells, *J. Geophys. Res.*, **98,** 809–823.

Montelli, R., Nolet, G., Dahlen, F.A., Masters, G., Engdahl, E.R. & Hung, S-.H., 2004. Finite-frequency tomography reveals a variety of plumes in the mantle, *Science*, **303,** 338–343, doi: 10.1126/science.1092485.

Montelli, R., Nolet, G., Dahlen, F.A. & Masters, G., 2006. A catalogue of deep mantle plumes: new results from finite-frequency tomography, *Geochem. Geophys. Geosys.,* **7,** Q11007, doi:10.1029/2006GC001248.

Morgan, W.J., 1983. Hotspot tracks and the early rifting of the Atlantic, *Tectonophysics,* **94,** 123–139.

Morgan, J.V., Barton, P.J. & White, R.S., 1989. The Hatton Bank continental margin .3. Structure from wide-angle OBS and multichannel seismic refraction profiles, *Geophys. J. Int.,* **98,** 367–384.

Morgan, J.P., Morgan, W.J. & Price, E., 1995. Hotspot melting generates both hotspot volcanism and a hotspot swell?, *J. Geophys. Res.,* **100,** 8045–8062.

Moritz, H., 1980. Geodetic Reference System 1980, *J. Geodesy,* **74,** 128–133, doi:10.1007/s001900050278.

Moser, T.J., 1991. Shortest path calculation of seismic rays, *Geophysics,* **56,** 59–67.

Moser, T.J., Nolet, G. & Snieder, R., 1992. Ray bending revisited, *Bull. Seismol. Soc. Am.,* **82,** 259–288.

Müller, R.D., Sdrolias, M., Gaina, C. & Roest, W.R., 2008. Age, spreading, and spreading asymmetry of the world's ocean crust, *Geochem. Geophys. Geosys.*, **9,** Q04006, doi:10.1029/2007GC001743.

Mutter, C.Z. & Mutter, J.C., 1993. Variations in thickness of layer 3 dominate oceanic crustal structure, *Earth Planet. Sci. Lett.,* **117,** 295–317.

Nafe, J.E. & Drake, C.L., 1957. Variation with depth in shallow and deep water marine sediments of porosity, density and the velocities of compressional and shear waves, *Geophysics,* **22,** 523–552, doi:10.1190/1.1438386.

Nettleton, L.L., 1976. *Gravity and magnetics in oil prospecting,* McGraw-Hill Inc., U.S.A.

Nyblade, A.A. & Robinson, S.W., 1994. The African Superswell, *Geophys. Res. Lett.,* **21,** 765–768.

Parsons, B. & Sclater, J.G., 1977. An analysis of the variation of ocean floor bathymetry and heat flow with age, *J. Geophys. Res.*, **82,** 803–827.

Pavlis, N.K. & Rapp, R.H., 1990. The development of an isostatic gravitational model to degree and order 360 and its use in global gravity modelling, *Geophys. J. Int.,* **100,** 369–378.

Pim, J., Peirce, C., Watts, A.B., Grevemeyer, I. & Krabbenhoeft, A., 2008. Crustal structure and origin of the Cape Verde Rise, *Earth Planet. Sci. Lett.,* **272,** 422–428, doi:10.1016/j.epsl.2008.05.012.

Peirce, C. & Barton, P.J., 1991. Crustal structure of the Madeira-Tore Rise, eastern North Atlantic – results of a DOBS wide-angle and normal incidence seismic experiment in the Josephine Seamount region, *Geophys. J. Int.,* **106,** 357–378.

Plesner, S., Holm, P.M. & Wilson, J.R., 2003. $^{40}Ar/^{39}Ar$ geochronology of Santo Antão, Cape Verde Islands, *J. Volc. Geotherm. Res.,* **120,** 103–121.

Pollack, H.N., Hurter, S.J. & Johnson, J.R., 1993. Heat flow from the Earth's interior: analysis of the global data set, *Rev. Geophys.*, **31,** 267–280.

Pollitz, F.F., 1991. Two-stage model of African absolute motion during the last 30 million years, *Tectonophysics*, **194,** 91–106.

Ribe, N.M. & Christensen, U.R., 1994. Three-dimensional modeling of plume-lithosphere interaction, *J. Geophys. Res.*, **99,** 669–682.

Robinson, E.M., 1988. The topographic and gravitational expression of density anomalies due to melt extraction in the uppermost oceanic mantle, *Earth Planet. Sci. Lett.*, **90,** 221–228.

Robinson, E.M. & Parsons, B., 1988. Effect of shallow low-viscosity zone on the formation of midplate swells, *J. Geophys. Res.,* **93,** 3144–3156.

Rona, P.A., 1970. Comparison of continental margins of eastern North America at Cape Hatteras and northwestern Africa at Cape Blanc, *Am. Assoc. Petr. Geol. Bull.,* **54,** 129–158.

Sandwell, D.T. & MacKenzie, K.R., 1989. Geoid height versus topography for oceanic plateaus and swells, *J. Geophys. Res.,* **94,** 7403–7418.

Sandwell, D.T. & Smith, W.H.F., 1997. Marine gravity anomaly from Geosat and ERS 1 satellite altimetry, *J. Geophys. Res.,* **102,** 10039–10054.

Sandwell, D.T. & Smith, W.H.F., 2009. Global marine gravity from retracked Geosat and ERS-1 altimetry: ridge segmentation versus spreading rate, *J. Geophys. Res.,* **114,** B01411, doi:10.1029/2008JB006008.

Sclater, J.G., Jaupart, C. & Galson, D., 1980. The heat flow through oceanic crust and continental crust and the heat loss of the Earth, *Rev. Geophys. Space Physics,* **18,** 269–311.

Seibold, E. & Hinz, K., 1974. Continental slope construction and destruction, West Africa, in *The geology of continental margins,* pp. 179–196, eds. Burk, C.A. & Drake, C.L., Springer Verlag, New York.

Sheehan, A.F. & McNutt, M.K., 1989. Constraints on thermal and mechanical structure of the oceanic lithosphere at the Bermuda Rise from geoid height and depth anomalies, *Earth Planet. Sci. Lett.,* **93,** 377–391.

Sleep, N.H., 1992. Hotspot volcanism and mantle plumes, *Ann. Rev. Earth Planet. Sci.,* **20,** 19–43.

Sleep, N.H., 1995. Geophysics – a wayward plume, *Nature,* **378,** 19–20.

Stein, C.A. & Stein, S., 1992. A model for the global variation in oceanic depth and heat flow with lithospheric age, *Nature,* **359,** 123–129.

Steinberger, B., 2000. Plumes in a convecting mantle: models and observations for individual hotspots, *J. Geophys. Res.,* **105,** 11127–11152.

Stillman, C.J., Furnes, H., Le Bas, M.J., Robertson, A.H.F. & Zielonka, J., 1982. The geological history of Maio, Cape Verde Islands, *J. Geol. Soc.,* **139,** 347–361.

Talwani, M., Worzel, J.L. & Landisman, M., 1959. Rapid gravity computations for two-dimensional bodies with application to the Mendocino submarine fracture zone, *J. Geophys. Res.,* **64,** 49–59.

Tanaka, S., Obayashi, M., Suetsugu, D., Shiobara, H., Sugioka, H., Yoshimitsu, J., Kanazawa, T., Fukao, Y. & Barruol, G., 2009. P-wave tomography of the mantle beneath the South Pacific Superswell revealed by joint ocean floor and islands broadband seismic experiments, *Phys. Earth. Planet. Interiors,* **172,** 268–277, doi:10.1016/j.pepi.2008.10.016.

Telford, W.M., Geldart, L.P. & Sheriff, R.E., 1990. *Applied geophysics second edition,* Cambridge University Press, Cambridge.

Vidale, J.E., 1988. Finite-difference calculation of traveltimes, *Bull. Seismol. Soc. Am.,* **78,** 2062–2076.

Vidale, J.E., 1990. Finite-difference calculation of traveltimes in three dimensions, *Geophysics,* **55,** 521–526.

Vogt, P.R., 1991. Bermuda and Appalachian-Labrador rises: common non-hotspot processes?, *Geology,* **19,** 41–44.

Wang, T., Lin, J., Tucholke, B. & Chen, Y.J., 2011. Crustal thickness anomalies in the North Atlantic Ocean basin from gravity analysis, *Geochem, Geophys, Geosys.,* **12,** Q0AE02, doi:10.1029/2010GC003402.

Watts, A.B., 1976. Gravity and bathymetry in the Central Pacific Ocean, *J. Geophys. Res.,* **81,** 1533–1553.

Watts, A.B., 2001. *Isostasy and flexure of the lithosphere,* Cambridge University Press, Cambridge.

Watts, A.B. & ten Brink, U.S., 1989. Crustal structure, flexure, and subsidence history of the Hawaiian Islands, *J. Geophys. Res.,* **94,** 10473–10500.

Watts, A.B. & Burov, E.B., 2003. Lithospheric strength and its relationship to the elastic and seismogenic layer thicknesses, *Earth Planet. Sci. Lett.,* **213,** 113–131, doi:10.1016/S0012-821X(03)00289-9.

Watts, A.B. & Zhong, S., 2000. Observations of flexure and the rheology of oceanic lithosphere, *Geophys. J. Int.,* **142,** 855–875.

Watts, A.B., ten Brink, U.S., Buhl, P. & Brocher, T.M., 1985. A multichannel seismic study of lithospheric flexure across the Hawaiian-Emperor seamount chain, *Nature,* **315,** 105–111.

Watts, A.B., Peirce, C., Collier, J., Dalwood, R., Canales, J.P. & Henstock, T.J., 1997. A seismic study of lithospheric flexure in the vicinity of Tenerife, Canary Islands, *Earth Planet. Sci. Lett.,* **146,** 431–447.

Watts, A.B., Rodger, M., Peirce, C., Greenroyd, C.J. & Hobbs, R.W., 2009. Seismic structure, gravity anomalies, and flexure of the Amazon continental margin, NE Brazil, *J. Geophys. Res.,* **114,** B07103, doi:10.1029/2008JB006259.

Weigel, W. & Grevemeyer, I., 1999. The Great Meteor seamount: seismic structure of a submerged intraplate volcano, *Geodynamics,* **28,** 27–40.

Wessel, P. & Smith, W.H.F., 1998. New improved version of the Generic Mapping Tools released, *EOS, Trans. Am. Geophys. Union,* **79,** 579.

White, R.S., McKenzie, D. & Onions, R.K., 1992. Oceanic crustal thickness from seismic measurements and rare-earth element inversions, *J. Geophys. Res.,* **97,** 19683–19715.

Williams, C.A., Hill, I.A., Young, R. & White, R.S., 1990. Fracture zones across the Cape Verde Rise, NE Atlantic, *J. Geol. Soc.,* **147,** 851–857.

Wilson, D.J., Peirce, C., Watts, A.B., Grevemeyer, I. & Krabbenhoeft, A., 2010. Uplift at lithospheric swells – I: seismic and gravity constraints on the crust and uppermost mantle structure of the Cape Verde mid-plate swell, *Geophys. J. Int.,* **182,** 531–550, doi:10.1111/j.1365-246X.2010.04641.x.

Wilson, J.T., 1963. Evidence from islands on spreading of ocean floors, *Nature,* **197,** 536–538.

Wolfe, C.J., Solomon, S.C., Laske, G., Collins, J.A., Detrick, R.S., Orcutt, J.A., Bercovici, D. & Hauri, E.H., 2011. Mantle *P*-wave velocity structure beneath the Hawaiian hotspot, *Earth Planet. Sci. Lett.*, **303,** 267–280, doi:10.1016/j.epsl.2011.01.004.

Ye, S., Canales, J.P., Rihm, R., Dañobeitia, J.J. & Gallart, J., 1999. A crustal transect through the northern and northeastern part of the volcanic edifice of Gran Canaria, Canary Islands, *Geodynamics,* **28,** 3–26.

Young, R. & Hill, I.A., 1986. An estimate of the effective elastic thickness of the Cape Verde Rise, *J. Geophys. Res.*, **91,** 4854–4866.

Zelt, C.A., 1998. Lateral velocity resolution from three-dimensional seismic refraction data, *Geophys. J. Int.,* **135,** 1101–1112.

Zelt, C.A. & Barton, P.J., 1998. Three-dimensional seismic refraction tomography: a comparison of two methods applied to data from the Faeroe Basin, *J. Geophys. Res.,* **103,** 7187–7210.

Zelt, C.A. & Smith, R.B., 1992. Seismic traveltime inversion for 2-D crustal velocity structure, *Geophys. J. Int.,* **108,** 16–34.

Zhao, D., 2001. Seismic structure and origin of hotspots and mantle plumes, *Earth Planet. Sci. Lett.,* **192,** 251–265.

Zhao, D., 2004. Global tomographic images of mantle plumes and subducting slabs: insight into deep Earth dynamics, *Phys. Earth Planet. Interior*, **146,** 3–34, doi: 10.1016/j.pepi.2003.07.032.

Appendix A

Wide-angle data and modelling

The WA data, traveltime picks and calculated arrivals through the *final* 2-D velocity-depth model are shown for each OBS included in the modelling for this study in Figures A.1-A.38. OBH18 and OBH22 are not shown as no data were recorded. See Figure 2.1 for OBS locations.

The following caption is applicable to each figure in addition to the text included specifically beneath:

a) Bandpass filtered (0-5-70-80 Hz) record section plotted without the application of any amplitude corrections. Calculated traveltimes for all modelled subseabed phases are plotted at all offsets and coloured according to phase assignment. b) Observed traveltime picks (black vertical bars, representing the assigned uncertainties) and calculated traveltimes at corresponding shot-receiver offsets, coloured as for a). The χ^2 value gives an indication of the quantitative fit of the calculated traveltimes to the observed picks ($\chi^2 = 1$: best achievable fit; $\chi^2 < 5$: acceptable fit – see Section 2.7.1; Equation 2.3). c) Ray diagram showing the rays traced to produce the calculated arrivals in b). Record sections and traveltimes are plotted with a reduction velocity of 6 km s^{-1}.

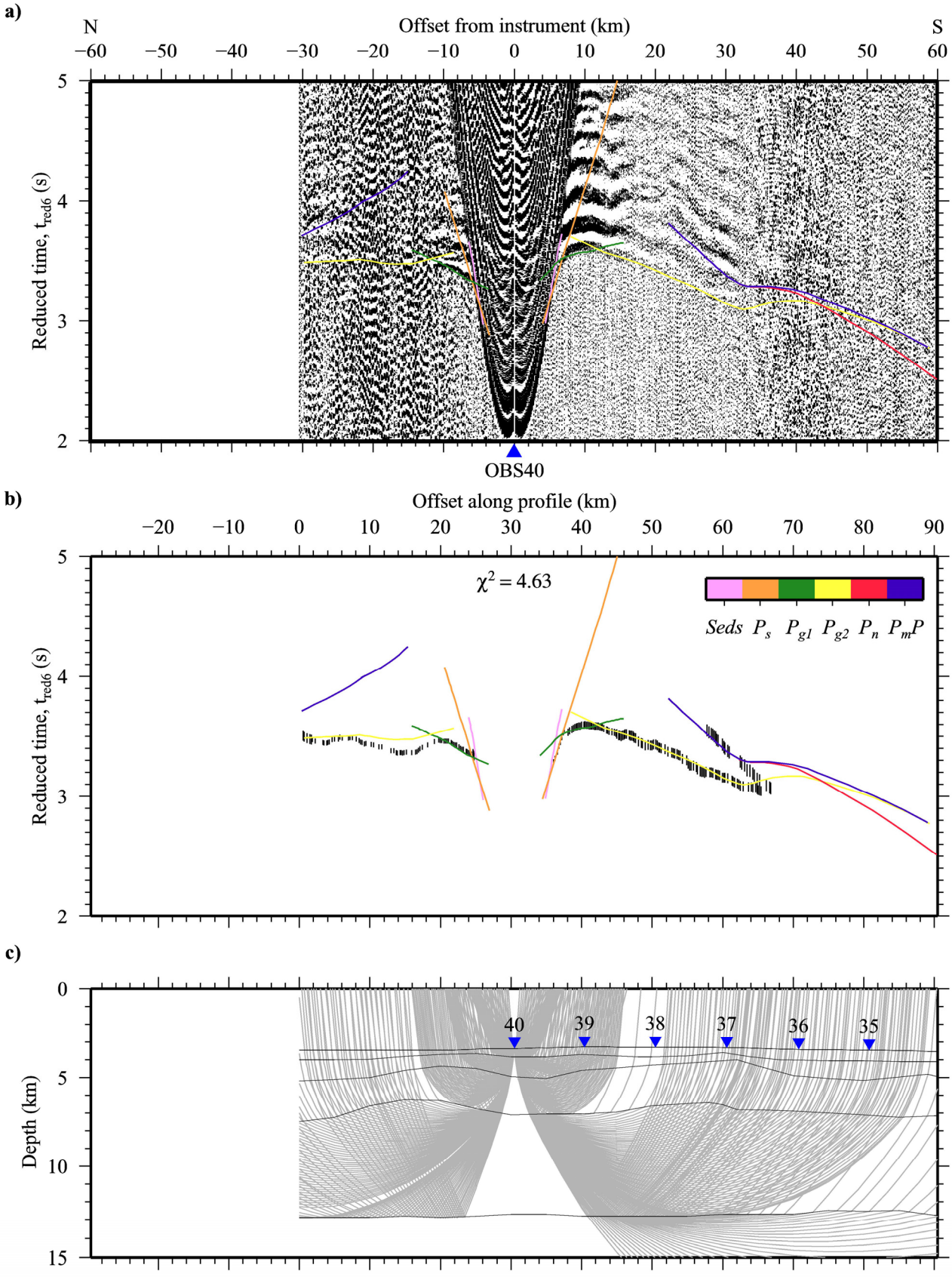

Figure A.1 Ray-trace modelling of traveltime picks from hydrophone data recorded by OBS40.

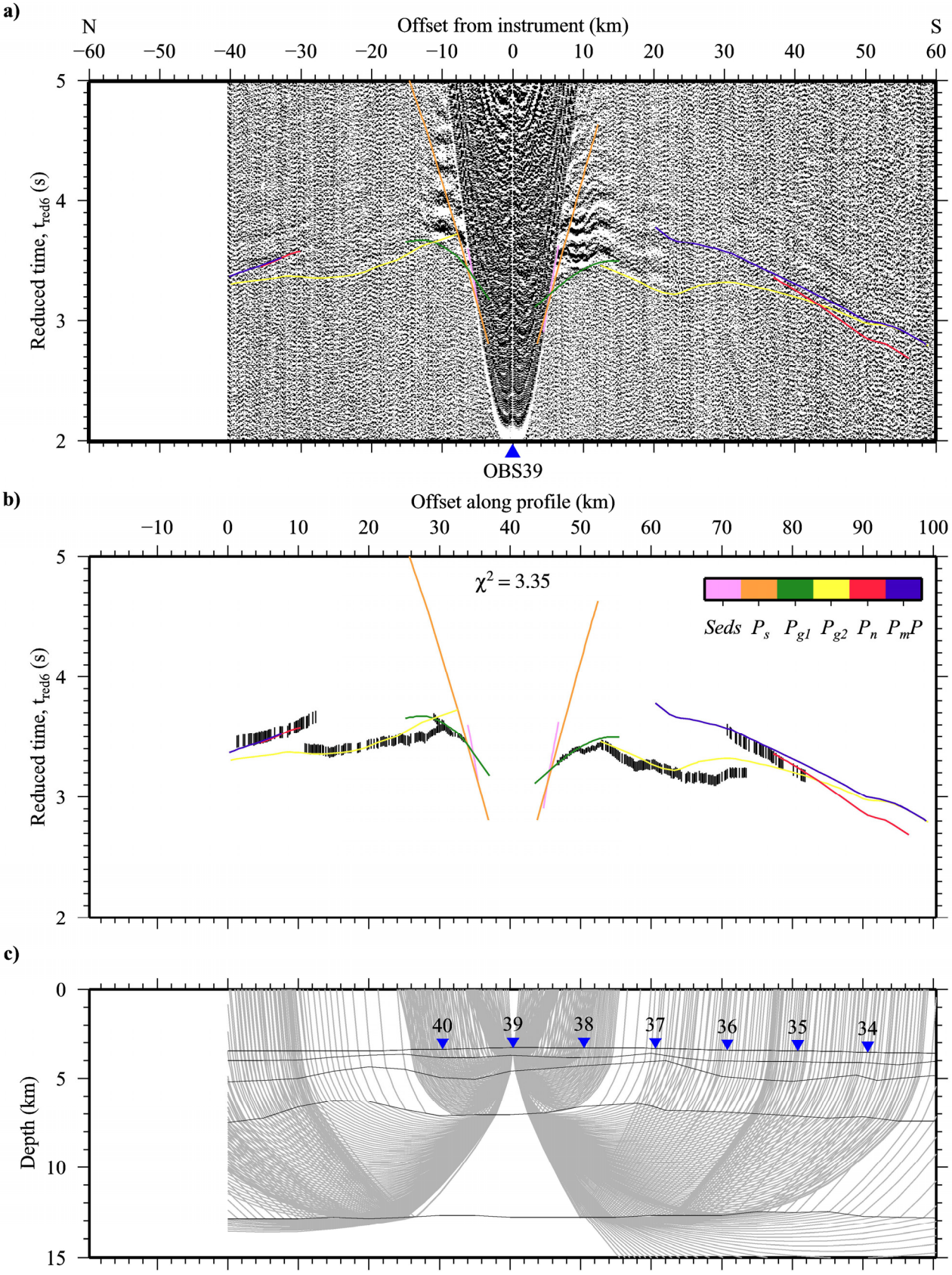

Figure A.2 Ray-trace modelling of traveltime picks from hydrophone data recorded by OBS39.

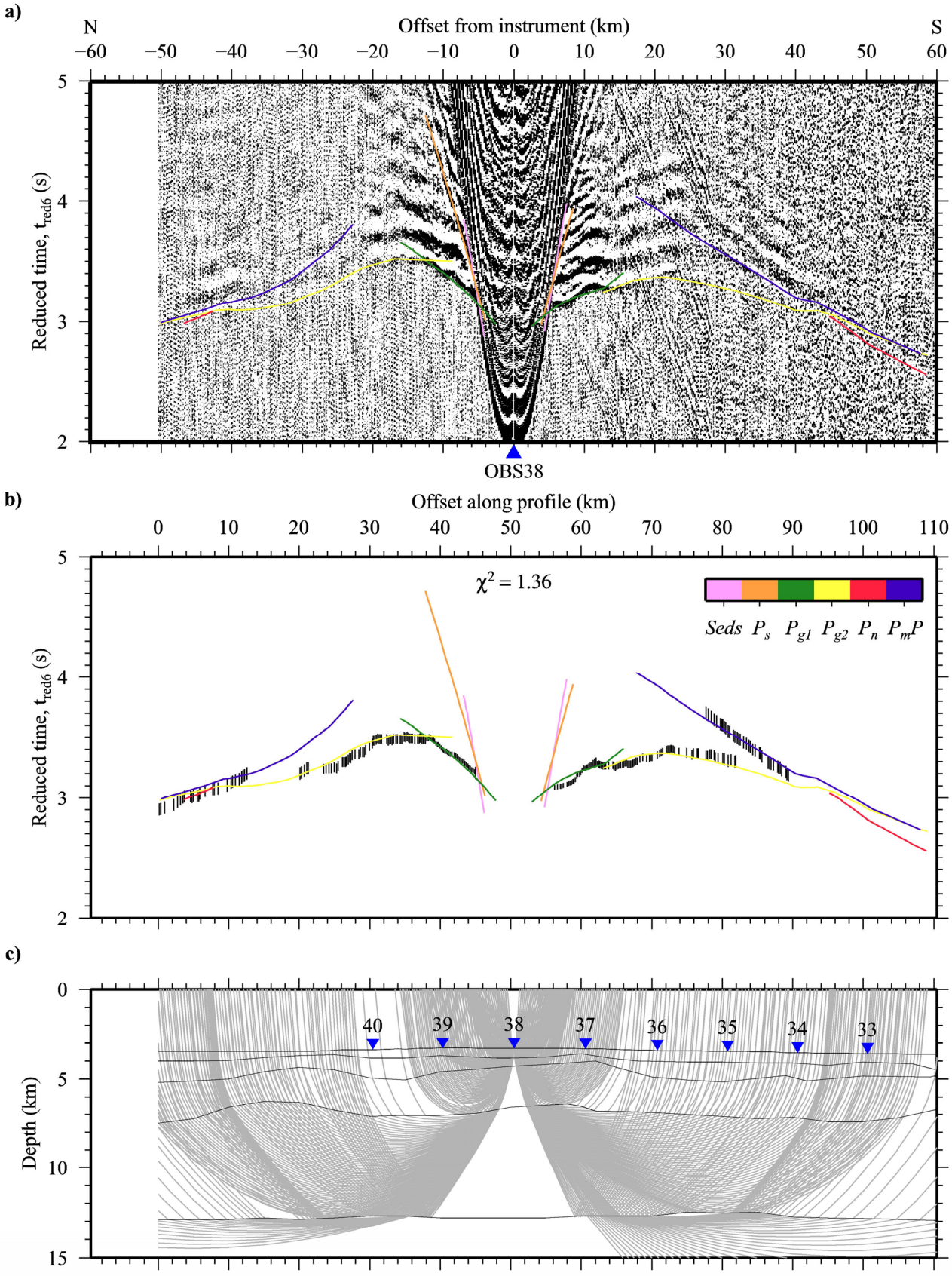

Figure A.3 Ray-trace modelling of traveltime picks from hydrophone data recorded by OBS38.

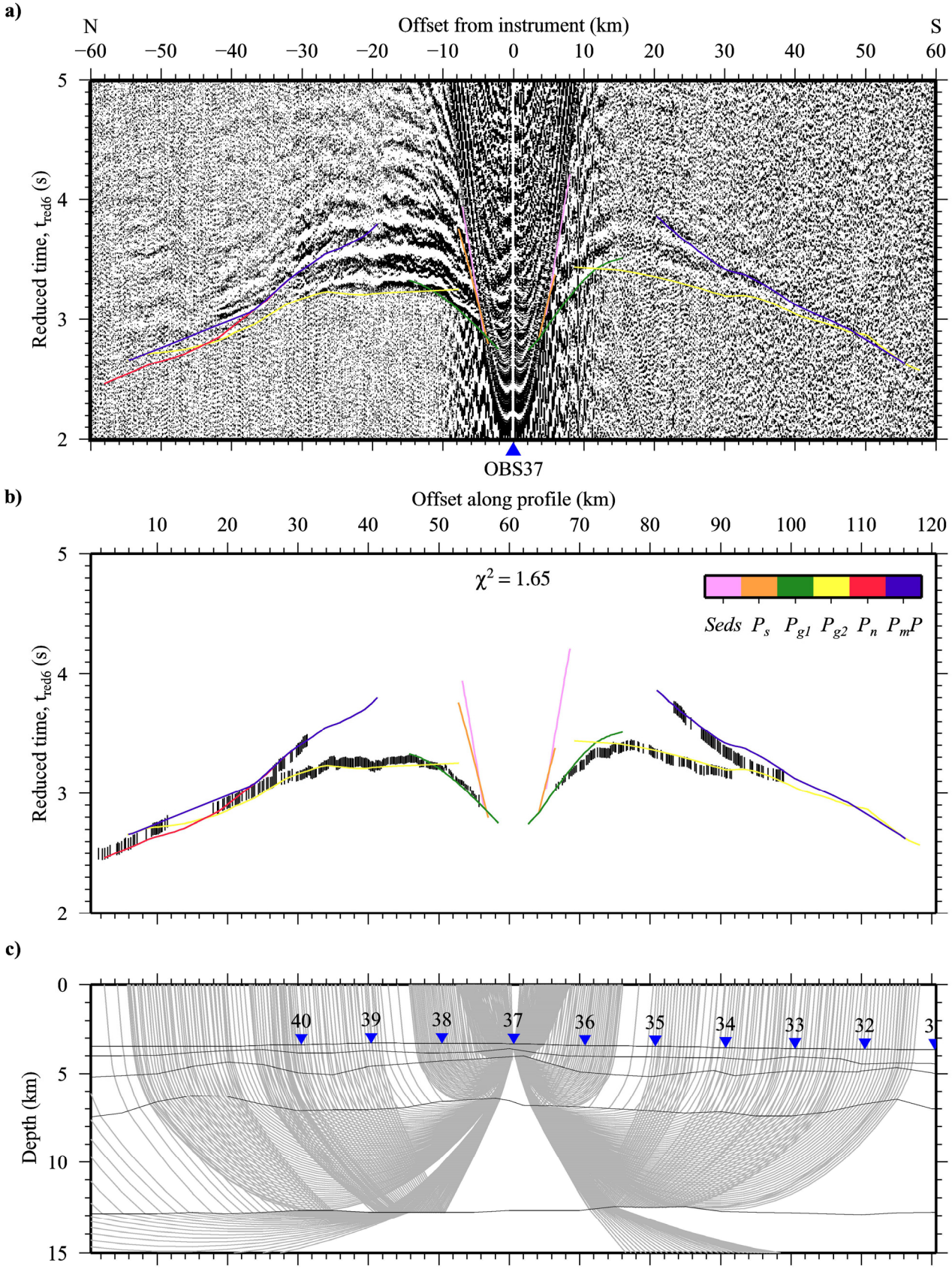

Figure A.4 Ray-trace modelling of traveltime picks from hydrophone data recorded by OBS37.

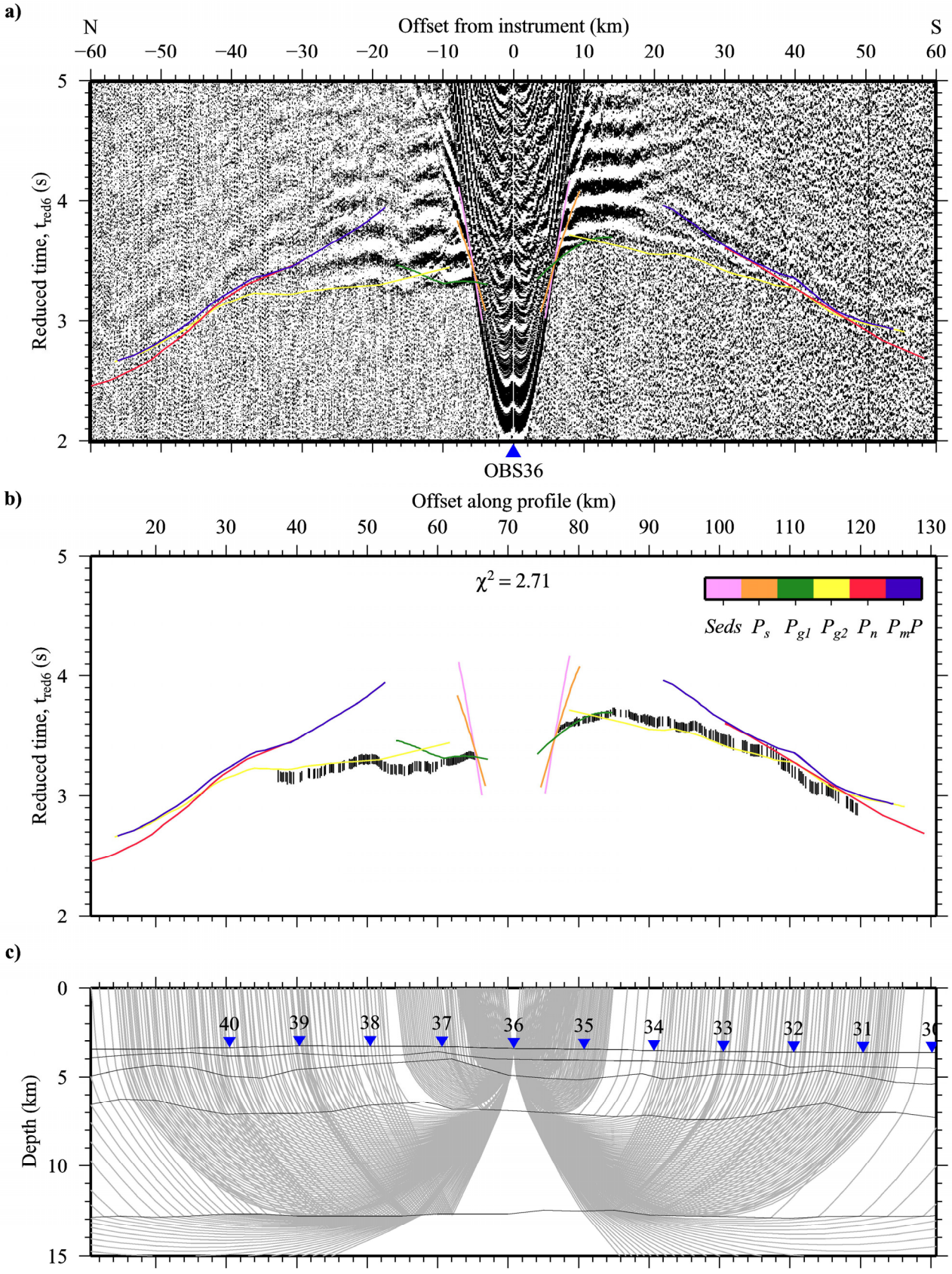

Figure A.5 Ray-trace modelling of traveltime picks from hydrophone data recorded by OBS36.

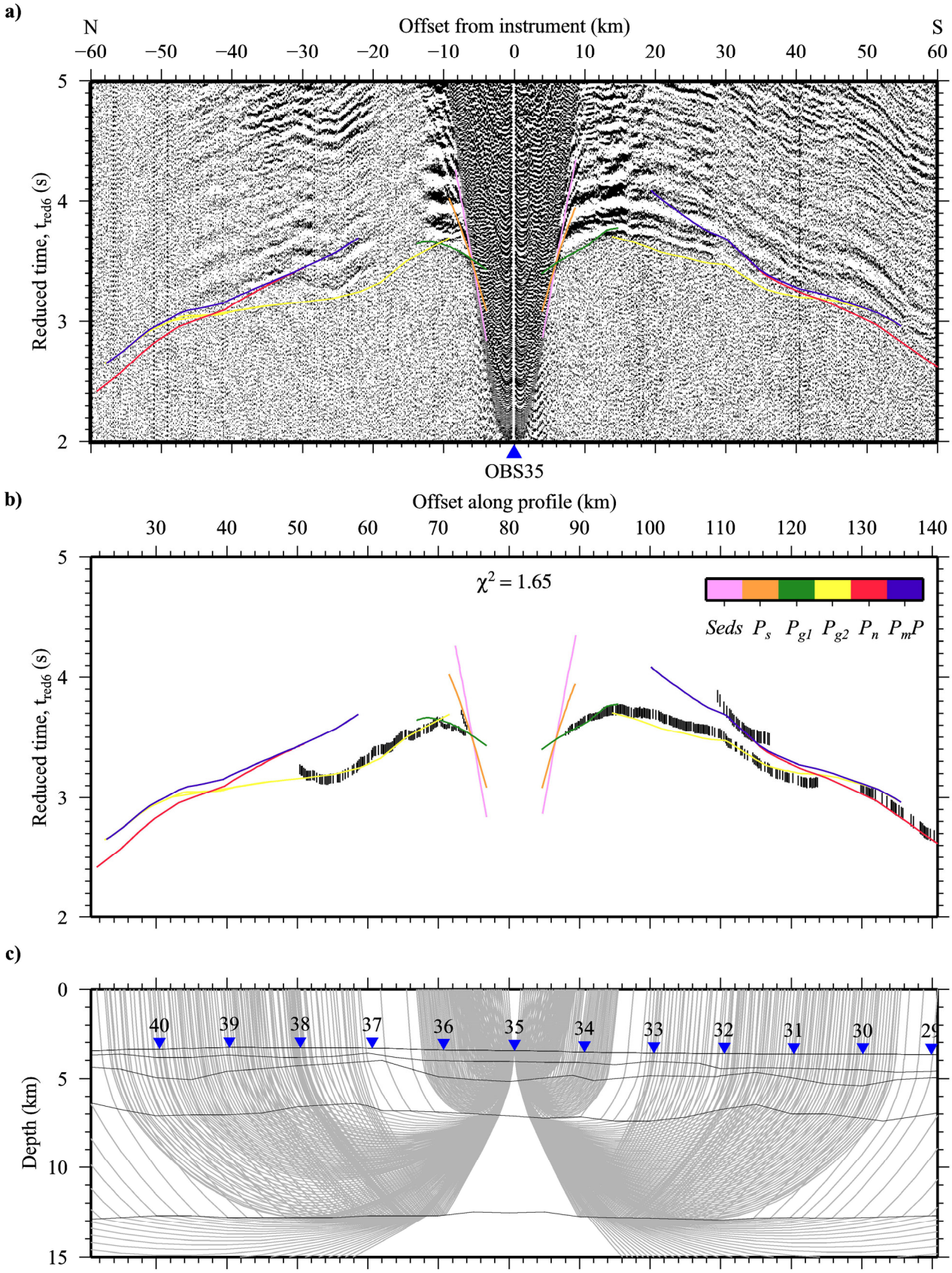

Figure A.6 Ray-trace modelling of traveltime picks from geophone data recorded by OBS35.

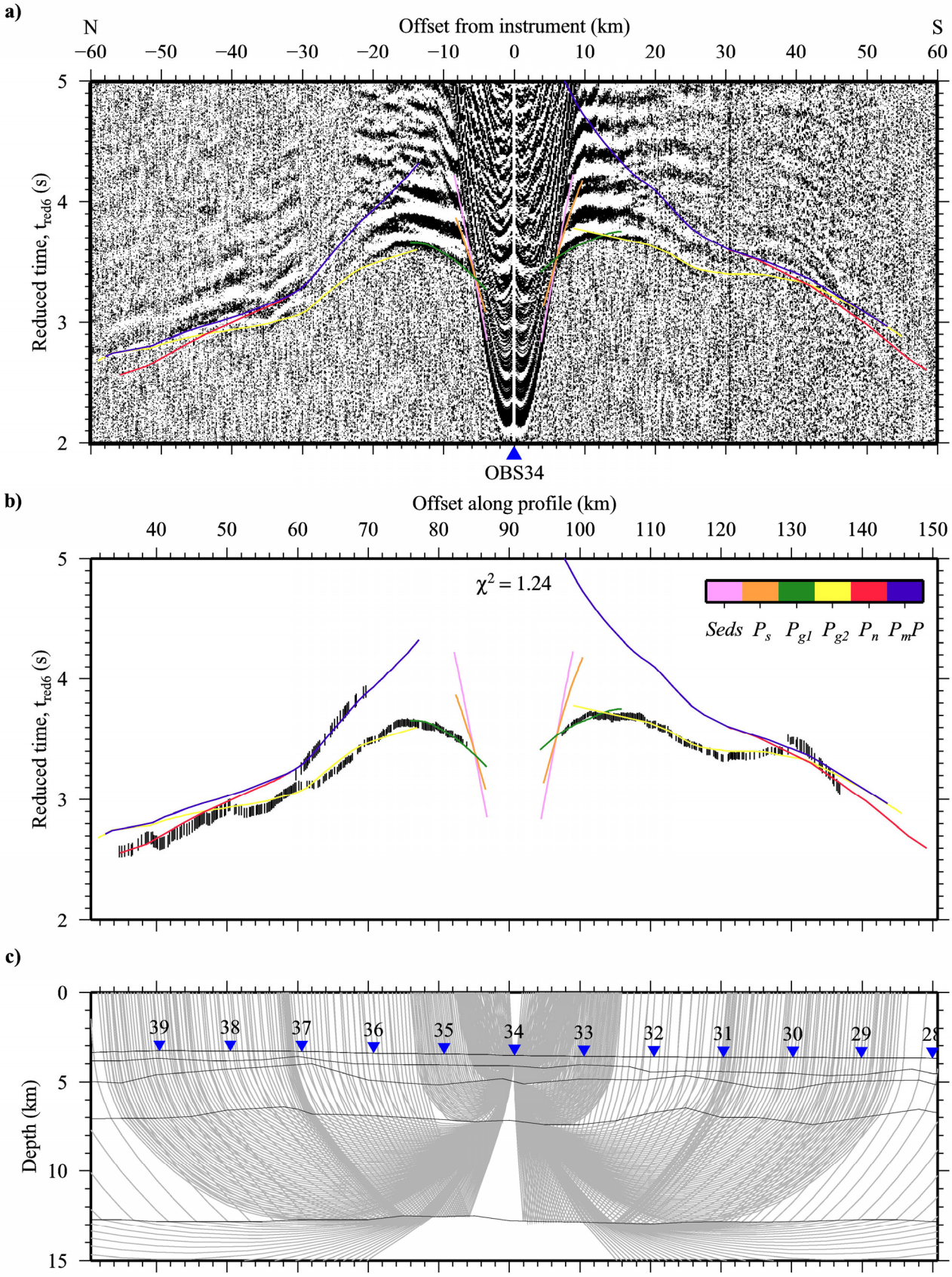

Figure A.7 Ray-trace modelling of traveltime picks from hydrophone data recorded by OBS34.

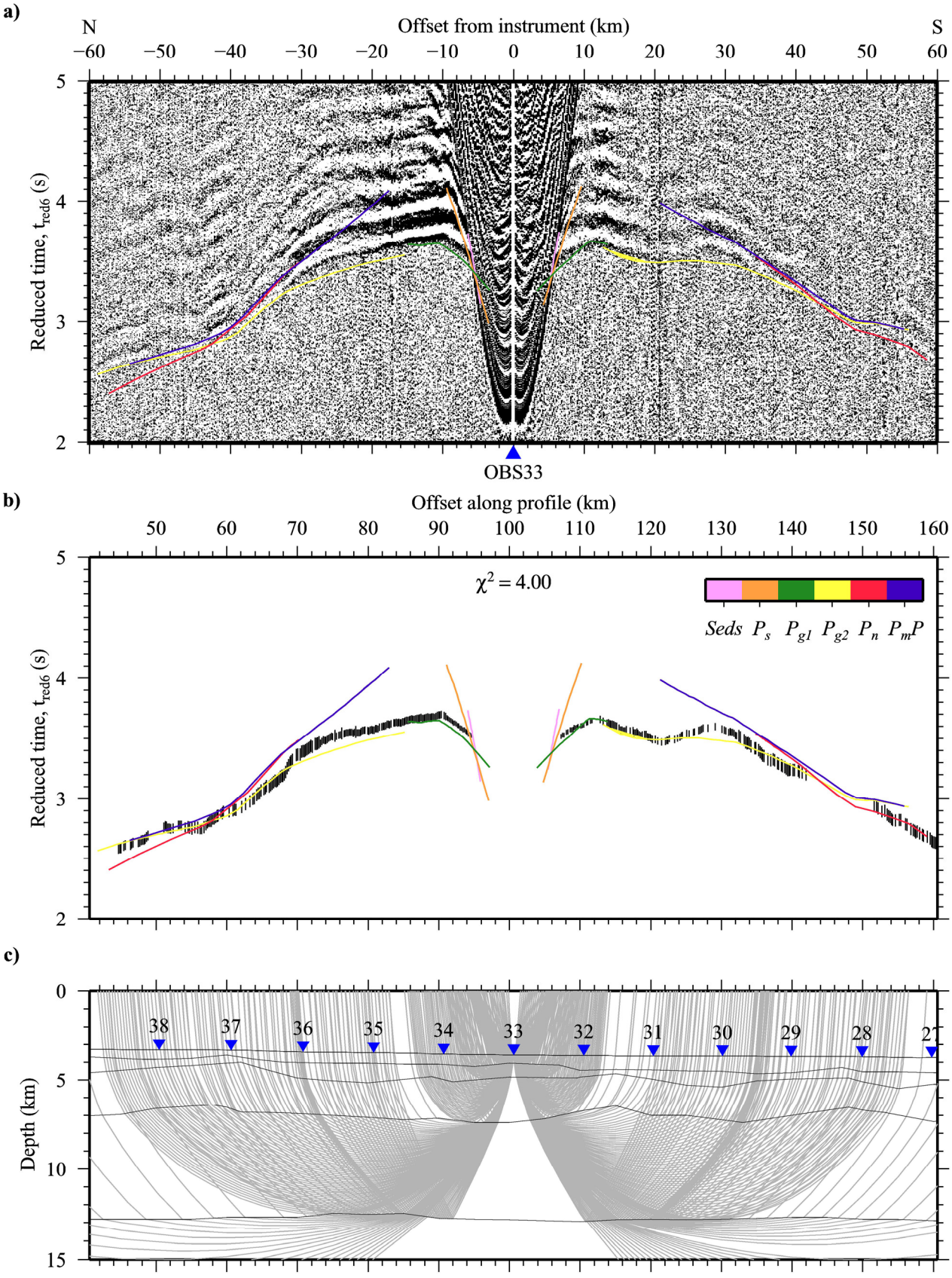

Figure A.8 Ray-trace modelling of traveltime picks from hydrophone data recorded by OBS33.

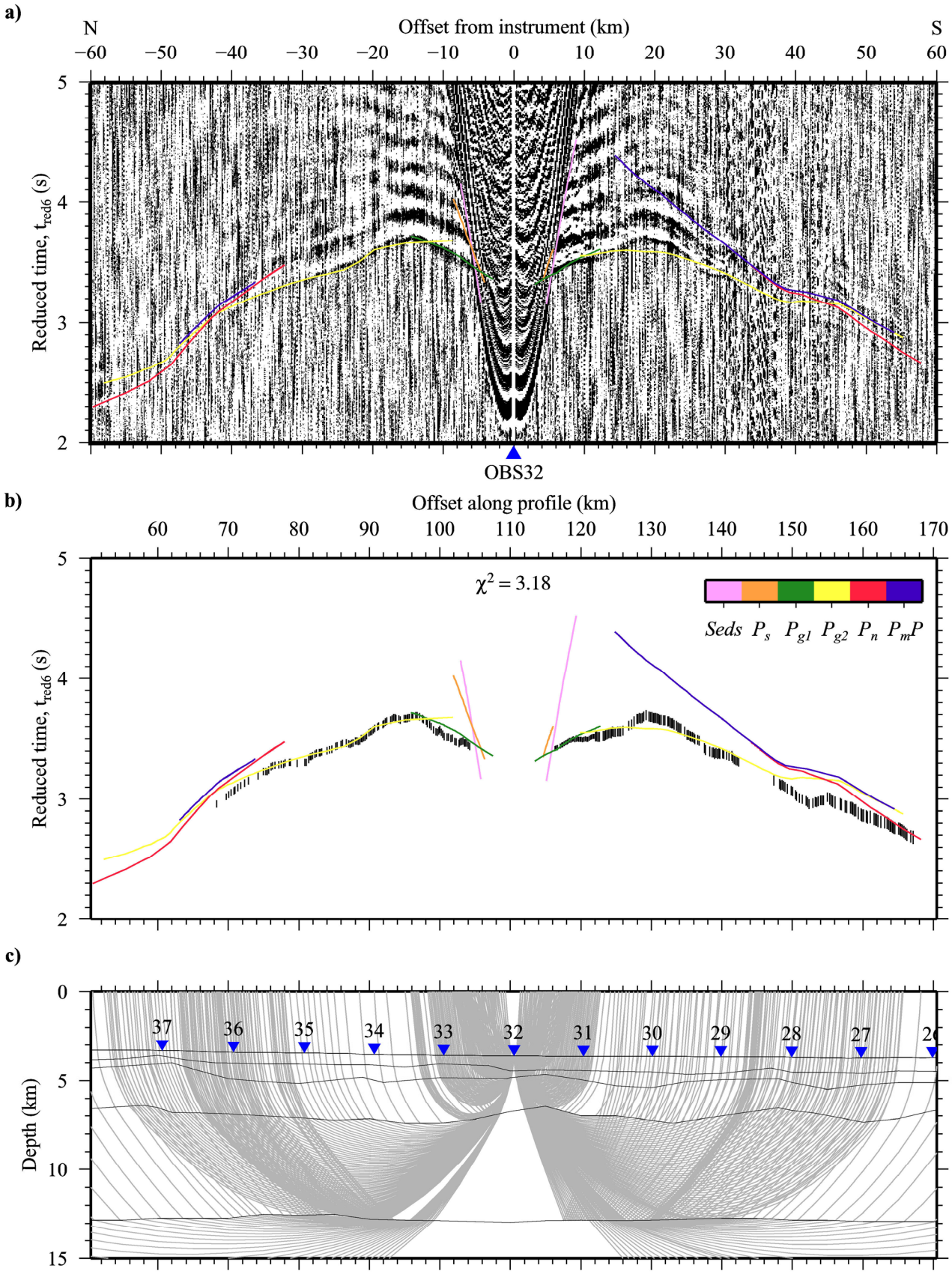

Figure A.9 Ray-trace modelling of traveltime picks from hydrophone data recorded by OBS32.

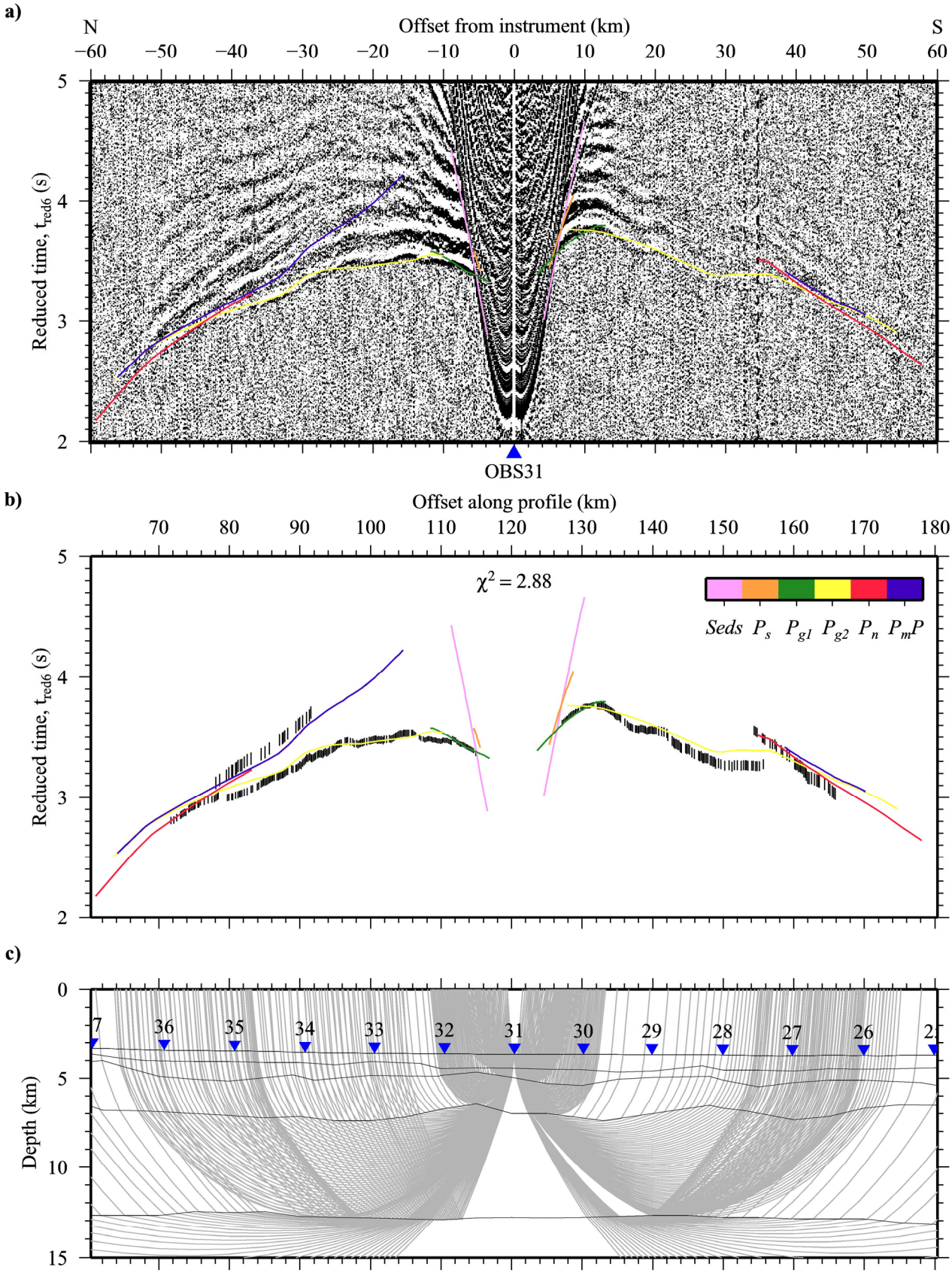

Figure A.10 Ray-trace modelling of traveltime picks from hydrophone data recorded by OBS31.

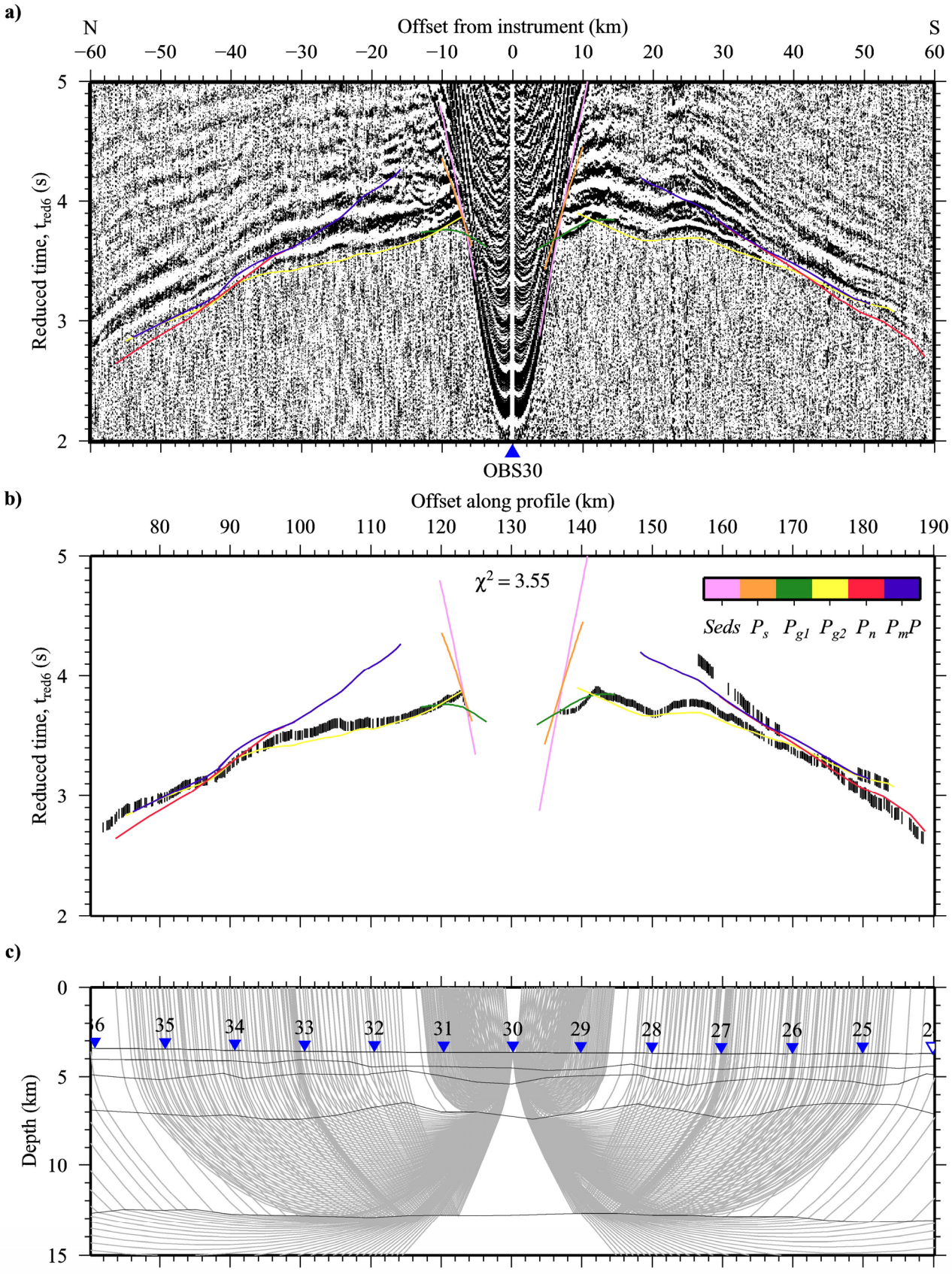

Figure A.11 Ray-trace modelling of traveltime picks from hydrophone data recorded by OBS30.

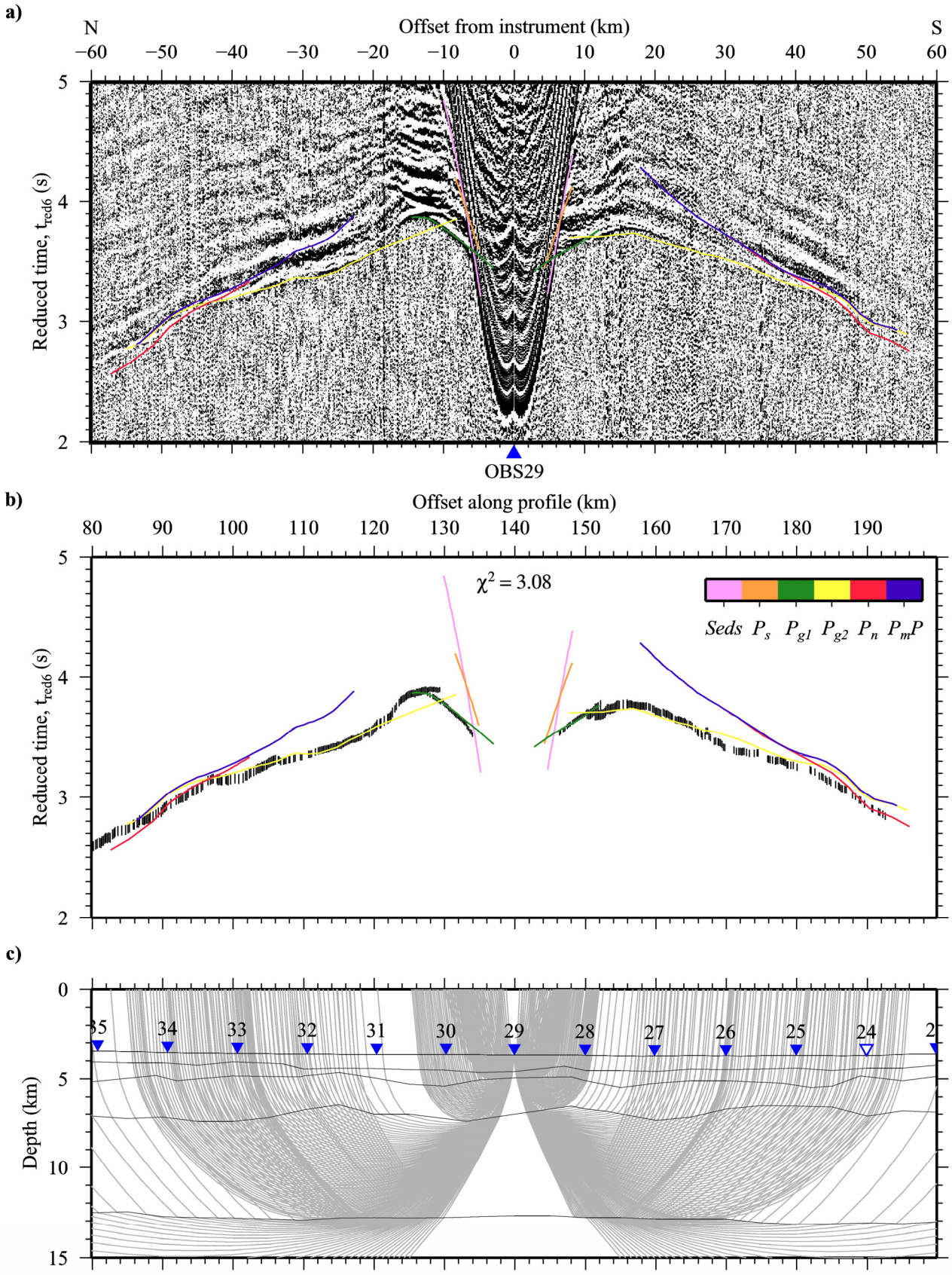

Figure A.12 Ray-trace modelling of traveltime picks from hydrophone data recorded by OBS29.

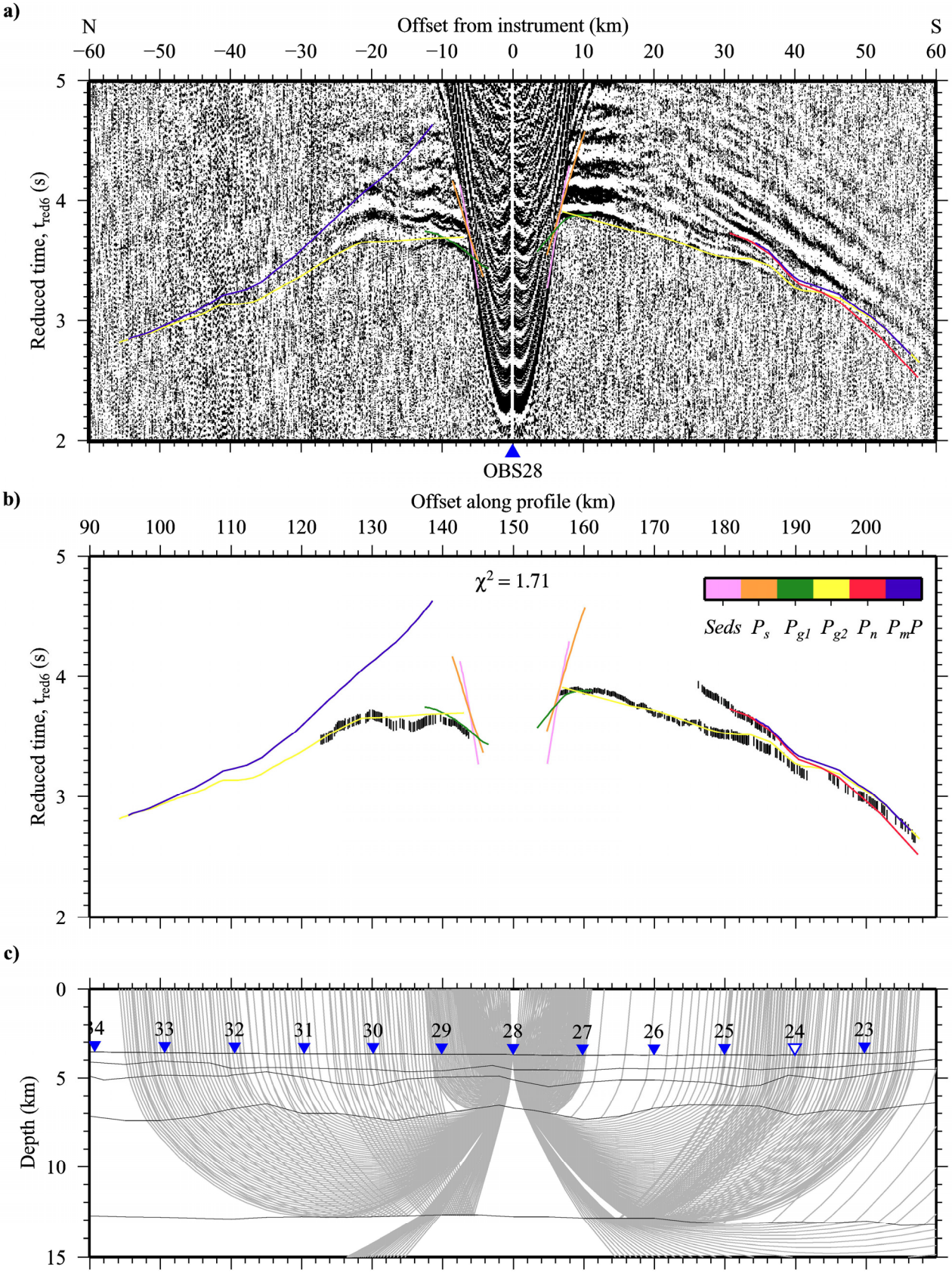

Figure A.13 Ray-trace modelling of traveltime picks from hydrophone data recorded by OBS28.

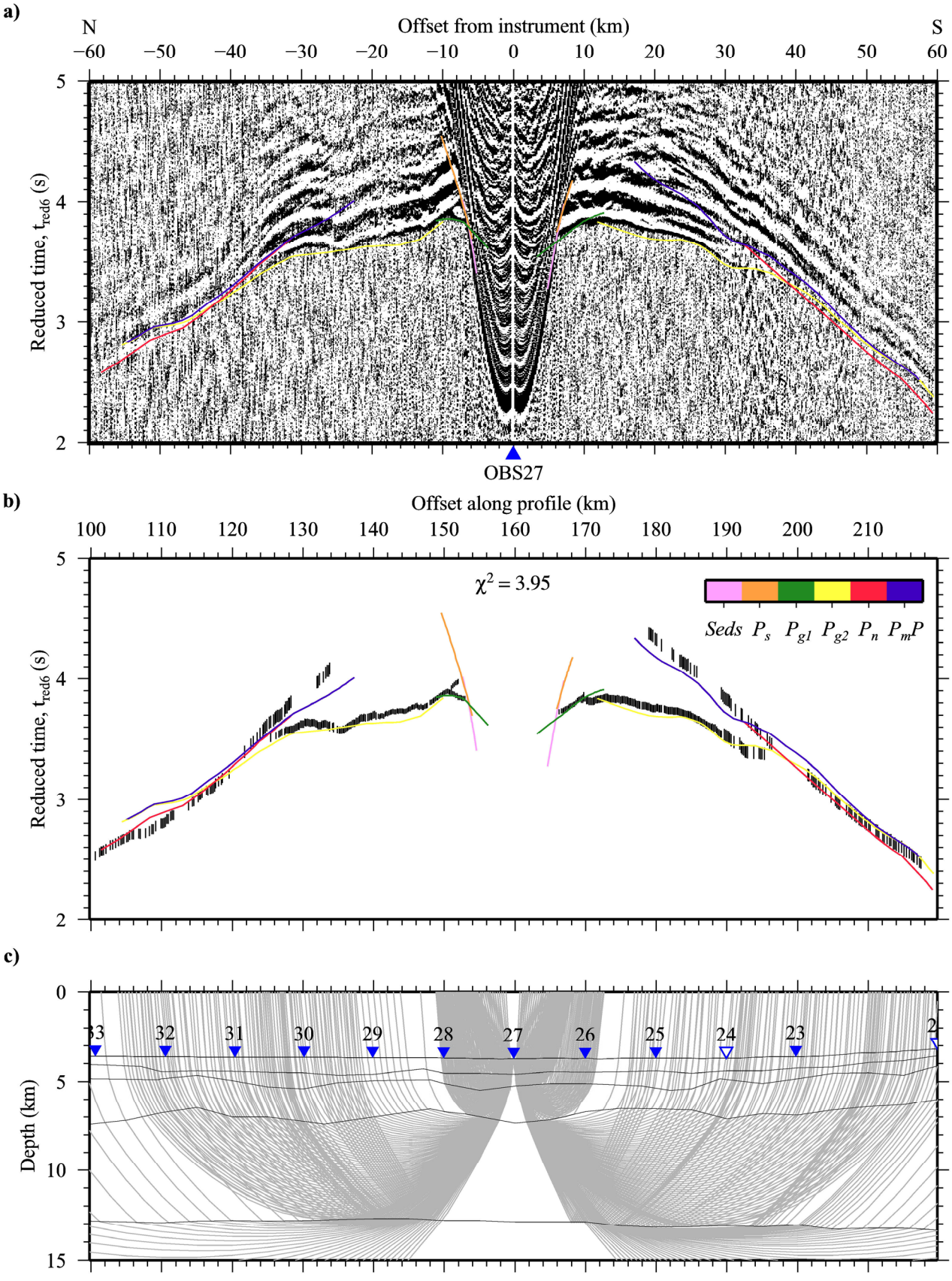

Figure A.14 Ray-trace modelling of traveltime picks from hydrophone data recorded by OBS27.

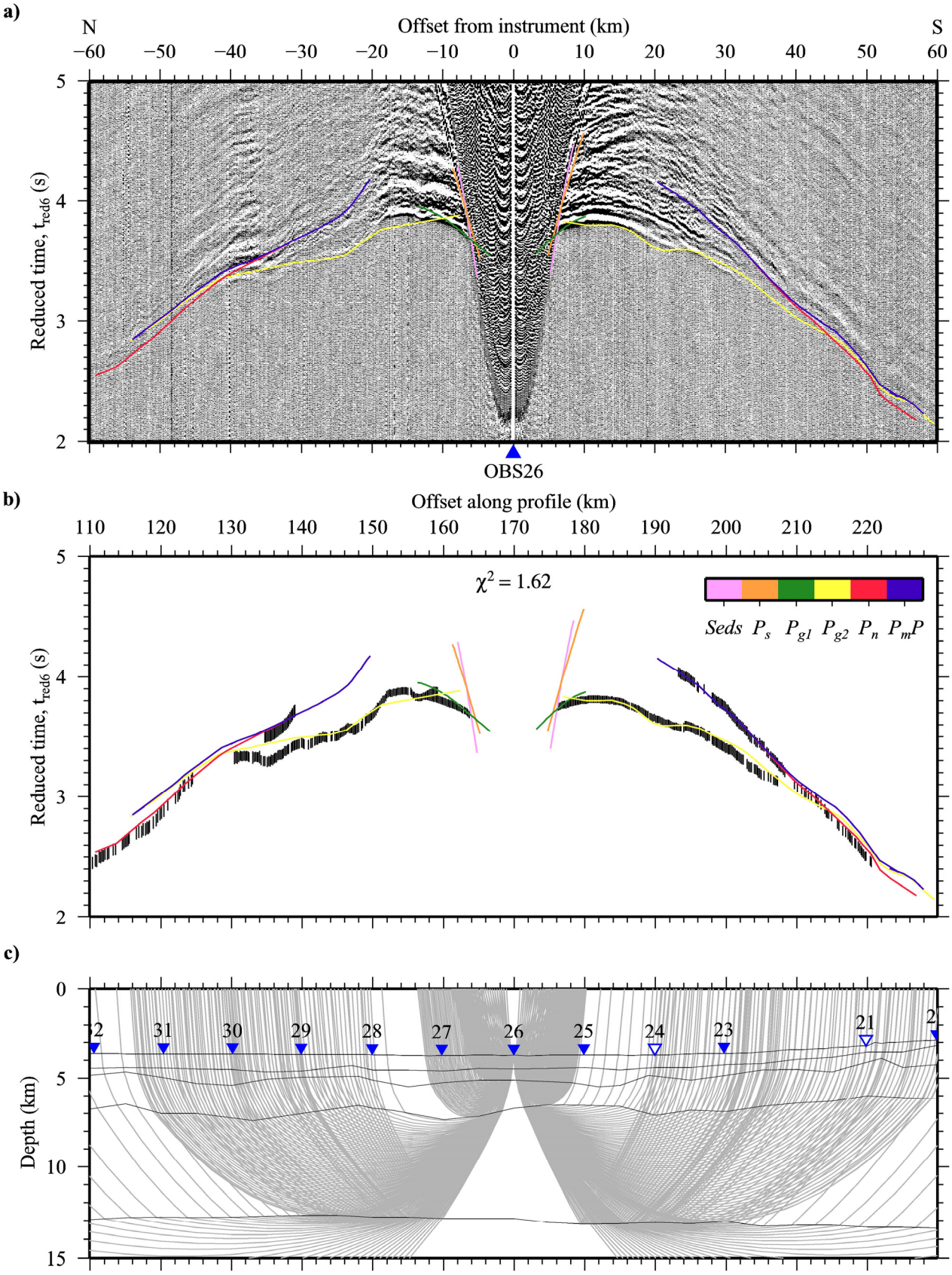

Figure A.15 Ray-trace modelling of traveltime picks from geophone data recorded by OBS26.

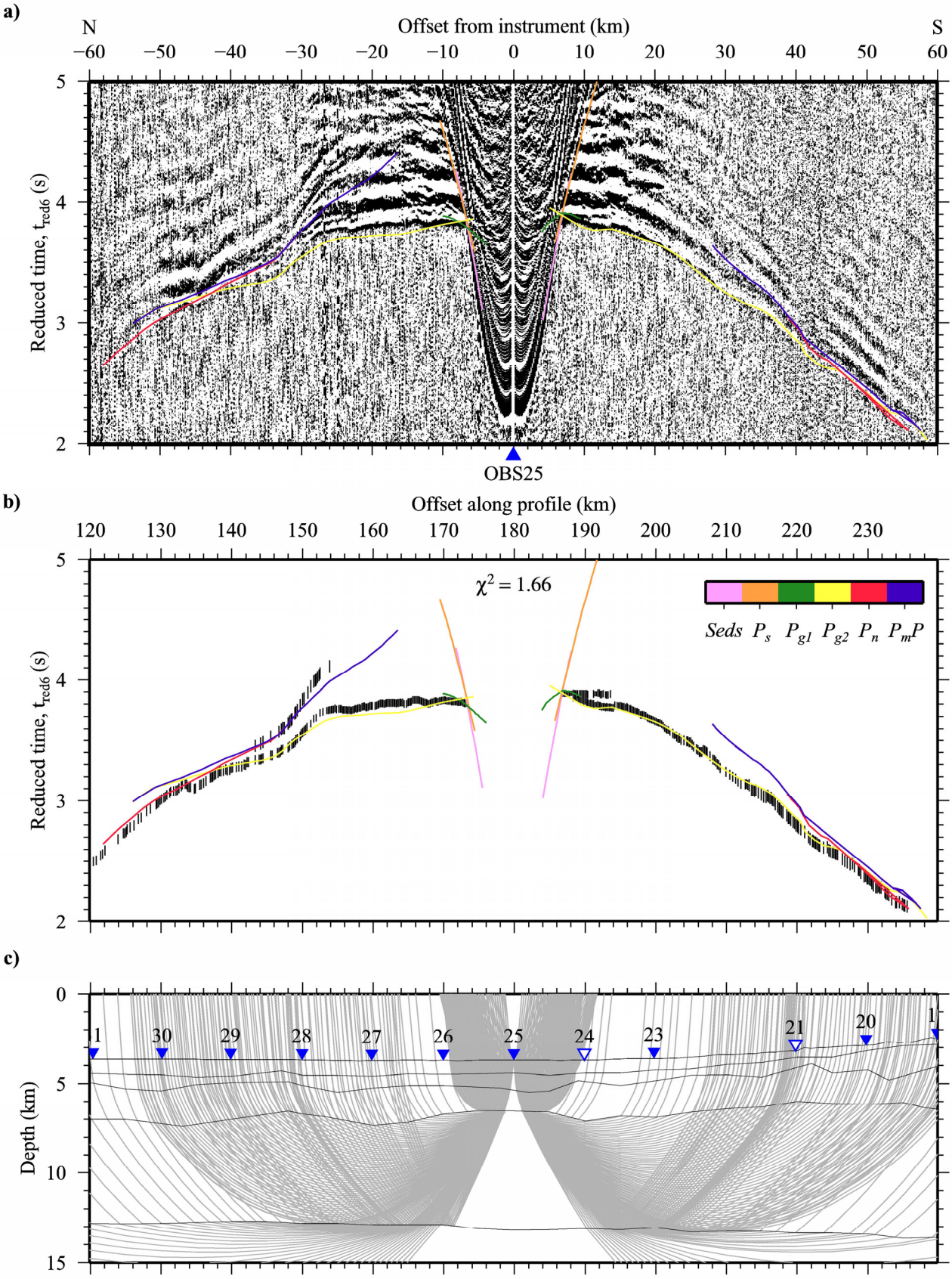

Figure A.16 Ray-trace modelling of traveltime picks from hydrophone data recorded by OBS25.

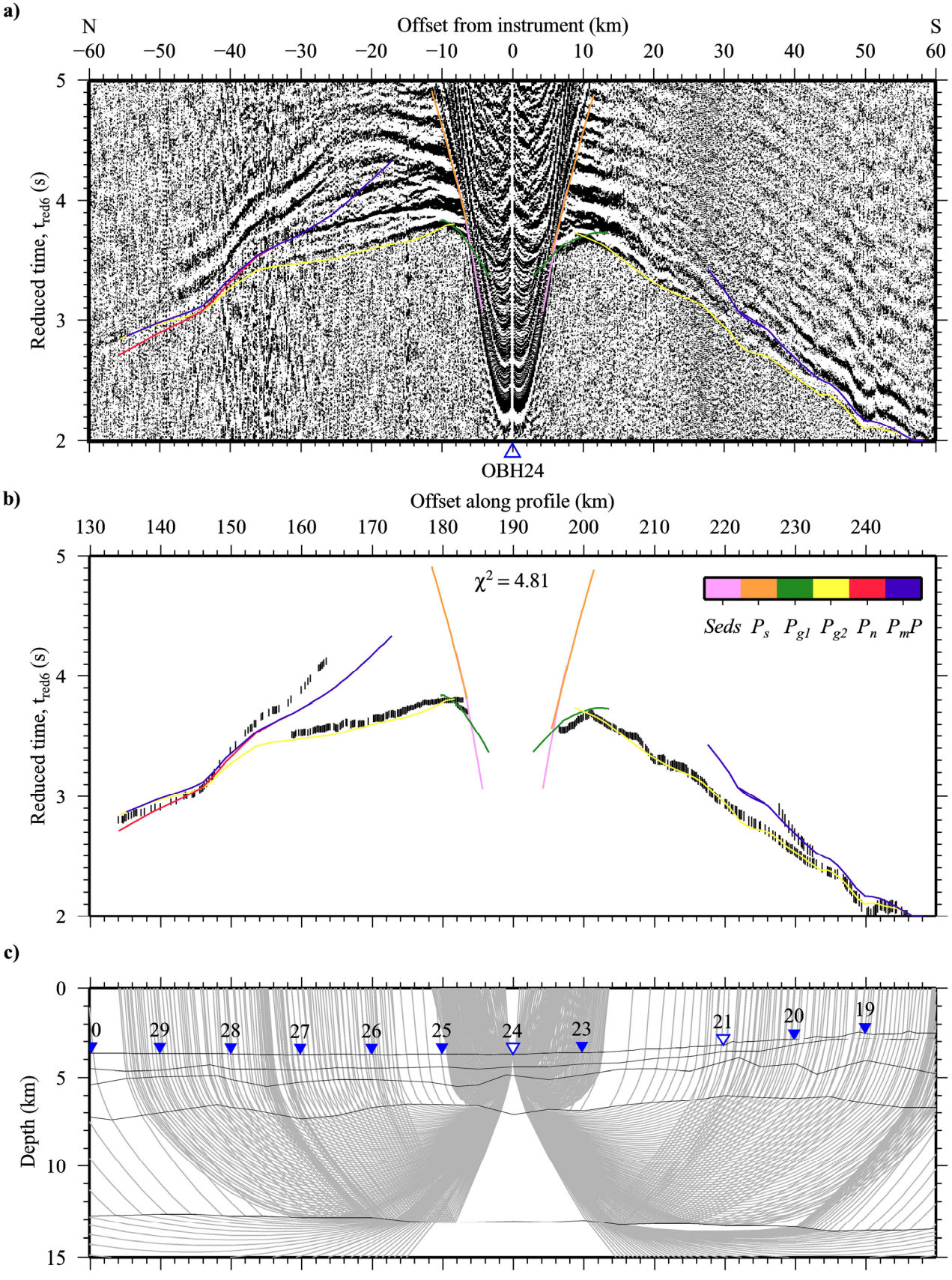

Figure A.17 Ray-trace modelling of traveltime picks from hydrophone data recorded by OBH24.

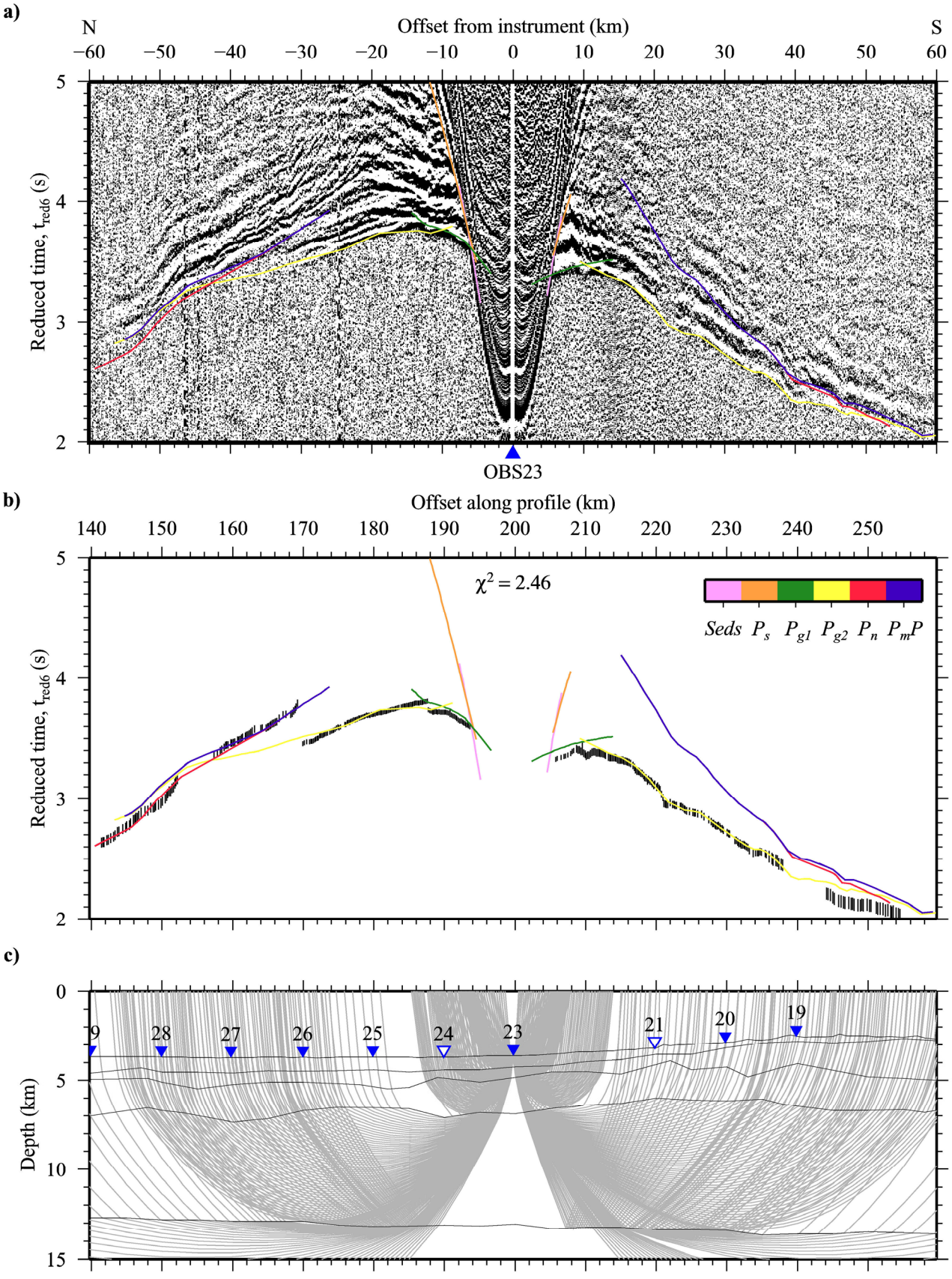

Figure A.18 Ray-trace modelling of traveltime picks from hydrophone data recorded by OBS23.

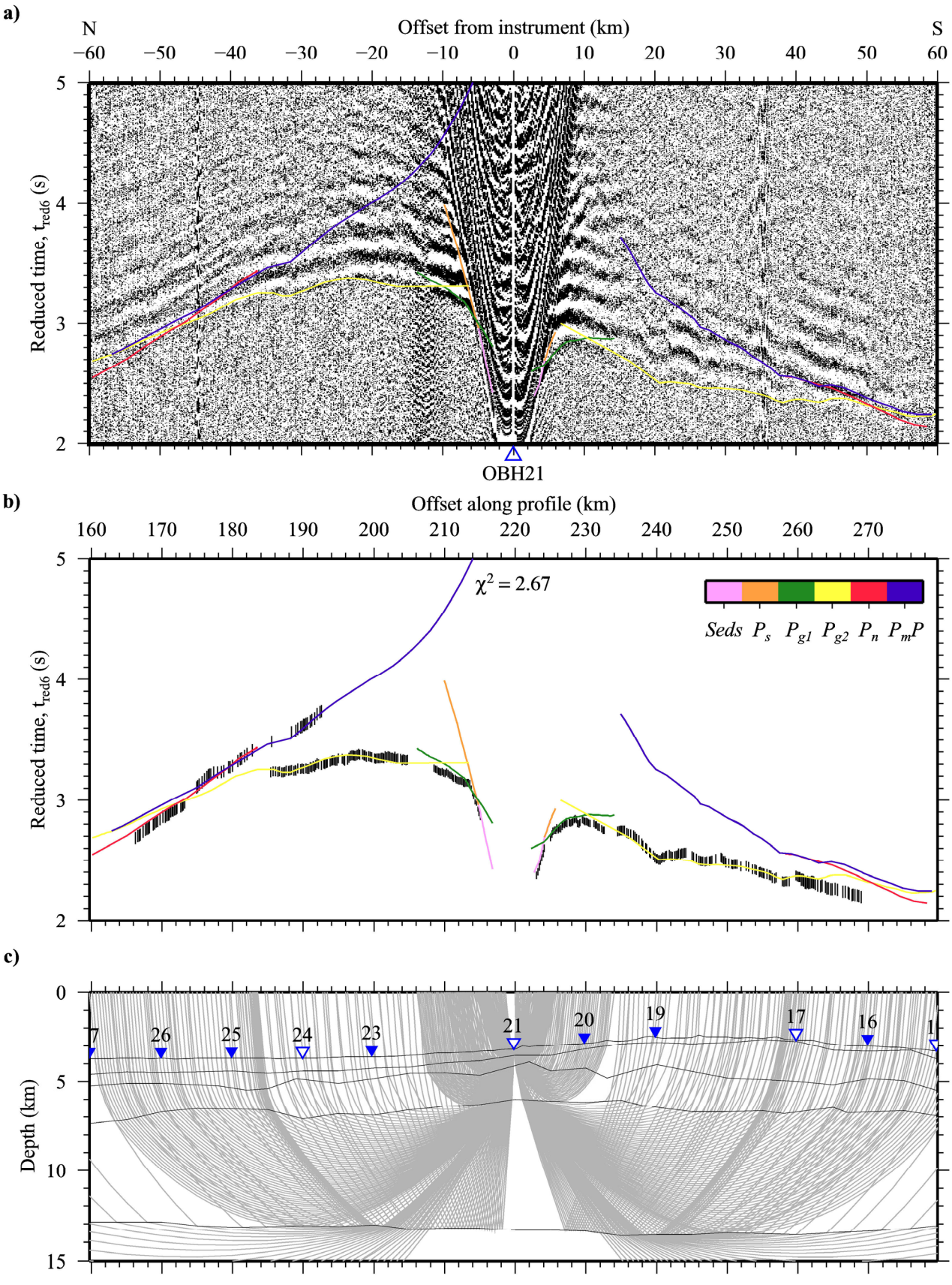

Figure A.19 Ray-trace modelling of traveltime picks from hydrophone data recorded by OBH21.

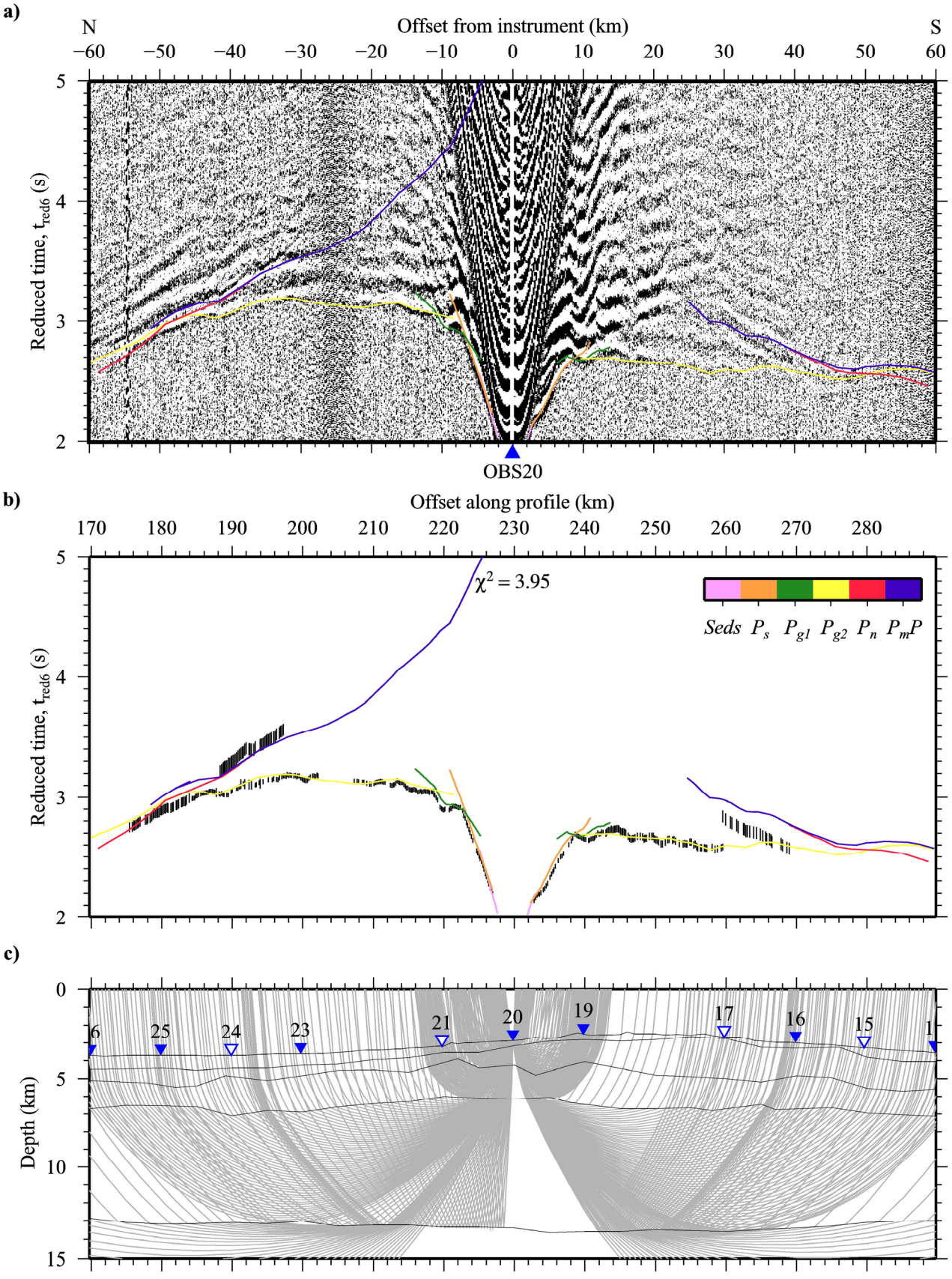

Figure A.20 Ray-trace modelling of traveltime picks from hydrophone data recorded by OBS20.

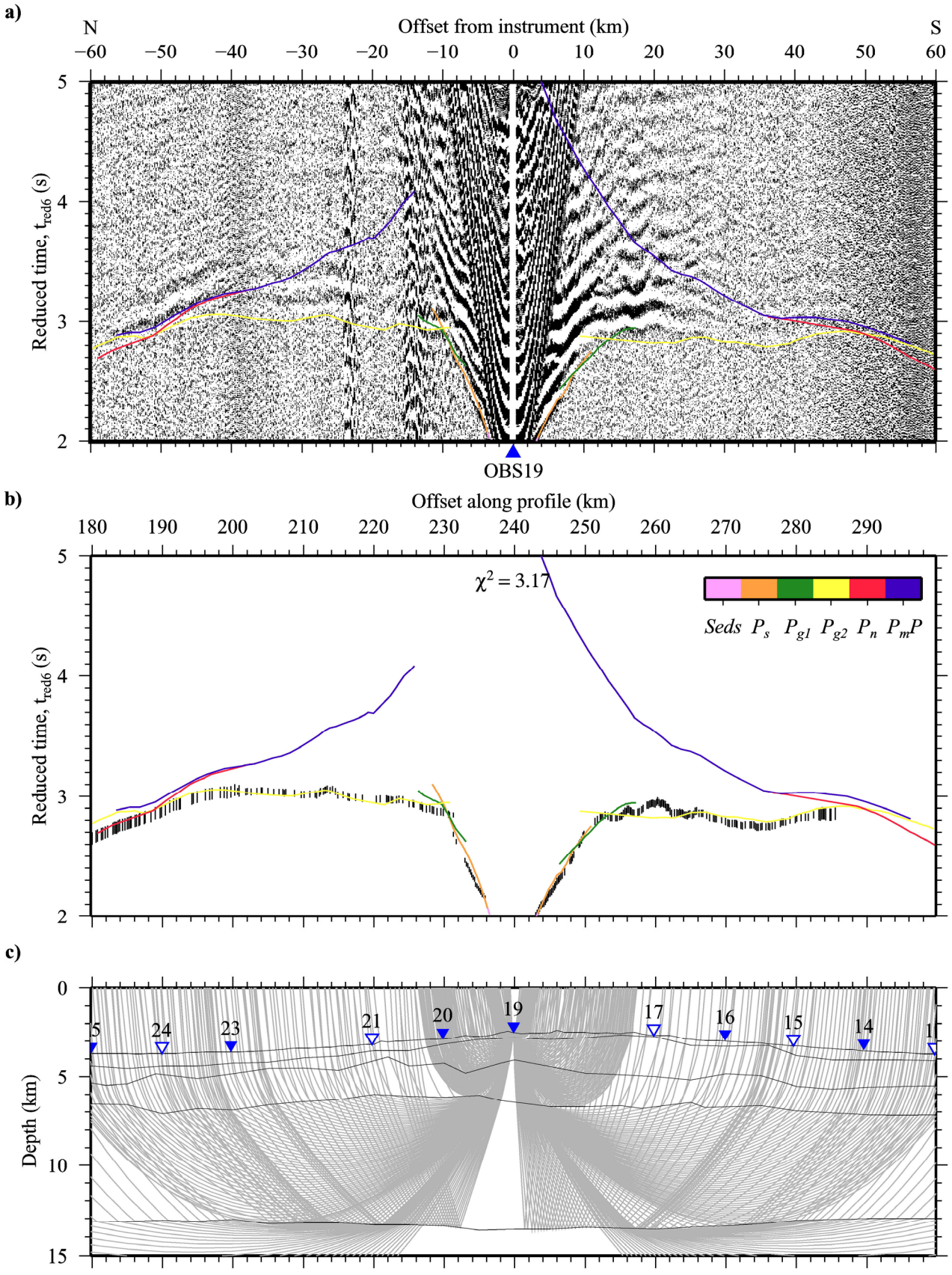

Figure A.21 Ray-trace modelling of traveltime picks from hydrophone data recorded by OBS19.

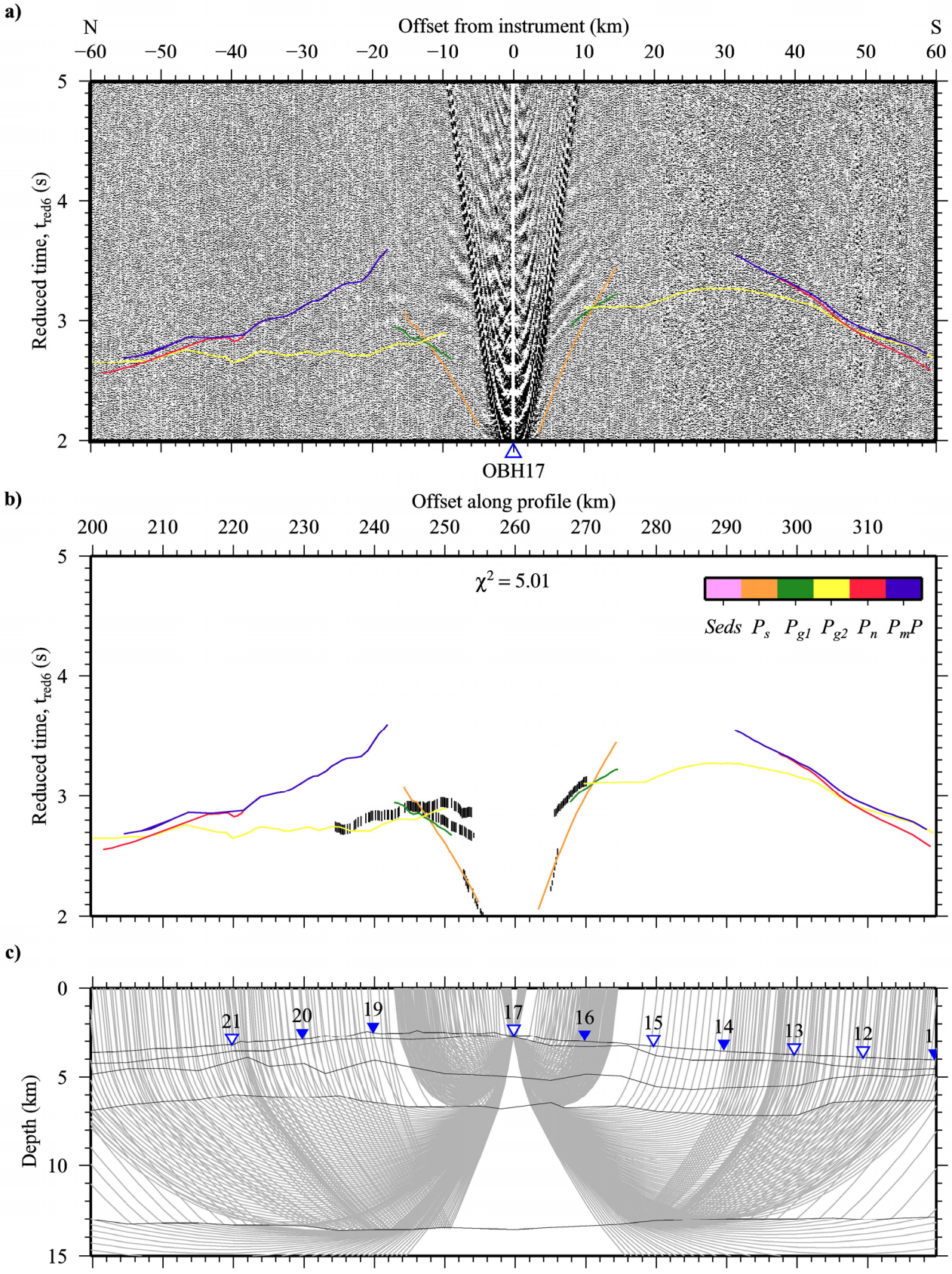

Figure A.22 Ray-trace modelling of traveltime picks from hydrophone data recorded by OBH17.

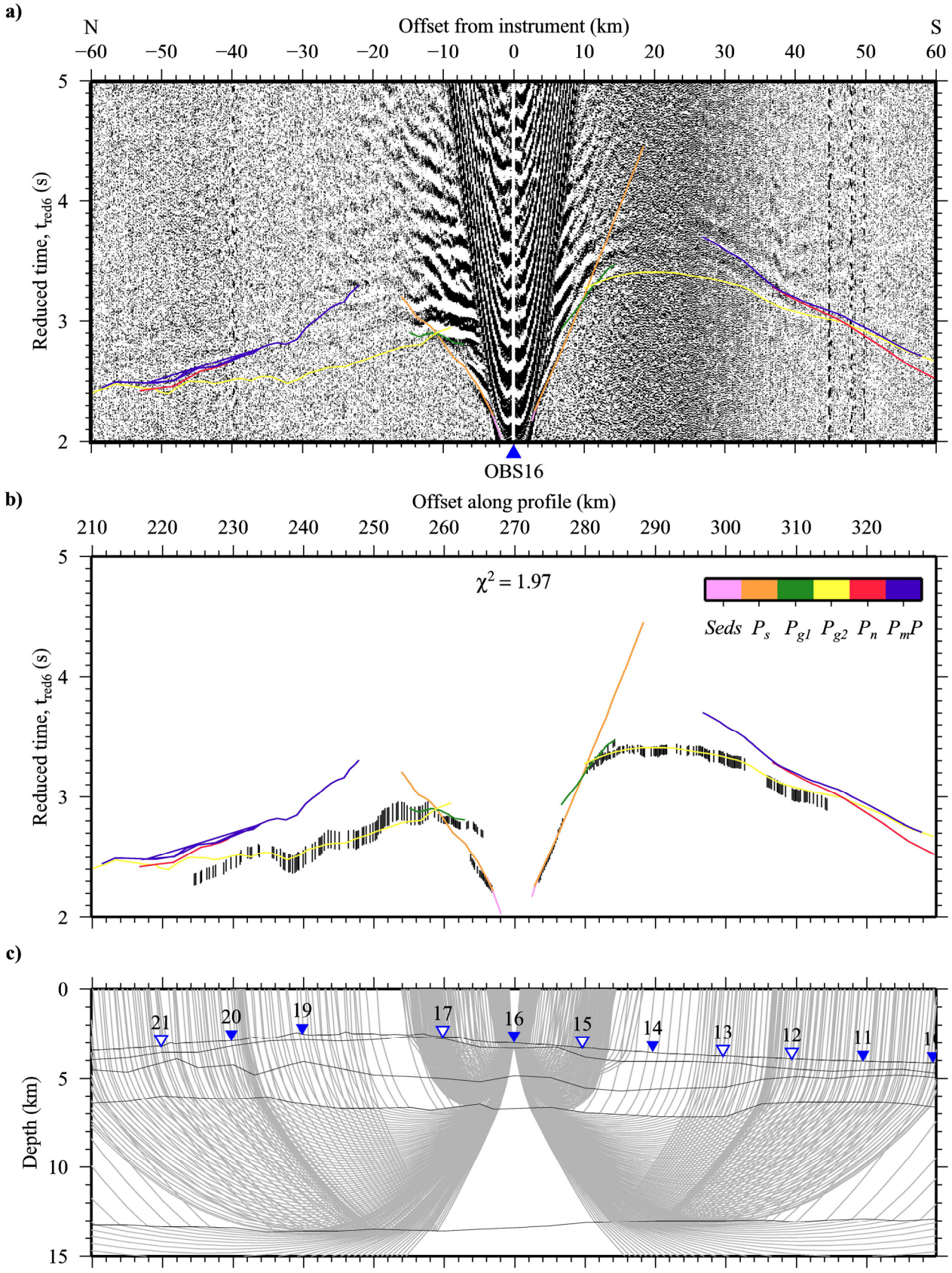

Figure A.23 Ray-trace modelling of traveltime picks from hydrophone data recorded by OBS16.

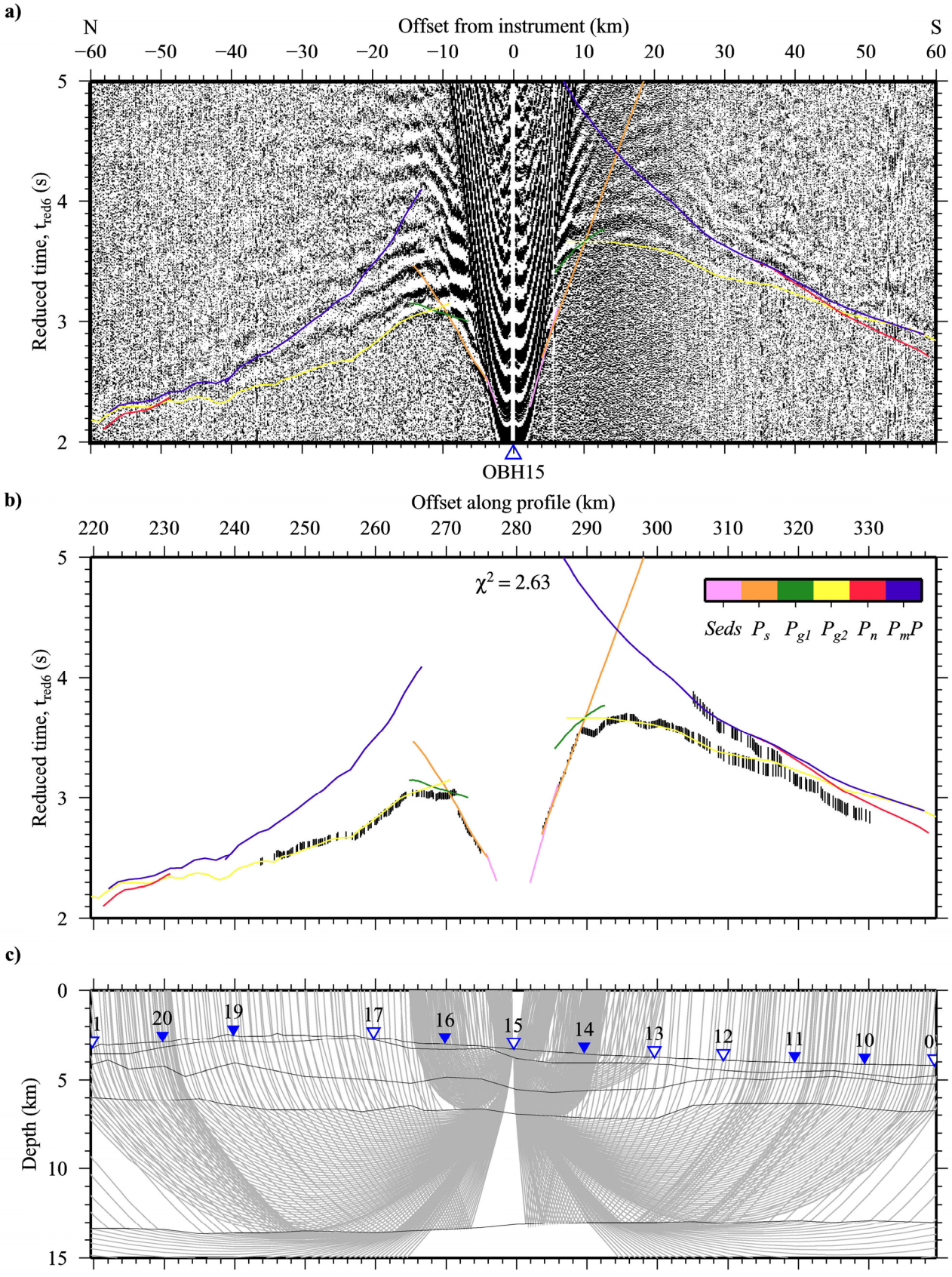

Figure A.24 Ray-trace modelling of traveltime picks from hydrophone data recorded by OBH15.

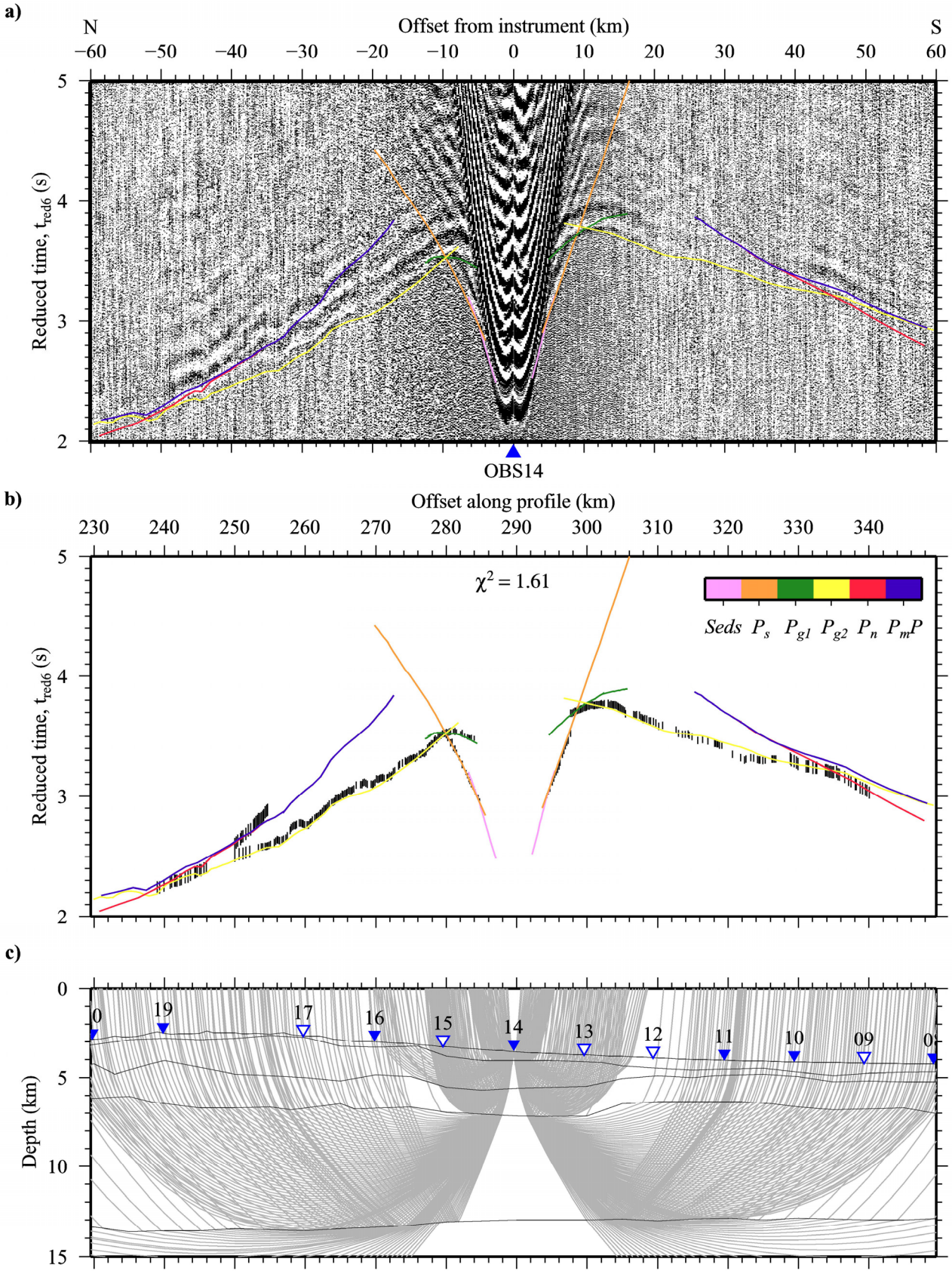

Figure A.25 Ray-trace modelling of traveltime picks from hydrophone data recorded by OBS14.

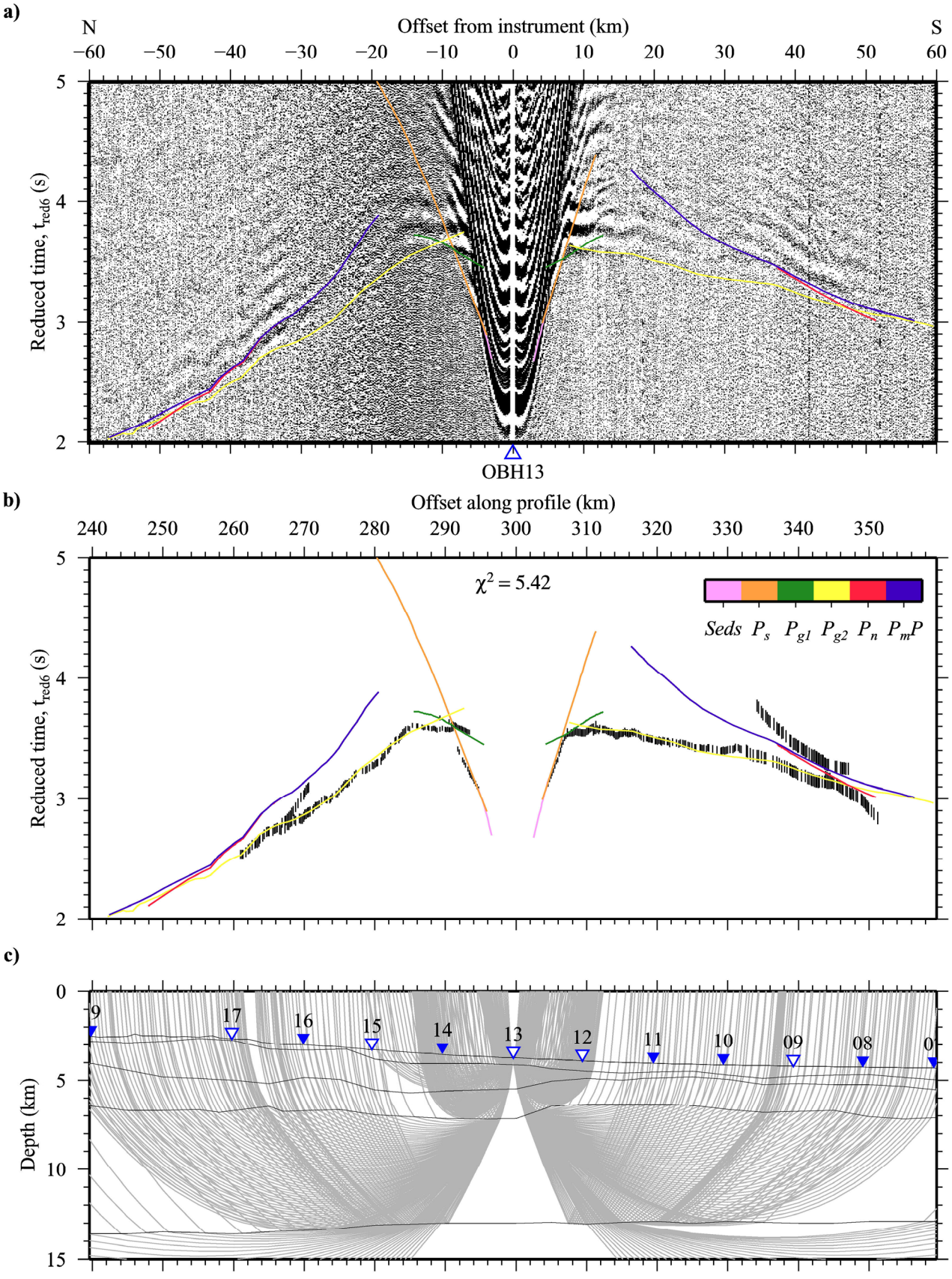

Figure A.26 Ray-trace modelling of traveltime picks from hydrophone data recorded by OBH13.

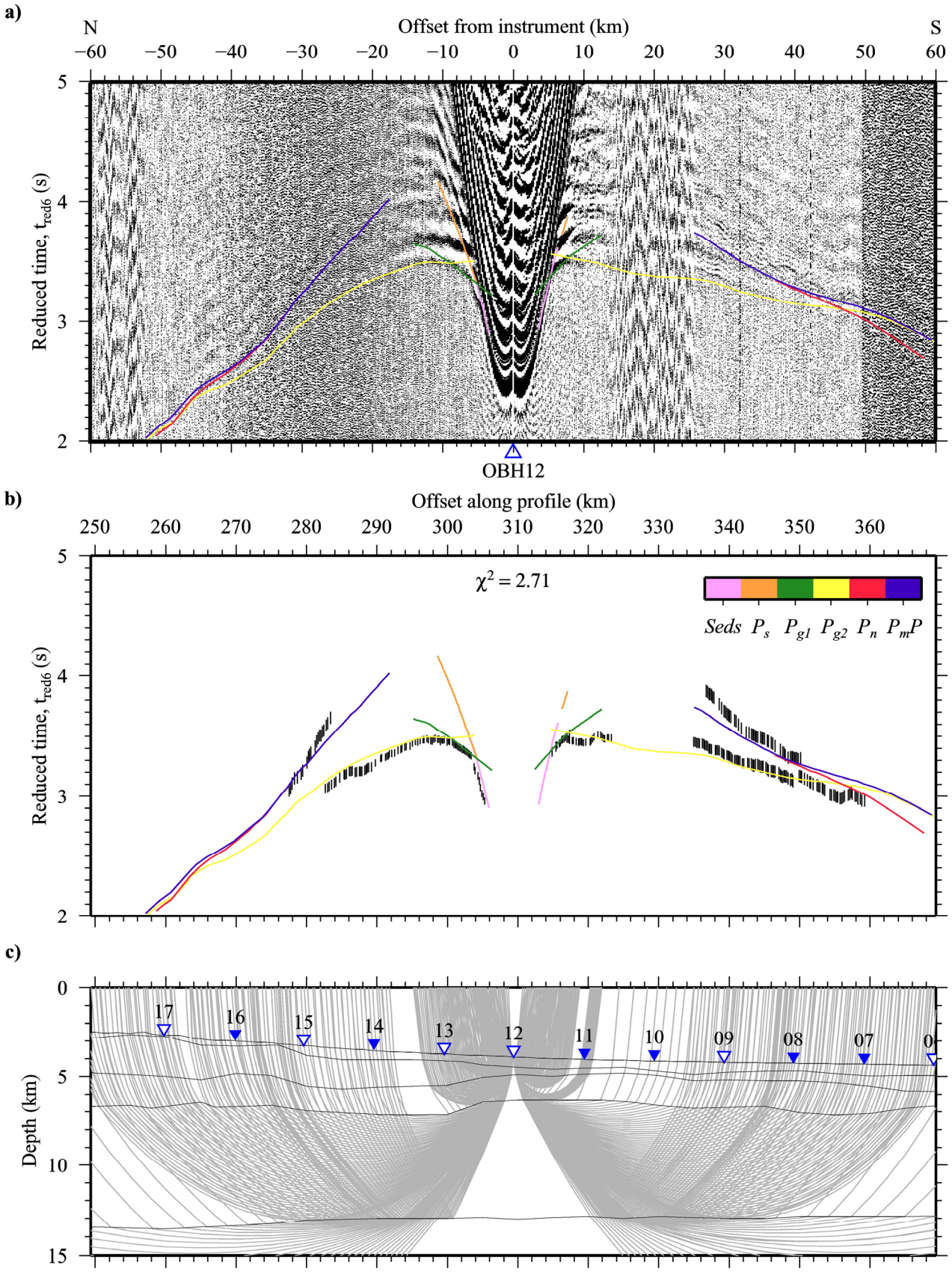

Figure A.27 Ray-trace modelling of traveltime picks from hydrophone data recorded by OBH12.

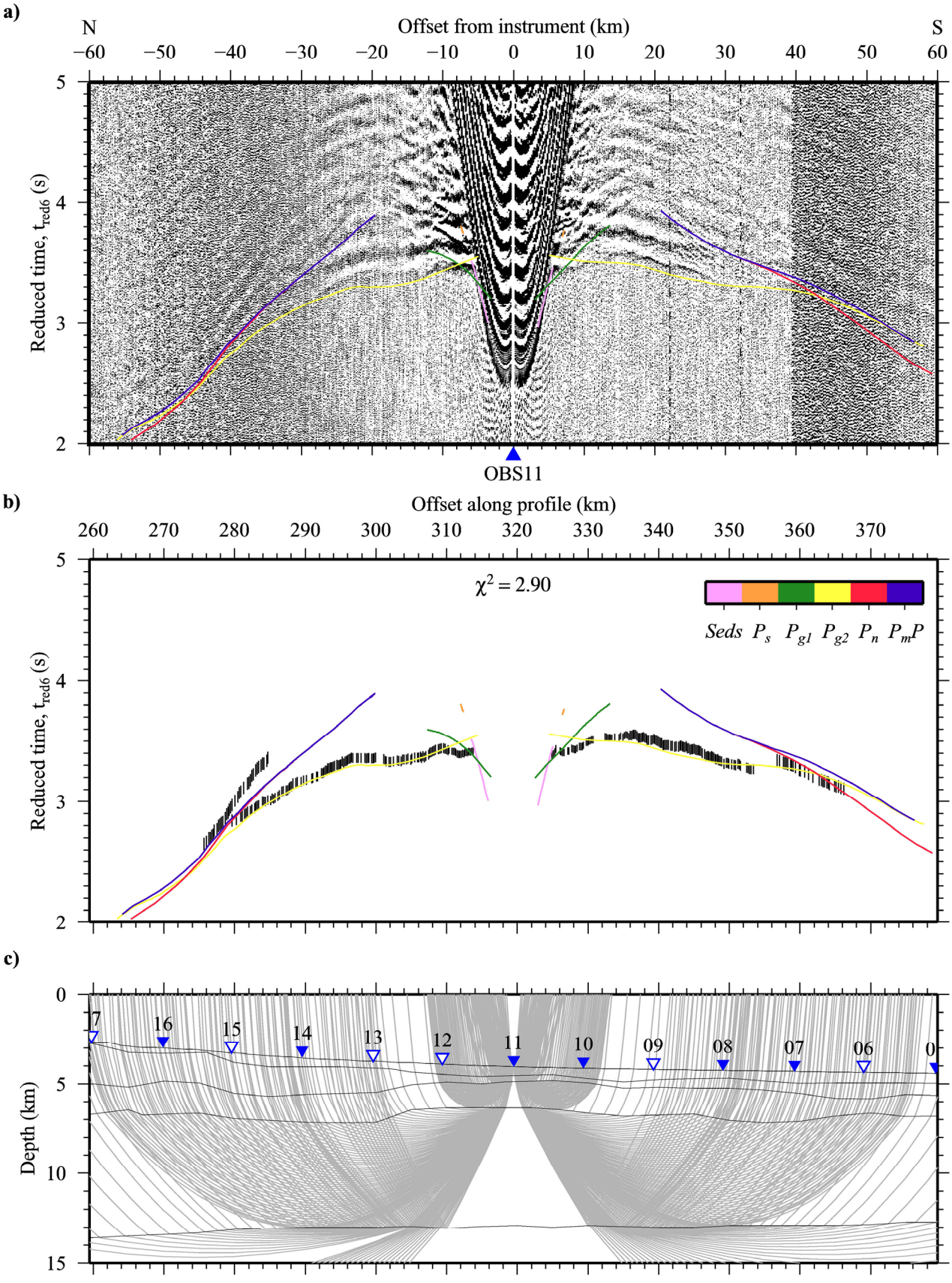

Figure A.28 Ray-trace modelling of traveltime picks from hydrophone data recorded by OBS11.

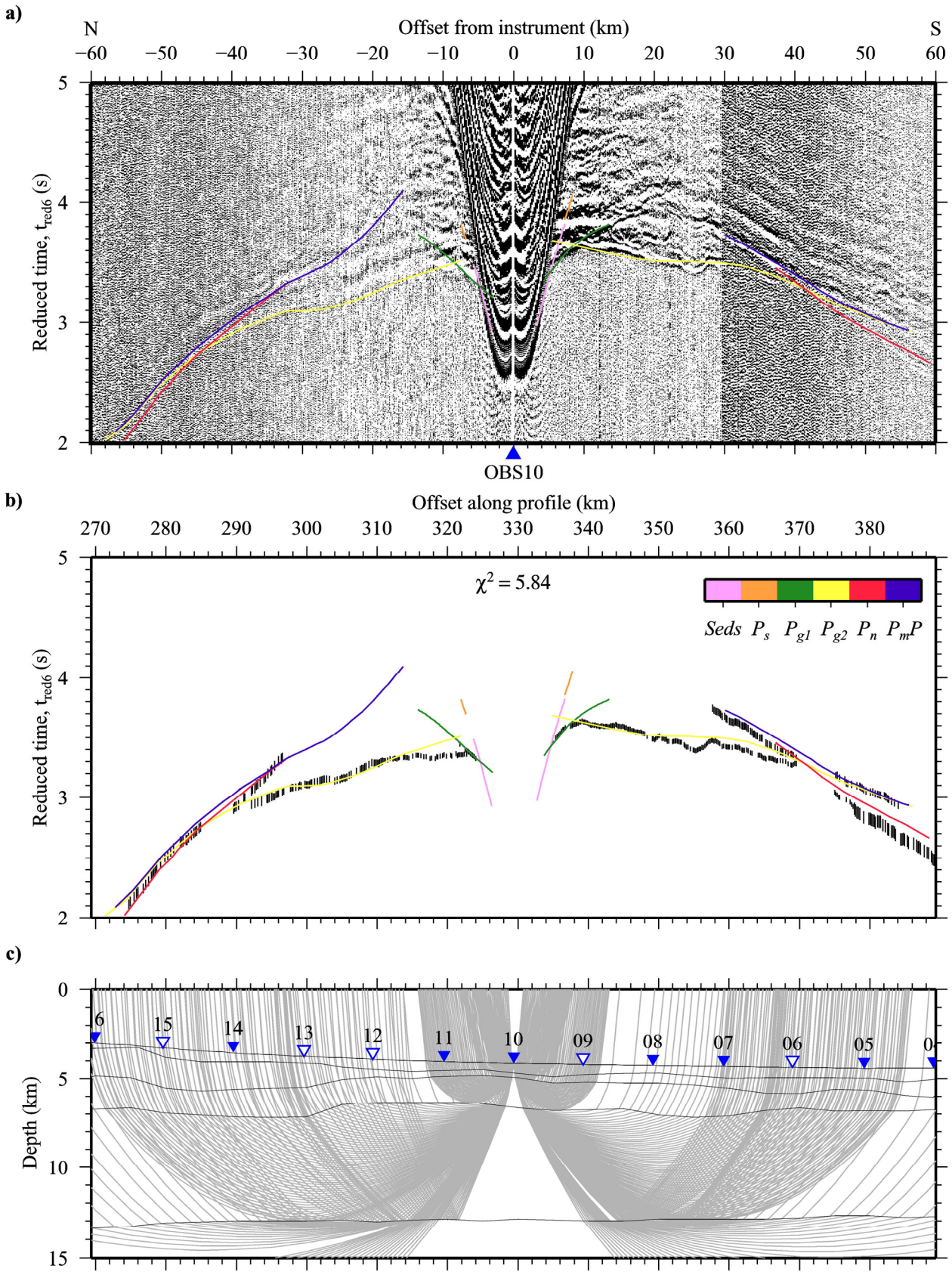

Figure A.29 Ray-trace modelling of traveltime picks from hydrophone data recorded by OBS10.

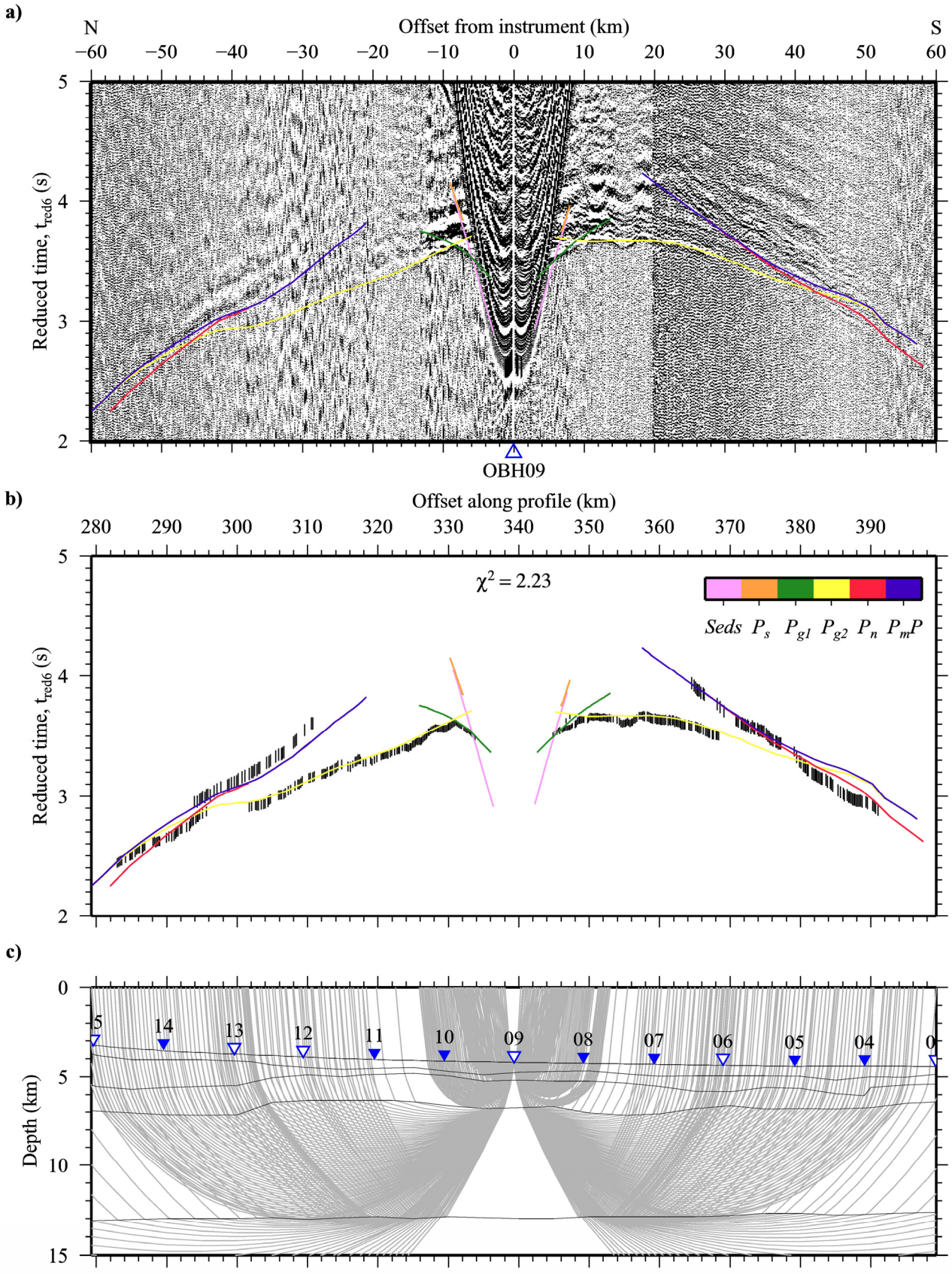

Figure A.30 Ray-trace modelling of traveltime picks from hydrophone data recorded by OBH09.

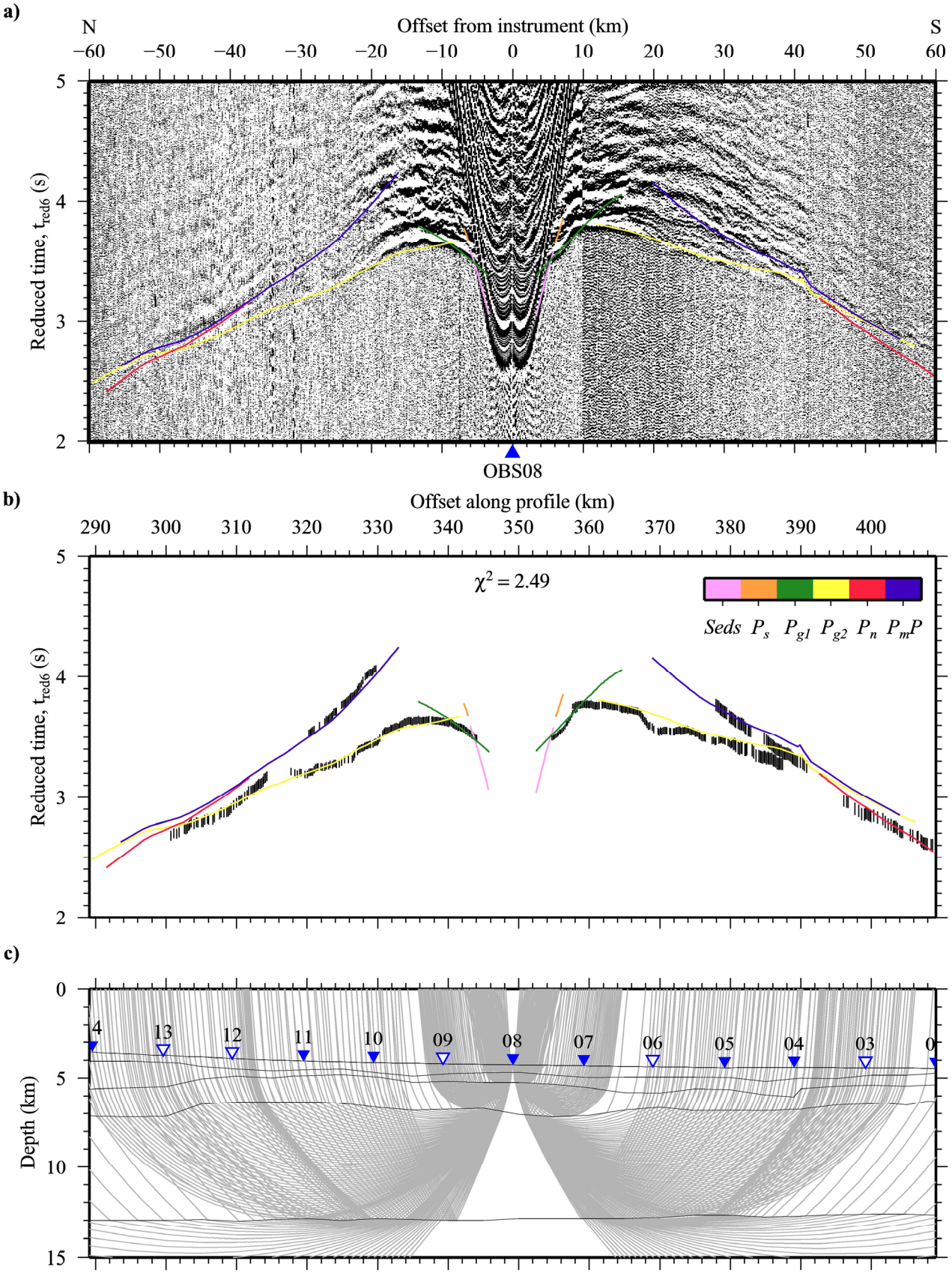

Figure A.31 Ray-trace modelling of traveltime picks from hydrophone data recorded by OBS08.

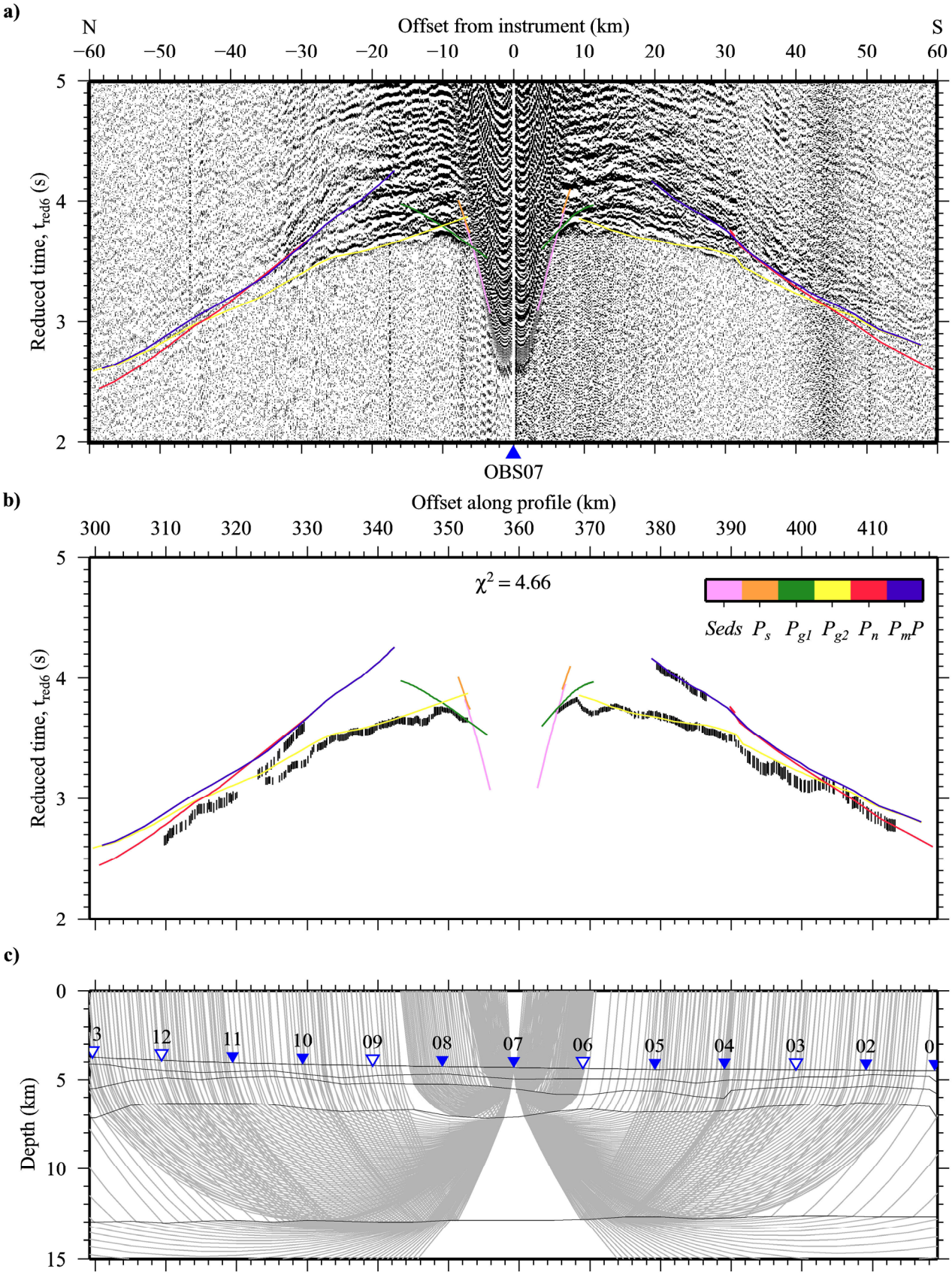

Figure A.32 Ray-trace modelling of traveltime picks from geophone data recorded by OBS07.

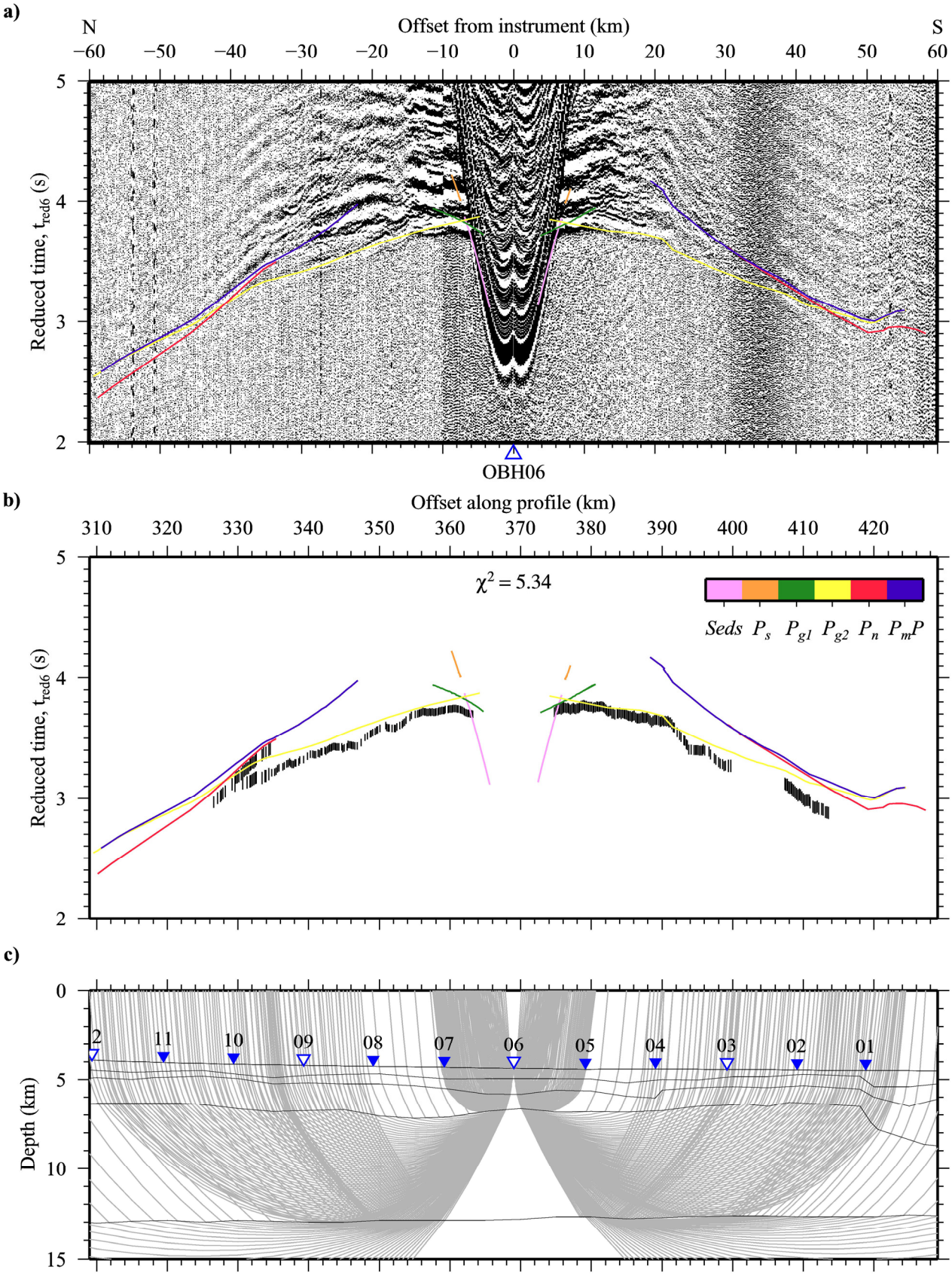

Figure A.33 Ray-trace modelling of traveltime picks from hydrophone data recorded by OBH06.

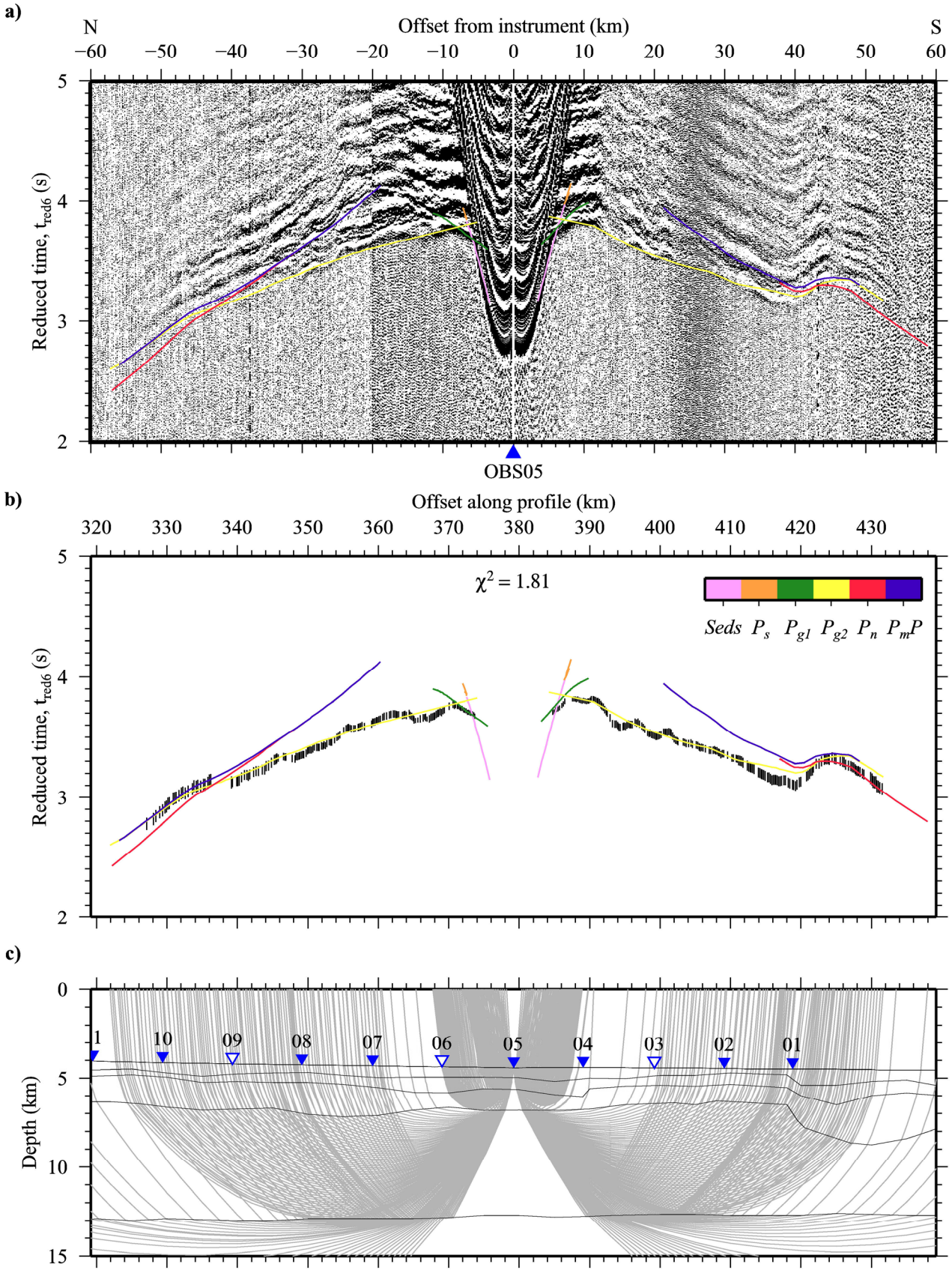

Figure A.34 Ray-trace modelling of traveltime picks from hydrophone data recorded by OBS05.

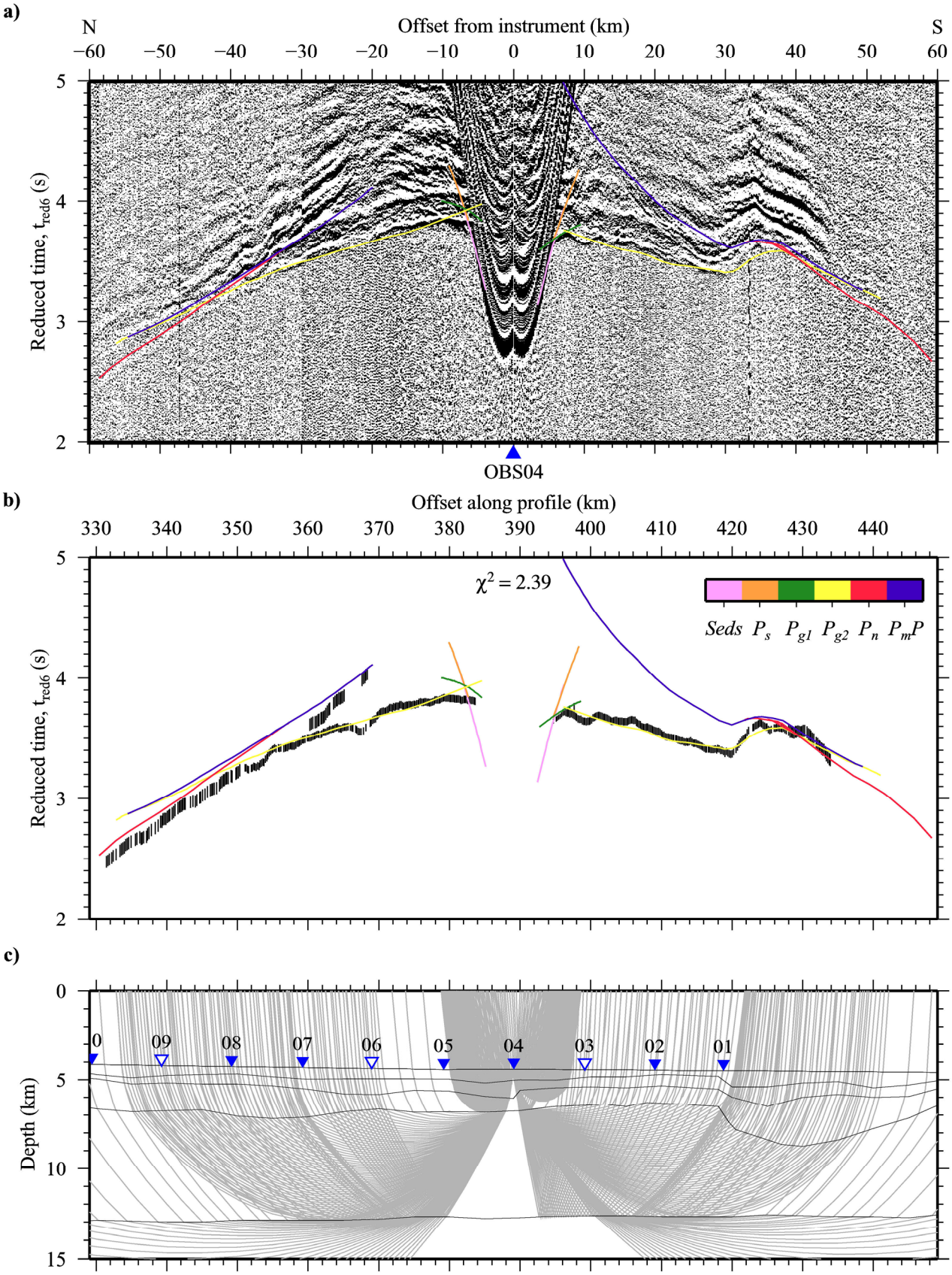

Figure A.35 Ray-trace modelling of traveltime picks from hydrophone data recorded by OBS04.

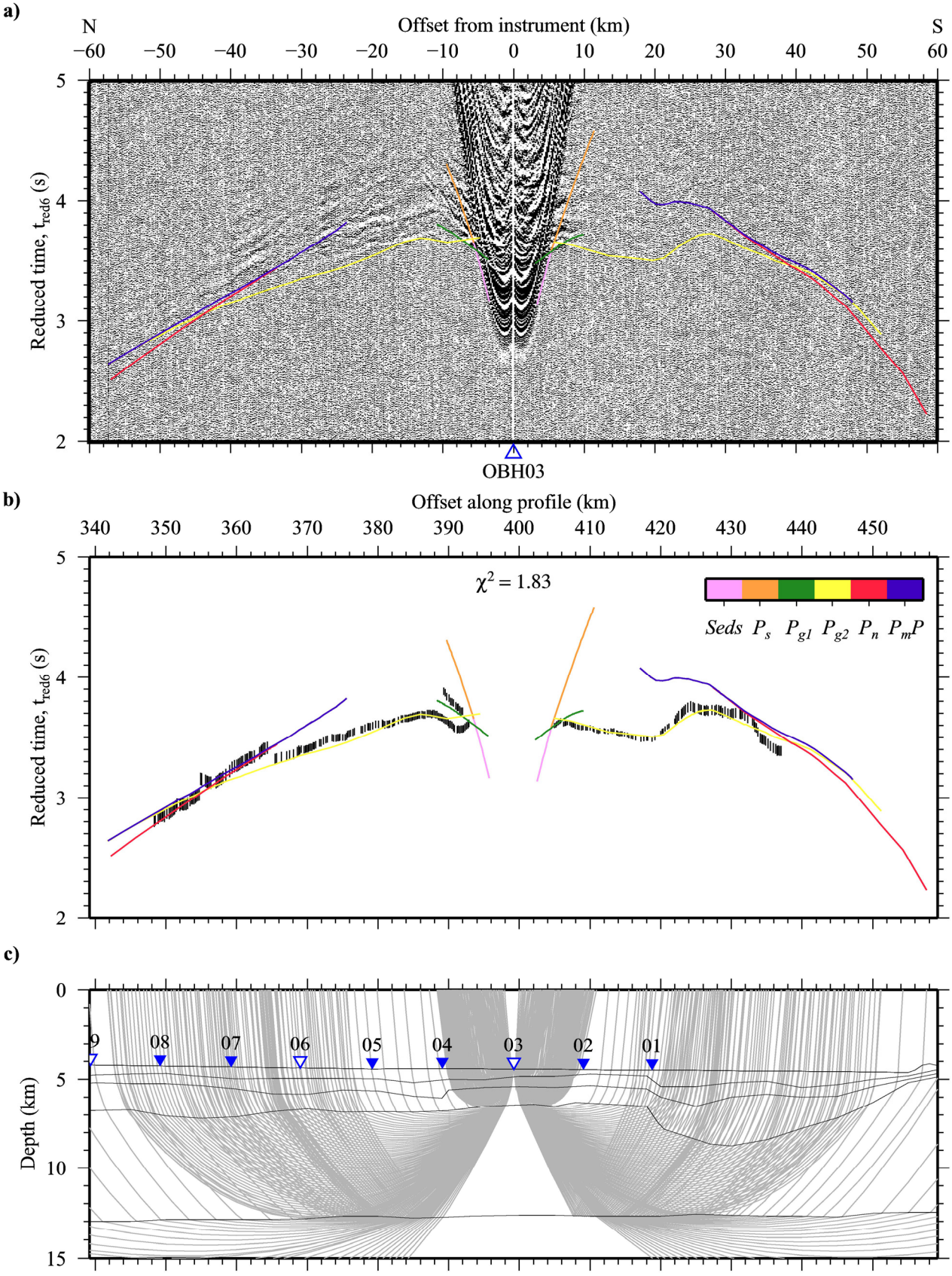

Figure A.36 Ray-trace modelling of traveltime picks from hydrophone data recorded by OBH03.

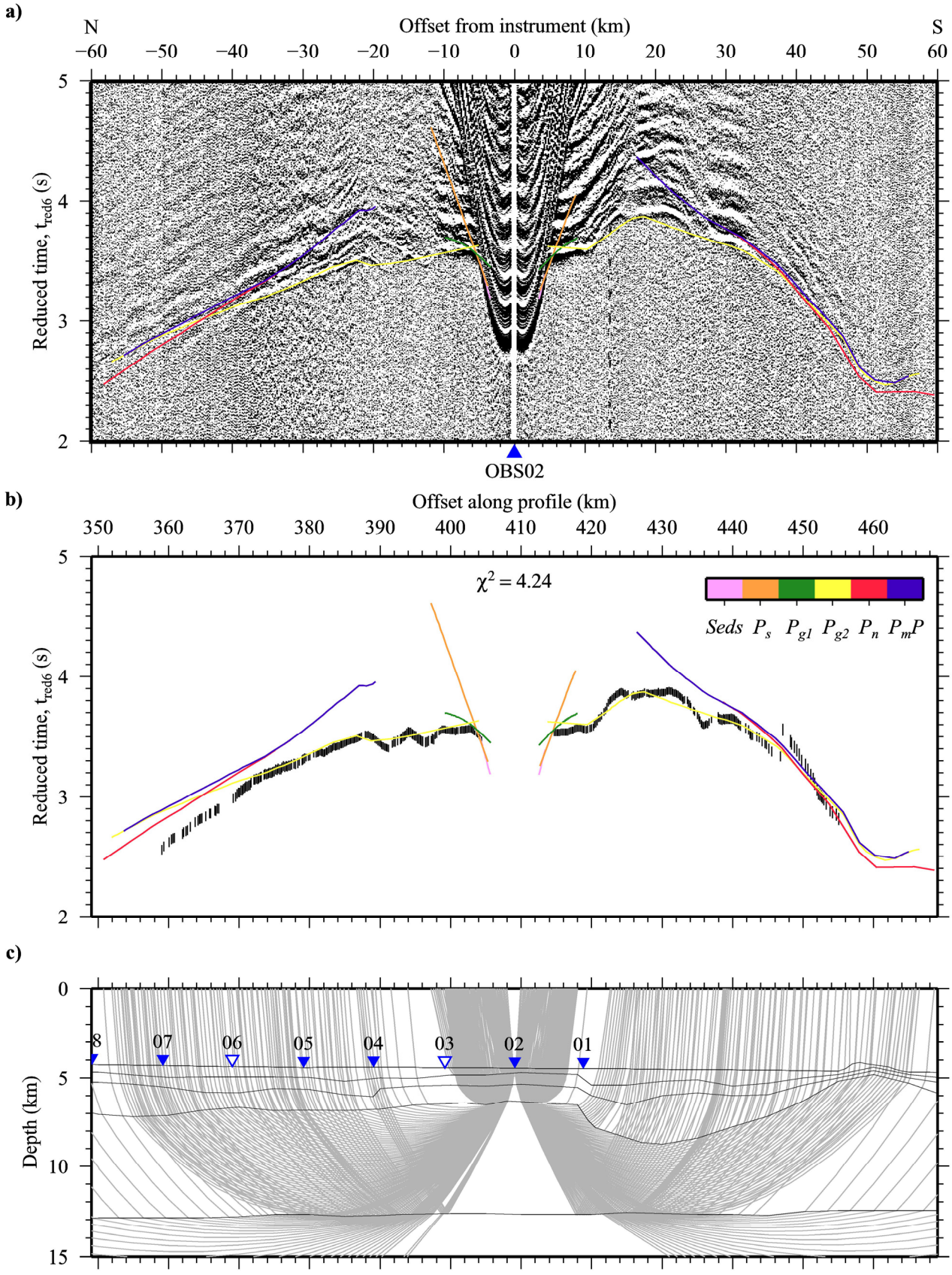

Figure A.37 Ray-trace modelling of traveltime picks from hydrophone data recorded by OBS02.

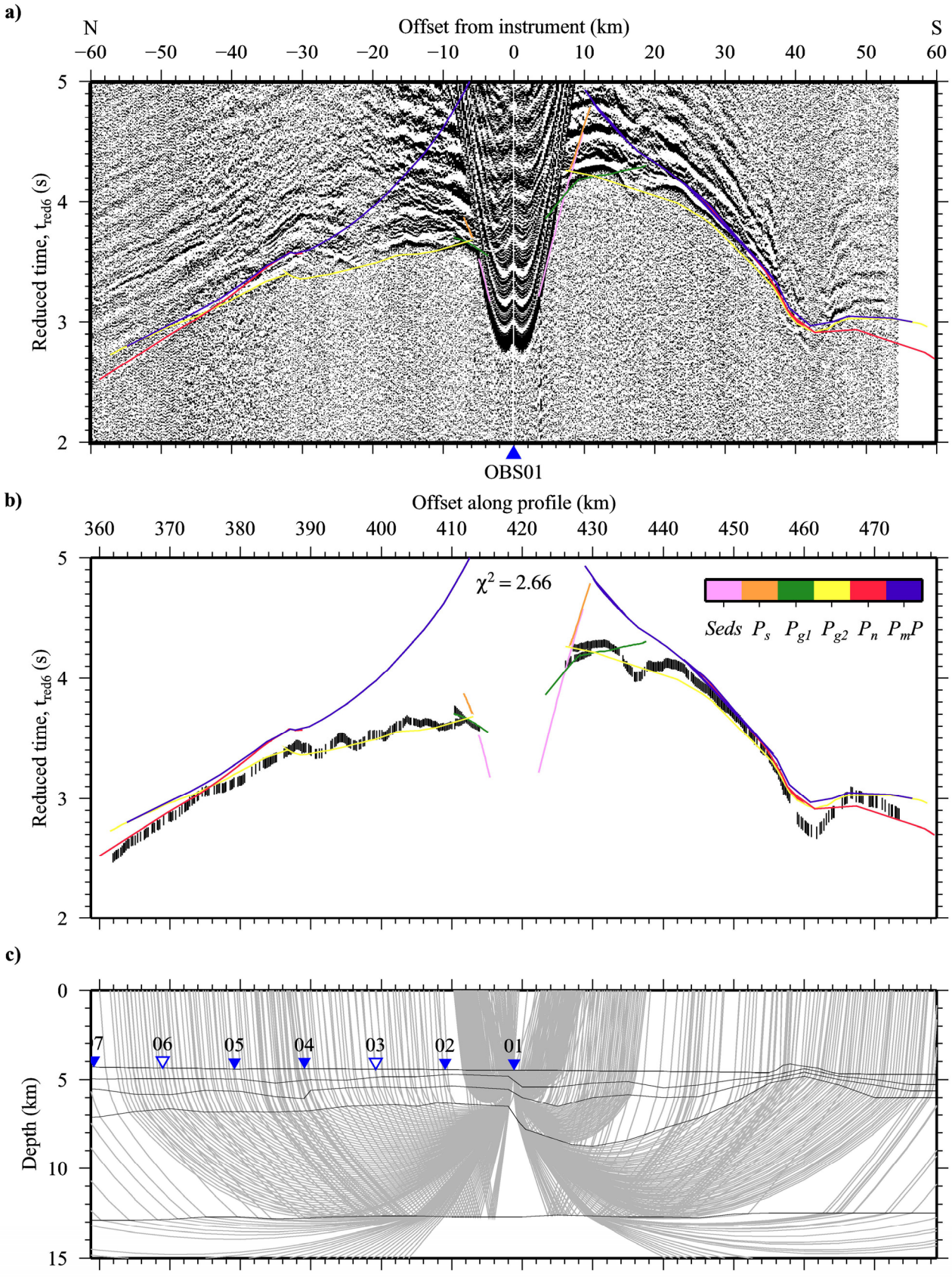

Figure A.38 Ray-trace modelling of traveltime picks from hydrophone data recorded by OBS01.

Appendix B

Wilson *et al.* (2010)

The following peer-reviewed paper contains a summary of the analysis of MCS and WA data, forward modelling of traveltime picks and 2-D gravity modelling presented in Chapters 2 & 3.

Geophysical Journal International

Geophys. J. Int. (2010) doi: 10.1111/j.1365-246X.2010.04641.x

Uplift at lithospheric swells—I: seismic and gravity constraints on the crust and uppermost mantle structure of the Cape Verde mid-plate swell

D. J. Wilson,[1] C. Peirce,[1] A. B. Watts,[2] I. Grevemeyer[3] and A. Krabbenhoeft[3]

[1]*Department of Earth Sciences, Durham University, South Road, Durham* DH1 3LE, *UK. Email: christine.peirce@durham.ac.uk*
[2]*Department of Earth Sciences, University of Oxford, Oxford,* OX1 3PR, *UK*
[3]*Leibniz-Institute of Marine Sciences, IFM-GEOMAR, East Shore Campus, Wischhofstr.* 1-3, D-24148 *Kiel, Germany*

Accepted 2010 April 26. Received 2010 April 19; in original form 2009 December 17

SUMMARY

Wide-angle seismic data have been used to determine the velocity and density structure of the crust and uppermost mantle beneath the Cape Verdes mid-plate swell. Seismic modelling reveals a 'standard' oceanic crust, ∼8 km in thickness, with no direct evidence for low-density bodies at the base of the crust. Gravity anomaly modelling within the constraints and resolution provided by the seismic model, does not preclude, however, a layer of crustal underplate up to 3 km thick beneath the swell crest. The modelling shows that while the seismically constrained crustal structure accounts for the short-wavelength free-air gravity anomaly, it fails to fully explain the long-wavelength anomaly. The main discrepancy is over the swell crest where the gravity anomaly, after correcting for crustal structure, is higher by about 30 mGal than it is over its flanks. The higher gravity can be explained if the top 100 km of the mantle beneath the swell crest is less dense than its surroundings by 30 kg m^{-3}. The lack of evidence for low densities and velocities in the uppermost mantle, and high densities and velocities in the lower crust, suggests that neither a depleted swell root or crustal underplate are the origin of the observed shallower-than-predicted bathymetry and that, instead, the swell is most likely supported by dynamic uplift associated with an anomalously low density asthenospheric mantle.

Key words: Controlled source seismology; Intraplate processes; Oceanic hotspots and intraplate volcanism; Lithospheric flexure; Crustal structure.

1 INTRODUCTION

The oceanic lithosphere is created at mid-ocean ridges and increases its long-term strength as it cools and subsides with age (e.g. Watts & Zhong 2000; Watts & Burov 2003). Acting as the outer thermal mechanical boundary layer of the solid Earth, the oceanic lithosphere also transfers excess heat, above background radiogenic production, from the underlying asthenosphere to the hydrosphere. A characteristic pattern of cooling and subsidence, increasing from the ridge axis to the continental margin, has been developed based on an exponential decrease in heat flow and increase in bathymetry with age (Davis & Lister 1974; Sclater *et al.* 1980). Since this correlation was first recognized, many anomalous bathymetric highs have been identified throughout the ocean basins (e.g. Marty & Cazenave 1989). These regions, or swells as they are commonly called, range in size up to 2000 km in diameter, with topography up to 2.5 km shallower than that expected based on plate age alone (Crough 1983; Stein & Stein 1992).

Oceanic mid-plate swells are also associated with long-wavelength gravity and geoid anomaly highs and excess heat flow (e.g. Crough & Jurdy 1980; Pollack *et al.* 1993), implying that the lithosphere is thermally reheated and/or mechanically weakened in some way, and are often accompanied by extensive and locally concentrated intraplate volcanism. These intraplate sites of persistent, long-term volcanic activity have been termed 'hotspots' (Wilson 1963) on account of the vast volumes of melt produced from the mantle without the aid of external tectonic forces, and are often associated with a similar scale of volcanism to that observed at plate boundaries. Examples of this hotspot-related volcanism are seamounts and oceanic islands superimposed upon the associated regional topographic swells and include Hawaii (Watts *et al.* 1985), the Canary Islands (Watts *et al.* 1997), the Marquesas Islands (Caress *et al.* 1995), the Cape Verde Islands (Pim *et al*. 2008; Grevemeyer *et al*. 2010) and the Society Islands (Grevemeyer *et al.* 2001b).

Geochemical $^{40}Ar/^{39}Ar$ dating of ocean island basalts also reveals that hotspots may be intermittently active for >100 Ma, often with more than 5 Ma between major eruptive phases, and some can be traced back to large igneous provinces using the age-progression of island chains and records of palaeoplate motions (Duncan &

© 2010 The Authors
Journal compilation © 2010 RAS

Richards 1991). The magnitude and longevity of hotspots therefore implies that they are the surface expressions of a significant melting process that may also act to dissipate excess heat energy from the deep interior.

One hypothesis for the formation of hotspots is that hot (low density) material rises from deep in the mantle, and interacts with the base of the crust (Sleep 1992; Ribe & Christensen 1994; Cserepes *et al.* 2000). Another is that weak zones in the lithosphere or crust, perhaps unusually thin or fractured, lead to preferential pathways for the injection and eruption of melt from the mantle (Turcotte & Oxburgh 1973; McNutt *et al.* 1997). Formation of hotspot-related volcanic edifices occurs either contemporaneously with crustal accretion at a mid-ocean ridge axis, for example at zero-plate age, or any time subsequently in a mid-plate setting as the underlying plate mechanically ages. No matter when they are constructed, these volcanic edifices represent a downward-acting force and undergo subsidence in order to maintain isostatic equilibrium as the plate on which they sit flexes under the load.

For a defined load of specific volume and density, the amplitude and wavelength of the associated subsidence is dependent upon the mechanical structure of the lithosphere. The elastic thickness, T_e, is a proxy for the long-term ($>10^5$ a) strength of the lithosphere. Lithosphere with a low T_e is weak and subsidence is confined to a concentrated area of deformation directly beneath the load, whereas lithosphere with a high T_e is strong and the total subsidence is accommodated within a larger region of lower amplitude flexure. Consequently, the ability to image marker interfaces within the crust that represent the amplitude and wavelength of the load-associated subsidence, enables the long-term thermal and mechanical properties of the lithosphere to be constrained. The flexural markers, in turn, can be used to determine the extent of modification to the thermomechanical structure of the lithosphere as a result of heating by sub-, intra- and extraplate magmatic processes (e.g. Ali *et al.* 2003).

Analysis of multichannel seismic (MCS) reflection data provides a means of mapping the geometry of such horizons within the sediment column, such as unconformities, which reflect major phases of subsidence or uplift. Wide-angle (WA) refraction data, on the other hand, not only provide velocities for depth conversion and subsequent top-of-plate load volume and mass calculation, but can also be interpreted to infer the extent of, if any, crustal thickening by underplating or intracrustal density change as a result of magmatic intrusion.

Such observed horizons can be compared to those predicted from elastic plate flexure models using an oceanic lithosphere with a T_e based on its expected age derived from magnetic anomalies. Any mismatch between the calculated and observed flexural surfaces implies an anomalous lithosphere. If, for example, the observed flexure is less pronounced than that predicted, then this implies that subsurface forces are acting to support the surface load (e.g. Watts & ten Brink 1989). If more pronounced, it implies that the lithosphere has been mechanically rejuvenated.

Comparison of bathymetric and geoid anomalies to the expected values for standard oceanic lithosphere together with evidence from flexural horizon modelling, suggests that there is some form of regional load support acting at mid-plate swells. Several mechanisms have been proposed to explain how large-scale topographic swells are sustained over geological timescales (Fig. 1, based on Crough 1983):

1. Shallow support within the crust (Fig. 1a)—e.g. Morgan *et al.* (1995). The eruption of volcanic islands on top of the oceanic lithosphere is often accompanied by underplating, the intrusive accumulation of neutrally buoyant magma at the base of the crust (e.g. Charvis *et al.* 1999; Grevemeyer *et al.* 2001b). A thickened oceanic basement provides additional buoyancy, due to its lower density relative to the surrounding mantle, analogous to the deep crustal roots that support continental mountain belts.

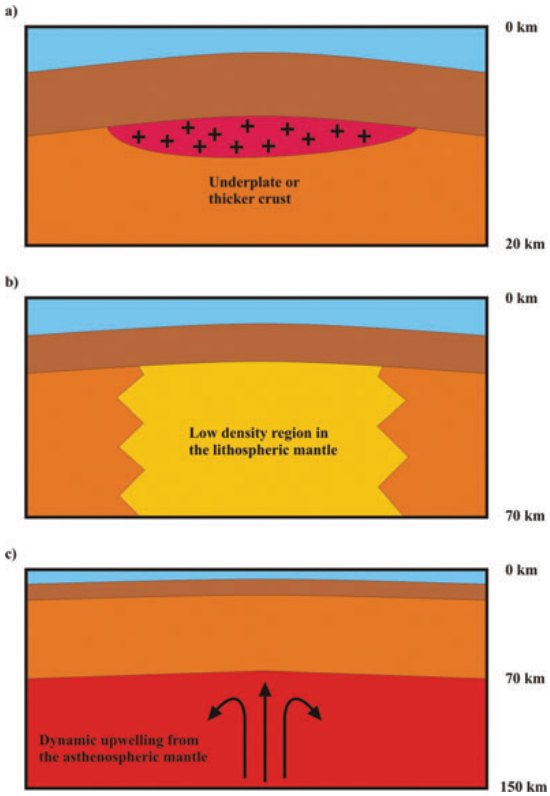

Figure 1. Mechanisms proposed to explain how large-scale topographic swells are sustained over geological timescales (after Crough 1983). (a) Shallow support in the crust. (b) Support in the lithospheric mantle. (c) Upwelling in the asthenospheric mantle.

2. Support within the upper mantle (Fig. 1b)—e.g. Detrick & Crough (1978) and Robinson (1988). A region of low density in the lithospheric mantle, either due to an elevated temperature or compositional variation, may provide sufficient upwards force to elevate the lithosphere. Morgan *et al.* (1995) observed a strong correlation between the volume of oceanic volcanism and the size of the associated bathymetric swell along the Hawaiian chain, and show that the density reduction in the lithospheric mantle and the upper asthenosphere due to thermal reheating and basaltic melt extraction contributes significantly to swell topography.

3. Dynamic mantle upwelling (Fig. 1c)—e.g. Sleep (1995). Material actively rising through the asthenosphere acts as a negative load on the base of the lithosphere that causes flexure of the entire plate. Monnereau *et al.* (1993) used numerical models to simulate dynamic uplift resulting from the ascent of low density material through a convective mantle to the base of a rigid lithosphere. Uplift was observed to occur in two stages: pure dynamical support during initial ascent, and a larger stage of uplift following ductile

© 2010 The Authors, *GJI*
Journal compilation © 2010 RAS

thinning of the lithosphere as the upwelled material impinges on the convective boundary layer.

In this paper, we present the results of analysis and forward modelling of a WA seismic refraction dataset acquired along an ∼475 km profile through the Cape Verde archipelago; a chain of volcanic islands superimposed on the crest of the Cape Verde mid-plate swell. Traveltime data are iteratively modelled using a ray tracing approach to produce a 2-D velocity–depth model of the crust and uppermost mantle. The resulting velocity–density–depth model is then tested against the coincident MCS-derived flexural horizons and shipboard and satellite free-air gravity anomaly (FAA) data for uniqueness and consistency.

Ultimately, the Cape Verdes study aims to evaluate the three proposed swell support mechanisms using various forward modelling methods applied to a range of observed geophysical data, as well as investigate the origin of swells. Anomalously thick crust would suggest that a swell is an old feature that originated during enhanced magmatic crustal accretion at a mid-ocean ridge, perhaps under the influence of enhanced mantle upwelling. Normal thickness crust would imply that a swell is a post-accretion feature, possibly related to vertical motion in the underlying mantle. Here, we take the first steps to resolving the origin of the uplift observed at the Cape Verde mid-plate swell by first resolving the lateral and vertical variation in layering structure and density within the 'background' crust which, in turn, will act as well-constrained input into plate flexure and thermal structure modelling of the whole plate, by allowing the superimposed shorter wavelength anomalies to be accounted for and removed. This 'whole plate' modelling, and a consideration of the geoid anomaly, will be presented in a subsequent paper.

2 TECTONIC SETTING

The Cape Verde Swell is the largest observed mid-plate swell on Earth; the approximately circular bathymetry anomaly alone encompasses a region 1800 km in diameter with a crest 2.2 km shallower than the surrounding abyssal plain, while the corresponding geoid anomaly reaches a maximum of +8 m (Monnereau & Cazenave 1990). Heat flow measurements show an increase from 43.5 mW m^{-2} away from the influence of the swell to 60.5 mW m^{-2} near the swell crest (Courtney & White 1986; Fig. 2), with the maximum heat flow anomaly 16 mW m^{-2} higher, using the plate model of Parsons & Sclater (1977), than predicted for the (regional average) 130 Ma oceanic lithosphere on which the swell is imposed. The slow-to-stationary absolute motion of the African Plate in the Cape Verde region, $<$10 mm yr^{-1} (Morgan 1983; Pollitz 1991), also results in a concentration of the associated uplift and volcanism into an approximately circular area and, consequently, makes this the ideal site to test the various proposed models for mid-plate swell support.

The Cape Verde archipelago is located ∼600 km off the coast of Senegal, West Africa, and is centred to the southwest of the crest of the associated swell. The cluster of nine main islands can be subdivided into a crescent of six islands to the southeast and a chain of three aligned towards the northwest (Fig. 2). Most of the island-building magmatism is thought to have occurred within the past 15 Ma (Stillman *et al.* 1982; Mitchell *et al.* 1983; Holm *et al.* 2008) and only Fogo has experienced historically recent volcanic activity. Magnetic anomalies M0–M21 can be identified in this region (Fig. 2), suggesting that the oceanic crust on which the islands were emplaced was accreted during the separation of the African continent from the Americas in the early Cretaceous (Albian to Berriasian, ∼110–150 Ma).

3 EXISTING DATA AND MODELS

The earliest seismic experiment in the Cape Verde region was by Dash *et al.* (1976) who undertook a refraction survey using land-based recording instruments deployed on the islands of Sal, Santiago and São Vicente. The data were analysed using a 1-D slope intercept method to determine the crustal structure along three split-spread profiles between the islands (Fig. 2). The resulting 1-D velocity–depth profiles indicate a velocity structure similar to that expected for standard oceanic crust (White *et al.* 1992), except for a consistently deeper Moho (16.2–16.7 km depth). However, these results are based on the assumptions of planar intracrustal layering and homogeneity within layers in the subsurface, and may reflect a bias towards local crustal thickening concentrated beneath the islands given the recording instrument locations.

Using MCS reflection and gravity data acquired during the 'RRS Charles Darwin' geophysical survey in 1985 (Fig. 2), Ali *et al.* (2003) mapped flexural horizons in the moat sediments of the islands and investigated the shallow crustal structure down to the igneous basement. By modelling the geometry of these markers, the degree of flexure could be quantified and compared to that obtained from numerical models of viscoelastic plates subjected to loads of comparable dimensions to the islands, to determine the T_e of the underlying lithosphere. Their calculated T_e of 29 km agrees with that predicted from the magnetic anomaly derived plate age predicted value, signifying that the lithosphere has not been significantly, if at all, thermally rejuvenated as part of load emplacement.

However, the interpretation (and subsequent modelling) of flexural markers picked in reflection data depends upon the accuracy of the time-to-depth conversion, which in turn depends on accurate velocity information. Only a few sparse and poor quality sources of velocity data were available to Ali *et al.* (2003), including: stacking velocities; a sonobuoy at the edge of their study area; and 1-D estimates from Dash *et al.* (1976). All of these velocity sources have limitations in accuracy, depth sampled below the surface and areal extent, and are far from ideal, even taken collectively.

Analysis of receiver functions from a temporary network of seismic recording stations on the Cape Verde islands has provided several additional 1-D estimates of crustal thickness and velocity–depth structure of the lithospheric mantle (Lodge & Helffrich 2006). The results have also been interpreted to suggest crustal thickening beneath some of the islands, but are unable to differentiate between models for localized crustal thickening related to island building, and regional underplating related to the support of the entire swell.

4 SEISMIC EXPERIMENT

The *R/V Meteor* cruise M62/3 conducted a marine geophysical survey over the Cape Verde mid-plate swell. The main objective of this cruise was to investigate the crust and upper mantle structure of the swell by means of a WA, controlled-source seismic refraction experiment. The location of the main seismic profile (a solely WA profile) across the swell was chosen to coincide with a MCS reflection profile acquired during *RRS Charles Darwin* cruise 8/85 (Ali *et al.* 2003) which would be used to inform the initial velocity–depth model in terms of the sediment column structure and geometry, and the depth to basement (defined here as the top of oceanic crustal layer 2—the extrusive sequence).

Ocean-bottom seismographs and hydrophones (OBS and OBH, respectively; henceforth collectively referred to as OBS for

© 2010 The Authors, *GJI*
Journal compilation © 2010 RAS

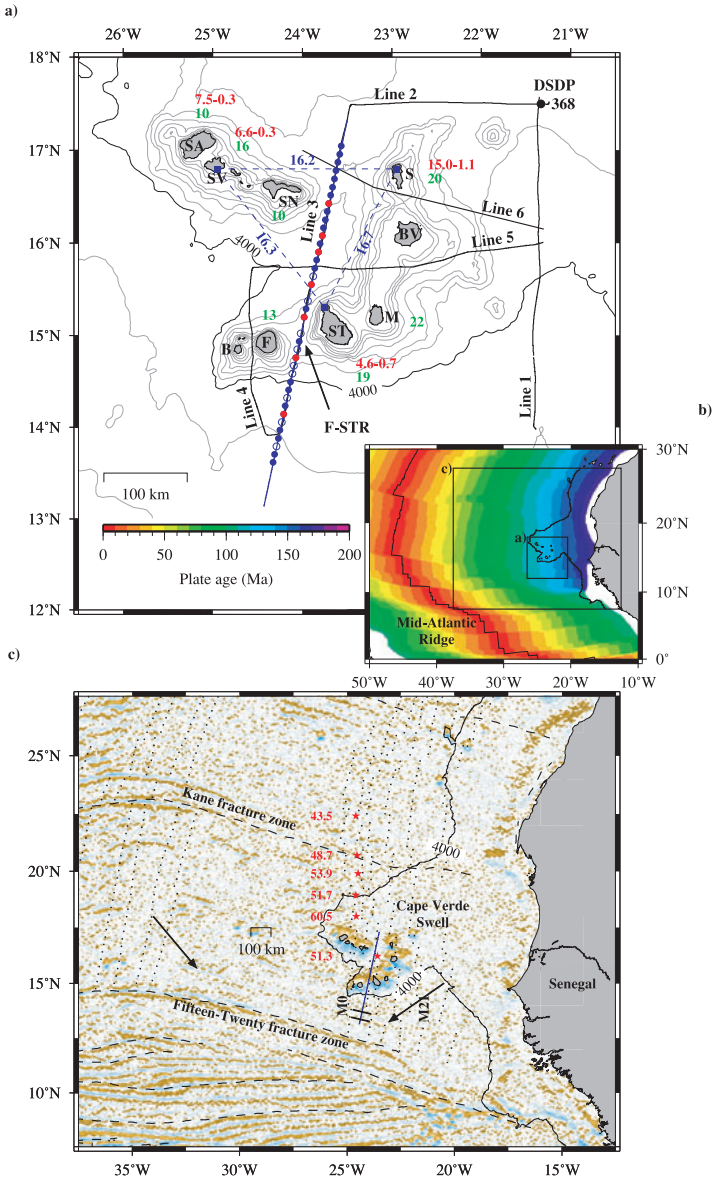

Figure 2. Geophysical surveys conducted at the Cape Verde archipelago and the tectonic setting of the Cape Verde Swell. The 4000 m bathymetric contour is used to outline the extent of the swell. (a) Location of MCS profiles from RRS Charles Darwin 1985 (black), see Ali *et al.* (2003), and the WA refraction profile from this study (blue). Filled/open blue circles mark OBS/OBH locations with red circles showing OBSs whose data is included in this paper. DSDP Site 368 is indicated with a black dot. Lodge & Helffrich's (2006) Moho depths, in km, beneath islands (green text) and Holm *et al.*'s (2006; 2008) volcanic evolution timescales, in Ma, (red text) are also shown together with Dash *et al.*'s (1976) 1-D seismic profiles and Moho depth determinations, in km (blue dashed lines and text). Islands: SA, Santo Antão; SV, São Vicente; SN, São Nicolau; S, Sal; BV, Boa Vista; M, Maio; ST, Santiago; F, Fogo; B, Brava. F-STR, Fogo-Santiago Ridge. Bathymetric contours (grey) with a 500 m contour interval. (b) Plate ages of Müller *et al*. (2008). Black boxes show the extent of the areas in (a) and (c). (c) The first derivative in latitude of the free-air gravity anomaly showing the locations of well-documented fracture-zones (dashed lines). A faint lineation can be observed trending perpendicular to the WA profile (as indicated by arrows) that intersects with the profile trend (blue line) at the southern end (as highlighted by parallel lines). Magnetic anomaly isochrons (dotted lines) show agreement with the plate ages in (b) and offsets correlate with fracture zone locations. Courtney & White's (1986) heat flow measurements, in mW m^{-2} (red stars and text), show a positive heat flow anomaly over the Cape Verde Swell.

© 2010 The Authors, *GJI*
Journal compilation © 2010 RAS

simplicity) were deployed at 10 km intervals along 390 km of the 475 km profile running north-south through the archipelago, intersecting the crest of the Cape Verde Swell at 16°00'N, 23°48'W (Fig. 2). OBS data were continuously recorded with a sampling rate of either 200 or 250 Hz, depending on instrument type (OBH or OBS, respectively). Swath bathymetry, gravity and magnetic data were also acquired contemporaneously along the profile. The seismic source consisted of eight airguns, configured as two subarrays towed at 8 m depth, and provided a total volume of ∼4000 in^3 (64 l). The source was triggered at 90 s intervals at a surveying speed of four knots, resulting in an average shot spacing of 180 m.

5 SEISMIC DATA

WA data were successfully recorded by 38 of the 40 instruments deployed, and example record sections showing features characteristic of all instruments are shown in Figs 3–6. Spectral analysis of these data shows that the seismic source had a frequency band of 5–30 Hz. On record sections with a high signal-to-noise ratio (SNR), arrivals can be identified to >60 km receiver offset (Fig. 3a). However, for instruments deployed on the crest of the Fogo-Santiago Ridge (F-STR) (Fig. 2), record sections have a low SNR (Fig. 3c) resulting in arrivals only being clearly observed at much shorter offsets.

Pim *et al.* (2008) present the results from a pilot study using a subset of the WA seismic and gravity data collected as part of *R/V Meteor* cruise M62/3. The aim of their study was to test the viability of the application of the data to 2-D seismic forward modelling and of the resultant velocity–depth model of a 2-D transect through the swell, as a crustal reference for 3-D flexure and gravity modelling of the entire swell. Pim *et al.*'s (2008) preliminary results show that the WA and gravity data can be best fit by a velocity–density–depth model which is not significantly different from standard oceanic crust and requires no underplate or regions of anomalous density in the lower crust or upper mantle, although this transect does not pass through any island and, thus, may also support Ali *et al.*'s (2003) conclusion that any underplate may be island load specific and not a major contributor to the swell.

Unlike Pim *et al.* (2008), who analysed the data from just nine instruments, in this paper we concentrated on the accurate identification of *P*-wave phases on both the hydrophone and vertical geophone record sections for all 38 instruments that recorded usable data. Primary refracted arrivals were grouped into four major phase types that could be correlated between adjacent instruments along the entire profile. The phase groups were labelled according to the expected subsurface structure, apparent *P*-wave velocities and receiver offset ranges (Fig. 3) as follows: a shallow subsurface arrival, P_s, which is often masked by other phases; two predominant crustal arrivals, P_{g1} and P_{g2}; and upper mantle arrivals, P_n. In addition, the traveltimes of secondary arrivals reflected from the Moho, P_mP, were also picked.

Although the co-incident MCS data reveal a layer of sediment along all of the profile except at the F-STR, sediment arrivals are not distinguishable as clear first arrivals, being effectively obscured by the direct water wave and crustal arrivals, P_{g1} and P_{g2} (Fig. 3d). This absence of first-arriving sediment phases indicates that the sediment succession is relatively thin and/or has a low range of *P*-wave velocities. This conclusion is consistent with results of interpretation of the coincident and all regional MCS data (Fig. 7a; Ali *et al.* 2003) and cores from DSDP site 368 (Lancelot *et al.* 1978), which indicate sediment thicknesses of <2 km and bulk sediment *P*-wave velocities of <2.50 km s^{-1}, respectively.

5.1 Shallow subsurface arrival, P_s

The P_s phase has an apparent velocity in the range 3.50–4.00 km s^{-1}, and the associated traveltime picks were assigned pick uncertainties in the range 20–30 ms. This phase is identified as a primary arrival at short receiver offsets (<10 km) exclusively on records from instruments deployed on the F-STR located between 220 and 310 km offset along the profile. The shot-receiver offset range over which this phase is observed increases heading towards the summit of the F-STR (250 km, profile offset), suggesting that the layer in which this arrival originates increases in thickness in this vicinity (Figs 3b and c). An absence of coherent reflectors is also noted in the MCS data in this region (Fig. 7). Instead, there is an intermittent high amplitude event beneath which reflections are chaotic and of high reflectivity, consistent with the reflection characteristics of igneous material erupted onto the seafloor or collapse debris from adjacent islands. These observations suggest that the F-STR is an intrasediment ridge comprising igneous material and only a thin veneer of sediment when compared to elsewhere along the profile.

5.2 Crustal arrivals, P_{g1} and P_{g2}

Upper-mid crustal arrivals, P_{g1}, are identified as clear, high-amplitude arrivals with a high SNR along the entire profile at shot-receiver offsets of <10–15 km (Fig. 3e). These phases typically exhibit apparent velocities of 4.50–5.50 km s^{-1}, within the range expected for typical oceanic crustal layer 2 (White *et al.* 1992). The lateral variation in arrival time of the upper-mid crustal phase mirrors the topography of the basement surface.

The transition to the mid-lower crustal phase, P_{g2}, is mainly continuous (Fig. 3f), displaying a gradual increase in apparent velocity to 5.75 km s^{-1} at the top of the layer, with the layer velocity increasing to 7.25 km s^{-1} at the base, comparable to that of the gabbroic oceanic crustal layer 3 (White *et al.* 1992). Mid-lower crustal arrivals are consistently observed to shot-receiver offsets of 30–40 km, suggesting that there is no significant change in crustal thickness along the entire profile. P_{g1} and P_{g2} are assigned traveltime pick uncertainties increasing with offset from 20 to 40 ms.

5.3 Arrivals from the Moho and upper mantle, P_mP and P_n

WA reflections from the Moho (P_mP phase) are observed intermittently along the profile (Figs 3a and g). However, the presence of a Moho as a distinct interface is interpretable from the change in the apparent velocity of the first arrivals from 7.25 to 8.00 km s^{-1} at ∼35 km shot-receiver offset, which is accompanied by a decrease in amplitude of the crustal arrivals (Fig. 3g). Unfortunately, the P_n phase generally has a low SNR and is rarely observed at shot-receiver offsets >50 km. The assigned traveltime pick uncertainties are 50 ms for all P_mP arrivals and range from 40 to 50 ms, assigned according to offset, for P_n arrivals.

There is no evidence for the secondary WA reflections that have been observed at some intraplate settings (e.g. Watts *et al.* 1985; Caress *et al.* 1995; Grevemeyer *et al.* 2001a). Such mid-crustal reflections, together with unusually high lower crustal velocities (>7.3 km s^{-1}), have been interpreted as a relic Moho, which separates pre-hotspot crust from subcrustal underplate. The absence of these reflections in the data from the Cape Verdes implies that there has been no significant (i.e. thicker than the vertical resolution of the seismic data at that depth) volume of underplated material added to the base of the crust along the profile.

© 2010 The Authors, *GJI*
Journal compilation © 2010 RAS

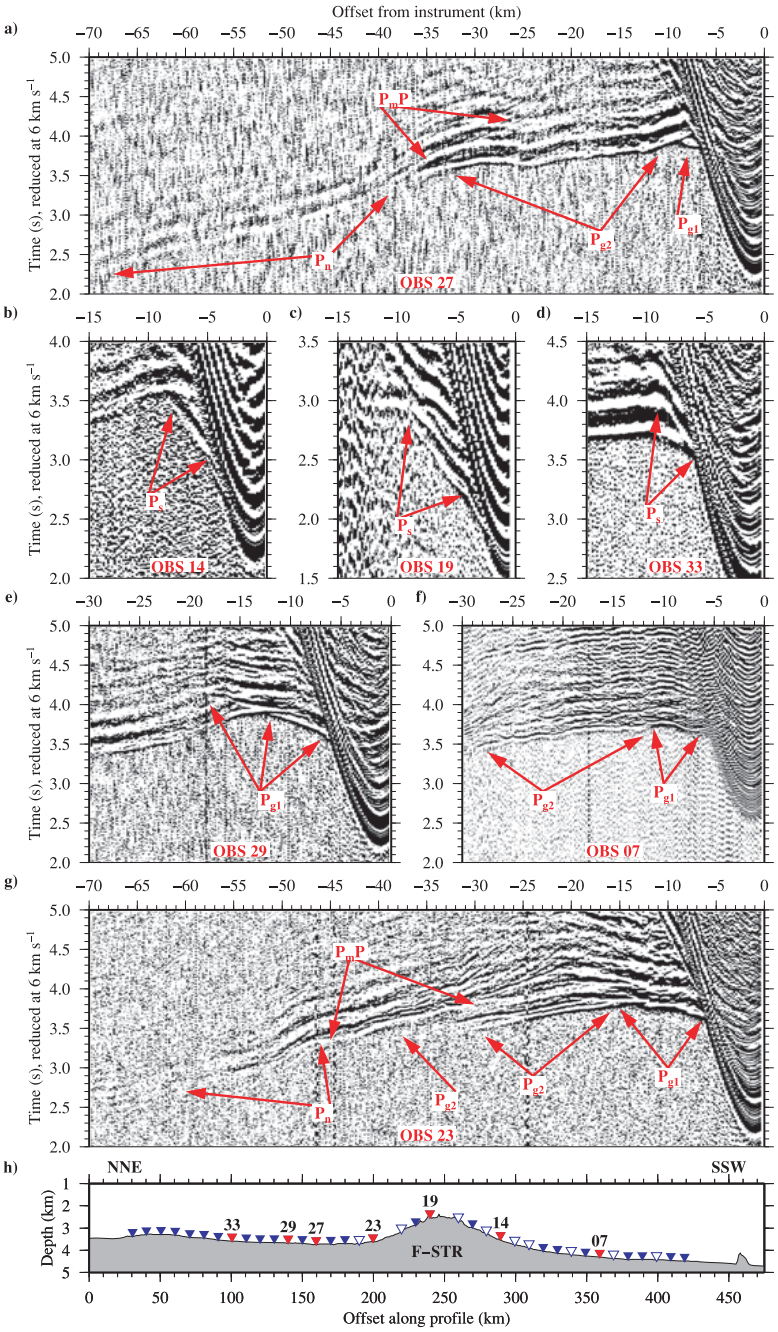

Figure 3. Examples of hydrophone data recorded on OBSs 14, 19, 23, 27, 29 and 33, and vertical geophone data recorded on OBS 07 (a)–(g). A bandpass filter of corner frequencies 0–5–35–40 Hz has been applied to the data. P_s, shallow subsurface arrivals; P_{g1} and P_{g2}, crustal arrivals; P_mP, wide-angle reflections from the Moho; P_n, arrivals from the upper mantle. Record sections are plotted with a reduction velocity of 6 km s^{-1}. (h) Along-profile locations of instruments that successfully recorded data. Instruments from which the records in (a)–(g) are taken are highlighted in red. See Fig. 2 for transect location, definitions and abbreviations.

© 2010 The Authors, *GJI*
Journal compilation © 2010 RAS

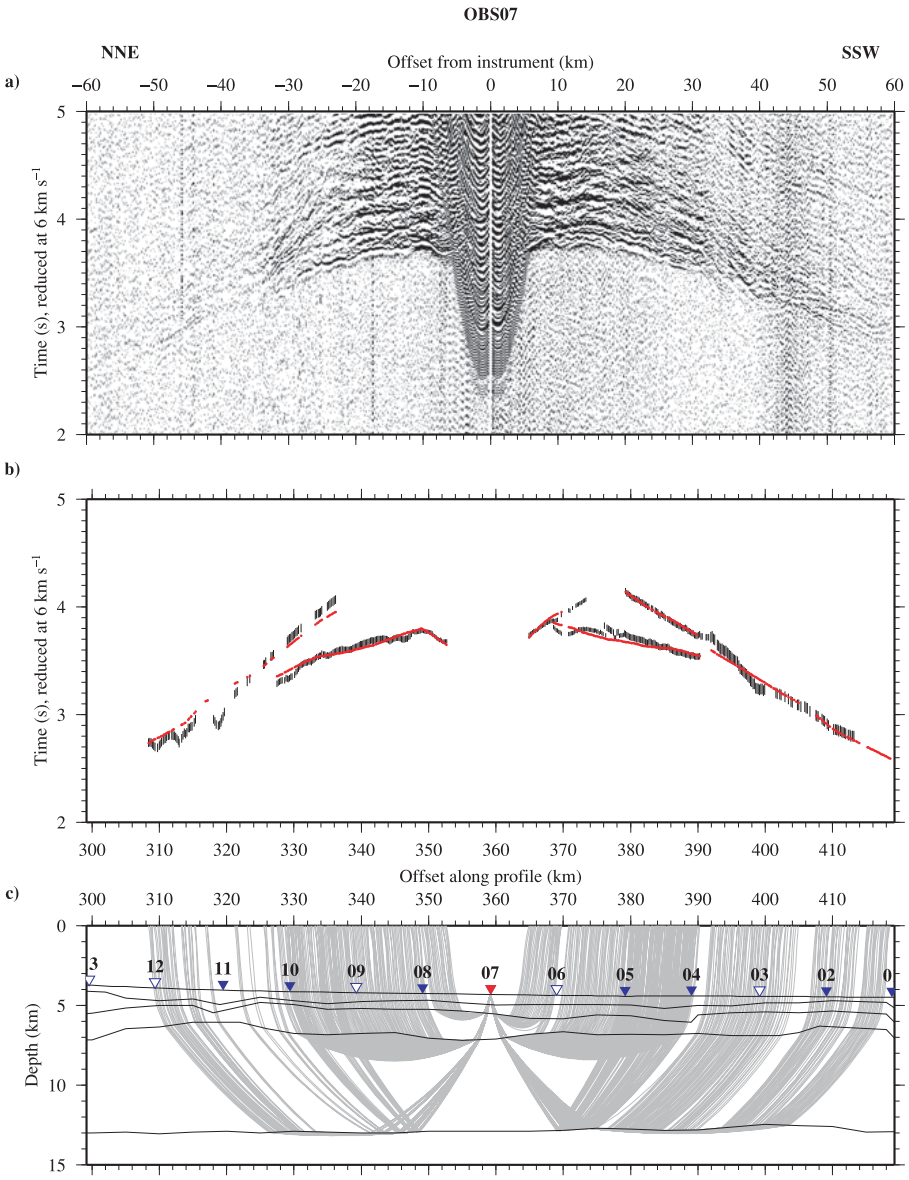

Figure 4. Ray-trace modelling of vertical geophone data recorded by OBS 07. (See Fig. 2 for instrument location). (a) Filtered record section plotted at true amplitude. (b) Observed traveltime picks (black vertical bars, representing the assigned picking error) and calculated traveltimes (red). (c) Ray diagram showing modelled arrivals. Record sections and traveltimes are plotted with a reduction velocity of 6 km s^{-1}.

5.4 MCS reflection data

Detailed analysis of the coincident MCS data provides an initial 2-D layer structure of the sediment stratigraphy along the profile. Ali *et al.* (2003) divide the sediment column into four layers based on the interpretation of key intrasediment horizons separating similar reflector packages (Fig. 7a), and using a detailed description of seismic facies for all profiles from *RRS Charles Darwin* cruise 8/85, of which Lines 2 and 5 intersect with the swell transect (Ali *et al.*'s 2003 Line 3; see Fig. 2 for profile location).

However, for the purposes of this study only the main units which demonstrate the load-related flexure are required, as these are necessary for the 'whole plate' modelling which will be presented in a subsequent paper, and so the sediment column was more simply divided into two layers, separated by an angular unconformity interpreted as representing the onset of subsidence due to surface loading, as follows.

Layer 1: Mesozoic sediments derived from the West African margin which formed following the rifting apart of North America and Africa and the formation of the North Atlantic ocean basin.

© 2010 The Authors, *GJI*
Journal compilation © 2010 RAS

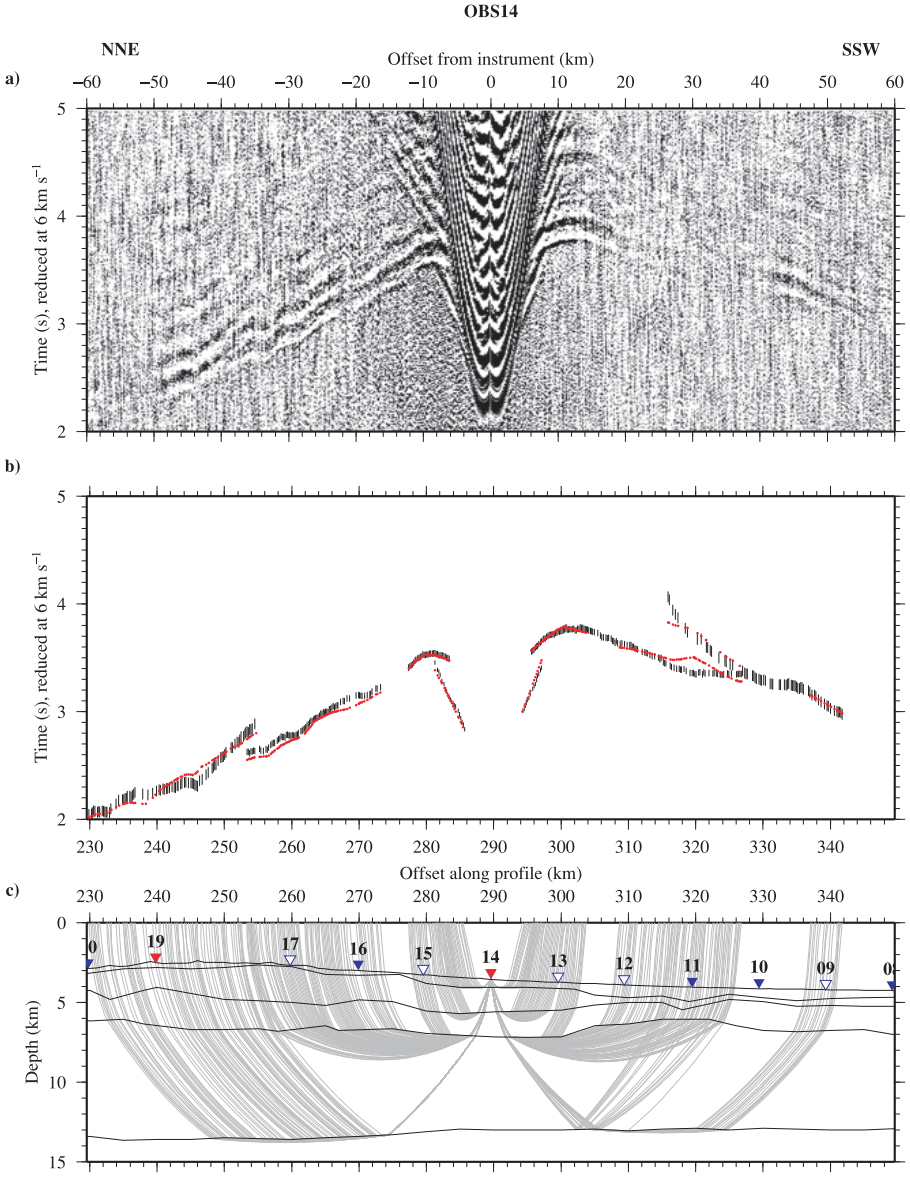

Figure 5. Ray-trace modelling of hydrophone data recorded by OBS 14. See Fig. 4 for details.

Layer 2: Neogene volcaniclastic sediments derived from the islands and pelagic sediments infilling the flexural moats formed by island-related plate loading.

The lack of primary sediment arrivals in the WA data requires interval velocities (to allow depth conversion of the unconformity reflection traveltime picks) to be sourced from a combination of standard sediment relationships (Hamilton 1978), Ali *et al.*'s (2003) stacking velocities, Dash *et al.*'s (1976) 1-D model and DSDP drilling logs (Lancelot *et al.* 1978) to facilitate the construction of the initial velocity–depth model. Although there are no directly observable arrivals from these layers, they will be included in the WA data modelling as described later except beneath the F-STR where the layer characteristics will be modified to match the observed P_s phase, 'basement high', arrivals.

It is worth noting at this point that sediment layer velocities from the final WA model (see Section 7) will ultimately be used to convert the two-way traveltime picks of the MCS-derived flexural makers into layer thicknesses and depth below seabed, and to best estimate bulk layer density. In turn, these depths, thicknesses and densities will be used to calculate the 'background' upper plate (crustal) characteristics and load input for 'whole plate' modelling, the results of which will be presented in a subsequent paper.

© 2010 The Authors, *GJI*
Journal compilation © 2010 RAS

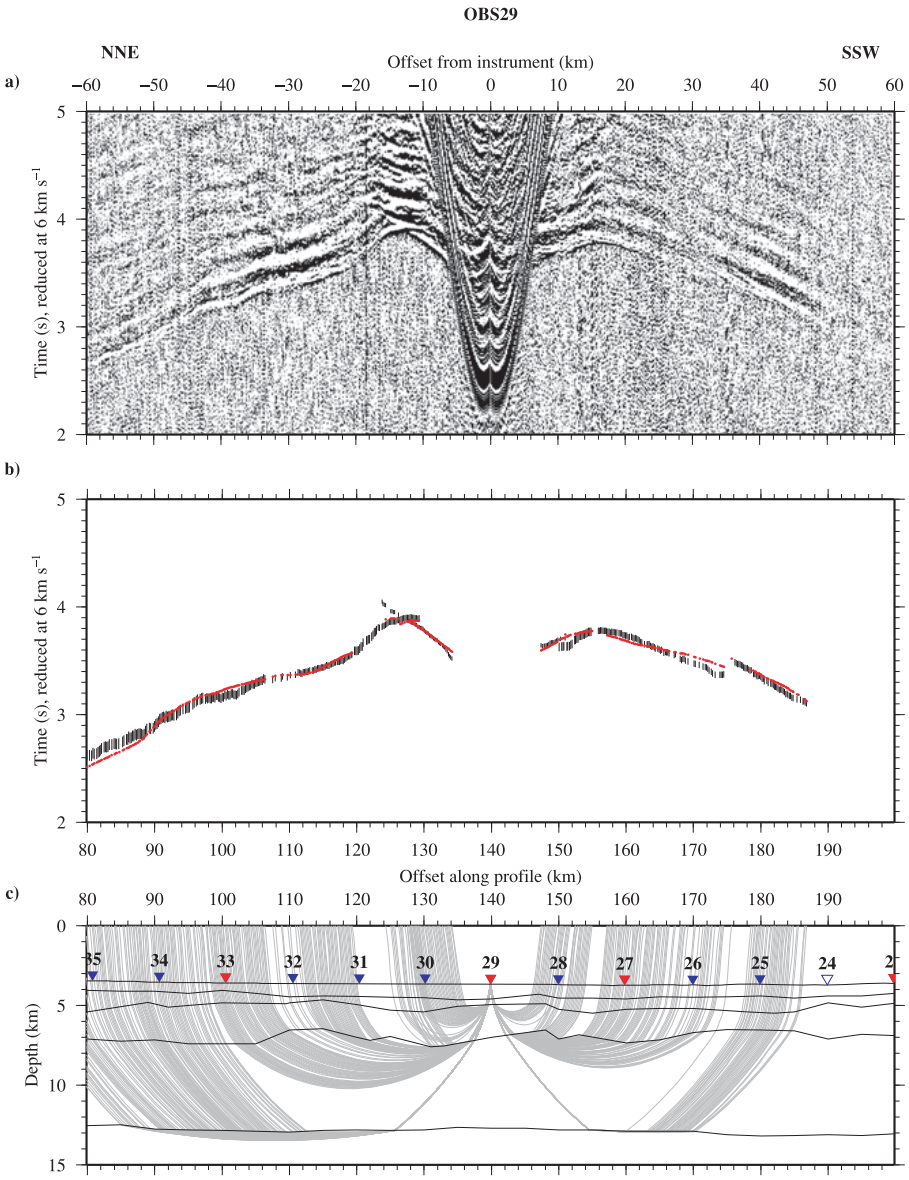

Figure 6. Ray-trace modelling of hydrophone data recorded by OBS 29. See Fig. 4 for details.

5.5 Traveltime picking

For traces with clear primary arrivals, the onset of the seismic wavelet was picked. Uncertainties, summarized in Table 1, were assigned according to offset as detailed above, and accounting for the decrease in SNR due to spherical divergence, scattering and absorption of the seismic energy. However, for secondary arrivals, and primary arrivals with low SNR, the zero-crossing immediately before the arrival waveform's first peak was picked and the assigned uncertainties adjusted accordingly.

6 SEISMIC MODELLING

A 2-D *P*-wave velocity–depth model of the crustal structure at the Cape Verde Swell has been created by combining the analysis of coincident MCS data, to constrain the shallow subsurface, with forward modelling of the WA data to obtain the structure of the oceanic basement and uppermost mantle. Sensitivity testing of velocity and depth nodes has also been conducted to determine the limits of model resolution. Finally, standard velocity–density relationships have been used to calculate the FAA to compare with that observed,

© 2010 The Authors, *GJI*
Journal compilation © 2010 RAS

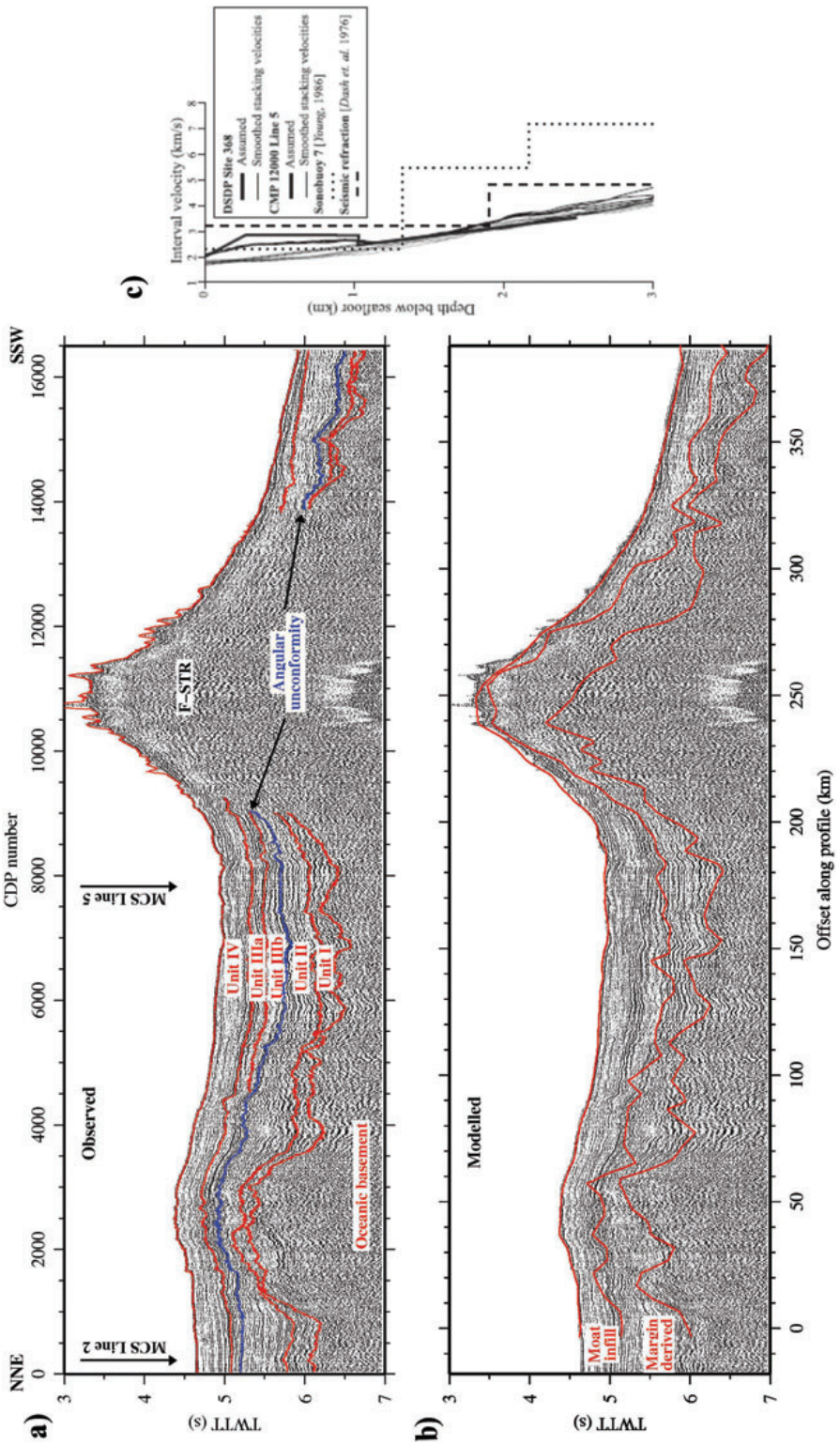

Figure 7. Comparison of the shallow subsurface layers picked from the MCS data with the time-converted boundaries from the final best-fitting velocity–depth model. (a) MCS Line 3, coincident with the WA profile of this study, annotated to show the five horizons identified in the sediment column following the seismic stratigraphy defined by Ali *et al.* (2003). The angular unconformity, shown in blue, represents subsidence due to loading and flexure, and defines a change in the primary sediment provenance from the African margin to the Cape Verde islands. Sediment units are named according to the terminology of Ali *et al.* (2003) and tie points with other *RRS Charles Darwin* 1985 MCS lines are indicated with annotated arrows. (b) Time-converted boundaries from the final 2-D velocity–depth model. The model boundaries, although more undulating, correspond with the originally interpreted positions of the angular unconformity and the top-basement reflector and agree well with distinct changes in reflector characteristics, giving confidence in the shallow model structure. (c) Summary of 1-D velocity–depth profiles (after Ali *et al.* 2003).

© 2010 The Authors, *GJI*
Journal compilation © 2010 RAS

Table 1. Pick uncertainties and misfits between calculated and observed traveltimes for each phase identified in the WA data set.

Phase	Pick uncertainty (ms)	Number of picks	rms traveltime (s)	χ^2 value
P_s	20–30	712	0.036	2.654
P_{g1}	20–30	1566	0.033	2.052
P_{g2}	30–40	8651	0.061	2.675
P_mP	50	1391	0.105	4.376
P_n	40–50	4171	0.119	5.850

as an independent check on the viability and uniqueness of the final model, prior to interpretation. Each of these stages will be discussed below, together with a description of the final best-fitting velocity–depth model.

6.1 Forward modelling

The best-fitting velocity–depth model was obtained using a 2-D forward ray tracing approach, *rayinvr* (Zelt & Smith 1992), and assuming that, in this locality, 3-D crustal heterogeneity has little affect on ray propagation, i.e. the crustal structure of the swell is effectively axisymmetric except immediately in the vicinity of each island of the archipelago. The initial starting model was populated with two types of nodes for each layer; depth nodes describe the upper boundary geometry, while velocity nodes define vertical and horizontal velocity gradients.

In the initial model, the water column was included as a single layer whose base, the seabed, was defined using the shipboard swath bathymetry data. This layer was assigned a velocity of 1.49 km s^{-1} at the top (sea level) increasing to ∼1.51 km s^{-1} at the seabed. Immediately beneath the water column, the two sediment layers are defined using *P*-wave velocity estimates taken from DSDP site 368 core analysis (Lancelot *et al.* 1978), together with stacking velocities used to process the MCS record sections (Fig. 7c; Ali *et al.* 2003), to depth convert the intrasediment unconformity and basement surface picked from the MCS section (Fig. 7a). Finally, a simplistic, one-dimensional, two-layered oceanic crustal basement, with underlying lithospheric mantle, was incorporated to complete the initial model using layer thicknesses, velocities and velocity gradients derived from White *et al.*'s (1992) model for standard, mature Atlantic oceanic crust.

Prior to subseabed modelling, instrument locations and the seabed topographic profile were checked using the direct water wave arrival and the seabed-sea surface multiple. Following ray tracing, minor adjustments to instrument locations and seabed depth were made, where needed, to obtain a fit within the picking errors for the two sets of water column arrivals.

A top-down approach was adopted for modelling, tracing progressively deeper layers to calculate arrivals to increasing shot-receiver offsets. For each layer, the arrivals from a subset of four-to-five adjacent instruments were modelled simultaneously, starting at the northern end of the profile. A 'rolling window' technique was adopted to progressively incorporate additional instruments along the profile while maintaining an overlap with the previous subset.

The fit of calculated arrivals to the traveltime picks was initially qualitatively assessed to produce a model that approximately satisfied the observed data. Subsequently, analysis of rms traveltime misfit and the χ^2 parameter (Zelt & Smith 1992) provided a quantitative assessment and acted as a statistical indicator when making minor adjustments to further refine the fit of the model.

The results of modelling are demonstrated by a selection of record sections and matching ray diagrams shown in Figs 4–6, and a summary of the assigned uncertainties, number of picks, rms misfit and χ^2 values for each of the identified phases can be found in Table 1. For reference, a χ^2 of 1 is considered a good fit, while a χ^2 of <1 is an over-fit to the observed traveltime picks. In this study, a χ^2 of <5 is considered an acceptable fit.

7 RESULTS

The best-fitting velocity–depth model (Fig. 8a) is 475 km long, with instruments located between 30 and 420 km model offset. Shots were fired from north to south between 0 and 474 km profile offset. The best-fitting model can be summarized as a succession of two discrete sedimentary packages overlying typical two-layered oceanic basement, which shows only slight thickening between the adjacent islands of the archipelago at the F-STR. A brief description of each model layer is included below.

7.1 Sediment layers

The first, shallowest, layer subseabed is interpreted as a sequence of moat infill sediments and it is present along the entire profile. Although relatively thin at the northern limit of the model, the infill reaches a maximum thickness of 1 km at ∼150 km profile offset, with velocities of 2.0–2.5 km s^{-1}. These infill sediments almost pinch out over the F-STR before returning to an average thickness of 0.7 km at profile offsets >320 km, where slightly higher velocities of 2.5–2.7 km s^{-1} are also observed. This range of *P*-wave velocities matches those recorded by Lancelot *et al.* (1978) for the marls and claystone turbidites observed up to 1 km below the seabed at DSDP site 368.

Although originally included in the model to reflect a package of terrigenous sediments derived from the African margin, the second, deeper, layer subseabed exhibits the most lateral variation in *P*-wave velocity within the entire best-fitting final model. In the final model, this layer generally exhibits an average thickness of <1 km and *P*-wave velocity of 3.0 km s^{-1}. However, between 210 and 310 km profile offset, this layer thickens to a maximum of 2.2 km with velocities of 3.5–4.5 km s^{-1}, constrained by the P_s phase observed on the mid-profile OBSs. This higher velocity region, concurrent with the bathymetric high of the F-STR, suggests the possibility that the emplacement of extrusive volcanic material to the crust at the Cape Verde Swell may not be localized entirely to the islands. Alternatively, analysis of the Hydrosweep swath bathymetry collected in this area shows a highly irregular, hummocky region with partly buried volcanic cones suggesting that at least part of the F-STR may comprise volcaniclastic debris from past landslide and flank collapse events originating on the adjacent islands of Fogo and Santiago (Day *et al.* 1999; Masson *et al.* 2008).

Due to the limited number of observed arrivals from the sedimentary layers, much of the shallow structure has been modelled using the deeper propagating ray groups. However, this approach does not always provide a unique solution due to the complex interrelationship between boundary geometries and velocities when modelling several nodes at once. As a means of continuously checking the geometry and velocity of the sedimentary layers as modelling progressed, the depth of the unconformity and top-basement horizons were converted back into two-way traveltime (TWTT) using the model-derived velocities and compared with the MCS data as an independent check for consistency (Fig. 7b).

© 2010 The Authors, *GJI*
Journal compilation © 2010 RAS

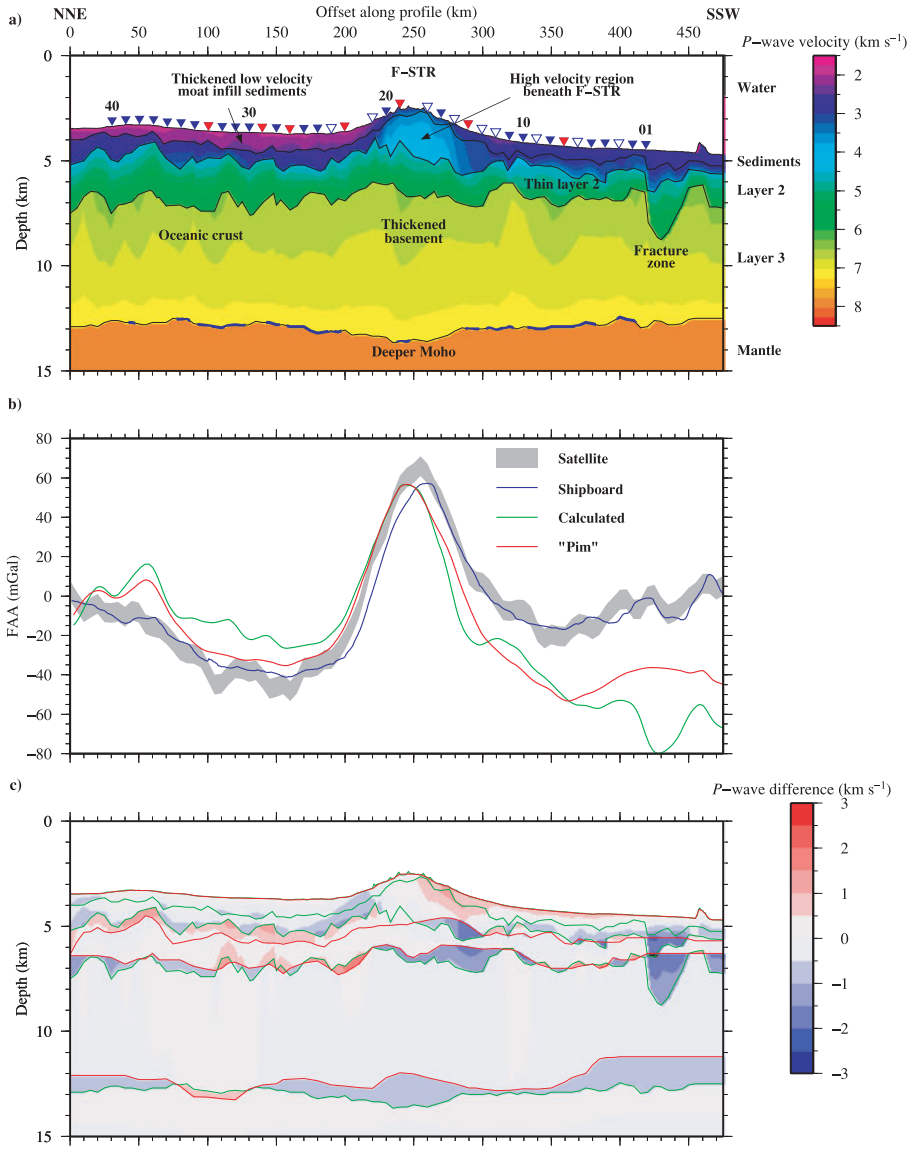

Figure 8. Best-fitting velocity–density–depth model. (a) Final velocity–depth model. The layer boundaries taken from the *rayinvr* model file are shown as solid black lines. Blue shading on the Moho indicates regions constrained by P_mP arrivals. Note that the mid-lower crust is only well constrained by crossing ray paths between *ca*. 40 and 425 km model offset, which may contribute to the misfit between the observed and calculated free-air gravity anomaly outside this region. See Figs 10–12. Key features, as discussed in the text, are labelled. OBS locations are shown by the inverted triangles. See Fig. 2 for transect location, definitions and abbreviations. (b) Comparison of the free-air gravity anomaly observed along the profile with the anomalies calculated from the best-fitting seismic model in (a) (see Fig. 12 for density information) and the model of Pim *et al*. (2008). (c) Difference between the best-fitting model and that of Pim *et al*. (2008) (Fig. 9). See text for discussion. The 'Pim' model layers are shown by solid red lines, this study by green.

In the final model, the mid-sediment model boundary correlates well with the angular unconformity in the MCS data; this can be seen most clearly between 75 and 190 km profile offset and it separates an acoustically transparent layer containing occasional chaotic reflectors, from a highly stratified package of moderate amplitude reflectors. The top-basement surface follows the lowest coherent, high-amplitude reflector. Beneath this surface the characteristic hummocky reflector pattern of the upper surface of the oceanic basement is evident.

7.2 Crustal layers

The oceanic basement was modelled as two layers to match the distinct crustal phases observed in the data. A second-order

© 2010 The Authors, *GJI*
Journal compilation © 2010 RAS

discontinuity within the crust was required to accommodate a decrease in vertical velocity gradient, interpreted to represent the transition from the pillow basalt and dykes of layer 2 to the gabbros of layer 3 (White *et al.* 1992).

The top-basement surface is coarsely hummocky, with irregular undulations of amplitude 0.5 km and wavelength >15 km, and at an average depth below sea level of 5.25 km. There are two prominent basement highs >1 km shallower than the average depth of the top-basement surface: the first is located at 20–50 km profile offset, where a peninsula of shallower bathymetry extends west from Sal (Fig. 2); the second is located beneath the northern edge of the F-STR. A basement low, 1 km below the average depth of the top-basement surface is located at 420 km.

There is little lateral variation in the velocity structure of the crust along the profile, with average values for the upper and lower layers of 5.4 and 6.9 km s^{-1}, respectively. The total crustal thickness increases from the north towards the F-STR as a consequence of the basement high and the slightly increased depth of the Moho, reaching a maximum thickness of 9 km at 230 km profile offset. Despite the observed thickening of the basement, there is no evidence of high *P*-wave velocities (>7.3 km s^{-1}) associated with crustal underplate (e.g. Charvis *et al.* 1999).

The maximum depth of penetration of rays traced through the lower crust is ∼11 km below sea level, which is on average 2 km shallower than the modelled Moho. The velocity structure of the deepest parts of the crust is, therefore, constrained by modelling the P_n and P_mP ray groups, the result of which is described in the next section.

To the south of the F-STR, between 320 and 420 km profile offset, the crust thins to 7 km, with most of the thinning accommodated in the upper crust. Beneath OBS 01, at the southern end of the profile, a large subvertical fault is interpreted to traverse the entire upper crust. This fault is located at the southern end of the region of thin upper crust and gives rise to the basement low described above. This upper crustal structure resembles a cross-section through an oceanic transform fault (e.g. White *et al.* 1984), indicating the possible location of an Atlantic fracture zone.

Many fracture zones have been interpreted to cross the Cape Verde region in an E-W orientation, perpendicular to the WA profile, through the correlation of offsets in magnetic anomaly lineations (e.g. Williams *et al.* 1990). The topographic relief of fracture zones is often concealed by pelagic sedimentation. However, the gravity anomaly due to the vertical offset of the top-basement surface is sometimes observed on profiles perpendicular to the fault.

The first derivative (in latitude) of the Sandwell & Smith (1997) 1 × 1 min global gravity dataset is a useful way to highlight the relatively short-wavelength ridges and troughs associated with fracture zones in the region of long-wavelength mid-plate bathymetry swells (Fig. 2c). Several lineations can be seen trending from west to east across the Cape Verde Swell, which correlate with known fracture zones (including Kane and Fifteen-Twenty) interpreted from the bathymetry of the Mid-Atlantic Ridge axis. One of these observed lineations intersects the WA profile at its southern end where the anomalous crustal structure has been incorporated into the model, providing supporting evidence for its interpretation as a previously unmapped fracture zone in the region.

7.3 Moho and upper mantle

The topography of the Moho is very subdued, with an average Moho depth of 13 km below sea level, which increases slightly to 13.5 km beneath the F-STR, at 250 km profile offset. The primary constraint on the depth to the Moho comes from arrivals reflected at the crust-mantle interface, the P_mP phase. Unfortunately, the P_mP phase is not clear on all records, and is particularly difficult to identify in the centre of the profile where records have a lower SNR, and clear arrivals are only observed at near offsets. Also, without further control on the velocity structure of the lower crust (>10 km depth), the error in the position of the Moho remains relatively large due to the trade-off between the interval velocity and thickness of the lower crustal layer.

On records with clear arrivals at shot-receiver offsets >30–40 km, the P_n phase can be identified and this provides a control on lower crustal velocities, allowing Moho depth to be independently modelled. The upper mantle velocity directly below the Moho is 7.9 km s^{-1} and a slight positive gradient in the mantle is required in order to turn the P_n rays, with 8.0 km s^{-1} assigned to the base of the model at 40 km depth. The absence of arrivals at >70 km shot-receiver offset throughout the dataset means that only the velocity of the upper mantle directly beneath the Moho is known directly.

7.4 Resolution

The goodness of fit of the final model was assessed using the rms traveltime and the χ^2 parameter. However, these parameters only reflect the statistical fit between the calculated arrivals and the observed picks. In order to test the resolution of the model, a sensitivity test was conducted in which seismic velocities and boundary depths were systematically varied and the fit reassessed. In resolution terms, a model was considered an acceptable fit as long as the difference in calculated and observed traveltimes did not exceed twice the standard error assigned to the picks. This analysis shows that *P*-wave velocities may differ by ±0.2 km s^{-1} in the sediment layers and by up to ±0.5 km s^{-1} in layer 3 and an acceptable fit is still achieved. On the same basis, the depth to the top of the oceanic basement is estimated to lie within ±0.2 km of the best-fitting model interface at worst, and the depth to the Moho is estimated to lie within ±1.5 km.

7.5 Comparison with Pim *et al*. (2008)

It is at this point worth directly comparing our best-fitting model (Fig. 8) with that from the pilot study of Pim *et al*. (2008) (Fig. 9—henceforth the 'Pim' model) using the data from just nine of the OBSs. Fig. 8(c) shows a difference plot between the two models where the 'Pim' model has been subtracted from our model. In general, the models are very similar which in one sense is reassuring, but in another sense is somewhat surprising given the significantly fewer and more widely spaced OBSs used to derive the 'Pim' model. The main differences between the two models are as follows.

1. The trade-off between the two sediment column and oceanic layer 2 thicknesses, with the velocity–depth profiles within each layer being effectively equivalent.
2. The rougher sediment–layer 2 and layer 2–layer 3 interfaces in our model, especially so at the SSW end of the model where a significant intrabasement offset discontinuity is implied, which could reflect a fracture zone.
3. The incorporation of all 38 OBS datasets leads to, on average, a 1–2 km deeper but less vertically varying Moho, although the velocity–depth profile in ocean layer 3 in both models is effectively equivalent.

© 2010 The Authors, *GJI*
Journal compilation © 2010 RAS

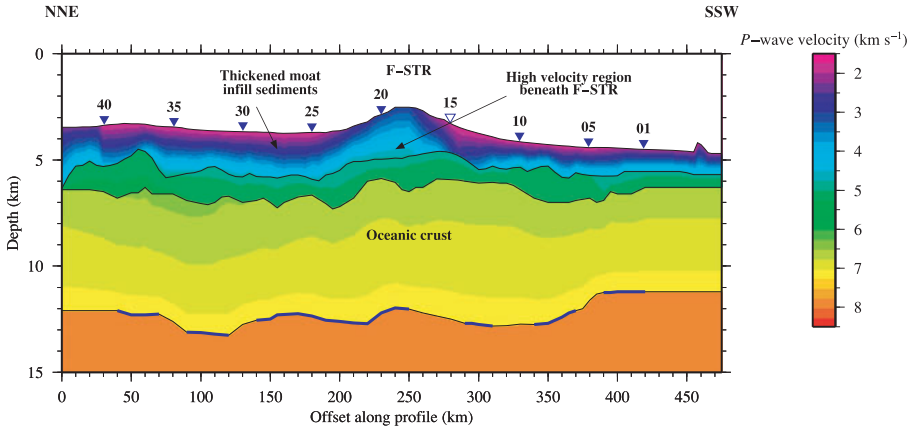

Figure 9. Best-fitting velocity–depth model of Pim *et al*. (2008). The layer boundaries taken from the *rayinvr* model file are shown as solid black lines. Blue shading on the Moho at *ca*. 12 km below sea level shows the constraint provided by P_mP arrivals. Key features, as discussed in the text, are labelled. The locations of the nine OBS used to develop this model are shown by the inverted triangles. See Fig. 2 for transect location, definitions and abbreviations.

4. The velocity–depth structure on the margins of the F-STR is aliased in the 'Pim' model towards the locations of the two OBS that constrain its shallow. structure.

Although the simpler and smoother 'Pim' model is likely to be more geologically realistic considering the resolution versus depth capabilities of the various methods used to acquire and analyse the data, the denser subsurface sampling achieved by the entire dataset results in, statistically, a better fit, especially when considering layer interface geometries and velocity transitions across interfaces. Also, given the limited depth of signal penetration subsurface, the depth and geometry of the Moho in our model is likely to be a more accurate representation not only of the lower crust and uppermost mantle velocity structure (and hence more definitive in terms of likely existence of lower crustal underplate/intrusion) but also Moho geometry.

A further, and probably obvious, conclusion that can be drawn is that in regions of rapid change in seabed bathymetry or likely significant lateral change in velocity and layer thickness, it is better to deploy more closely spaced instruments over and either side of such features, while for more subdued or strike-line type profiles, more widely spaced instruments may provide more than adequate subsurface imaging and resolution at all crustal depths.

8 GRAVITY MODELLING

The uniqueness of the best-fitting velocity–depth model was also tested by calculating the gravity anomaly for the corresponding density–depth model and comparing this to both the Sandwell & Smith (1997) 1×1 minute global free-air gravity dataset and the higher-resolution shipboard data (Fig. 8b) acquired during seismic acquisition. In addition, gravity modelling also offers the potential of additional constraint on the deeper parts of the model otherwise not well constrained by seismic arrivals.

For all gravity modelling presented in this paper, a 2-D approach was adopted in which a block density model was derived from the *rayinvr* best-fitting velocity–depth model and standard velocity–density relationships for sediments and oceanic crustal rocks were used to convert velocities to densities (Hamilton 1978; Carlson & Raskin 1984; Carlson & Herrick 1990). Model layer boundaries and iso-velocity contours were used to divide the model into a succession of layers and blocks which were assigned interval density values in the range 1750–2950 kg m^{-3}, with fixed water column and mantle densities of 1030 and 3330 kg m^{-3}, respectively. The 2-D gravity program, *grav2d*, written by J.H. Leutgart and based on the algorithm of Talwani *et al*. (1959), was then first used to calculate the gravity anomaly for the modelled crustal structure beneath the profile (Figs 8a and b), and then for assessing the likely origin of the observed long-wavelength component in the FAA discussed later.

Based on the seismic model alone, the calculated FAA shows a reasonable agreement with the short and medium wavelength features in the observed data; the small highs at 60 and 400 km profile offset, and the main peak at 250 km profile offset, respectively. However, the calculated anomaly also contains a long wavelength, effectively linear trend of −0.1 mGal km^{-1} from north to south.

Interestingly, the long wavelength trend implies a density anomaly deeper in the lithosphere, possibly subcrustal. This long-wavelength anomaly may be a result of crustal thickness variations unconstrained by the seismic modelling (i.e. within seismic resolution at Moho depth), or a result of deeper-seated density variation in the mantle, again largely unconstrained by the seismic data.

In order to assess the likely origin of the long-wavelength mismatch, bathymetry and gravity data along a 2500 km extended profile centred on the WA profile were analysed. A simplified two-layer density model of the water column and seabed was constructed (Fig. 10a) to calculate the gravity anomaly due to changes in bathymetry (Fig. 10b). The bathymetry anomaly was then removed from the satellite-derived FAA to obtain the subseabed anomaly. Various 2-D filters were applied in the space domain to the subseabed anomaly to match the long-wavelength low centred at ∼150 km offset. It was not possible to isolate the long wavelength signal south of 150 km due to the medium-wavelength peak at 250 km offset. As a best approximation, a combination long-wavelength signal was created using a cosine filter of width 400 km at the flanks of the profile and a cosine filter of width 100 km between −200 km and 150 km with the filtered signal mirrored about 150 km to fit the long-wavelength trend between 150 km and 500 km, thus assuming it to be symmetrical (Fig. 10c). The long-wavelength signal was subsequently removed from the subseabed anomaly to

© 2010 The Authors, *GJI*
Journal compilation © 2010 RAS

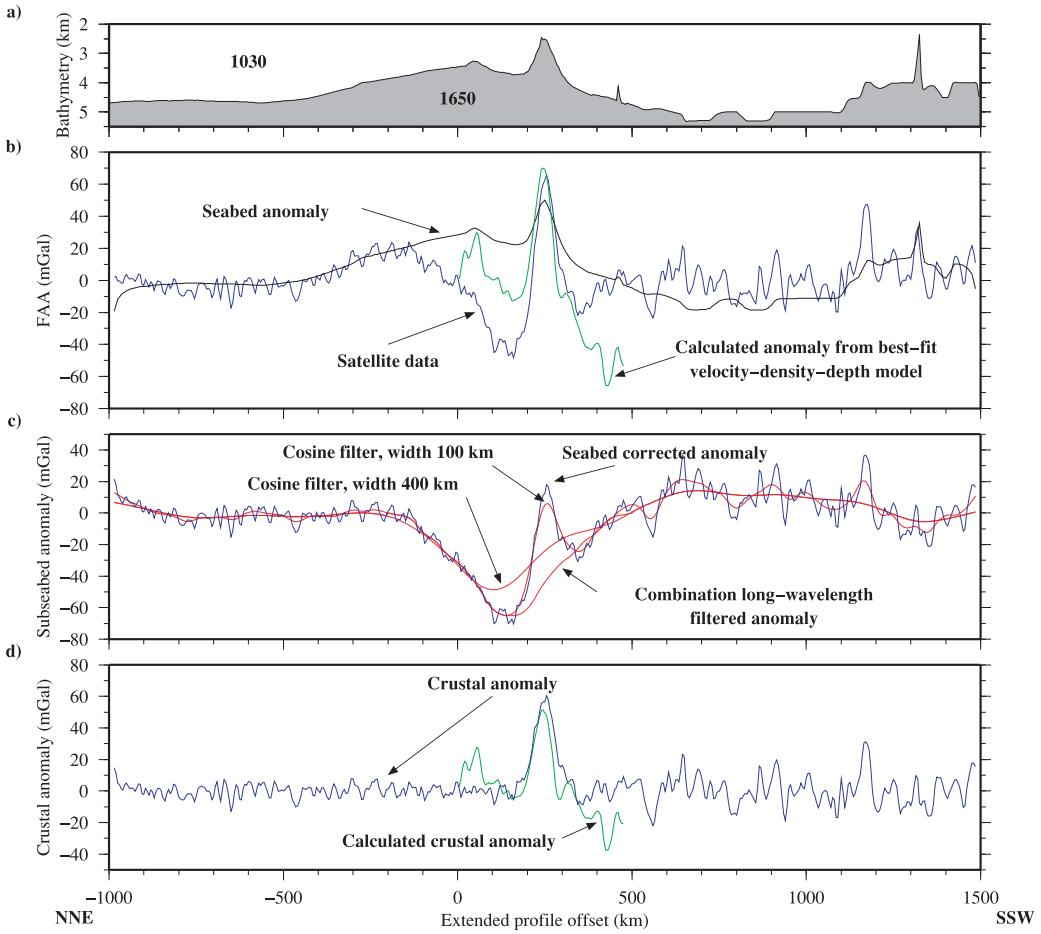

Figure 10. Long-wavelength component of the free-air gravity anomaly. (a) and (b) Calculation of the contribution of the seabed alone. Densities are annotated in kg m^{-3}. The seabed topography is defined by the combination of GEBCO 1 × 1 min (IOC, IHO & BODC, 2003) and shipboard swath bathymetry data. (c) Deconstruction of the long-wavelength components in the free-air anomaly. (d) Observed crustal component of the free-air anomaly with the long-wavelength component removed (blue line) compared with the anomaly calculated from the best-fitting velocity–density–depth model of Fig. 8 with the seabed anomaly removed (green line).

reveal the 'crustal' anomaly, which has been compared to the output from the best *rayinvr* model with the bathymetry anomaly removed (Fig. 10d). The observed and calculated crustal anomalies show a reasonable agreement between 100 and 350 km offset but diverge at the extremities of the model.

Before testing the sensitivity of the density–depth model to subtle changes in the crustal density structure, the possible origin of the long-wavelength anomaly will be investigated. Firstly, the crustal density model was modified to incorporate lateral variations in the density of the lithospheric mantle by incorporating a region of low density (relative to 'normal' mantle) centred at 150 km offset. A range of density contrasts, compensation depths and low-density region widths were tested in an attempt to reproduce the amplitude of the long-wavelength anomaly. The example model shown in Fig. 11(b) is clearly non-unique. However, with a density contrast of 30 kg m^{-3} and compensation depth of 100 km, the subcrustal gravity anomaly calculated using this model (Fig. 11a) matches the amplitude of the long-wavelength signal. However, its wavelength characteristics are not well matched, suggesting that the low-density region may have gradual lateral density transitions rather than the sharp boundaries modelled here.

The density–depth model of Pim *et al.* (2008) also has a low-density region in the lithospheric mantle, between ∼50 and ∼250 km offset. However, several other short-wavelength mantle density variations are also incorporated into the Pim *et al.* (2008) model which may produce the necessary gradational transition outlined above. The major difference to the model presented here is the magnitude of the density contrasts (maximum 160 kg m^{-3}), which is a direct result of the shallow compensation depth (16 km) that Pim *et al.* (2008) use. However, the model presented here is considered a better solution because its deeper compensation depth better matches estimates from other studies of the swell (e.g. McNutt 1988) and the more regional-scale low density anomaly in the lithospheric mantle beneath the Cape Verde islands which, in turn, better fits the passive seismological models of Lodge & Helffrich (2006).

© 2010 The Authors, *GJI*
Journal compilation © 2010 RAS

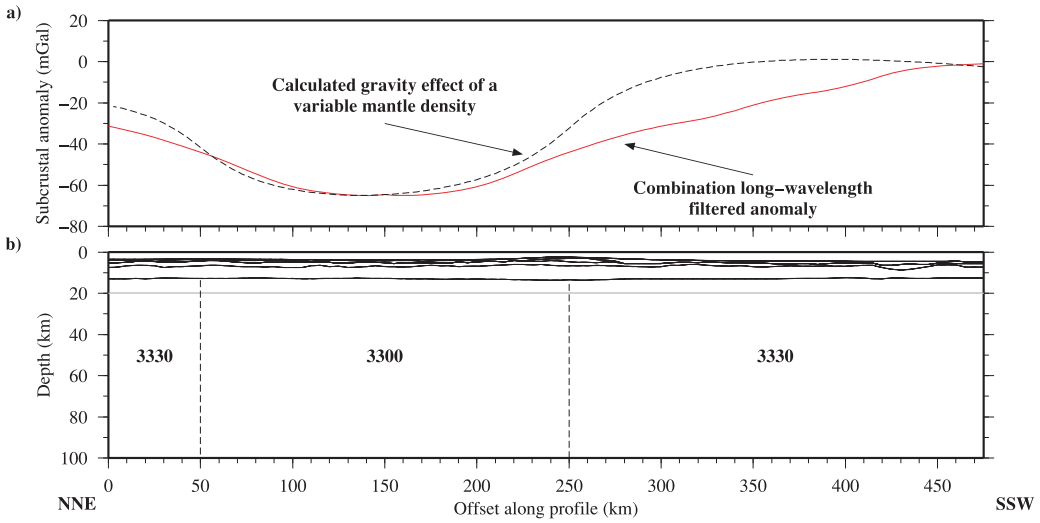

Figure 11. Modelling of the long-wavelength component free-air gravity anomaly. a) and b) Modelling of the long-wavelength anomaly (red line) shown in Fig. 10, by a laterally varying mantle and a compensation depth of 100 km (black dashed line). Densities are annotated in kg m^{-3}.

The fit of the crustal gravity anomaly will now be considered. Variations in the total crustal thickness were modelled in an attempt to account for the misfit at the extremities of the model (<50 km model offset; >350 km offset). A 1 km increase in the depth of the Moho between 0 and 60 km and a gradual decrease of up to 2 km from 325 to 475 km improved the fit of the flanking regions of the crustal anomaly to the observed data (Figs 12a–c). The adjustments made to the depth of the Moho only exceed the uncertainties of the seismic model at the southern end of the model, past the maximum extent of the WA seismic data coverage.

As the best-fitting seismic model provides limited constraint on the lower crust, a further series of tests were conducted to investigate whether the gravity modelling is sensitive to the presence of underplate, and if so, to what resolution limits. To undertake these tests a series of modifications were made to the best-fitting seismic model to represent the presence of various thicknesses of underplate beneath the crust and magmatic intrusion into the lower crust. These modifications were constrained to range from below to above the seismic resolution in velocity (hence density) and interface geometry at Moho depth.

A range of velocity–depth models were created in which a layer of underplate with *P*-wave velocities ranging from 7.3 to 7.8 km s^{-1} (e.g. Morgan *et al.* 1989) was incorporated below the Moho or within the lower crust using a cosine function centred at 250 km profile offset with a width of 150 km and amplitudes ranging between ±5 km to perturb the Moho in the best-fitting model. Following each modification, the fit to the seismic data was reassessed and the FAA recalculated to show the change in the crustal gravity anomaly, which is manifest mainly in the amplitude of the peak. Modelling shows that, within the seismic data resolution in the lower crust and at the Moho, it is possible that up to a 3 km thickness of 'underplate' (i.e. within the lower crust and/or within the mantle) could be incorporated into the model to improve the fit to the peak FAA without significantly reducing the fit to the seismic data (Figs 12d and e). Combining the changes in crustal thickness and the maximum extent of any potential intracrustal magmatic intrusion produces a final model (Fig. 12f) that fits the main features of the observed crustal anomaly, suggesting that a small amount (up to 3 km maximum thickness) of magmatic material (either as underplate or intrusion) may be present at the base of the oceanic crust, located beneath the F-STR. A similar feature is observed at the Louisville Seamount chain in the SW Pacific (Contreras-Reyes *et al*. 2010).

The main conclusions that can be drawn from the gravity modelling are as follows.

1. Investigation of an extended profile through the Cape Verde Swell indicates that a long-wavelength FAA low exists at the northern half of the WA profile, and subsequent 2-D modelling suggests that the origin of this anomaly is within the lithospheric mantle.
2. A model incorporating lateral variations in mantle density can account for the long-wavelength low and is similar to that described by Pim *et al.* (2008), although here we demonstrate a compensation depth which is in accord with other studies (McNutt 1988; Lodge & Helffrich 2006). The area of low density mantle agrees well with the boundaries of the archipelago and a decrease in the observed heat flow anomaly (Fig. 2)
3. The seismic model is fairly unique in that it provides a good basic fit to the short and medium wavelength features in the crustal component of the FAA.
4. Up to 3 km of material of higher density than the crust could be incorporated at its base beneath the F-STR, within the errors of both the seismic and the gravity modelling.

9 DISCUSSION

The Cape Verde archipelago is situated on the crest of the largest observed hotspot swell on Earth, making it the ideal location to conduct a detailed geophysical investigation of proposed swell and plate load support models. The results of 2-D seismic and gravity modelling presented in this paper, are the first steps to testing the various models proposed and, in turn, may provide a better understanding of the origin and evolution of the Cape Verde Swell. The models that have been proposed to explain how the large-scale

© 2010 The Authors, *GJI*
Journal compilation © 2010 RAS

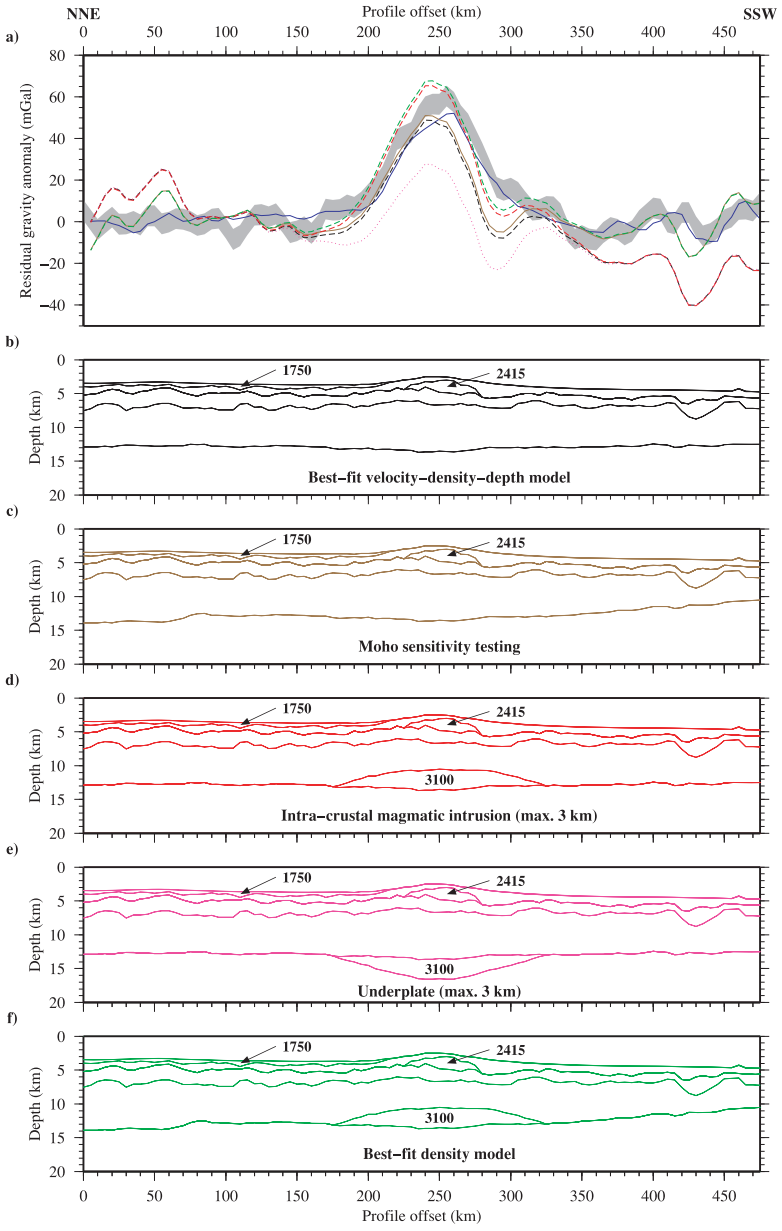

Figure 12. Sensitivity testing of the crustal density–depth model. (a) Comparison of the free-air gravity anomaly observed using satellite measurements (grey band including error) and shipboard data (blue line) with the gravity anomaly calculated from the final density–depth models shown in (b)–(f). Note that the long-wavelength component of the observed free-air anomaly (Fig. 10) has been removed. The density constants used for the water column (1030 kg m^{-3}), shallow subsurface layer (2010 kg m^{-3}), oceanic layer 2 (2630 kg m^{-3}) and layer 3 (2930 kg m^{-3}), and the mantle (3330 kg m^{-3}) are consistent for all models shown in (b)–(f), other densities specific to isolated regions are annotated in kg m^{-3}. For parts (b)–(f) of this figure, the colour coding of the model corresponds to the colour coding of the associated calculated anomaly plotted in (a). See text for discussion.

topographic swells associated with hotspots are sustained over geological timescales can be briefly summarized as:

1 – shallow support within the crust (e.g. Morgan *et al.* 1995),
2 – support within the upper mantle (e.g. Detrick & Crough 1978; Robinson, 1988), and
3 – dynamic mantle upwelling (e.g. Sleep, 1995).

Shallow crustal support would be evidenced by a thicker than average oceanic basement, originating either at the time of formation at a mid-ocean ridge due to above average magmatic accretion or during island building by the synchronous addition of magmatic

© 2010 The Authors, *GJI*
Journal compilation © 2010 RAS

underplating to the base of the crust. Assuming a simplified block model of the lithosphere under Airy isostatic equilibrium, the igneous layer within the oceanic crust would have to be ∼15 km thick in order to support the ∼2 km high swell observed at the Cape Verdes, placing the Moho at ∼17.5 km depth below sea level, 4 km deeper than is observed and well outside the best-fitting modelled Moho error bounds as demonstrated by the sensitivity testing.

Instead, the final velocity–depth model shows an igneous section that is 8 km thick on average, well within the range expected for standard oceanic crust (White *et al.* 1992), and similar to that observed in the pilot study conducted by Pim *et al.* (2008), although the crust does appear to slightly thicken towards the centre of the profile beneath the F-STR, to a maximum of 9.5 km. High shallow crustal velocities suggest, however, that the thickening is accommodated within the upper crust either by extrusion as part of island emplacement or as a high velocity volcaniclastic debris deposit on top of the basement, a consequence of adjacent island failure. Analysis of the detailed swath bathymetry data in the area better supports the latter possibility, with evidence of mass transport from the adjacent island of Fogo (Day *et al.* 1999; Masson *et al.* 2008). Receiver function analysis (Lodge & Helffrich 2006) suggests that crustal thickening, perhaps by magmatic underplating, may be more prolific beneath the islands where Moho depths up to 20 km are inferred. There is no evidence from this study to suggest that such an enhanced crustal thickness exists throughout the swell.

Additionally, there is no direct evidence from the seismic data for lower crustal velocities >7.3 km s^{-1}, a common feature observed at oceanic islands which show significant volumes of underplated material (e.g. Caress *et al.* 1995). However, it is possible that a thin layer of magmatic underplate exists at or within the base of the oceanic crust, that is below the resolution and constraint provided the WA seismic data, given the degree of uncertainty on the depth of the Moho and on lower crustal *P*-wave velocities.

Modelling of the FAA provides an independent assessment of the likely presence of underplate, and shows that such a layer with a thickness <3 km is possible within the resolution of both the gravity and seismic datasets combined. Although the resolution limits of the WA seismic data do not discount the possibility of crustal underplating, it is certainly not as prevalent at the Cape Verdes as has been observed at other hotspots which have smaller swells (Watts *et al.* 1997), implying that crustal underplating is not the primary cause of swell uplift.

Swell support originating from within the upper mantle due to a region of low density would be evidenced by a long wavelength negative FAA which is not accounted for by the crustal density model alone, implying a deeper (subcrustal) origin. McNutt (1988) calculates, using forward filtering and admittance techniques, that the depth of compensation for the topographic anomaly of the Cape Verde Swell is 69 ±10 km. Lateral changes in mantle density of 20–40 kg m^{-3} account for the misfit of the crustal density–depth model to the FAA, and this corresponds to a velocity difference of 0.25 km s^{-1}, which is within the errors of the seismic modelling, making this a realistic solution that satisfies both the gravity and seismic data.

If the density variation is due to elevated temperature as opposed to a change in geochemical composition, then a heat flow anomaly will also be detected. Courtney & White (1986) observed such a heat flow anomaly with peak amplitude of +16 mW m^{-2} over the Cape Verde Swell using a series of thermal probe measurements. They show that the magnitude of this anomaly is smaller than expected if the swell uplift is solely the result of the thermal rejuvenation of the lithosphere. In addition, the lateral decrease in upper mantle density required in this study to match FAA modelling is also not sufficient to create the buoyancy required to support the swell topography alone. These findings imply that dynamic mantle upwelling must play a significant role in supporting the Cape Verde Swell.

10 CONCLUSIONS

The main conclusions that can be drawn from this study are as follows.

1. The average thickness and velocity structure of the igneous crust beneath the Cape Verde Swell is consistent with that of the standard definition for mature Atlantic oceanic crust of White *et al.* (1992). There is no evidence to support a significantly thickened crust and, consequently, that the swell is supported by a thickened crustal root.
2. At the centre of the WA profile, beneath the F-STR, the only observed crustal thickening along the entire swell transect is attributed to high velocity volcaniclastic material deposited onto the oceanic basement as a result of debris flows from the off-line islands of Fogo and Santiago. Oceanic layer 2 at this location, may also be slightly thickened as a result of magmatic intrusion related to the emplacement of the adjacent islands.
3. Although there is no direct evidence of lower crustal velocities exceeding 7.3 km s^{-1}, indicative of magmatic underplating, a thin layer of high velocity material may exist within the resolution limits of the seismic and gravity data (<3 km).
4. The long wavelength component of the FAA is not accounted for by the crustal density model alone, suggesting that there is an additional density anomaly deeper within the subcrustal lithosphere. A lateral variation in the upper mantle density of 30 kg m^{-3}, above a compensation depth of 100 km, can account for this misfit although it does not alone provide the necessary buoyancy required to support the entirety of the swell topography.
5. The results of this study imply that some form of dynamic upwelling within the asthenospheric mantle must provide the majority of the upward force required to sustain the anomalous topography of the Cape Verde Swell, with minor contributions from both a marginally thickened oceanic crust and partial thermal rejuvenation of the lithospheric mantle.

ACKNOWLEDGMENTS

DJW was supported by a Durham University Doctoral Fellowship. Seismic data acquisition was funded by the Natural Environment Research Council (grant NER/B/S/2003/00861) and the Deutsche Forschungsgemeinschaft (grants GR1964/5–1 + 7–1). We thank the officers and crew of the R/V Meteor and the sea-going scientists for their efforts. The GMT and Seismic Unix software packages (Wessel & Smith, 1998; Cohen & Stockwell, 2000, respectively) were used to create the figures for this paper. George Hellfrich and an anonymous reviewer are thanked for their positive and helpful comments.

REFERENCES

Ali, M.Y., Watts, A.B. & Hill, I., 2003. A seismic reflection profile study of lithospheric flexure in the vicinity of the Cape Verde Islands, *J. geophys. Res.,* **108,** 2239, doi:10.1029/2002JB002155.

Caress, D.W., McNutt, M.K., Detrick, R.S. & Mutter, J.C., 1995. Seismic imaging of hotspot-related crustal underplating beneath the Marquesas Islands, *Nature,* **373,** 600–603.

© 2010 The Authors, *GJI*
Journal compilation © 2010 RAS

Carlson, R.L. & Herrick, C.N., 1990. Densities and porosities in the oceanic-crust and their variations with depth and age, *J. geophys. Res.,* **95,** 9153–9170.

Carlson, R.L. & Raskin, G.S., 1984. Density of the ocean crust, *Nature,* **311,** 555–558.

Charvis, P. *et al*., 1999. Spatial distribution of hotspot material added to the lithosphere under La Reunion, from wide-angle seismic data, *J. geophys. Res.,* **104,** 2875–2893.

Cohen, J. & Stockwell, J., 2000. CWP/SU: Seismic Unix Release 34: a free package for seismic research and processing, Centre for Wave Phenomenon, Colorado School of Mines.

Contreras-Reyes, E., Grevemeyer, I., Watts, A.B., Planert, L., Flueh, E.R. & Peirce, C., 2010. Crustal intrusion beneath the Louisville hotspot track, *Earth planet. Sci. Lett.,* **289,** 323—333, doi:10.1016/j.epsl.2009.11.020.

Courtney, R.C. & White, R.S., 1986. Anomalous heat-flow and geoid across the Cape Verde Rise—evidence for dynamic support from a thermal plume in the mantle, *Geophys. J. R. astr. Soc.,* **87,** 815–867.

Crough, S.T., 1983. Hotspot swells, *Ann. Rev. Earth planet Sci.,* **11,** 165–193.

Crough, S.T. & Jurdy, D.M., 1980. Subducted lithosphere, hotspots, and the geoid, *Earth planet. Sci. Lett.,* **48,** 15–22.

Cserepes, L., Christensen, U.R. & Ribe, N.M., 2000. Geoid height versus topography for a plume model of the Hawaiian swell, *Earth planet. Sci. Lett.,* **178,** 29–38.

Dash, B.P., Ball, M.M., King, G.A., Butler, L.W. & Rona, P.A., 1976. Geophysical investigation of Cape Verde archipelago, *J. geophys. Res.,* **81,** 5249–5259.

Davis, E.E. & Lister, C.R.B., 1974. Fundamentals of ridge crest topography, *Earth planet. Sci. Lett.,* **21,** 405–413.

Day, S.J., da Silva, S.I.N.H. & Fonseca, J.F.B.D., 1999. A past giant lateral collapse and present-day flank instability of Fogo, Cape Verde Islands, *J. Volc. Geotherm. Res.,* **94,** 191–218.

Detrick, R.S. & Crough, S.T., 1978. Island subsidence, hot spots, and lithospheric thinning, *J. geophys. Res.,* **83,** 1236–1244.

Duncan, R.A. & Richards, M.A., 1991. Hotspots, mantle plumes, flood basalts, and true polar wander, *Rev. Geophys.,* **29,** 31–50.

Grevemeyer, I., Flueh, E.R., Reichert, C., Bialas, J., Klaschen, D. & Kopp, C., 2001a. Crustal architecture and deep structure of the Ninetyeast Ridge hotspot trail from active-source ocean bottom seismology, *Geophys. J. Int.,* **144,** 414–431.

Grevemeyer, I., Weigel, W., Schussler, S. & Avedik, F., 2001b. Crustal and upper mantle seismic structure and lithospheric flexure along the Society Island hotspot chain, *Geophys. J. Int.,* **147,** 123–140.

Grevemeyer, I., Helffrich, G., Faria, B, Booth-Rea, G., Schnabel, M. & Weinrebe, W., 2010. Seismic activity at Cadamosto seamount near Fogo Island, Cape Verdes-formation of a new ocean island? *Geophys. J. Int.,* **180,** 552–558, doi:10.1111/j.1365-246X.2009.04440.x.

Hamilton, E.L., 1978. Sound velocity-density relations in sea-floor sediments and rocks, *J. acoust. Soc. Am.,* **63,** 366–377.

Holm, P.M. *et al*., 2006. Sampling the Cape Verde mantle plume: evolution of melt compositions on Santo Antao, Cape Verde Islands, *J. Petrol.,* **47,** 145–189.

Holm, P.M., Grandvuinet, T., Friis, J., Wilson, J.R., Barker, A.K. & Plesner, S., 2008. An Ar-40-Ar-39 study of the Cape Verde hot spot: temporal evolution in a semistationary plate environment, *J. geophys. Res.,* **113,** B08201, doi:10.1029/2007JB005339.

I.O.C. I.H.O. & B.O.D.C., 2003. Centenary Edition of the GEBCO Digital Atlas, published on CD-ROM on behalf of the Intergovernmental Oceanographic Commission and the International Hydrographic Organisation as part of the General Bathymetric Chart of the Oceans: British Oceanographic Data Centre, Liverpool.

Lancelot, Y. & the Shipboard Scientific Party, 1978. Site 368: Cape Verde Rise, in *Init. Rep. DSDP,* Vol. 41, pp. 233–254, eds Lancelot, Y., Seibold, E. & Gardner, J.V., US Government Printing Office, Washington, DC.

Lodge, A. & Helffrich, G., 2006. Depleted swell root beneath the Cape Verde Islands, *Geology,* **34,** 449–452.

Marty, J.C. & Cazenave, A., 1989. Regional variations in subsidence rate of oceanic plates—a global analysis, *Earth planet. Sci. Lett.,* **94,** 301–315.

Masson, D.G., Le Bas, T.P., Grevemeyer, I. & Weinrebe W., 2008. Flank collapse and large-scale landsliding in the Cape Verde Islands, off West Africa, *Geochem. Geophys. Geosyst.,* **9,** Q07015, doi:10.1029/2008GC001983.

McNutt, M., 1988. Thermal and mechanical-properties of the Cape Verde Rise, *J. geophys. Res.,* **93,** 2784–2794.

McNutt, M.K., Caress, D.W., Reynolds, J., Jordahl, K.A. & Duncan, R.A., 1997. Failure of plume theory to explain midplate volcanism in the southern Austral Islands, *Nature,* **389,** 479–482.

Mitchell, J.G., Lebas, M.J., Zielonka, J. & Furnes, H., 1983. On dating the magmatism of Maio, Cape Verde Islands, *Earth-planet. Sci. Lett.,* **64,** 61–76.

Monnereau, M. & Cazenave, A., 1990. Depth and geoid anomalies over oceanic hotspot swells—a global survey, *J. geophys. Res.,* **95,** 15 429–15 438.

Monnereau, M., Rabinowicz, M. & Arquis, E., 1993. Mechanical erosion and reheating of the lithosphere—a numerical model for hotspot swells, *J. geophys. Res.,* **98,** 809–823.

Morgan, J.P., Morgan, W.J. & Price, E., 1995. Hotspot melting generates both hotspot volcanism and a hotspot swell, *J. geophys. Res.,* **100,** 8045–8062.

Morgan, J.V., Barton, P.J. & White, R.S., 1989. The Hatton Bank continental margin .3. Structure from wide-angle OBS and multichannel seismic refraction profiles, *Geophys. J. Int.,* **98,** 367–384.

Morgan, W.J., 1983. Hotspot tracks and the early rifting of the Atlantic, *Tectonophysics,* **94,** 123–139.

Müller, R.D., Sdrolias, M., Gaina, C. & Roest, W.R., 2008. Age, spreading rates, and spreading asymmetry of the world's ocean crust, *Geochem. Geophys. Geosyst.,* **9,** Q04006, doi:10.1029/2007GC001743.

Parsons, B. & Sclater, J.G., 1977. Analysis of variation of ocean-floor bathymetry and heat-flow with age, *J. geophys. Res.,* **82,** 803–827.

Pim, J., Peirce, C., Watts, A.B., Grevemeyer, I. & Krabbenhoeft, A., 2008. Crustal structure and origin of the Cape Verde Rise, *Earth planet. Sci. Lett.,* **272,** 422–428.

Pollack, H.N., Hurter, S.J. & Johnson, J.R., 1993. Heat-flow from the earths interior—analysis of the global data set, *Rev. Geophys.,* **31,** 267–280.

Pollitz, F.F., 1991. 2-stage model of African absolute motion during the last 30 million years, *Tectonophysics,* **194,** 91–106.

Ribe, N.M. & Christensen, U.R., 1994. 3-dimensional modeling of plume-lithosphere interaction, *J. geophys. Res.,* **99,** 669–682.

Robinson, E.M., 1988. The topographic and gravitational expression of density anomalies due to melt extraction in the uppermost oceanic mantle, *Earth planet. Sci. Lett.,* **90,** 221–228.

Sandwell, D.T. & Smith, W.H.F., 1997. Marine gravity anomaly from Geosat and ERS 1 satellite altimetry, *J. geophys. Res.,* **102,** 10 039–10 054.

Sclater, J.G., Jaupart, C. & Galson, D., 1980. The heat-flow through oceanic and continental-crust and the heat-loss of the earth, *Rev. Geophys.,* **18,** 269–311.

Sleep, N.H., 1992. Hotspot volcanism and mantle plumes, *Ann. Rev. Earth planet Sci.,* **20,** 19–43.

Sleep, N.H., 1995. Geophysics—a wayward plume, *Nature,* **378,** 19–20.

Stein, C.A. & Stein, S., 1992. A model for the global variation in oceanic depth and heat-flow with lithospheric age, *Nature,* **359,** 123–129.

Stillman, C.J., Furnes, H., Lebas, M.J., Robertson, A.H.F. & Zielonka, J., 1982. The geological history of Maio, Cape Verde Islands, *J. Geol. Soc.,* **139,** 347–361.

Talwani, M., Worzel, J.L. & Landisman, M., 1959. Rapid gravity computations for two-dimensional bodies with application to the Mendocino submarine fracture zone, *J. geophys. Res.,* **64,** 49–59.

Turcotte, D.L. & Oxburgh, E.R., 1973. Mid-plate tectonics, *Nature,* **244,** 337–339.

Watts, A.B. & Burov, E.B., 2003. Lithospheric strength and its relationship to the elastic and seismogenic layer thickness, *Earth planet. Sci. Lett.,* **213,** 113–131.

Watts, A.B. & Tenbrink, U.S., 1989. Crustal structure, flexure, and subsidence history of the Hawaiian Islands, *J. geophys. Res.,* **94,** 10 473–10 500.

© 2010 The Authors, *GJI*
Journal compilation © 2010 RAS

Watts, A.B. & Zhong, S., 2000. Observations of flexure and the rheology of oceanic lithosphere, *Geophys. J. Int.,* **142,** 855–875.

Watts, A.B., Tenbrink, U.S., Buhl, P. & Brocher, T.M., 1985. A multichannel seismic study of lithospheric flexure across the Hawaiian-Emperor seamount chain, *Nature,* **315,** 105–111.

Watts, A.B., Peirce, C., Collier, J., Dalwood, R., Canales, J.P. & Henstock, T.J., 1997. A seismic study of lithospheric flexure in the vicinity of Tenerife, Canary Islands, *Earth planet. Sci. Lett.,* **146,** 431–447.

Wessel, P. & Smith, W.H.F., 1998. New improved version of the Generic Mapping Tools released, *EOS, Trans. Am. geophys. Un.,* **79,** 579.

White, R.S., Detrick, R.S., Sinha, M.C. & Cormier, M.H., 1984. Anomalous seismic crustal structure of oceanic fracture-zones, *Geophys. J. R. astr. Soc.,* **79,** 779–798.

White, R.S., McKenzie, D. & Onions, R.K., 1992. Oceanic crustal thickness from seismic measurements and rare-earth element inversions, *J. geophys. Res.,* **97,** 19 683–19 715.

Williams, C.A., Hill, I.A., Young, R. & White, R.S., 1990. Fracture-zones across the Cape Verde Rise, NE Atlantic, *J. Geol. Soc.,* **147,** 851–857.

Wilson, J.T., 1963. Evidence from islands on spreading of ocean floors, *Nature,* **197,** 536–538.

Zelt, C.A. & Smith, R.B., 1992. Seismic traveltime inversion for 2-D crustal velocity structure, *Geophys. J. Int.,* **108,** 16–34.

© 2010 The Authors, *GJI*
Journal compilation © 2010 RAS